2007

Particle Based Plasma Simulation for an Ion Engine Discharge Chamber

Sudhakar Mahalingam
Wright State University

PARTICLE BASED PLASMA SIMULATION

FOR AN ION ENGINE DISCHARGE CHAMBER

A dissertation submitted in partial fulfillment of the
requirements for the degree of
Doctor of Philosophy

By

SUDHAKAR MAHALINGAM
B.E.M.E., Madurai Kamaraj University, 1996
M.S.M.E., Wright State University, 2002

2007
Wright State University
Dayton, Ohio 45435-0001

WRIGHT STATE UNIVERSITY
SCHOOL OF GRADUATE STUDIES

September 28, 2007

I HEREBY RECOMMEND THAT THE DISSERTATION PREPARED UNDER MY SUPERVISION BY Sudhakar Mahalingam ENTITLED Particle Based Plasma Simulation for an Ion Engine Discharge Chamber BE ACCEPTED IN PARTIAL FULFILLMENT OF THE REQUIREMENTS FOR THE DEGREE OF `Doctor of Philosophy`.

James A. Menart, Ph. D.
Dissertation Director

Ramana V. Grandhi, Ph. D.
Director, Engineering Ph.D. Program

Joseph F. Thomas, Jr., Ph. D.
Dean, School of Graduate Studies

Committee on
Final Examination

James A. Menart, Ph. D.

Scott K. Thomas, Ph. D.

Henry Daniel Young, Ph. D.

Ravi Penmetsa, Ph. D.

William F. Bailey, Ph.D.

ABSTRACT

Mahalingam, Sudhakar. Ph.D. Department of Mechanical and Materials Engineering, Wright State University, 2007. Particle Based Plasma Simulation for an Ion Engine Discharge Chamber.

Design of the next generation of ion engines can benefit from detailed computer simulations of the plasma in the discharge chamber. In this work a complete particle based approach has been taken to model the discharge chamber plasma.This is the first time that simplifying continuum assumptions on the particle motion have not been made in a discharge chamber model. Because of the long mean free paths of the particles in the discharge chamber continuum models are questionable.

The PIC-MCC model developed in this work tracks following particles: neutrals, singly charged ions, doubly charged ions, secondary electrons, and primary electrons. The trajectories of these particles are determined using the Newton-Lorentz's equation of motion including the effects of magnetic and electric fields. Particle collisions are determined using an MCC statistical technique. A large number of collision processes and particle wall interactions are included in the model. The magnetic fields produced by the permanent magnets are determined using Maxwell's equations. The electric fields are determined using an approximate input electric field coupled with a dynamic determination of the electric fields caused by the charged particles. In this work inclusion of the dynamic electric field calculation is made possible by using an inflated plasma permittivity value in the Poisson solver. This allows dynamic electric field calculation with minimal computational requirements in terms of both computer memory and run time. In addition, a number of other numerical procedures such as parallel processing have been implemented to shorten the computational time.

The primary results are those modeling the discharge chamber of NASA's NSTAR ion engine at

its full operating power. Convergence of numerical results such as total number of particles inside the discharge chamber, average energy of the plasma particles, discharge current, beam current and beam efficiency are obtained. Steady state results for the particle number density distributions and particle loss rates to the walls are presented. Comparisons of numerical results with experimental measurements such as currents and the particle number density distributions are made. Results from a parametric study and from an alternative magnetic field design are also given.

Table of Contents

List of Figures

List of Tables

Nomenclature

$\vec{A}$	Magnetic vector potential, Tesla m or Gauss cm
A_θ	θ component of the magnetic vector potential, Tesla m or Gauss cm
$\vec{B}$	Magnetic flux density vector, Tesla or Gauss
$B(\epsilon_{inc,e})$	Known function energy value in ionization reaction, 10 eV
B_r	Radial component of the magnetic flux density, Tesla or Gauss
B_z	Axial component of the magnetic flux density, Tesla or Gauss
$\vec{D}$	Electric displacement vector, C m^2
$\vec{dl}$	Differential position vector, m
$\vec{dS}$	Differential surface area vector, m^2
$\|e\|$	Absolute electron charge, 1.6×10^{-19} C
e	Electron charge, -1.6×10^{-19} C
$\vec{E}$	Electric field vector, V m^{-1}
E_r	Radial component of the electric field, V m^{-1}
E_z	Axial component of the electric field, V m^{-1}
F_t	Thrust reduction factor
f_B	Fraction of ion current losses in the chamber as beam ion current
f_w	Factor for fictitious time step control in DADI iteration
$f_{x,wall}(sp)$	Number of macro particles of species type, sp, collected at the wall location during $t_{interval}$
g	Gravitational force, 9.81 ms^{-2}

$\vec{H}$	Magnetic field vector, A m^{-1}
H_c	Coercive force of the magnets, A m^{-1}
I_{AC}	Accelerator grid current
I_B	Beam ion current, A
I_B^*	Variant of beam ion current, A
I_B^+	Beam ion current due to singly charged ion, A
I_B^{++}	Beam ion current due to doubly charged ion, A
I_C	Cathode current, A
I_D	Discharge current, A
I_N	Neutralizer cathode current, A
$I_{neutral}$	Neutral flow rate, A-eq (or) kg s^{-1}
I_P	Total ion production current inside the discharge chamber, A
I_{sp}	Specific impulse, s
$I_{sp,wall}$	Wall current collected for species type sp, A
$\vec{J}$	Current density, A m^2
K_n	Knudsen number
k_B	Boltzmann constant, 1.38025×10^{-23} J K^{-1}
L	Characteristic lenght, m
L_2	Normalized residual value
m_i	Mass of an i-th type particle, kg
m_e	Electron mass, 9.11×10^{-31} kg
m_{ion}	Xenon ion mass, 2.18024×10^{-25} kg
m_{inc}	Incident particle mass, kg
m_{Xe}	Neutral xenon mass, 2.18024×10^{-25} kg
$\dot{m}_{cathode}$	Neutral flow rate through discharge chamber hollow cathode, kg s^{-1} or sccm

$\dot{m}_{main}$	Neutral flow rate through main plenum, kg s^{-1} or sccm
$\dot{m}_p$	Propellant or neutral flow rate, kg s^{-1} or sccm
$NchargeTypes$	Total number of charge particle types in the discharge chamber
N_{coll}	Total number of colliding particles
N_{cp}	Number of computer particles
$N_{e,cell}$	Average number of computer electron particles per cell
$N_{e,coll}$	Total number of colliding electrons
$N_{iter,charge}$	Number of iterations for charge particles convergence
$N_{iter,Xe}$	Number of iterations for Xe convergence
N_{macro}	Total number of computer or macro particles
$N_{physical}$	Total number of physical particles
$N_{+,coll}$	Total number of colliding Xe^+ particles
N_{proc}	Number of processors
N_r	Number of radial grid points
N_{SRB}	Number of Spatial Region Boundaries
$N_{T,sp}$	Total number of particles present in the chamber for species type sp
N_{total}	Total number of particles in the discharge chamber
N_z	Number of axial grid points
n	Number density of plasma particle, m^{-3}
n_e	Number density of electrons, m^{-3}
n_i	Number density of ions, m^{-3}
$n_{sp,i,j}$	Species number density at (i,j) computational grid point, m^{-3}
$n_{t,i,j}$	Number density value of the target particle at (i,j)th computational cell, m^{-3}
$n_{t,max}$	Maximum number density value of the target particle, m^{-3}
n_+	Number density of Xe^+ particle, m^{-3}

$n_{+,max}$	Maximum number density value of the Xe^+ particle, m^{-3}
n_0	Number density of neutrals, m^{-3}
$n_{0,max}$	Maximum number density value of the neutral particle, m^{-3}
$\dot{n}_P$	Primary electron source rate, m^{-3} s^{-1}
$\dot{n}_{Xe,cathode}$	Neutral source rate through the discharge chamber hollow cathode, m^{-3} s^{-1}
$\dot{n}_{Xe,main}$	Neutral source rate through the main plenum, m^{-3} s^{-1}
$ncell_{sp,i,j}$	Cell-centered species number density at (i,j)th computational cell, m^{-3}
$ncell_{sp,iu,ju}$	Cell-centered species number density at (iu,ju)th uniform computational cell, m^{-3}
$ngrid_{sp,iu,ju}$	Species number density at (iu,ju) grid point in the uniform computational mesh, m^{-3}
P	Probability
P_{CH}	Cathode heater power, W or kW
P_{NH}	Neutralizer cathode heater power, W or kW
P_{IN}	Input power, W or kW
P_{null}	Null collision probability
$P_{e+,null}$	Null collision probability for electron-Xe^+ collisions
$P_{e0,null}$	Null collision probability for electron-neutral collisions
$P_{+0,null}$	Null collision probability for Xe^+-neutral collisions
$Q_{i,j}$	Charge at the cell corner node (i,j)
$Q_{sp,i,j}$	Species charge at the cell corner node (i,j)
q	Charge value of a particle
q_i	Charge of an i-th type particle, C
q_{sp}	Charge of *sp* type species , C
R, R_1, R_2	Random numbers between 0 and 1
R_3, R_4	Random numbers between 0 and 1
Res_{global}	Global residual value of Poisson equation

Res_{local}	Localized residual value of Poisson equation
$\hat{r}$	Unit vector in the radial direction
T	thrust, N or mN
T_{actual}	Actual thrust generated, N or mN
T_e	Electron temperature, eV or K
T_{ideal}	Ideal thrust, N or mN
$T_{Xe,cathode}$	Wall temperature at the cathode neutral source location, eV or K
$T_{Xe,main}$	Wall temperature at the main feed location, eV or K
TP	Test parameter in DADI iteration
t	Time, s
t_s	Wall sheath thickness, m
u_{ion}	Ion exit velocity, ms^{-1}
V	Volume, m^{-3}
V_{AC}	Accelerator grid voltage, V
V_B	Beam voltage, V
V_C	Cathode voltage, V
V_S	Screen grid voltage, V
V_D	Discharge voltage, V
V_N	Neutralizer cathode voltage, V
$V_{1/2cell,i,j}$	Half-cell volume for the computational cell corner node (i,j), m^3
$V_{cell,i,j}$	Full cell volume for the computational cell corner (i,j), m^3
V_{ucell}	Uniform grid cell volume, m^3
V_{cTip}	Cathode tip volume, m^3
V_{main}	Main neutral feed tip volume, m^3
$\lvert\vec{v}_e\rvert$	Speed of an electron, m s^{-1}

$\|\vec{v}_{inc}\|$	Speed of an incident particle, m s^{-1}
$\|\vec{v}_{pe}\|$	Speed of a primary electron, m s^{-1}
$\|\vec{v}_{+}\|$	Ion particle speed, m s^{-1}
$\|\vec{v}_{Xe,cathode}\|$	Speed of a neutral at the cathode feed location, m s^{-1}
$\|\vec{v}_{Xe,main}\|$	Speed of a neutral at the main feed location, m s^{-1}
W_{macro}	Computer or macro particle weight
w_z	Axial position fraction of particle in a computation cell
w_r	Radial position fraction of particle in a computation cell
w_z^+, w_z^-	Weighting functions in the axial direction
w_r^+, w_r^-	Weighting functions in the radial direction
Xe, XeI	Neutral xenon
Xe, XeI	Neutral xenon
Xe^+, $XeII$	Singly charged xenon ion
Xe^{++}, $XeIII$	Doubly charged xenon ion
Xe^*	Excited neutral xenon
Xe^{+*}	Excited singly charged xenon ion
Xe^{++*}	Excited doubly charged xenon ion
Xe_2	Molecular xenon
$\vec{x}_i$	Particle position vector, m
Z	Charge-state for xenon ions
z_p	Particle's position in grid units in the axial direction
r_p	Particle's position in grid units in the radial direction

Greek

α	Correction factor due to the double ion content in the beam current

α_L	Collision energy loss factor
α_r^{ee+}	Electron-electron-Xe^+ three-body recombination rate coefficient, $m^6\ s^{-1}$
α_r^{ee++}	Electron-electron-Xe^{++} three-body recombination rate coefficient, $m^6\ s^{-1}$
χ	Scattering angle
$\overrightarrow{\nabla}$	gradient operator
Δt	Time step size, s
Δt_e	Time step size for electron, s
Δt_f	Fictitious time step in the DADI iteration
Δt_{ion}	Time step size for ion, s
Δt_{Xe}	Time step size for neutral xenon, s
$\Delta r_{i,j}$	Radial grid spacing for the (i,j)th cell, m
$\Delta z_{i,j}$	Axial grid spacing for the (i,j)th cell, m
η_i	Grid units in the axial direction
$\eta_{i,j}$	Lower left corner of the computational cell in grid units in the axial direction
η_{prop}	Discharge chamber propellant utilization efficiency, %
η_t	Overall thruster efficiency, %
ϵ_B	Beam ion production cost, eV/ion or W/A
ϵ_e	Incident electron particle kinetic energy, eV
ϵ_{ex}	Threshold energy for e-Xe excitation collision, eV
$\epsilon_{ex,+}$	Threshold energy for e-Xe^+ excitation collision, eV
$\epsilon_{ex,++}$	Threshold energy for e-Xe^{++} excitation collision, eV
ϵ_{ionz}	Ionization potential, eV
ϵ_{inc}	Incident particle kinetic energy, eV
$\epsilon_{inc,ion}$	Incident ion particle kinetic energy, eV
ϵ_N	Neutral particle kinetic energy, eV

ϵ_p	Plasma ion production cost, eV/ion or W/A
ϵ_+	Ion particle kinetic energy, eV
$\epsilon_{scat,e}$	Scattered electron energy after collision, eV
$\epsilon_{scat,ion}$	Scattered ion energy after collision, eV
ϵ_{se}	Secondary electron energy, eV
ε_0	Permittivity of free space constant, 8.8541×10^{-12} F m^{-1}
ε_a	Artificial plasma permittivity, F m^{-1}
γ_i	Secondary electron emission coefficient
λ	Mean free path of collision, m
λ_D	Debye length, m
$\vec{\mu_0}$	Permeability vector, H m^{-1}
ν_c	Constant collision frequency, s^{-1}
$\nu_{e0,c}$	Constant collision frequency for electron-neutral collisions, s^{-1}
$\nu_{e0,el}(\epsilon_e)$	Collision frequency for electron-neutral elastic collisions, s^{-1}
$\nu_{e0,ex}(\epsilon_e)$	Collision frequency for electron-neutral excitation collisions, s^{-1}
$\nu_{e0,iz}(\epsilon_e)$	Collision frequency for electron-neutral ionization collisions, s^{-1}
$\nu_{e0,j}(\epsilon_e)$	Collision frequency for j^{th} type electron-neutral collisions, s^{-1}
$\nu_{e+,c}$	Constant collision frequency for electron-Xe$^+$ collisions, s^{-1}
$\nu_{e+,ex}(\epsilon_e)$	Collision frequency for electron-Xe$^+$ excitation collisions, s^{-1}
$\nu_{e+,iz}(\epsilon_e)$	Collision frequency for electron-Xe$^+$ ionization collisions, s^{-1}
$\nu_{+0,c}$	Constant collision frequency for Xe$^+$-neutral collisions, s^{-1}
$\nu_{+0,el}(\epsilon_+)$	Collision frequency for Xe$^+$-neutral elastic collisions, s^{-1}
$\nu_{+0,cx}(\epsilon_+)$	Collision frequency for Xe$^+$-neutral charge-exchange collisions, s^{-1}
ω_{pe}	Plasma frequency, radians s^{-1}
ϕ	Electric potential, V

ϕ_{bulk}	Bulk plasma potential, V
ϕ_{static}	Static electric potential, V
$\phi_{dynamic}$	Dynamic electric potential, V
ϕ_{wf}	Work function necessary for secondary emission, eV
ϕ_{wall}	Wall electric potential, V
ψ	Azimuthal angle
ρ	Charge density, C m^{-3}
$\rho_{i,j}$	Charge density value at the grid cell node (i,j), C m^{-3}
$\rho_{sp,i,j}$	Charge density value at cell node (i,j) for the species type *sp*
σ	Collision cross section area, m^2
$\sigma_T(\epsilon_{inc})$	Total collision cross section, m^2
$\sigma_T(\epsilon_{inc})\|\vec{v}_{inc}\|$	Total collision swept volumetric rate, m^3 s^{-1}
$\sigma_T(\epsilon_{inc})\|\vec{v}_{inc}\|$	Total collision swept volumetric rate, m^3 s^{-1}
$\sigma_{e0,T}(\epsilon_e)$	Total electron-neutral collision cross section area, m^2
$\sigma_{e0,el}(\epsilon_e)$	Electron-neutral elastic collision cross section area, m^2
$\sigma_{e0,ex}(\epsilon_e)$	Electron-neutral excitation collision cross section area, m^2
$\sigma_{e0,iz}(\epsilon_e)$	Electron-neutral ionization collision cross section area, m^2
$\sigma_{e+,T}(\epsilon_e)$	Total electron-Xe^+ collision cross section area, m^2
$\sigma_{ee+,r}(\epsilon_e)$	Electron-electron-Xe^+ three-body recombination collision cross section area, m^2
$\sigma_{e+,ex}(\epsilon_e)$	Electron-Xe^+ excitation collision cross section area, m^2
$\sigma_{e+,iz}(\epsilon_e)$	Electron-neutral ionization collision cross section area, m^2
$\sigma_{+0,T}(\epsilon_+)$	Total Xe^+-neutral collision cross section area, m^2
$\sigma_{+0,el}(\epsilon_+)$	Xe^+-neutral elastic collision cross section area, m^2
$\sigma_{+0,cx}(\epsilon_+)$	Xe^+-neutral charge-exchange collision cross section area, m^2
$\sigma_{ee+,r}$	Electron-electron-Xe^+ three-body collision cross section area, m^2

$\sigma_{ee++,r}$	Electron-electron-Xe^{++} three-body collision cross section area, m^2
Θ	Scattering angle in the center of mass frame for Xe^{+}-neutral collision
ξ_j	Grid units in the radial direction
$\xi_{i,j}$	Lower left corner of the computational cell in grid units in the radial direction

Subscripts

e	Referring an electron
i	Grid cell node index in the z-direction or referring an i^{th} particle type
ion	Referring a positively charged particle
j	Grid cell node index in the r-direction
max	Referring a maximum value
$+$	Referring singly charged xenon ion
$++$	Referring doubly charged xenon ion
sp	Species type
Xe	Refers a xenon particle
Xe^{+}	Refers a singly charged ion particle
Xe^{++}	Refers a doubly charged ion particle

Superscripts

k	Iteration index in DADI scheme

Acronyms

ADI	Alternating Direction Implicit Scheme
DADI	Dynamic Alternating Direction Implicit Scheme
DCIU	Digital Control Interface Unit
DS1	Deep Space 1 Mission

ELT	Extended Life Test
EMT	Engineering Model Thruster
EOL	End-of-Life Measurement
FT	Flight Thruster
FMT	Functional Model Thruster
GRC	Glenn Research Center
JPL	Jet Propulsion Laboratory
LDT	Life Demonstration Test
NEXT	NASA's Evolutionary Xenon Thruster
NMP	New Millennium Program
NSTAR	NASA Solar Electric Propulsion Technology Application Readiness Program
PEPL	Plasmadynamics & Electric Propulsion Laboratory
PPU	Power Processing Unit
SEPS	Solar Electric Propulsion System
SRB	Spatial Region Boundary
TH	Throttle condition
XFS	Xenon Feed System
XOOPIC	X-grafix Object Oriented Particle In Cell Code

ACKNOWLEDGEMENTS

I would like to take this opportunity to thank my advisor Dr. James Menart who is my Guru at Wright State University. He had introduced me to the world of ion engines and computational modeling since from the days of my M.S. degree at WSU. Dr. Menart is my prime motivator on this computational project who accelerated me to working towards the advancement of discharge chamber modeling. His ideas are innovative which have helped me to understand the physical concepts of ion engines and plasmas in general. It is my great pleasure to work with a great advisor like him. I would like to thank my dissertation committee members Dr. William Bailey, Dr. Ravi Penmetsa, Dr. Scott Thomas, and Dr. Daniel Young for their valuable time and to critique my dissertation report. Also I would like to thank Dr. Thomas York who had served in my research proposal committee. I would like to specially thank Dr. William Bailey for forwarding the references and the journal articles on plasma simulations. I would like to thank Dr. Joseph Shang for his constant encouragement to see the benefits of the research/hard work and for his frequent words "Hang in there". I would like to thank Dr. Ramana Grandhi, Director of PhD in Engineering program for granting my final year PhD fellowship.

I would like to thank NASA Glenn Research Center and Grant Monitors Mr. Michael J Patterson and Dr. Thomas Stueber for their financial support throughout my PhD education and their time to critique my technical papers. I would like to thank Dr. Daniel Herman at NASA GRC who had provided the experimental data which are really helpful on this computational model.

Special thanks to my friend Tim Leger who is the administrator of computer clusters at WSU. He has helped me on numerous things on this computational project. My discussions especially with Tim on computational techniques, parallelization of codes, tracking of the coding problems, and compilation issues have helped me to learn and update myself on the computational code

developments. I would like to thank my lab mates who were in Dr. Menart's Plasma Lab Group during my research at WSU: Anuya Joglekar, Andrew Kurpik, Carl Atzbach, Dr. Hong Yan, Malik, Scott Stanfield, Sean Henderson, Shirin Deshpande, Taiwo Ogunjobi, William Bennett and other colleagues at WSU who helped me directly or indirectly in this project. A special thank to Scott Stanfield for proof reading my document.

I would like to thank my parents Mr. Mahalingam Natarajan and Mrs. Thilagavathy Mahalingam in India whose continuing blessings throughout my life and studies at WSU have made possible to achieve one of their dreams. I would like to thank my sister Usha Akka and my brothers: Saravana Anna, Sankar and Karthick for their encouragement on this project. Special thanks to Karthick for proof-reading my final document and making my Nomenclature possible. I would like to acknowledge the last and special person my wife Mythili who encouraged me throughout my Ph.D and that has made possible for me to achieve many things on my project. During my PhD work we are blessed with two kids Thillainayaki and Nathan whom I am hoping that they will accomplish the goals that I am setting forth on this research. I dedicate my dissertation to all of my family members!

1

Introduction

The ion engine has proven to be a successful electric propulsion system for space missions in NASA's Solar Electric Propulsion Technology Application Readiness (NSTAR) program on the Deep Space 1 (DS1) mission [Polk et al. 1999]. The NSTAR ion thruster on DS1 mission has given a life time operation of 16,265 hours ($\sim$ 2 years) while the NSTAR ion thruster studied in the extended life test (ELT) program at the Jet Propulsion Laboratory (JPL) was operated for 30,352 hours ($\sim$ 3.5 years) [Sengupta et al. 2003]. NASA is interested in expanding these electric thrusters so that they provide longer term life in space for missions to study distance planets such as Jupiter, and to study the galaxy around us. The next-generation ion engine, such as NASA's Evolutionary Xenon Thruster (NEXT) [Patterson et al. 2002], NASA's High Power Electric Propulsion Thruster program (HiPEP) [Elliott et al. 2004] and the Nuclear-Electric Xenon Ion System(NEXIS) [Polk et al. 2003] are expected to provide a life time of 5 to 10 years of continuous operation in space.

1.1 Research Goals

The design of the next generation of ion engines which for long-travel space missions can benefit from computational models. Since life times tests of 5 to 10 years are not realistic, lifetime predictions will have to be done by modeling or at least extrapolated by using computer models. In addition

to the time restriction the experimental technique for extending the performance of ion engines there are other limitations to experimental development work. Experimentally based ion engine research is constricted by its exorbitant cost, the difficulty in performing extensive and detailed parametric studies, and limitations of using the Langmuir probes to access and measure different plasma characteristics for all regions within the discharge chamber. Computational modeling can help researchers and designers understand the plasma characteristics and how these characteristics can be used to improve the performance of the ion engine. Detailed parametric studies are possible with computational tools. While experimental work in ion engines will always be needed, the current situation is such that better and better computer models of all aspects of the ion engine need to be developed. The goal of the current work is to develop a detailed model of the plasma in the discharge currently available. Specifically this work will:

1. produce the only model of the plasma in the discharge chamber that treats all important species as particles and never invokes the diffusion approximation,

2. produce the first ion engine discharge chamber model that has some coupling between the charged particle density calculations and the solution of Poisson's equation for the electric fields present in the discharge chamber,

3. produce the first ion engine discharge chamber model that includes the effects of recombination collisions in a detailed manner, and

4. test the developed computational model on the NSTAR ion engine discharge chamber.

In the future this computational model can be used to improve the design of the next-generation of ion engines and enhance experimental research currently being undertaken. It is believed that this computational model will lead the way to even more detailed model development. It is believed that the way to obtain more detailed models is to push the direction of model development from the continuum based approaches to a particle based approach. The computational models that exist currently for ion engine discharge chambers either model only a few species in the discharge

chamber using particle-tracking methods [Arakawa and Yamada 1990; Mahalingam and Menart 2002; Stueber 2005] or use a hybrid approach where the primary electrons are tracked with a particle based technique and the rest of the plasma species are modeled using a diffusion approach i.e., based on fluid assumptions [Arakawa and Ishihara 1991; Wirz and Katz 2005]. Our present model employs a particle-tracking approach for all of the major particles inside the discharge chamber, primary electrons, secondary electrons, first ions, second ions, and neutrals. By employing a particle based approach, the need for poorly defined diffusion coefficients is eliminated and no assumptions are made on the distribution functions for any of the particle species. Full particle techniques also eliminate assumptions that are sometimes made in modeling particle collisions. A detailed discussion on the computational models currently available to model the plasma in an ion engine discharge chamber are presented in the literature survey section of this dissertation.

1.2 Working Principle of an Ion Engine

An ion engine produces thrust by ejecting positively charged ions, at high speed, out the back end of the thruster. The positive ions are created inside the discharge chamber due to ionizing collisions of high energy electrons with the neutral particles. These ions are accelerated to high speeds by applied electric fields and leave the back end of the discharge chamber. This exiting of ions from the back end of the thruster produces thrust for the spacecraft. The faster these ions leave the rear of the engine the more thrust per unit mass of propellant is produced.

The operation of an ion engine can best be understood by first studying the components that make up the engine. Figure 1.1 shows a schematic of different components of an ion engine and particle trajectories. The primary components of an ion engine are: the discharge chamber, the cathode, the grids, the neutralizer, the magnetic circuit, the propellant injection system, and the power supplies. The components and their operation are given in the following paragraphs.

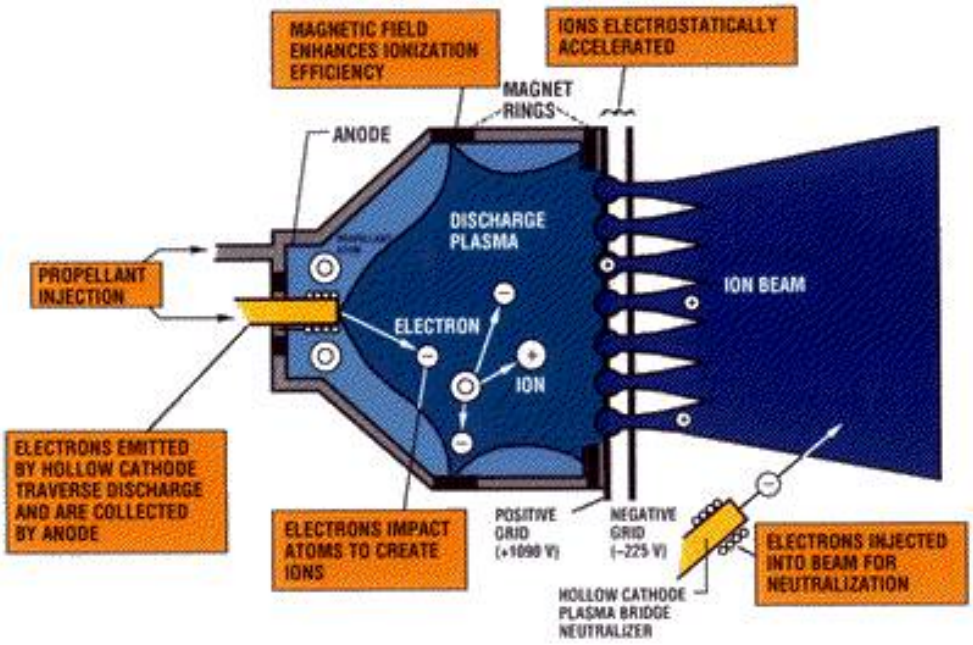

Figure 1.1: Schematic of an ion engine (Source: NASA Glenn Research Center).

1.2.1 Discharge Chamber Components

The discharge chamber is a large cavity where the positive ions are generated. The discharge chamber is either of an axisymmetric design or a rectangular shaped design. Discharge chambers of the ion thrusters used on Deep Space 1 (DS1) [Polk et al. 1999] and on NASA's Evolutionary Xenon Thrusters (NEXT) [Patterson et al. 2002] are of cylindrical shape. At present NASA also investigates rectangular shaped discharge chambers for use on future space missions [Elliott et al. 2004]. The discharge chamber houses has all the components required for the operation of an ion engine attached to it. The choices for ion engine discharge chamber wall materials are aluminum, titanium or steel. Aluminum and titanium materials are preferred over steel as a wall material because of their resistance to rust, their light weight, and their poles align parallel with the magnetic field and produce feebly affect the magnetic field inside the discharge chamber. If steel is used, the permanent magnets need to be placed inside the discharge chamber wall. In most of the discharge chamber designs the walls are maintained at the anode potential to complete the electrical circuit.

The cathode is placed normally at the center of the discharge chamber near the back wall of the discharge chamber. The cathodes used in ion engines are normally of the hollow cathode type. The emission of electrons from the cathode walls is carried out by heating an electron emitting material to a high temperature. This causes the electrons to be ejected from the surface. The electrons which exit the cathode are known as the primary electrons and have an energy approximately equivalent to the discharge voltage times the electron charge. The discharge chamber cathode assembly is enclosed in a cathode keeper assembly which helps to mitigate erosion of the hollow cathode. Keepers also help to maintain the plasma discharge.

The grids are two parallel plates which are placed adjacent to each other at the downstream end of the discharge chamber. The plates are convex shaped and have an array of holes in them. These plates have a high electric potential difference between them. The first plate, called the screen grid, is maintained at a high positive electric potential; and the second plate, called the accelerator grid, is maintained at a high negative electric potential. There are ion engines that use a three parallel plate system. In this arrangement, the third plate, referred to as the decelerator grid, is placed next to the accelerator grid. The decelerator grid is maintained at a positive electric potential relative to the accelerator grid. The purposes of the decelerator grid system are: 1) to stop the neutralizer cathode electrons from back streaming into the discharge chamber and 2) to slow down the high energetic ions. This slowing down of ions is useful for low specific impulse missions [Jahn 1968].

In Figure 1.1 an example of the voltage values on the two grid plates is given. The ions produced inside the discharge chamber are attracted towards the highly negative charged plate which accelerates them to a high speed. These high speed ions leave the discharge chamber via the grid holes. This stream of ions leaving through the grid holes is called the ion beam. The electric potential at grids strongly repels the electrons back in to the discharge chamber. The flux of neutrals through the grids is controlled by the size of grid holes. The material used for the grid plates possesses low-sputter yield properties such as molybdenum, titanium, and carbon graphite.

The neutralizer is another hollow cathode which is normally located at the wall outside of the

discharge chamber close to the grids. The purpose of a neutralizer is to neutralize the ion beam that leaves the discharge chamber. This is necessary to prevent the outer surfaces of the ion thruster from obtaining a net positive charge. The neutralizer emits compensating electrons from those collected at the discharge chamber walls and injects them into the exiting ion beam. These electrons recombine with the ions and convert them into neutrals. Similar to the discharge chamber cathode assembly, there is an enclosure cathode keeper assembly used on the neutralizer.

The magnetic circuit in the discharge chamber is generated with permanent magnets located on the walls of the discharge chamber. These magnets are normally made out of samarium-cobalt. Presently ion engine discharge chambers use ring-cusped magnetic fields. They are so named because the cusp region of the field forms a ring around the circumference of the discharge chamber. This ring cusp magnetic circuit creates a barrier over the anode biased discharge chamber walls which hinders the electrons from reaching the walls. This barrier does not hinder all electrons from reaching the walls because some electron loss is required to maintain the electrical circuit. The design of these magnetic circuits is important to efficient ion engine performance. If primary electrons are lost to the anode biased walls before undergoing ionizing collisions with neutrals, the efficiency of the engine will be poor.

The propellant feed system supplies the neutral gas to the inside of the discharge chamber. The neutral gas is the propellant for an ion engine. Xenon is the most used propellant in ion thrusters. Argon, cesium, krypton and mercury are the other choices of neutral propellants which have been used. The propellant feed location is either at the upstream end or at the downstream end of the discharge chamber. At present NASA uses propellant feed locations at the downstream end which inject the gas towards the back wall of the discharge chamber. This increases the neutral's residence time in the discharge chamber and ionization frequency. Also a fraction ($\sim 5-10\%$) of the propellant is fed into the chamber is through the hollow cathode tube. Propellant is also fed through the neutralizer. The propellant mass flow rates at the cathode locations are normally an order of magnitude smaller than the mass flow rates through the main propellant feed locations. The DS1

NSTAR in-flight ion thruster carried about 80 kg of xenon propellant. Modern ion thrusters may be expected to carry a few tons of propellant [Polk et al. 2003].

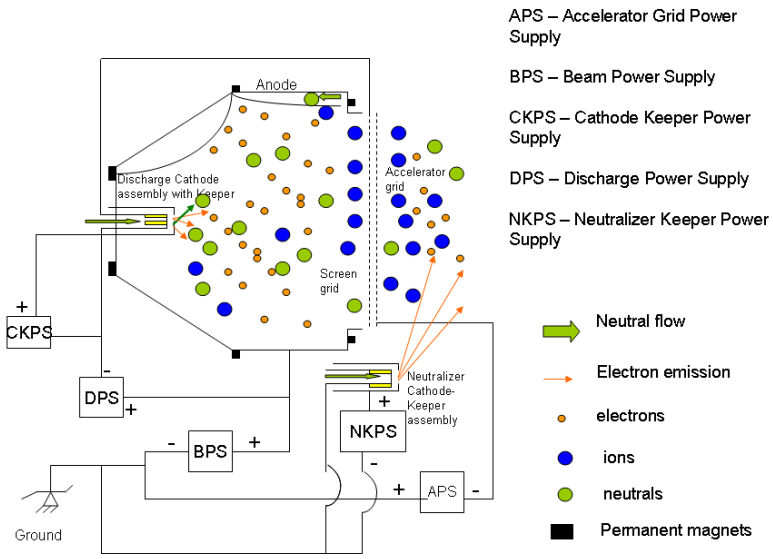

Figure 1.2: Ion engine discharge chamber electric circuit.

A number of power supply units are used on an ion engine. Electrical power needs to be supplied to the following components: cathode, cathode keeper, discharge chamber walls, grids and neutralizer. The power supply units are shown in Figure 1.2. The cathode heater supply and the neutralizer cathode heater supply are not shown in this figure. The electrical power required to operate an ion engine can range from a few hundred watts to 100's of kilowatts. In the DS1 NSTAR ion thruster the electrical power used was 0.5 - 2.3 kW [Polk et al. 1999]. The next generation ion thrusters are designed to operate with larger required power and with higher propellant throughput.

1.2.2 Plasma Particle Motion

In the discharge chamber cavity the plasma is created by the ionizing collisions of electrons with the neutrals. Discharge chamber plasmas consist of the following five major particle types: primary

electrons, secondary electrons, singly charged positive ions, doubly charged positive ions, and neutrals. In this section the means by which these particles are created inside the discharge chamber, their interactions with other particles, and their interactions with electric and magnetic fields are discussed. In this work all charge particles are modeled separately to analyze the behavior of the plasma inside the discharge chamber.

Primary electrons are high energy electrons that are emitted from the hollow cathode which is placed inside the discharge chamber. The emitted electrons move outward in all downstream directions. Once emitted out of the cathode tip the primary electrons direction of travel is influenced by collisions with other particles, collisions with the walls, and by the electric and magnetic fields inside the discharge chamber. These electrons are important since they start and sustain the plasma. Primary electrons deliver a substantial amount of energy to the plasma. If kept in the discharge chamber primary electrons have the best chance of creating an ion.

During a primary electron's motion it undergoes collision with neutrals, ions, and secondary electrons. When a primary electron undergoes a collision with a neutral particle the collision can be one of the following types: 1. A primary electron ionizes a neutral particle. In this process a neutral atom becomes an ion and it releases one electron from its orbit. The released electron is known as a secondary electron. 2. A primary electron collides with a neutral and produces a double ion. In this process two secondary electrons are knocked from the neutral particle. This type of collision rarely happens in ion engines because of the high energies required. 3. A primary electron excites a neutral particle. In this type of collision the primary electron losses a portion of its energy. 4. A primary electron interacts elastically with a neutral. This type of collision simply changes the direction of travel of the primary electron and almost no energy is lost. In the first three collisions listed above the primary electron loses a part of its energy and can turn into a secondary electron. After each of these four types of collisions the direction of travel of the colliding primary electron changes.

Similar to the electron-neutral collisions, a primary electron undergoes collisions with an ion with

the following possible outcomes: 1. The primary electron ionizes the ion. In this process the ion moves to the next higher charged state (a single ion becomes a double ion) by releasing one electron from its orbit. This electron is known as a secondary electron. 2. The primary electron excites an ion to a higher state and loses part of its energy. 3. The primary electron recombines with an ion and a neutral is produced. In this case the primary electron is lost. 4. The primary electron collides elastically with the ion. This type of collision simply redirects the primary electron. After collision types 1, 2, and 4 the direction of travel of the primary electron changes. Collisions 1 and 2 reduce the energy of the primary electron, while collision 3 results in the electron becoming part of an atom and no longer existing as a separate entity. In collision 4 the primary electron's motion is simply redirected and energy loss is minuscule.

When one electron collides with another electron the possible outcomes are: 1) the electrons simply change their direction of travel or 2) the colliding electrons exchange some of their energy. These types of collisions are generally two electrons repelling one another because of their like charge. Such collisions can be properly modeled if the electric fields between particles are handled precisely. This is a difficult task to do and is only weakly accounted for in this work.

The magnetic field produced by the permanent magnets confines the primary electrons inside the discharge chamber. In the discharge chamber the mean free path of an electron involved in an ionizing collision with a neutral is on-the-order of one meter. Hence the electron has to be confined because most discharge chambers have diameters that are less than one meter and some can be as small as 0.08 m. The direct loss of electrons to the anode biased walls makes the probability of an ionizing collision small. For this reason a magnetic field must be used to inhibit the motion of the electrons to the chamber walls. It is possible to achieve this magnetic field with an electromagnet, but this increases the electrical power requirements of the engine. With permanent magnetics one can eliminate this power requirement. At this time most ion engines use permanent magnets to confine electrons within the discharge chamber.

On the other side of the electron confinement issue is the necessity of keeping the discharge

stable. If some electrons do not get absorbed by the anode biased walls, the electric circuit in the ion engine will not be complete. This extinguishes the discharge or makes it behave in an unsteady manner. It is necessary to lose some electrons at the anode biased walls to complete the electrical circuit. Hence it is most desirable to keep the high energy primary electrons inside the discharge chamber for a long time, while preferentially losing the low energy secondary electrons to the anode biased walls.

The electric field maintained between the cathode and anode drives electrons to the anode biased walls. When an electron collides with an anode biased wall it is absorbed and lost from the discharge chamber. The electric field maintained at the grids reflects electrons back into the discharge chamber.

Secondary electrons are all the other electrons in the discharge chamber besides the electrons that have been emitted from the cathode and still have a high energy. Electrons extracted from the cathode generally have or acquire a high energy. Electrons produced in other manners generally have a low energy. These other electrons are called secondary electrons. Secondary electrons are produced during the ionizing collisions of primary electrons with the neutrals, the ionizing collisions of electrons with ions, recombination collisions, the slowing of primary electrons, and secondary electron emission. In general these electrons do not possess as much energy as the primary electrons. These electrons travel at slower speeds compared to the primary electrons and their chances of being involved in ionizing collisions are less compared to the primaries. The secondary electrons are also referred to as Maxwellian electrons.

Ions (both singly and doubly charged ions) are created inside the discharge chamber due to the collision of electrons with neutrals. Singly charged ions are also created inside the discharge chamber through three-body recombination processes of electron-doubly charged ion collisions. The chances of producing multiply charged ions (i.e., triply charged or higher charged states) have a low probability in an ion engine discharge chamber. This is because the creation of multiply charged ions requires higher electron ionization threshold energies ($> 35eV$) than that required to ionize the lower charges particles. The number of high energy electrons ($> 35eV$) which are in the tail of

the electron energy distribution function (EEDF) is considered to be very minimal. Ions are much heavier particles when compared to the electrons and they possess approximately the same mass as the neutral particles; hence ions travel at a much slower speed than the electrons. During the ion's motion inside the discharge chamber it may undergo collisions with the neutrals and electrons. When an ion collides with a neutral the possible outcomes are: 1) exchange of charge in which case the ion turns into a neutral and the colliding neutral becomes an ion. The newly created ion will have less energy compared to the colliding ion. 2) elastic scattering collision. After each of these collisions the direction of travel of the ion changes.

The effect of magnetic field on the ions is minimal because the ions are much heavier than the electrons. Ions are attracted by the negatively charged accelerator grid. This increases the speed of ions exiting the discharge chamber and they leave via holes in the grid plates. Some of the exiting ions may stream back towards the outside of the accelerator grid. These ions impact the grid plates causing erosion. Modeling and experimental research are performed to mitigate the erosion of grid plates.

Neutrals are fed into the discharge chamber through the main propellant feed locations and via the hollow cathode. Also a fraction of neutrals are supplied to the neutralizer cathode assembly. Neutrals are heavier particles and they are not affected by the electric and magnetic fields present inside the discharge chamber. Recombination of ions inside the discharge chamber and at the walls also produce neutrals inside the discharge chamber. Neutrals are lost in an ion engine discharge chamber through the electron-impact ionization process and convection through the grid holes. Electron-impact excitation of neutrals creates excited states of neutrals which generally quickly de-excite through a radiation process.

1.2.3 Discharge Chamber Performance

Ion engine discharge chamber performance characteristics are measured using different parameters. The main performance parameters are: thrust, specific impulse, discharge chamber propellant uti-

lization efficiency, ratio of double ion to single ion current in the beam, beam divergence, beam ion production cost, input power and thruster efficiency. Each of these performance parameters are discussed in detail below. The various currents observed in the discharge chamber are ion beam current, discharge current, screen grid ion current, and the cathode emission current.

The thrust, T, produced by an ion engine is determined in the same way as in a chemical rocket propulsion device where T is based on the exit velocity and the exiting propellant mass flow rate. In ion engines xenon is commonly used as a propellant. Hence the thrust produced in an ion engine is determined using the exit velocity, u_{ion} of the ions and the mass efflux of the ions, $\dot{m}_p$, leaving through the back end of thruster (i.e., through the grid plates). It is given by [Jahn 1968]

$$T = \dot{m}_p u_{ion}. \tag{1.1}$$

This equation indicates that thrust can be increased by either forcing the ions to exit the discharge chamber faster or by increasing the mass efflux through the grid plates. Because weight is important in space missions, the required thrust is generally achieved by increasing the exit velocity rather than the mass efflux of propellant.

It should be realized that ion engines need to be operated in a vacuum condition and the thrust produced by an ion engine is very small. Its thrust level is generally a fraction of a Newton. Hence ion engines cannot be launched directly from earth. In order to escape the force of gravity an engine needs to produce thrust must larger than the weight of the vehicle. In outer space the amount of thrust required to propel a spacecraft is minimal. Thus ion engines are a possible choice of propulsion in outer space but not within the atmosphere of earth. Presently ion engines are mostly used for satellite station keeping. In the Deep Space 1 mission [Polk et al. 2000] an ion engine successfully propelled a spacecraft to a distant asteroid.

Another way of looking at the thrust produced in a propulsion device is by computing the specific impulse, I_{sp}. The specific impulse is the thrust per unit mass of propellant used relative to

gravitational acceleration found on the surface of the earth,

$$I_{sp} = \frac{\dot{m}_p u_{ion}}{\dot{m}_p g} = \frac{u_{ion}}{g}. \tag{1.2}$$

A high specific impulse signifies better utilization of fuels and small specific impulse signifies poorer utilization. Ion engines have some of the highest specific impulses capable of being produced. The specific impulse of an ion engine is generally an order-of-magnitude greater than the specific impulse of a chemical rocket engine.

Ion engines achieve high specific impulse by accelerating the propellant out of the discharge chamber at high speeds through the use of electric fields. In order to electrostatically accelerate the xenon propellant, the xenon atoms need to be ionized. If the neutral atoms exit out of the discharge chamber without being ionized they contribute minimally to the thrust. Thus it is important to turn as many neutrals as possible into ions before leaving the discharge chamber. The positive ions produced inside the discharge chamber are extracted from the chamber by the high electrostatic potential imposed between the grid plates. The exiting ions velocity is given by [Sovey 1984; Patterson et al. 1993]

$$u_{ion} = \sqrt{\frac{2|e|V_B}{m_{ion}}} \tag{1.3}$$

where the beam voltage, V_B is determined by

$$V_B = V_S + V_D - V_N. \tag{1.4}$$

Here V_S is the screen voltage which is tied to the negative side of the discharge power supply (refer Figure 1.2), V_D is the discharge voltage, and V_N is the neutralizer floating potential relative to ground. The mass flow rate of propellant, $\dot{m}_p$ leaving through the grid is determined using the ion beam current, I_B. It is given by,

$$\dot{m}_p = m_{ion} * \frac{I_B}{|e|}. \tag{1.5}$$

The ideal thrust produced in an ion engine discharge chamber is determined using Equation (1.1). Substituting Equations (1.3) and (1.5) into Equation (1.1) and simplifying Equation (1.1)

gives

$$T_{ideal} = \sqrt{2\frac{m_{ion}}{|e|}} I_B \sqrt{V_B}. \tag{1.6}$$

However, the actual thrust produced in an ion engine discharge chamber is affected by of the presence of double ions in the ion beam current and the divergence of the ion beam. The actual thrust is given by

$$T_{actual} = \alpha F_t T_{ideal} \tag{1.7}$$

where α is the correction factor due to the double ion content

$$\alpha = \frac{(1 + \frac{1}{\sqrt{2}}\frac{I_B^{++}}{I_B^{+}})}{(1 + \frac{I_B^{++}}{I_B^{+}})} \tag{1.8}$$

and F_t is the thrust reduction factor due to the beam divergence which is given by the ratio of the axially aligned ion beam current to the total ion beam current. The total ion beam current is the sum of beam ion currents due to the singly charged ions, I_B^+, and the doubly charged ions, I_B^{++}. It is given by,

$$I_B = I_B^+ + I_B^{++}. \tag{1.9}$$

Another important parameter that is generally used to measure the ion engine discharge chamber performance is the discharge chamber propellant utilization efficiency, η_{prop}. It is determined using

$$\eta_{prop} = \frac{I_B}{I_{neutral}} = \frac{(I_B^+ + I_B^{++})m_{ion}}{(\dot{m}_{main} + \dot{m}_{cathode})|e|}. \tag{1.10}$$

Here $I_{neutral}$ is the total neutral flow rate supplied into the discharge chamber measured in amperes equivalent. This neutral flow rate is based on the sum of the neutral flow rate through the main feed system, $\dot{m}_{main}$ and the neutral flow rate through the hollow cathode, $\dot{m}_{cathode}$ where $\dot{m}_{main}$, and $\dot{m}_{cathode}$ are measured in $\frac{kg}{s}$. The neutralizer cathode propellant flow rate is on the same order as the propellant flow rate through the discharge cathode. We do not include the neutralizer cathode flow rate in the efficiency calculation since we are studying the effective utilization of neutrals supplied to the discharge chamber.

Using the actual thrust, T_{actual}, the specific impulse given in Equation (1.2) can be re-written as

$$I_{sp} = \frac{T_{actual}}{\dot{m}_p g}. \tag{1.11}$$

Substituting Equation (1.7) and (1.10) into Equation (1.11) and simplifying gives

$$I_{sp} = \alpha F_t \eta_{prop} \sqrt{2\frac{|e|}{m} V_B} \frac{1}{g}. \tag{1.12}$$

The input power, P_{IN}, for an ion engine discharge chamber is measured in terms of the power supplied to the different components. The main components are: screen grid, discharge power, accelerator grid, main cathode, neutralizer cathode, cathode heater, and neutralizer cathode heater. The input power, P_{IN}, is given by,

$$P_{IN} = V_S I_B + V_D I_D + V_{AC} I_{AC} + V_C I_C + V_N I_N + P_{CH} + P_{NH}. \tag{1.13}$$

Here V_C is the main cathode voltage, I_C is the main cathode current, V_N is the neutralizer cathode voltage, I_N is the neutralizer cathode current, P_{CH} is the cathode heater power, and P_{NH} is the neutralizer cathode heater power.

The effectiveness of ions produced inside the discharge chamber is measured in terms of plasma ion production cost, ϵ_p and the beam ion production cost, ϵ_B. The plasma ion production cost is given by

$$\epsilon_p = \frac{(I_D - I_P)V_D}{I_P} \tag{1.14}$$

where I_P is the total ion production rate inside the discharge chamber. The beam ion production cost is computed using

$$\epsilon_B = \frac{V_D(I_D - I_B)}{I_B}. \tag{1.15}$$

The beam ion production cost is related to the plasma ion production cost with the following expression

$$\epsilon_B = \frac{\epsilon_p}{f_B} + \frac{1 - f_B}{f_B} V_D. \tag{1.16}$$

Here f_B is the ion beam fraction and it is given by

$$f_B = \frac{I_B}{I_P}. \tag{1.17}$$

From Equation (1.16) we can see that the ion beam production cost is minimized by effectively increasing the beam ion fraction, f_B, and minimizing the plasma ion production cost, ϵ_p.

Finally, the overall thruster efficiency is determined using

$$\eta_t = \frac{T_{actual} I_{sp} g}{2P_{IN}}. \tag{1.18}$$

1.3 Modeling Literature Survey

Both experimental and computational investigations have been performed on ion engine discharge chambers to study the plasma processes and to improve the performance characteristics of an ion engine. Though this research is only on computational modeling, this section begins by mentioning some references for the experimental based investigations.

The plasma processes in an ion engine discharge chamber are studied in detail by conducting separate experimental investigations on each of the different components. The main discharge chamber components of interest are: the discharge chamber, the hollow cathode, the neutralizer cathode, and the grid optics. Numerous experimental investigations on ion engine discharge chambers have been performed since the 1960s at NASA Research Laboratories, Universities and industries in the United States. Other countries such as the European nations, Brazil, and Japan have been working doing experimental studies on ion engine as well. It would be difficult to reference all of these papers in this dissertation. Hence only a few of the recent experimental investigation on ion engine discharge chambers are cited here. The experimental results of the discharge chamber plasma inside the 30-cm diameter thruster are given in various references [Matossian and Beattie 1991; Patterson et al. 1993; Williams 2000; Herman 2005; Sengupta et al. 2004; Sengupta 2005; Sengupta et al. 2006] and the ion engine hollow cathode experimental studies are given in a number of references [Domonkos et al. 1999; Goebel et al. 2004; Jameson et al. 2005; Polk et al. 2006]. Similarly experimental investigations of NSTAR ion engine grid optics and results can be seen at NASA GRC references [Soulas et al. 1999; Soulas 2001].

Experimentally based investigations on ion engine discharge chambers have certain limitations and difficulties associated with them. The limitations of performing experiments are many. For example producing an appropriately sized Langmuir probe to measure the non-uniform plasma density distribution inside the discharge chamber is difficult. In the high density plasma regions near the hollow cathode emission point, Langmuir probes can not be made small enough to resolve the physical scales of the plasma. Also, if the same small sized probe is used in the low density plasma regions near the chamber walls erratic results are obtained [Herman 2005]. Another difficulty in experimental investigations is performing a detailed parametric studies or design optimization studies. Ion engine experimental research is expense and time consuming to setup and perform. Thus many parametric studies and optimization studies that have been performed on ion engines experimentally only contain a few number of results.

Computer models are quick and inexpensive to set up and run. Computer models can be used to perform a detailed analysis of the plasma produced inside the discharge chamber. Since it is easy to change the input to a computer program, it is relatively easy to perform parametric and design optimization studies. Computer programming also provides flexibility in designing the discharge chamber. Computer modeling of an ion engine discharge chamber will enhance the state of the art in ion engines developed for future space missions. In this work one such detailed computational model is presented. To see where the present work fits into the computational modeling work already done in this area, a brief history of the computational tools used to model the ion engine discharge chamber are discussed here. Similar to the experimental studies, the computational tools consider analyzing each component of the engine separately. At present this research is focused on the ion engine discharge chamber plasma only. This is necessary because developing computational models for the discharge chamber itself is a difficult task to perform. Hence the computational work on ion engine discharge chamber plasma modeling are presented here. In the future this computational model can be extended to model the other components of the discharge chamber such as hollow cathode and ion grid optics. Interested readers can refer following reference papers

for the computational works on ion engine hollow cathode and grid optics [Domonkos 2002; Katz et al. 2003; Mikellides et al. 2005b; 2005a; Emhoff and Boyd 2004; Wang et al. 2003].

Brophy and Wilbur [1985] are the first ion engine modelers to develop a computer tool to model the performance of a ring-cusped magnetic field, high flux density ion engine discharge chamber. They developed a theoretical model to calculate the overall ion beam production cost. This model [Brophy and Wilbur 1985] related the performance of an ion engine discharge chamber to four configuration/propellant dependent parameters: the primary electron confinement length, the baseline ion energy cost, the extracted ion fraction, and the cathode potential surface ion fraction; and two operating parameters: the propellant flow rate and the discharge voltage. From their model they suggest that improved thruster performance is characterized by large extracted ion fractions, long primary electron confinement lengths, small effective grid transparencies to neutral atoms, and operation at high propellant flow rates. Since they did not track the primary electrons, they made assumptions about the primary electron confinement length value which is used as an input in their model.

Matossian and Beattie [1989] developed a model to calculate the volume averaged plasma properties inside the discharge chamber using Langmuir probe measurements of the spatially varying plasma inside the discharge chamber. This volume averaging of plasma properties allowed them to obtain a single average plasma performance parameter. This model differed from Brophy and Wilbur's [1985] model in that the thruster performance was expressed in terms of thruster design variables and operating conditions. Their model given in reference [Matossian and Beattie 1989] on two 30 cm diameter mercury ion thrusters; a ring-cusp thruster and a J-series thruster for different values of discharge voltage. They presented comparisons of their volume averaged model results with the measured performance results for the two thrusters in terms of the Maxwellian electron density, the Maxwellian electron temperature, and the primary electron number density. Their modeling results had qualitative agreement with the results from Brophy and Wilbur's theoretical model.

Arakawa and Wilbur [1991] developed a plasma flow model to study the discharge chamber. In

this model the magnetic field was modeled using a two-dimensional finite element method and the plasma ions were modeled using a diffusion process. Arakawa and Wilbur described the flow of ions as a continuum and set up two diffusion coefficients to consider the movement of ions parallel and perpendicular to the magnetic field. Their model estimated the primary electron number density by ignoring collisions and modeled the electrons using fluid approximations. It also appears that they did not use a separate model for the secondary electrons. They presented results of the plasma density profiles and ion flow fractions leaving through the grids and the absorbing wall surfaces. They showed how the placement of a hollow cathode inside the discharge chamber changes the ion fractions leaving through the grids.

Arakawa and Yamada [1990] were the first to develop a detailed model to study the primary electrons inside the discharge chamber. They developed a computer tool called PRIMA to model the primary electron trajectories in cusped discharge chambers. They used a Runge-Kutta technique to model the primary electron motion and a Monte Carlo method to simulate primary electron collisions. This model calculated the primary electron confinement length and the primary electron utilization factor and applied for modeling the experimental discharge chambers given in references [Hiatt and Wilbur 1986; Vaughn and Wilbur 1988]. They presented numerical results for these thrusters using three different types of collisions: no collisions, elastic collisions, and anomalous collisions to account for the plasma oscillations. Their primary electron utilization factor results showed good comparisons with the experimental results from Hiatt and Wilbur's two ring, 8 cm beam diameter, discharge chamber with the anode region located on the cusp. They had poor comparisons with the no collisions case and elastic collision case results when compared to the experimental results from Vaughn and Wilbur's 3-ring, 7 cm diameter discharge chamber using a loop anode. When they included anomalous collisions in their numerical model Arakawa and Yamada obtained better comparisons.

Later Arakawa and Ishihara [1991] integrated the modeling tools developed by Arakawa and Wilbur [1991], Arakawa and Yamada [1990], and Brophy and Wilbur [1985]. By combining these

investigations the magnetic field effect, the primary electrons, the secondary electrons and the first ions were all included. This tool can be applied to model cylindrical discharge chambers with an axisymmetric magnetic field configuration. They model the magnetic field, the grid transparencies of the ions and neutrals, the primary electron confinement length, and the ion fractions that are extracted out as the beam, and the ions that reach the wall surfaces. Using Brophy's performance model they calculated the ion production cost and the propellant utilization. In addition they studied ion motions through the grid holes in their model. This code was the most complete in 1990s and for many years after.

Hirakawa and Arakawa [1993] developed a particle-in-cell code to study the charged particle motion in the magnetic cusp regions of an ion engine discharge chamber. They included the electric fields self-consistently and considered the charge separation effects in order to calculate the ion loss mechanisms to the walls. Only a small computational domain (< 1 cm) around the magnetic cusp region was considered and charged particles were injected into this small region to perform particle simulation near the magnetic cusp region. Both electric and magnetic field effects were considered in the charge particles tracking. However they assumed a collision free motion for the charge particles and used artificial low mass ion particles in the simulation. These were done to reduce the computational simulation time. This PIC model obtained results of electron density, ion density, space potential profiles for the cusp regions, and the ion loss flux to the cusp areas. This model given in reference [Hirakawa and Arakawa 1993] was a fairly complete particle simulation; however, it only looked at a small fraction of the total discharge chamber volume.

Sandonato et al. [1996] developed an analytical model to measure the plasma parameters of the discharge chamber of an ion engine. The model presented in reference [Sandonato et al. 1996] consider the magnetic field in the discharge chamber and tracked the primary electrons to calculate the primary electron confinement length. Their primary electron model was similar to that of Arakawa and Ishihara's work. They used a simplistic plasma model to calculate the singly charged ion and secondary electron number densities. An analysis similar to Brophy and Wilbur's [1985]

was done to calculate the performance parameters.

Yashko et al. [1997] investigated the performance of micro ion thrusters using the numerical codes developed by Arakawa and Ishihara [1991]. They used the same code, except they adopted a different magnetic field code called MAGNETO to determine the magnetic field strengths within the discharge chamber. The reason this was done was that they obtained unreasonable results for certain cases with Arakawa and Ishihara's magnetic field code MAG. The numerical results given in reference [Yashko et al. 1997] indicate that small sized ion thrusters provide poor electron and ion confinement inside the discharge chamber even when using best permanent magnets available. They also investigated rectilinear micro thruster designs. To model this geometry they modified the primary electron trajectory simulation of Arakawa and Ishihara's code.

Mahalingam and Menart [2002] improved and enhanced the performance of the primary electron modeling tool PRIMA. This model was originally developed by Arakawa and Yamada and was also used in Arakawa and Ishihara's code. Mahalingam and Menart fixed some of the inaccuracies found in Arakawa and Ishihara's version of PRIMA and enhanced its computational performance by adopting parallel computing. Arakawa and Ishihara performed a renormalization of the primary electron velocities at each time step to control the numerical heating problems. Mahalingam and Menart fixed this by using a much smaller time step to minimize the numerical heating so the primary electron trajectories are modeled more accurately. Mahalingam and Menart's version of PRIMA can handle any shaped discharge chamber configuration which can be formed from the combinations of straight lines. Mahalingam and Menart studied theoretical magnetic field configurations with PRIMA to get an idea of the values of magnetic field strength and shape required to obtain better primary electron confinement. They studied three different design parameters of discharge chambers: the shape, the diameter, and the number of magnetic rings used for confinement. They showed that a 2-ring, 10 cm diameter discharge chamber [Mahalingam and Menart 2007a] and a 4-ring, 20 cm diameter discharge chamber have a better primary electron confinement length than 3 or 4-ring configurations. This result holds for 20 cm diameter chambers and smaller. In addition, Mahalingam

and Menart's results indicated that most of the primary electrons are lost at the magnet cusps.

Mahalingam and Menart's version of PRIMA was used by Menart and co-workers [Deshpande et al. 2004; Deshpande et al. 2005; Ogunjobi and Menart 2006; Bennett et al. 2007] to model the primary electron motions inside the discharge chamber of an ion engine. Deshpande et al. [2004] performed a survey of runs to see how the shape and size of the magnetic cusp regions affect the primary electrons travel. The angle and location at which the primary electron enters the cusp region were analyzed. The study found that a 3 cm and a 15 cm magnet spacing provide a better magnetic mirroring effect among the different number of magnet spacings analyzed between 3 cm and 15 cm. Deshpande et al. [2004] showed that a 5 cm magnet spacing provided the poorest mirroring effect. In addition to this analysis they presented comparisons of results from PRIMA to Hiatt and Wilbur's [1986] experimental results for a 9.2 cm diameter discharge chamber with two magnetic rings. These results validated Mahalingam and Menart's modified version of the computer code PRIMA. Ogunjobi and Menart [2006] performed studies on determining the optimum magnetic circuit that provides longer confinement length. Bennett et al. [2007] performed primary electron studies on determining the best magnetic field for electron confinement.

Wirz and Katz [2005] developed a two dimensional computational model to analyze the plasma present inside the discharge chamber. In their discharge chamber model they account for five design parameters (chamber geometry, magnetic field, discharge cathode, propellant feed, and ion extraction characteristics) and tracked five different plasma species (neutral atoms, secondary electrons, primary electrons, single ions, and double ions) to calculate the plasma properties inside the discharge chamber. They used four separate modules to study the discharge chamber which are: neutral sub model, electron collision sub model, ion diffusion sub model, and electron thermal sub model. Neutrals were modeled using the techniques that have been used to calculate radiative transport view factors. The primary electrons were modeled as macro particles and they adopted a Boris type particle advance to track the primary electrons with collisions. From this model they calculated the ionization rate inside the discharge chamber which could be used in an ion diffusion

model. Then they modeled the motion of positive ions and secondary electrons using a continuum description based on quasi-neutrality. The diffusion model equations were set up to track the motion of ions and secondary electrons in the magnetic field. To do this they calculated diffusion coefficients for directions parallel and perpendicular to the magnetic field lines. They presented results of the magnetic field, volume averaged particle number densities, and discharge chamber performance parameters for the 3 ring magnetic arrangement of the 30 cm diameter NSTAR thruster discharge chamber. In addition to this they made comparisons of beam current density profiles at the exit plane of the discharge chamber with available experimental data. They observed that the beam current density profiles obtained with the diffusion model that included both singly charged ions and doubly charged ions has a better comparison with the experimental results than the diffusion model which is based only on singly charged ions. Using their computer model they predicted that the 30 cm NSTAR thruster would have better performance characteristics if the middle magnet ring were doubled in thickness. Doubling the thickness of a permanent magnet increases the strength of the magnetic field further out from the magnet.

A 3-D computational tool was developed at NASA GRC to consider 3-D effects on studying the ion engine discharge chamber plasma [Stueber 2004; 2005]. Presently this 3-D code models the magnetic circuit designs, the primary electron trajectories, and the neutral atoms in the discharge chamber. Magnetic field analysis was performed to identify the low magnetic field volume for any given magnetic circuit design. The region with low magnetic field volume upstream of the ion grid optics was proposed as a design feature for improving thruster performance. A large number of possible magnetic circuits were analyzed to select an optimum magnetic field configuration for a given discharge chamber. The primary electrons are tracked to calculate the primary electron confinement length, the primary electron cusp leakage width, and the primary electron density distributions inside the discharge chamber. But this model ignores the particle collisions. The neutral propellants are modeled as a cluster of particles and tracked inside the discharge chamber to determine the neutral number density distributions. Parallel processing is employed to shorten computational time. At

this time Stueber has not enabled the interlinking of the primary electron model with the neutrals model.

A 0-dimensional analytical discharge chamber model was recently proposed by Goebel and coworkers [2006] based on equations that are developed from the theoretical assumptions. This model given in reference [Goebel et al. 2006] is similar to the work of Brophy and Wilbur [1985], except it computes the confinement length, ion loss, and electron loss rate. This model is designed based on the assumptions of uniform ion and electron number densities which is an approximation of the nonuniform plasma present in a discharge chamber.

This literature search of the work done in ion engine discharge chamber modeling is comprehensive. None of the models presented do a complete particle simulation of the plasma. Of the models presented above, the hybrid diffusion model by Wirz and Katz [Wirz and Katz 2005] is one of the recent computational model available to study the discharge chamber. As mentioned, they only track the primary electrons as particles and the ions and secondary electrons are handled using a diffusion approximation. The neutrals are handled using a zonal approach. Given the mean free paths of the particles and the length scales present, this assumption should be held in question. While this assumption may be somewhat justifiable in the low field region in the center of the discharge chamber, in the cusp regions the length scales over which the magnetic field strength changes significantly become much smaller than the mean free path of any of the particles. It is known from studies by [Mahalingam 2002], that most primary electrons leave the discharge chamber through the cusps. The particle movement in a number of regions in the discharge chamber is not continuum diffusion. The only model present which does a detailed calculation of the electric fields, including the effects of the particles, is that by Hirakawa and Arakawa [1993]. As mentioned above Hirakawa and Arakawa [1993] only studied a small cusp region, used lighter ions, and assumed charged particles were collisionless. Wirz and Katz [2005] calculate the electric field strengths from the electron energy based on Boltzmann's exponential equation. It is felt that this technique is crude. Wirz and Katz do not present any electric field or electric potential results in their publications.

The importance of the present work is to develop a more realistic model of the discharge chamber plasma. The way this is done is to use a particle-in-cell (PIC) [Birdsall and Langdon 1991] technique in combination with a Monte Carlo Collision (MCC) technique [Birdsall 1991; Vahedi and Surendra 1995]. PIC simulations have been considered successfully in modeling various plasma simulation problems not associated with ion engines [Tech-X Corporation 2007; Luginsland et al. 1998; Bruhwiler et al. 2001; Morris and Gilchrist 2004; Kolev et al. 2005; Marek et al. 2005; Sakurabayashi et al. 2004; Mardahl 2001; Kim et al. 2005]. Partial PIC techniques have also been used to model the ion engine grids [Wang et al. 2003; Emhoff and Boyd 2004; Wang et al. 2006; Okawa and Takegahara 2001] and in hall thruster simulations [Passaro et al. 2006; Fox et al. 2006; Taccogna et al. 2005; Szabo 2001]. As mentioned above partial PIC techniques have also been used to model some of the particles present in an ion engine discharge chamber. In this work all particles are modeled with a particle technique. As discussed in the next section the problem in applying a PIC technique to all particles present in an ion engine discharge chamber is the size of the discharge chamber and the densities of the particles present.

1.4 Particle-In-Cell (PIC) Simulations in Electric Propulsion

The computational modeling of an ion engine discharge chamber plasma can be handled using a continuum approach based on the fluid assumptions or a kinetic approach where the plasma is considered at the particle level. The applicability of an appropriate computational model is based on numerous considerations.

An important physical parameter that should be considered in the selection of a kinetic or a continuum approach is the Knudsen number, K_n. The Knudsen number is a non-dimensional parameter which is defined as the ratio of the mean free path of collisions, λ, to some characteristic length, L, scale in the system,

$$K_n = \frac{\lambda}{L}. \tag{1.19}$$

The mean free path is the distance traveled by a particle between two successive collisions. It is calculated using

$$\lambda = \frac{1}{\sqrt{2} n \sigma} \tag{1.20}$$

where n is the number density of target particles and σ is the collision cross-section area for the particles involved in the collision. Let us compute the mean free path of electrons involved in ionizing collisions with neutrals. This mean free path length can be estimated by utilizing one of the larger xenon neutral number densities encountered in discharge chambers and one of the larger electron-neutral ionization cross sections encounter. Considering a value of $10^{19} m^{-3}$ as the neutral number density and a value of $5 \times 10^{-20} m^2$ for the xenon ionization cross section [Rejoub et al. 2002] gives a mean free path value of about 1.4 m. This path length is more than four times the diameter of the discharge chamber. Typically the Knudsen number for discharge chambers is observed to be greater than 1. At this high of a K_n the continuum approach to model the plasma is questionable. This argument against the use of a continuum model for modeling the plasma in a discharge chamber is even more compelling if one looks at the length scales over which the magnetic field strength changes considerably. These can be as small as 1 mm. Using this length scale the K_n is 1400. To obtain accurate numbers using the continuum approach the K_n should be below 0.2 [Bird 1994]. These simple K_n calculations indicate that PIC simulations should be used to model the plasma in a discharge chamber.

Though a PIC simulation is the best tool to model the discharge chamber plasma, its main limitations are the requirements of large computational resources, the numerical instabilities encountered, and the statistical noise due to the particle weighting. In a full PIC-MCC simulation all plasma particles are tracked using a macro particle assumption along with solving the electric fields based on the charge particle distributions. Each macro particle is set to represent billions to trillions of real particles of the plasma. In general many computer particles are required to track the 10^{17} to 10^{18} real particles present in the plasma. The large computational requirements for the PIC simulations mainly arise from the need to satisfy numerical parameters such as the grid spacing and the time

step size, and to satisfy the stringent stability conditions posed by the basic plasma characteristics. The computational grid size needs to resolve the Debye length and the time step should capture the largest characteristic frequency present in the plasma, such as the plasma frequency. Also the time step and grid spacing needs to resolve the thermal speed condition posed by the electron energy.

The Debye length is an important characteristic length found in plasmas and the plasma frequency is an important characteristic time found in plasmas. The Debye length is the characteristic distance over which electrons shield the charge effects of a positive charged particle. The Debye length is given by [Hockney and Eastwood 1988]

$$\lambda_D = \sqrt{\frac{\varepsilon_0 k_B T_e}{n_e |e|^2}} = 7441\sqrt{\frac{T_e}{n_e}} \tag{1.21}$$

where ε_0 is the permittivity of free space, $8.8541 \times 10^{-12} F/m$, k_B is the Boltzmann constant, $1.3805 \times 10^{-23} J/K$, T_e is the electron temperature in eV, n_e is the electron number density in m^{-3}. The plasma frequency signifies the characteristic time scale of the plasma oscillations. It is given by,

$$\omega_{pe} = \sqrt{\frac{n_e |e|^2}{\varepsilon_0 m_e}} = 56.3\sqrt{n_e} \tag{1.22}$$

where m_e is the mass of an electron, $9.11 \times 10^{-31} kg$.

For ion engine discharge chambers, the maximum electron number density observed in experimental measurements is on-the-order of $10^{19} m^{-3}$ and the electron temperature is on-the-order of 2-30 eV [Herman 2005]. Thus the Debye length value in the high plasma number density regions is on-the-order of a few tens of microns and the plasma frequency is on-the-order of $10^{11} s^{-1}$. Since the length scale of an ion engine discharge chamber is on-the-order of 0.1 m to 0.4 m, a large number of computational mesh points ($\sim$ million grid points) is required. In order to resolve plasma frequencies a small time step value ($\sim$ few picoseconds) is required. The thermal speed condition is usually not as severe as the plasma frequency condition. To avoid statistical noise a large number of macro particles ($\sim$ millions) are required. Along with these large computational resources, steady state solutions for the simulation are on-the-order of the neutral transit which can take 10 to 100's of milliseconds [Taccogna et al. 2005]. If the time step used in the simulation is on-the-order of a

few picoseconds, while the steady state solution is expected in milliseconds, billions of time steps are required in the computation simulation. Advancing a large numbers of macro particles for this large number of time steps requires long computational times, on-the-order of a few months to a few years. Such long computer run times are unreasonable.

Numerous methods and techniques have been adopted in the present and in the past PIC simulations to circumvent these monstrous computational times. Many of these techniques are listed below.

1. Hybrid approach: In this approach one or more particles in the plasma is modeled using a fluid approach while the other particles are handled using a particle approach. Arakawa and Wilbur [1991] and Wirz and Katz [2005] ion engine models track the ions and the secondary electrons using fluid assumptions, while tracking only the primary electrons using a particle approach. Similar approach was followed in modeling the hollow cathode, the grid optics in the ion engine discharge chamber and for modeling hall thruster discharge chambers (see References [Wang et al. 2003; Emhoff and Boyd 2004; Boyd et al. 2005; Passaro et al. 2006; Scharfe et al. 2006]). However these references treat the electrons using the fluid approach, while the ions and neutrals are modeled using a particle based technique.

2. Artificial decrease of the mass of heavy particles: In ion thrusters, the mass ratio between heavy xenon particles and the electrons is on-the-order of $\sim 3 \times 10^5$. By decreasing the heavy particle mass, the speed of the heavy particle is increased. This allows one to obtain steady state results quicker because other heavy particle transit time in the plasma is reduced [Hirakawa and Arakawa 1993; Kawamura et al. 2000; Szabo 2001].

3. Artificially increase the plasma permittivity, ε_a: This increases the Debye length value and decreases the plasma frequency (see Equations (1.21) and (1.22)); thus allowing the selection of a larger grid spacing and a larger time step value [Szabo 2001].

4. Scaling the characteristic length scales in the discharge chamber: This enables a reduction of the

computational domain which in turns requires fewer spatial grid points. Results obtained in the scaled dimensions are correlated to the actual thruster using self-similarity principles [Taccogna et al. 2005].

5. Input electric field: In this technique the electric field distribution measured in experiments or estimated based on prior measured data on other ion engine discharge chambers is given as an input to the PIC simulation. All the plasma particle types are still modeled using a particle based scheme. This technique enables selection of a much coarser grid and a bigger time step value. Steady state results can be obtained in a few weeks [Mahalingam and Menart 2007b].

All of the above schemes listed reduce the PIC simulation computer run time significantly. In addition to the above schemes, several other computational techniques are considered to speed up the simulation runtime [Kawamura et al. 2000]: a subcycling process where different time scales are adopted for the electrons and heavy particles, different weighting to the particles in the simulation domain [Szabo 2001], particle rezoning [Lapenta and Brackbill 1994; Bowers 2001], initiating the simulation with a predistribution of particles, and parallel processing [Mahalingam and Menart 2006; 2007b]. However each of the above described computational approaches have certain limitations, inaccuracies, and difficulties associated with them. The problems associated with each of the above computational schemes are discussed below.

Of course the drawback of the hybrid approach is that certain particles are treated as a fluid instead of discrete particles. This is fine as long as the mean free path of the particles is less than any characteristic lengths important in the solution. Most of the time the hybrid model is applied as a matter of necessity, as opposed to the particles actually being in the continuum realm. The ion engine discharge chamber model by Wirz and Katz [2005], can be considered a hybrid model, the ions and secondary electrons are treated as a continuum fluid while the primary electrons are treated with a particle approach. This was done out of necessity as opposed to correctly modeling the physics. At ion and secondary electron densities of 10^{18} ions/m^3 the continuum assumption is

questionable. In many regions of the thruster the density of ions is even less than this, making this assumption even more questionable.

Drawbacks of the schemes listed in items 2 through 5 also need to be stated. Using a reduced mass for the heavy particles changes the way the heavy particles move inside the discharge chamber and alters their interaction with the magnetic and electric fields. The artificial increase of vacuum permittivity has the effect of changing the applied electric field inside the discharge chamber. Scaling the characteristic lengths helps miniaturizing the computational problem, but this self-similarity principle relies on the assumption that the plasma is fully ionized ($n_i > n_0$) and uniform in the entire discharge chamber. The ion engine discharge chamber plasma can not be modeled using self-similarity principles as the plasma inside the discharge chamber is non-uniform. Decoupling the electric field solver from the PIC simulation has the issue of maintaining the charge balance between ions and electrons because of no charge-separation effects.

In this work the PIC-MCC method developed for the ion engine discharge chamber utilizes some of the above described computational approaches to reduce computational run time. The schemes which are used in the current work are: parallel processing, artificial vacuum permittivity, subcycling processes, and using a predistribution of particles. The only approach that affects the results is the artificial vacuum permittivity which will alter the computed electric field inside the discharge chamber. These computational schemes are discussed in detail in Chapter 3.

1.5 Salient Contributions of Current Research

1.5.1 Physical Model Contributions

The significant contributions made by the current research to advance the state-of-art in ion engine discharge chamber modeling are:

- This work has produced the first complete particle simulation of the plasma in the discharge chamber of an ion engine. Essentially all of the major particle types in the discharge chamber

are tracked; this includes primary electrons, secondary electrons, singly charged ions, doubly charged ions, and neutrals. The only particle type that is not included is triply charged ions which are not important at the energy levels used in ion engines. Other investigators have done partial particle simulations but no one has done all the particles.

- This work is one of few that includes the effects of both the electric and magnetic fields on the charged particle trajectories.

- This work includes more types of particle collisions than any other model of the plasma in a discharge chamber.

- This work introduces a new technique for alleviating the many numerical restrictions put on PIC modeling. This new technique is to input experimental values for the electric field where available and use appropriate knowledge to fill in the rest of the electric fields where this data is not available. A dynamic electric field is calculated so that unrealistic electric charge inequalities are not computed and it is added to the input experimental field. This is believed to be the first time this has been done in PIC modeling. To keep the dynamic field calculation from introducing overly huge numerical concerns, an artificial plasma permittivity is used. While using an inflated permittivity has been used in the past, its primary purpose in this work is to maintain a reasonable charge balance. This will be discussed in the following chapters.

- The computational tool developed in this work provides detailed information on the primary electron distributions, the secondary electron distributions, the first ion distributions, the second ion distributions and the neutral particle distributions. Also determined are discharge current, beam current, average energies of the particles, where particles are lost from the discharge chamber, where particles are produced or enter the discharge chamber, etc. Since a full particle method is used a great deal of information on the particles can be obtained. On top of this important discharge chamber performance parameters such as the fraction of ions extracted to the beam current, propellant utilization efficiency, ion losses to the chamber walls, plasma ion

production cost, and beam ion production cost can be obtained. It is believed that current work will aid in the design and development of ion engine discharge chambers for future space missions. This computer modeling will provide a detailed analysis of a particular discharge chamber design which will aid researchers in determining the optimum discharge chamber configuration. Because this model can provide results that are either very difficult or impossible to obtain experimentally a greater understanding of discharge chamber operation should be able to be obtained in future use of this ion engine tool developed as part of this work.

1.5.2 Computational Code Contributions

In this work the computational tools called XOOPIC [Verboncoeur et al. 1995] and MAXWELL-2D [Ansoft Corporation 2007]are used as the starting point to model the plasma inside the discharge chamber of an ion engine. XOOPIC is an object oriented PIC code written in C++ developed by the Plasma Theory and Simulation Group at the University of California, Berkeley. OOPIC Pro [Tech-X Corporation 2007], a commercial version of the XOOPIC, utilizes the same physics as XOOPIC, except OOPIC Pro supports multiple operating systems. While XOOPIC is not specifically developed to model the ion engine discharge chamber, it has been successfully applied to other plasma simulation problems. It tracks charged particles as macro particles and takes into account the effects of electric and magnetic fields. In the simulation each macro particle represents a large number of individual charge particles. XOOPIC handles both static and dynamic electric fields and the dynamic part of the magnetic fields. It does not handle the static magnetic fields; this is the reason the static magnetic field produced by the permanent magnets inside the discharge chamber is modeled using another computational tool called MAXWELL-2D [Ansoft Corporation 2007]. MAXWELL-2D was developed by the Ansoft Corporation. The static part of the electric and magnet fields is the portion of these fields that is not a function of the charged particles present in the discharge chamber. The dynamic part of the electric and magnetic fields is the portion that depends on the charged particle location and motion. As part of this work a number of alterations

have been made to the computer code XOOPIC. These changes had to be made to implement the model developed as part of this work. In addition new features and alterations have been made to XOOPIC to enhance the performance of the code. While many modifications have been performed on XOOPIC as part of this research, only a few of the more significant changes are listed below:

1. A parallel electrostatic (ES) solver was added to XOOPIC [Mahalingam and Menart 2006]. XOOPIC does have parallel solver for the dynamics electro-magnetic model (EM) but not for the ES model. The EM algorithm can not be used in this work because of the huge computational time requirements. The EM model is much more computationally restrictive than the ES algorithm due to the Courant condition based on the speed of light. [Birdsall and Langdon 1991]. This parallelization of the ES model achieves a speed-up factor of about 8 when 16 processors are used.

2. Inelastic collisions between charged particles were added to XOOPIC. The original XOOPIC code only models inelastic charge particle collisions with neutrals. The assumption being made by XOOPIC is that the charged particle number densities are small. For most applications of XOOPIC this is the case because the computational times became excessive if the charged particle number density was large. Since a plasma in an ion engine is one of these severe conditions that investigators have avoided in the past, inelastic charged particle collisions were not included. As part of this work the handling of inelastic electron-ion collisions and three-body electron-ion recombination processes has been added. Of course the elastic collisions between charged particles is still handed through the electric fields.

3. A neutral particle tracker was added to XOOPIC. In XOOPIC the neutrals are assumed to be a uniform background gas. As will be seen in the results presented in this work the neutrals are not uniform throughout the discharge chamber.

4. The ability to handle non-uniform grids was added to XOOPIC. The original XOOPIC code could only utilize uniform grids.

5. The ability to calculate a number of performance parameters for ion engines was added to XOOPIC. It is reasonable that XOOPIC did not contain routines to determine ion engine performance parameters because it was not written for an ion engine application.

Details on all of these alterations to the XOOPIC code can be found in the following chapters. In future chapters the name XOOPIC will seldom be stated. The code will be called the PIC-MCC code.

1.6 Dissertation Outline

This dissertation is composed of 6 Chapters. The intent of the first chapter was to provide the reader with background information on ion engines, with a literature survey on what has been done on modeling the plasma in an ion engine, and to outline to the reader why this work is being done, what is its significance, and why it adds to the state-of-the-art in ion engines. In Chapter 2 the mathematical models used in the current research for particle tracking, particle collisions, field solving, and boundary conditions are presented. The numerical techniques to solve the mathematical model and the new algorithms added in the computer code are discussed in Chapter 3. Along with the numerical techniques, the issue of stability criteria, the selection of numerical parameters, initiating the simulation with a pre-distribution of particles, and parallel processing are discussed. In Chapter 4, the developed particle based plasma model is utilized for performing numerical convergence study on the 30 cm diameter NSTAR discharge chamber at its full operating power. In Chapter 5, results from the Base Case NSTAR design, and the sensitivity analysis of different parameters considered in the discharge chamber model are presented. Also in Chapter 5 a design change to the NSTAR thruster is studied. Conclusions from this research are presented in Chapter 6. Future work and possible improvements to the computational model are also discussed in Chapter 6.

2

Discharge Chamber Mathematical Model

This chapter presents the governing equations used for modeling the discharge chamber of an ion engine. The well known Maxwell's equations for electromagnetic fields are presented. The electromagnetic fields inside the discharge chamber are modeled in two parts: static and dynamic fields. First, the mathematical models used for the static magnetic fields and static electric fields are given. The static fields are those that are not influenced by the location of the charged particles. Secondly, the models used for the dynamic fields and the charged particle trajectories are given. The dynamic portion of the electric fields are affected by changes in charged particle locations. For this reason, the dynamic electric field model is discussed in the section that covers the models for tracking charged particles. Thirdly, the wall boundary conditions used in this model are discussed. Finally, the collision models used for the particle-particle interactions are presented.

A schematic of the computational domain considered in this work is given in Figure 2.1. This computational domain includes the discharge chamber cavity, the cathode exit, the cathode keeper walls, the chamber walls, the screen grid, and the magnetic circuit. The static magnetic field inside the discharge chamber is created by permanent magnets. These magnets are located on the outside

surface of the discharge chamber walls and are not shown in Figure 2.1. In this research, the following discharge chamber regions are not included: the inside of the cathode, the region between the keeper and the cathode, and the grid regions. The boundaries of the computational domain are drawn along the inside walls of these devices. This boundary is chosen to focus the computational modeling effort on the plasma inside the ion engine discharge chamber. In the future this modeling work can be extended to include these regions so that a comprehensive tool will be available for modeling the ion engine discharge chamber plasma.

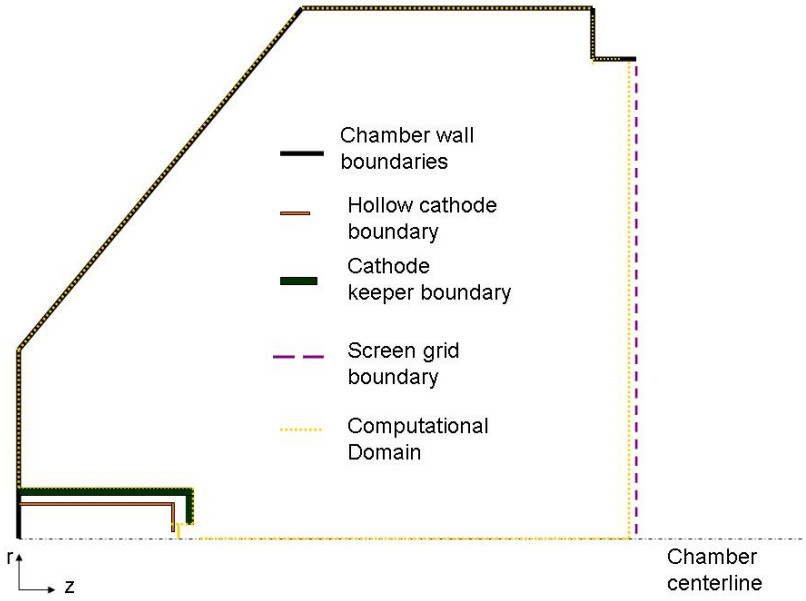

Figure 2.1: A schematic of the discharge chamber computational domain.

2.1 Electromagnetic Fields

The integral form of Maxwell's equations are given by [Griffiths 1989],

$$\int_s \vec{E} \cdot d\vec{S} = \int_V \rho dV, \tag{2.1}$$

$$\int_s \vec{B} \cdot d\vec{S} = 0, \tag{2.2}$$

$$\oint \vec{E} \cdot d\vec{l} = \int \partial_t \vec{B} \cdot dS, \tag{2.3}$$

and

$$\oint \vec{H} \cdot d\vec{l} = \int \partial_t \vec{D} \cdot dS + \int \vec{J} \cdot d\vec{S} \tag{2.4}$$

where $\vec{E}$ is the electric field, ρ is the charge density, $\vec{B}$ is the magnetic induction, $\vec{H}$ is the magnetic field, $\vec{D}$ is the electric displacement, $\vec{J}$ is the current density, V is the volume, $d\vec{S}$ is the differential surface area vector, $d\vec{l}$ is the differential distance vector, and t is the time. In later chapters $\vec{B}$ will be referred to as the magnetic field and the magnitude of $\vec{B}$ will be referred to as the magnetic flux density. In practice both "magnetic induction" and "magnetic field" terminologies are used for $\vec{B}$ (see Griffith, 1989). The first equation above is Gauss's law. This law states that the electric field flux from a closed surface is proportional to the charge enclosed in a given volume V. The second equation has no name to it and it states that magnetic flux from a closed surface is zero. The third equation is Faraday's law of induction. This law states that the line integral of an electric field is proportional to the negative time rate of change of the magnetic field flux through a surface. The fourth equation is Ampere's law which states that the line integral of the magnetic field is proportional to the time rate of change of the electric displacement and the electric current,J.

The constitutive relation for the electric displacement $\vec{D}$ in terms of the electric field $\vec{E}$ in vacuum is given by

$$\vec{D} = \varepsilon_0 \vec{E}. \tag{2.5}$$

Similarly a constitutive relation for the magnetic field in vacuum is established below. For linear materials $\vec{H}$ and $\vec{B}$ can be related as

$$\vec{H} = \frac{1}{\vec{\mu_0}} \cdot \vec{B} + \vec{H}_c \tag{2.6}$$

where $\vec{\mu_0}$ is the permeability tensor and $\vec{H}_c$ is the coercive force of the permanent magnets. These constituent equations are used in to reduce the number of field variables in Maxwell's equations.

Because of the principle of superposition for both the electric and magnetic fields the portion of the fields caused by the static phenomena may be added to that caused by the dynamic phenomenon.

The total electric and magnetic field at a given point in the discharge chamber is then obtained by adding the two effects. Utilizing this type of technique speeds up the calculation.

2.2 Static Fields

2.2.1 Static Magnetic Field

The magnetic field produced by the permanent magnets inside the discharge chamber is modeled using a subset of Maxwell's equations. Only the magnetostatic part of Maxwell's equations are required to determine the magnetic field. By considering steady state and no free currents, the magnetostatic equations [Griffiths 1989] become,

$$\vec{\nabla} \cdot \vec{B} = 0 \tag{2.7}$$

and

$$\vec{\nabla} \times \vec{H} = \vec{0}. \tag{2.8}$$

From Equation (2.7), $\vec{B}$ can be expressed as a curl product of a vector potential because the divergence of a curl is always zero. This can be shown as

$$\vec{B} = \vec{\nabla} \times \vec{A} \tag{2.9}$$

where $\vec{A}$ is the magnetic vector potential. Substituting Equation (2.9) into (2.6) gives

$$\vec{H} = \frac{1}{\vec{\mu_0}} \cdot \vec{\nabla} \times \vec{A} + \vec{H}_c. \tag{2.10}$$

Then substituting Equation (2.10) into Equation (2.8) gives

$$\vec{\nabla} \times [\frac{1}{\vec{\mu_0}} \cdot \vec{\nabla} \times \vec{A} + \vec{H}_c] = \vec{0}. \tag{2.11}$$

For the axisymmetric case of a two dimensional model, the magnetic vector potential, $\vec{A}$, only has a circumferential component; thus the magnetic vector potential can be written as,

$$\vec{A} = A_\theta \hat{\theta}. \tag{2.12}$$

Substituting this result into Equation (2.11) and expanding all cross product terms in cylindrical coordinates gives

$$\begin{aligned}\frac{1}{r}\left[\frac{1}{r\mu}\frac{\partial}{\partial\theta}\left(\frac{\partial(rA_\theta)}{\partial r}\right)\right]\hat{r}+\left[\frac{1}{\mu}\frac{\partial}{\partial z}\left(-\frac{\partial A_\theta}{\partial z}\right)-\frac{1}{\mu}\frac{\partial}{\partial r}\left(\frac{1}{r}\frac{\partial(rA_\theta)}{\partial r}\right)\right]\hat{\theta}\\ +\frac{1}{r}\left[-\frac{1}{\mu}\frac{\partial}{\partial\theta}\left(-\frac{\partial A_\theta}{\partial z}\right)\right]\hat{z}+\left[\frac{1}{r}\frac{\partial H_{cz}}{\partial\theta}-\frac{\partial H_{c\theta}}{\partial z}\right]\hat{r}+\\ \left[\frac{\partial H_{cr}}{\partial z}-\frac{\partial H_{cz}}{\partial r}\right]\hat{\theta}+\frac{1}{r}\left[\frac{\partial(rH_{c\theta})}{\partial r}-\frac{\partial H_{cr}}{\partial\theta}\right]\hat{z}=\vec{0}.\end{aligned} \tag{2.13}$$

Here the permeability of free space tensor is assumed to be uniform across the computational domain. Equation (2.13) can be further simplified with the assumptions of an axisymmetric geometry. In an axisymmetric design all quantities in the circumferential direction are uniform which means A_θ does not change in the θ-direction. This simplifies Equation (2.13) to

$$\frac{\partial}{\partial r}\left(\frac{1}{r\mu}\frac{\partial(rA_\theta)}{\partial r}\right)+\frac{\partial}{\partial z}\left(\frac{1}{\mu}\frac{\partial A_\theta}{\partial z}\right)=\frac{\partial H_{cr}}{\partial z}-\frac{\partial H_{cz}}{\partial r}. \tag{2.14}$$

The right-hand side in Equation (2.14) are properties of the permanent magnets used in the discharge chamber. The boundary conditions required for solving Equation (2.14) are:

$$A_\theta \rightarrow 0 \; as \; r \rightarrow \infty, \tag{2.15}$$

$$A_\theta \rightarrow 0 \; as \; z \rightarrow -\infty, \tag{2.16}$$

$$A_\theta \rightarrow 0 \; as \; z \rightarrow \infty, \tag{2.17}$$

and

$$\frac{\partial A_\theta}{\partial r} = 0 \; at \; r = 0. \tag{2.18}$$

Figure 2.2 shows the above boundary conditions considered in the magnetic field model. The far field boundary conditions are considered by modeling a somewhat larger region than the size of the discharge chamber (see Figure 2.2). Solving Equation (2.14) in conjunction with the boundary conditions in Equations (2.15) - (2.18) the magnetic vector potential values at all spatial locations can be found. The magnetic vector potential results are then substituted into Equation (2.9) to calculate

the values of the magnetic field vector, $\vec{B}$. The axial and radial components of the magnetic field vector are related to the magnetic vector potential with

$$B_r = -\frac{\partial A_\theta}{\partial z} \tag{2.19}$$

and

$$B_z = \frac{1}{r}\frac{\partial (rA_\theta)}{\partial r}. \tag{2.20}$$

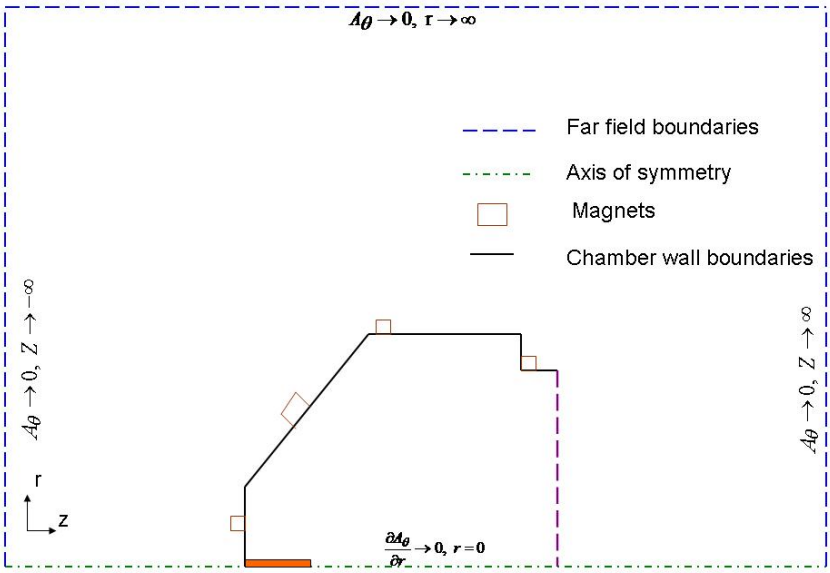

Figure 2.2: The boundary conditions considered in the static magnetic field model.

2.2.2 Static Electric Field

This research includes the electric field effects on the motion of the charge particles. Thus it is necessary to model the electric fields present inside the discharge chamber. In an ion engine discharge chamber the electric fields are generated by the static electric potentials applied to the chamber boundaries and from the charge particle distributions. Using superposition principles, the electric

potentials generated through each of these components can be modeled independently. Finally the electric potential results from each of these components can be added together to determine the total electric field. Thus the electric potential, ϕ, is given by

$$\phi = \phi_{static} + \phi_{dynamic} \tag{2.21}$$

where ϕ_{static} is the static electric potential and $\phi_{dynamic}$ is the dynamic electric potential. As will be shown latter the electric field components can then be calculated from the electric potential field.

In this work the static electric potentials inside the discharge chamber are modeled as shown in Figure 2.3. This figure essentially shows three regions. The dark region next to the cathode comes from experimental measurements. The white region is the bulk of the discharge chamber volume and is labeled the bulk plasma. This region is essentially at the floating potential of the plasma and set to be at this same potential for the entire bulk plasma region. The third region is a small strip next to the walls that is called the sheath. The sheath region is where the electrical potential quickly changes from the bulk plasma potential to the wall potential. The electric potential shown in Figure 2.3 is treated as the static portion of the total electric field determined by this model.

It should be recognized that the fields shown in Figure 2.3 are an approximation of the fields that would actually exist in a discharge chamber with a plasma. That means they include the effects of the wall potentials and the effects of the charged particles. Technically the static fields are only suppose to include the effects of the wall potentials. For our model it is beneficial to include particle effects into the static field. It is reasonable to still call the field in Figure 2.3 a static field because it does not change throughout the computation even though the particle number densities are changing. This is the most severe assumption made in this work. It is also the assumption that makes this work possible. To alleviate one of the major problems caused by this assumption, dynamic electric fields are still calculated. How and why these dynamic fields are determined is discussed in the next section.

The reason for the small region of experimentally determined potentials is that there is only

limited experimental data available. The limited experimental results of the electrical potentials are mainly due to the difficulties of getting Langmuir probes into the discharge chamber. The most critical region in which to have electrical potential details is around the cathode. Fortunately this is where experimental data is available [Herman 2005; Sengupta et al. 2004]. In actuality there is experimental data available over more of the discharge than what was utilized in this work. While this experimental data is noisy, it indicates a somewhat uniform plasma potential at locations removed from the cathode tip in the radial direction. In addition to the electric potentials throughout the volume of the discharge chamber, all anode biased discharge chamber walls are maintained at the discharge voltage potential. This includes the upstream wall of the discharge chamber where the cathode is located, the slanted wall, the side wall, and the flange attached to which the grids are attached. The screen grid is maintained at 0 volts. The cathode-keeper assembly is modeled as an enclosed box in which the cathode top surface is maintained at the cathode keeper potential. The cathode source tip area, the region where the primary electrons are produced, is maintained at an electric potential as measured in the experiments of [Jameson et al. 2005]. The wall sheath thickness is estimated using [Herman 2005]

$$t_s = 1.02\lambda_D\left[\left(-\frac{1}{2}ln\left(\frac{m_e}{m_{Xe}}\right)\right)^{\frac{1}{2}} - \frac{1}{\sqrt{2}}\right]^{\frac{1}{2}}\left[\left(-\frac{1}{2}ln\left(\frac{m_e}{m_{Xe}}\right)\right)^{\frac{1}{2}} + \sqrt{2}\right] \tag{2.22}$$

where λ_D is based on the Debye length given in Equation (1.21). While a real sheath would look like that shown in Figure 2.4, the sheaths in this work use a simple linear profile.

2.3 Particle Advance

2.3.1 Dynamic Fields

Dynamic fields in plasmas have been modeled using an EM or ES algorithm [Birdsall and Langdon 1991; Hockney and Eastwood 1988]. The EM algorithm considers the full set of Maxwell's equations (Equations (2.1)-(2.4)) to model the dynamic electric and magnetic fields. The ES algorithm assumes

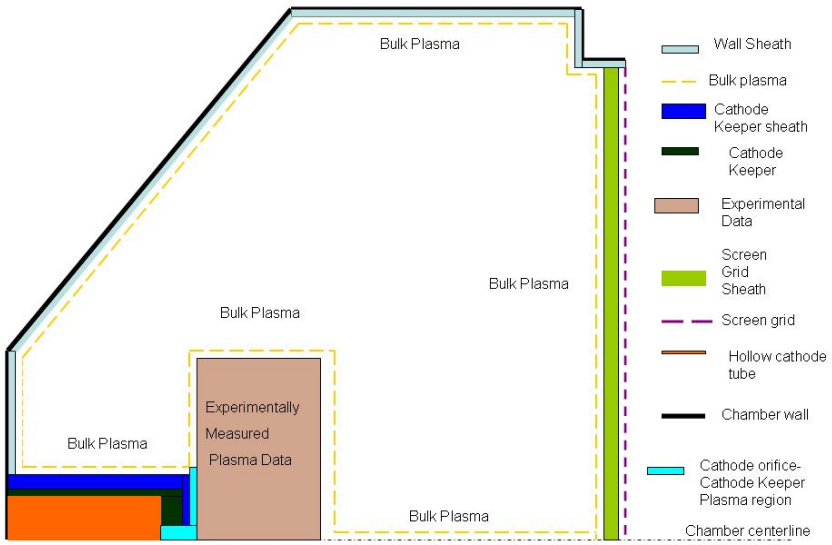

Figure 2.3: A schematic of the different electric field regions included in this model.

that the currents are small so that no significant self induced magnetic fields exist and that the charge particle densities do not change quickly relative to the speed of propagation of electromagnetic waves. The plasma in an ion engine satisfies both of these conditions. This is fortunate because these conditions cause the time dependent terms and the current integral in Maxwell's equations (Equations (2.3) and (2.4)) to vanish. This allows for quicker computations. The ES algorithm is essentially a pseudo static electric and magnetic field solver. It allows for changing magnetic and electric fields by changing from one static configuration to the next. The reason the electric fields change is the charge particles change locations. A possible reason why the magnetic fields would change is the position of the magnets may change. In this work the magnet locations are fixed and only a static magnetic field needs to be computed. This means the ES algorithm for this work essentially requires that the first Maxwell equation (Equations (2.1)) be solved as a function of time. The first Maxwell equation (Equations (2.1)) is nothing more than an electric field version of Poisson's equation.

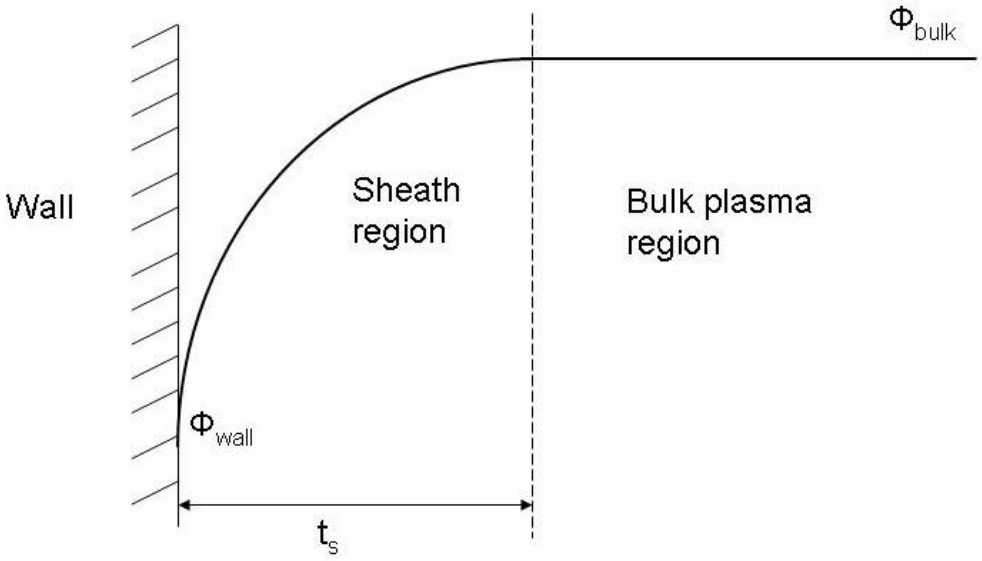

Figure 2.4: Sheath region near the wall.

Poisson's equation deals with the electrical potential $\phi_{dynamic}$ and can be written as

$$\nabla \cdot (\varepsilon_0 \nabla \phi_{dynamic}) = -\rho \tag{2.23}$$

where

$$\rho = |e|(n_i - n_e). \tag{2.24}$$

Here n_i is the net ion number density and n_e is the net electron number density.

In order to solve Equation (2.23)in a reasonable amount of computational time an approximation needs to be implemented. The approximation that is implemented in the solution of Equation (2.23) is that the value of ε_0 is artificially increased to a larger value. This inflated permittivity is denoted as ε_a. Inflating the plasma permittivity value was done in a PIC simulation done for Hall thrusters by Szabo [2001]. If this is not done a fine grid spacing and small time step would have to be used. These numerical parameters would have to be made so small as to render computational times on the order of several months or years. When ε_0 is made significantly larger the effect of the dynamic electric potentials on the total potentials in the discharge chamber is relatively small. This is fine

because the static field assumption made in this work included the effects of particles as it is based on the actual experimental plasma potential data. Thus the electric potential does not need to be altered extensively. The primary reason for solving the dynamic electric field equation is to allow charge neutrality to be obtained. If the dynamic electric fields are not computed, a large mismatch in the number of ions and the number of electrons in the discharge chamber arises. This is physically unrealistic and this technique avoids this problem. Using the artificial plasma permittivity on Equation (2.23) gives

$$\nabla \cdot (\varepsilon_a \nabla \phi_{dynamic}) = -\rho. \tag{2.25}$$

Also required to obtain a solution to Equation (2.23) are some boundary conditions. The boundary that needs to be defined is the same as that for the static electric field shown in Figure 2.1. Since the potentials applied to the wall boundaries of the discharge chamber when it is in operation are taken care of by the static electric field model, the dynamic field model has these potentials set to a value of zero. The boundary condition at the symmetry line of the discharge chamber is

$$\frac{\partial \phi}{\partial r} = 0. \tag{2.26}$$

Lastly using the principle of superposition, the electric potentials are obtained by adding dynamic electric potential values to the static electric potential values as shown in Equation (2.21).

Once the total electric potential is determined with Equation (2.21)the electric field, $\vec{E}$, is obtained from

$$\vec{E} = -\vec{\nabla}\phi. \tag{2.27}$$

By using Equation (2.27) the axial and radial component of the electric field are given by

$$E_z = -\frac{\partial \phi}{\partial z}, \tag{2.28}$$

and

$$E_r = -\frac{\partial \phi}{\partial r}. \tag{2.29}$$

2.3.2 Particle Advance

In this section the governing equations for modeling the trajectories of the charged particles and chargeless neutral particles are given. The following charged particles are considered: primary electrons, secondary electrons, singly charged ions, and doubly charged ions. The governing equations for these particle motions are given by the classical Newton-Lorentz equations of motion [Birdsall and Langdon 1991]. The charge particle equations of motion are

$$m_i \frac{dv_i}{dt} = q_i \big[\vec{E} + \vec{v}_i \times \vec{B}\big], \tag{2.30}$$

and

$$\frac{d\vec{x}_i}{dt} = \vec{v}_i \tag{2.31}$$

where m_i is the mass of a particle, $\vec{v}_i$ is the particle velocity, q_i is the electric charge of the particle, and $\vec{x}_i$ is the particle position. The subscript index i in the above equations refers to one of the four charged particle types that is being modeled. The left-hand side of Equation (2.30) shows the mass times the acceleration portion of Newton's law, and the right-hand side represents the forces applied to the particle by the electric and magnetic fields. The particle velocities are computed using Equation (2.30) and the positions of the charged particles are updated using Equation (2.31). The particle's velocity and position are advanced along a trajectory from the point of its creation to the point its destruction.

In this work, the electrons inside the discharge chamber are broken into two groups: primary and secondary electrons. Primary electrons are the high energy electrons that are emitted from the hollow cathode source. Secondary electrons are all of the rest of the electrons in the discharge chamber. Secondary electrons are mostly produced from the ionizing collisions of electrons with Xe I and Xe II. Primary electrons that have slowed below a certain velocity after undergoing an inelastic collision with neutrals or ions are also included with the secondary electrons. A primary electron is converted into a secondary electron when its energy goes below 4 eV. This grouping has advantages when trying to understand the behavior of high and low energy electrons independently

of one another. The way this is handled in this work may allow a number of secondary electrons to obtain high energies. The reason high energy secondary electrons are not moved to the primary electron group is that these electrons were not emitted from the cathode.

For the zero charge neutrals, the right hand side of Equation (2.30) becomes zero. Thus the neutral particles will remain at the same velocity throughout their trajectory. Just like the charged particles the positions of the neutrals are updated based on their velocity. Another factor that greatly alters the trajectories of all types of particles considered is collisions. The effects of collisions will be discussed in Section (2.5).

2.4 Boundary Conditions

Emission, reflection and absorption type boundary conditions are considered for the particles in the discharge chamber. Since a plasma is ignited by the emission of electrons from the cathode this boundary condition is described first.

2.4.1 Emission Boundary Conditions

2.4.1.1 Electron Source

In a discharge chamber primary electrons are created from a hollow cathode that is placed inside the discharge chamber. The physical phenomena occurring inside the hollow cathode is very complex. Inside the cathode, electrons are produced by heating a thermionic emitting surface, the cathode insert, to a high temperature. These electrons undergo ionizing collisions with neutrals before exiting the cathode orifice. The electrons created during the ionization processes can also exit the cathode orifice thus increasing the emission current. Neutral particles are provided from the propellant supply system. The plasma near the cathode surface is quasi-neutral [Domonkos 2002]. At the exit of the hollow cathode orifice both primary electrons and ions are present. The ions are produced near the cathode tip mainly because of ionizing collisions of primary electrons with the neutrals.

This ion production at the cathode tip facilitates a high electron emission current [Patterson et al. 1993]. Figure 2.5 shows the illustration of a hollow cathode emission. Experimental research work [Goebel et al. 2004; Jameson et al. 2005; Domonkos et al. 1999] and computational work [Domonkos 2002; Kamayema and Wilbur 1998; Polk et al. 2006] has been performed to investigate the plasma inside and at the exit of the hollow cathode. The work being presented in this dissertation focuses only on the discharge chamber modeling. At this stage there is no desire to increase the complexity of the model to include the complex physics present in the hollow cathode. To eliminate the hollow cathode from the computation the output from the hollow cathode must be used as a boundary condition to the discharge chamber. This is simply done by using experimental results to determine a value for the emission current. In this work the emission current entering the discharge chamber from the hollow cathode is treated as an electron source. This source produces the emission current and is located at the exit to the hollow cathode, but before the exit from the keeper.

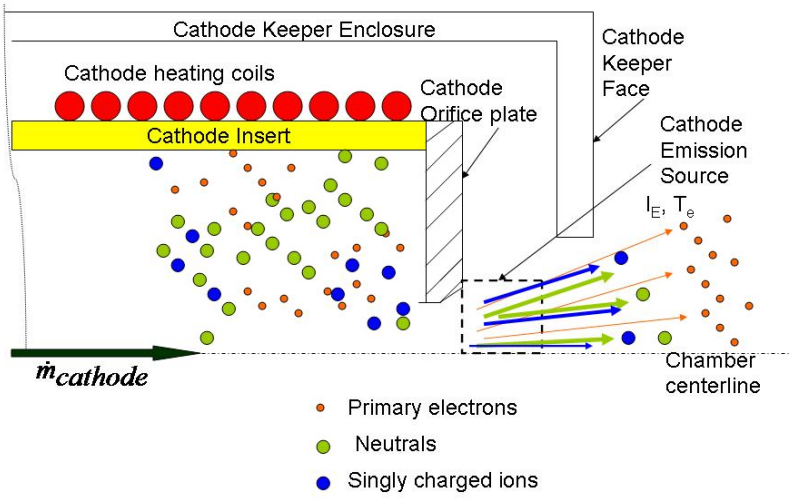

Figure 2.5: Illustration of hollow cathode emission.

The rate of plasma, $\dot{n}_p$, produced is based on the emission current from the cathode, I_E, and the

chosen volume near the cathode tip, V_{c_tip}. The source rate of electrons is

$$\dot{n}_p = \frac{I_E}{|e|V_{c\_tip}} \tag{2.32}$$

Physically there are ions leaving the cathode tip but they are small in number and not directly included in the analysis. They are indirectly included in the analysis in that some ionization is occurring in the small region labeled as the emission source. The speed at which the primary electrons are leaving the cathode tip is based on the electron temperature measured at the cathode tip location. The speed of the mono-energetic primary electrons, $|\vec{v}_{pe}|$, is

$$\vec{v}_{pe} = \sqrt{\frac{2|e|T_e}{m_e}} \tag{2.33}$$

where T_e is the electron temperature in eV. The flow path of primary electrons that leave the cathode source is taken as a stream directed towards the screen grid with a 15 degree half angle divergence. In the actual hollow cathode arrangement the cathode orifice is a chamfered hole through which the electrons leave into the bulk discharge chamber plasma.

2.4.1.2 Neutral Source

Neutral particles are supplied to the discharge chamber through the hollow cathode and through a main feed location on the discharge chamber. Both neutral sources are modeled as volumetric sources where the rate is based on the respective flow rates. The source rate of neutrals, $\dot{n}_{Xe,cathode}$, through the hollow cathode is determined using

$$\dot{n}_{Xe,cathode} = \frac{\dot{m}_{cathode}}{m_{Xe}V_{c\_tip}}. \tag{2.34}$$

Similarly the main neutral source rate, $\dot{n}_{Xe,main}$ is determined using

$$\dot{n}_{Xe,main} = \frac{\dot{m}_{main}}{m_{Xe}V_{main}}, \tag{2.35}$$

where V_{main} is the main feed location volume.

The neutrals speed at the source is determined using the wall temperature measured at the emission locations. The neutral speed at the cathode source, $|\vec{v}_{Xe,cathode}|$, is determined using,

$$\vec{v}_{Xe,cathode} = \sqrt{\frac{2|e|T_{cathode}}{m_{Xe}}} \tag{2.36}$$

where $T_{cathode}$ is the wall temperature observed at the cathode orifice plate in eV. Similarly the neutral speed at the main feed location, $|\vec{v}_{Xe,main}|$, is determined using,

$$\vec{v}_{Xe,main} = \sqrt{\frac{2|e|T_{main}}{m_{Xe}}} \tag{2.37}$$

where T_{main} is the wall temperature observed at the main feed locations given in eV.

The flow path of neutrals exiting the hollow cathode are modeled in a similar fashion to the emission of primary electrons from the cathode. Figure 2.5 illustrates the flow of neutrals through the cathode orifice. The neutral flow path from the main source is based on its location inside the discharge chamber. Normally this source is placed either at the back wall with the flow stream directed towards the grid or at the side wall with the flow stream directed upstream. In this work it is placed in the latter position.

2.4.2 Reflecting and Absorbing Boundary Conditions

Inside the discharge chamber there are four types of surfaces that need to be modeled in terms of particle boundary conditions. These are: cathode potential surfaces, anode potential surfaces, grids, and the symmetry boundary line. These surfaces are shown in Figure 2.1. How these surfaces are modeled in regards to a boundary depends on the type of particle hitting them. From a boundary condition viewpoint there are positively charged particles which include all ions, negatively charged particles which include electrons, and particles that have no charge. The cathode potential surfaces in the discharge chamber include the cathode and the keeper. The grids are also at the cathode potential, but these need to be handled differently than the cathode and the keeper. At the cathode potential boundaries electrons are reflected, ions are absorbed, and neutral particles are reflected.

Two types of reflections are dealt with in this work: specular and diffuse. In general charged particles are handled with specular reflections and neutral particles are handled with diffuse reflections.

The anode potential surfaces include the upstream vertical wall, the side wall, and the flange to which the grids are attached at the downstream end of the discharge chamber. At these surfaces the electrons and ions are absorbed, while the neutrals are reflected. When an ion is absorbed at an anode biased wall it is not taken from the computation, but converted into a neutral. Physically what is happening is the ion goes to the wall and recombines with an electron at the wall surface. This turns the ion into a neutral. This process is modeled as an ion absorption with a subsequent neutral particle emission. When electrons hit an anode biased wall they are physically absorbed into the wall. An additional event that may occur when an ion hits an anode biased wall is secondary emission. When an ion hits an anode biased wall there is a chance that an electron will be released from the wall surface to behave as a free electron in the computational domain. Whether this happens is determined by the secondary electron emission coefficient. The empirical formula for the secondary electron emission coefficient, γ_i is obtained using [Raizer 1991]

$$\gamma_i = 0.016\big(\epsilon_{ionz} - \phi_{wf}\big) \tag{2.38}$$

where ϵ_{ionz} is the ionization potential given in eV and ϕ_{wf} is the work function necessary to extract an electron from a metal surface. This work function is given in eV in the above equation. The γ_i relation given above is independent of incident ion energies up to 1 keV [Raizer 1991], but it depends on the work function of the metal surface and the ionization potential. Whether a secondary electron is produced when an ion hits the wall is based on the γ_i value. This γ_i value is compared to a random number to determine whether secondary electron emission occurs.

Because the grids have holes from which ions and neutrals can escape the discharge chamber, special care must be used at this boundary. Both ions and neutrals have a transparency specified at the screen grid boundary. This transparency determines the faction of particles that make it through the holes in the grid wall to the outside of the discharge chamber. With these transparencies the

number of ions and neutrals leaving the discharge chamber through the grid holes can be determined. The number of ions being absorbed by the grid wall is determined by using one minus the ion transparency. Neutrals that hit the grid and do not go through the grids holes are reflected back in to the discharge chamber. The number of neutrals that do this is one minus the neutral transparency.

The symmetry boundary condition along the centerline of the discharge chamber is the easiest to explain. At this boundary all particles are reflected in a specular manner.

2.5 Particle Collisions

In this work particle collisions between electrons and neutrals, ions and neutrals, and electrons and ions are handled using collision cross sections. From the collision cross section a collision probability can be determined. Once the collision probability is determined a computational procedure using a Monte Carlo Collision (MCC) technique [Birdsall 1991; Vahedi and Surendra 1995] can be used to handle the collisions. Elastic collisions between charged particles are not handled with the MCC technique. These types of collisions are naturally accounted for in the dynamic electric field model. The dynamic electric fields are a function of the charge particle locations. The calculated particle trajectories are in turn a function of the electric fields. It is through these electric fields that the charged particles undergo elastic collisions with one another. According to [Birdsall and Langdon 1991] a PIC technique simulates the long range coulomb collision effects and smoothes the short range coulomb collision effects.

The types of collisions between electrons and neutral particles handled with the MCC technique in this work are elastic collisions, excitation collisions, and ionizing collisions. In an elastic collision, the electron loses little or none of its kinetic energy when it hits a neutral particle. The collision simply changes the direction of travel of the electron. In an elastic collision the electron can pass some of its energy of motion to the motion of the particle with which it is colliding, even though none of the energy goes into increasing the internal energy of the particle. In an excitation collision,

the electron loses a significant amount of its kinetic energy and gets scattered after the collision. The electron has to lose at least the excitation threshold energy in these types of collisions. In an ionizing collision an electron ionizes a neutral atom and creates a secondary electron. The electron which caused the neutral to be ionized loses kinetic energy equal to or greater than the amount of energy required to ionize the neutral atom. This energy is known as the ionization energy.

Ion collisions with neutral particles are modeled as elastic or charge exchange collision types. In an elastic collision, the incident ion loses some or none of its energy and scatters. In a charge exchange collision, the incident ion excites a colliding neutral particle and after the collision the neutral particle becomes an ion and the incident ion becomes a neutral particle.

Electron collisions with ions are modeled as excitation, ionization, and three-body recombination. In an excitation collision, the incident electron excites the ion to a higher energy level. In an ionization collision, the incident electron ionizes the ion to its next charged state and a secondary electron is released. In the above two collisions, the colliding electron loses some of its kinetic energy and gets scattered after the collision. In an electron-first ion-electron three-body recombination process, the slow moving electron recombines with the ion and becomes a neutral particle. The other electron remains an electron. In the case of three body recombination between two electrons and a second ion the slow moving electron recombines with the double ion producing a singly charged ion.

2.5.1 Null Collision Technique

The occurrence of a particle collision is determined using a null collision technique as described in [Birdsall 1991] and [Vahedi and Surendra 1995]. This technique uses a constant collision frequency to determine the maximum fraction of particles that may undergo collisions. Doing this eliminates the need to look up collision cross sections for every particle in the computation domain. The null collision probability [Vahedi and Surendra 1995] is given by,

$$P_{null} = 1 - exp(-\nu_c * \triangle t), \tag{2.39}$$

where ν_c is the constant collision frequency and $\triangle t$ is the time step size. The constant collision frequency, ν_c is obtained by looking for the maximum sum of all collision frequencies over all possible energies

$$\nu_c = max(n_t \sigma_T(\epsilon_{inc})|\vec{v}_{inc}|). \tag{2.40}$$

In this equations n_t is the number density of the target particle, $\sigma_T(\epsilon_{inc})$ is the total collision cross-section, and $|\vec{v}_{inc}$ is the incident particle's speed. The constant collision frequency is a computational convenience that is made to represent reality by adding a null collision frequency to the actual collision frequency at each energy level (see [Vahedi and Surendra 1995]). The total collision cross-section, $\sigma_T(\epsilon_{inc})$, is given by

$$\sigma_T(\epsilon_{inc}) = \sigma_1(\epsilon_{inc}) + \sigma_2(\epsilon_{inc}) + ... + \sigma_N(\epsilon_{inc}) \tag{2.41}$$

where N is the total number of collision types considered. The collision cross section area for all collision types is based on the kinetic energy of the incident particle which is

$$\epsilon_{inc} = \frac{1}{2} m_{inc} |\vec{v}_{inc}|^2 \tag{2.42}$$

where m_{inc} is the mass of the incident particle. With the null collision probability determined using Equation (2.39) and Equation (2.40) the number fraction of particles that experience collisions is calculated using

$$N_{coll} = N_{total} * P_{null}. \tag{2.43}$$

Only this number of particles is tested for collisions and some of these particles may not undergo a collision.

3

Solution of Mathematical Model

This chapter presents the numerical techniques used to solve the mathematical model given in the previous chapter. As is commonly done in the literature this algorithm will be referred to as the PIC-MCC algorithm. A PIC algorithm tracks particles throughout a computational mesh comprised of computational cells including effects of magnetic and electric fields. Because these fields can change with particle position, the PIC simulation includes routines to determine the electric and magnetic fields. The MCC technique simulates particle collisions using statistical techniques.

Figure 3.1 shows a flow chart of the computing sequence used by the PIC-MCC simulation utilized in this work. In this flow chart the PIC-MCC simulation is divided into two pieces: a static piece and a dynamic piece. The dynamic piece of this algorithm deals with calculations that depend on the position of the particles in the discharge chamber. The static piece of the algorithm deals with input, boundary conditions, the computational mesh, the static magnetic field, and the static electric field. All computations done in the static portion of the algorithm are independent of the particle locations determined in the dynamic portion of the algorithm.

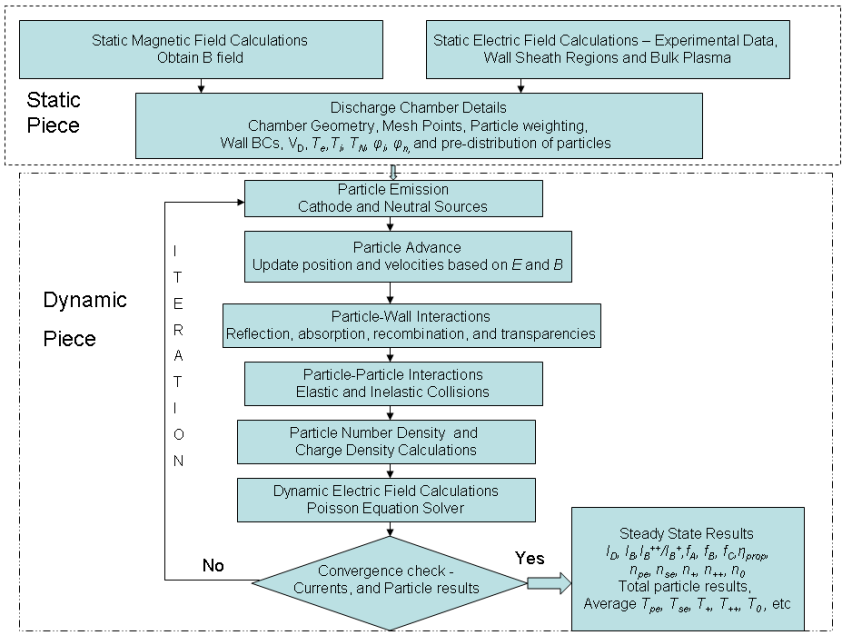

Figure 3.1: A flow chart of PIC-MCC model showing the computing sequence of an ion engine discharge chamber plasma simulation.

3.1 Static Piece of PIC-MCC Simulation

The information generated in the static piece of the PIC-MCC algorithm that must be delivered to the iterative portion of the PIC-MCC algorithm is: the discharge chamber geometry, the wall boundary conditions, the computational mesh, the static electric field, the static magnetic field, a number of numerical parameters, the operating conditions of the discharge chamber, and maybe an initial guess at the distribution of particles in the discharge chamber. This guess could include particle distributions for the first ions, second ions, primary electrons, secondary electrons, and neutrals. The wall boundary conditions for the electric fields, the magnet fields, and the particle trajectories have been discussed in Chapter 2. The discharge chamber geometry studied in this work will be given in Chapter 4. Also given in Chapter 4 are the numerical parameters used and the operating conditions of the discharge chamber. In this section the computational mesh, the static electric field, and the static magnetic field are discussed.

3.1.1 Computational Mesh

The dynamic portion of this simulation requires a computational mesh. This mesh will be called the PIC-MCC mesh. Since the PIC-MCC mesh does not change as the particle locations change, generating this mesh can be performed in the static portion of the simulation. The mesh has several functions: the static electric and magnetic fields are stored on this mesh, the particle number density distributions are determined on this mesh, the dynamic electric fields are determined using this mesh, the electric and magnetic forces that need to be applied to the particles are determined using this mesh, the number density of the particles are determined using this mesh, and any calculation that requires knowledge of position in the discharge chamber uses this mesh. The static magnetic fields are calculated on a finite element mesh generated by the computer program MAXWELL 2D [Ansoft Corporation 2007]. Once the static magnetic field is determined these results are transferred to the PIC-MCC mesh. The static magnetic field mesh extends outside the walls of the discharge chamber as shown in Figure 2.2, while the PIC-MCC mesh is confined by the walls of the discharge chamber.

The dynamic calculations are done using two meshes. The base mesh will be referred to as the full-cell mesh and the staggered mesh will be referred to as the half-cell mesh. These names are used because this is what seems to commonly be used in the literature [Birdsall and Langdon 1991]. A schematic of the full and half-cell control volumes are shown in Figure 3.2. This figure clearly shows the half-cell mesh staggered from the full-cell mesh. The half-cell mesh can be remembered by the fact that it extends half-way into the four full-cell volumes that surround it. The grid point numbering scheme is also shown on Figure 3.2. The numbering is based on the corner grid points of the full-cell control volumes.

In this PIC-MCC simulation the field variables, as shown in Figure 3.3, are stored at the full-cell face centers. This follows the Yee mesh technique given in reference [Yee 1966]. Here the $\sim$ sign on top of a field variable indicates the integral form of a field variable. The two field variables used in

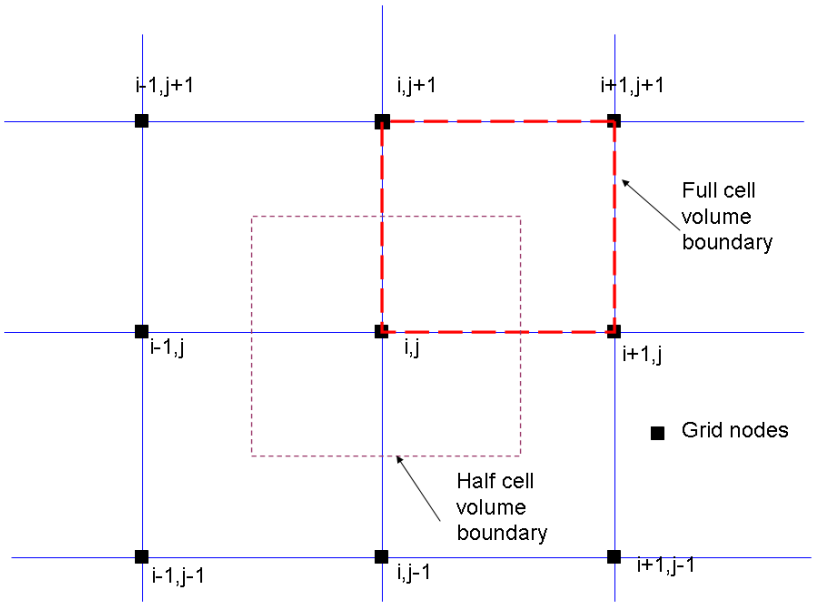

Figure 3.2: Computational mesh showing the half cell volume and full cell volume boundaries.

this work are defined as:

$$\tilde{\vec{E}} = \int \vec{E} \cdot d\vec{l} \tag{3.1}$$

and

$$\tilde{\vec{B}} = \int \vec{B} \cdot d\vec{S}. \tag{3.2}$$

The line integral in Equation (3.1) is along a cell side, and the surface integral in Equation (3.2) is over a surface formed by the cell faces. The charge density, ρ, electric potential, ϕ, electric field, $\vec{E}$, and magnetic field, $\vec{B}$, variables are stored at the cell nodes which are shown in Figure 3.3. The cell nodes, the cell face centers, and the grid spacings are identified in Figure 3.3.

The two dimensional computational mesh can be either a uniform or a non-uniform grid. In this research, both are used. The nonuniform grid is used to perform all calculations in the PIC-MCC simulation. The uniform grid is used for the post processing application of smoothing the results.

Using the nonuniform grid in the PIC-MCC calculations allows for higher spatial resolution in regions where the fields have large gradients, while saving computer time by using lower resolution in

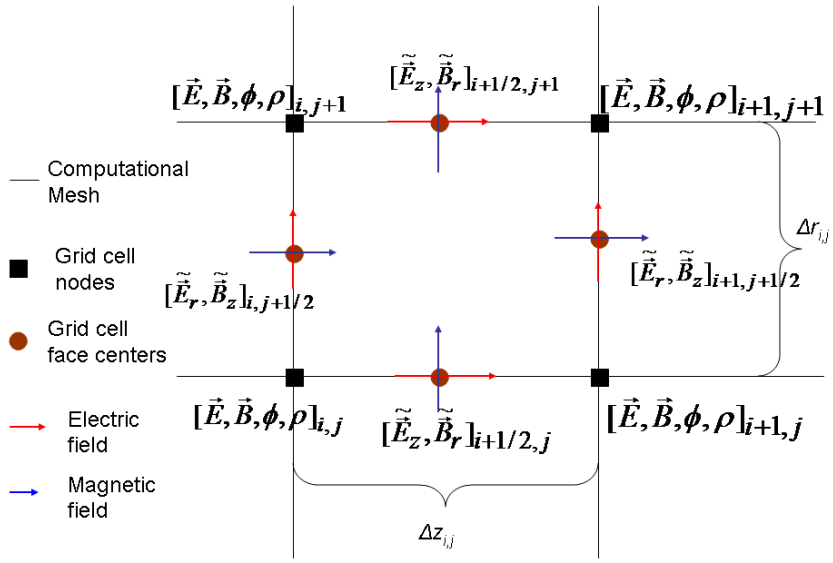

Figure 3.3: Field Variables are stored as used in Yee Mesh.

regions where the fields are more uniform. The high field gradient regions in the discharge chamber which require grid refinement are: 1) near the cathode emission source, 2) the sheath regions at the walls and at the screen grid, and 3) the cusp regions of the magnets. The selection of grid spacing sizes is based upon the stability criteria of the numerical techniques used and by doing a grid refinement study (see Chapter 4). The stability issues are discussed in detail near the end of this chapter. A separate code has been written external to the main PIC-MCC code to produce non-uniform computational meshes. The main PIC-MCC code is set to read the non-uniform mesh points from an external file.

For computational convenience, the mesh points are stored in terms of the actual dimensions (i.e., in meters) and also in terms of the grid units (η_i, ξ_j). The grid units, η_i and ξ_j, are values which are based on the integer numbers of the grid points in the z and r directions respectively. They are given as

$$\eta_i = i \quad \text{where} i \in [0, N_z] \tag{3.3}$$

and

$$\xi_j = j \quad \text{where} j \in [0, N_r]. \tag{3.4}$$

Here N_z, and N_r are the total number of mesh points in the z and r directions respectively. In this PIC-MCC simulation, the particle positions are stored in terms of the grid units. The grid units aid in getting the information stored in the computational cell where the particle is present. This allows quicker evaluation of the electric and magnetic field forces at the particle locations during particle advancing. In addition, the representation of particle locations in grid units helps to compute the charge density values at the grid points and in grouping the colliding heavy target particles at each computational cell during the MCC portion of the simulation. At the end of particle advancing sequence the particle locations need to be transferred back to dimensional values. Once the new positions are known, the particle position information is reformatted back to grid units.

When a nonuniform computational mesh is utilized in the PIC-MCC simulation, the output particle distribution results are found to be distorted and to have lot of noise in the dense mesh regions. This occurs because of the fewer number of particles per cell in these regions. These distortions can be smoothed by considering a larger number of computer particles in the simulation. The problem with increasing the number of particles in the simulation is computational times become unreasonable. Because computational time is a major issue in this work a technique for smoothing the results determined on the nonuniform grid has been developed. This is simply done by transferring all nonuniform field results to a coarser uniform grid. The transferring of results from the fine nonuniform grid to the coarse uniform grid is a post processing function.

3.1.2 Static Magnetic Fields

Based on the location, size, orientation, and strength of the permanent magnets Equation (2.14) is solved along with the boundary conditions given in Equations (2.15) - (2.18) to obtain the magnetic vector potential values at all spatial locations in the PIC-MCC computational domain. These equations are solved using a finite element technique with an iterative matrix solver. The axial

and radial magnetic field values are then determined from the magnetic vector potential by solving Equations (2.19) and (2.20). It is the axial and radial values of the magnetic field which are supplied to the PIC-MCC simulation. Before these values are supplied to the PIC-MCC simulation they are transferred from the finite element mesh used in the static magnetic field calculation to the PIC-MCC mesh. An external code has been developed to read the output information from MAXWELL-2D and write it into a readable format for the PIC-MCC code.

In this work none of the materials from which the discharge chamber and cathode assembly are made interact with the magnetic field. If the discharge chamber contained materials that do interact with a magnetic field, then the magnetic properties of these materials would have to be entered into the static magnetic field solver as well as the magnet properties.

As mentioned above this calculation is carried out using the computer code MAXWELL-2D [Ansoft Corporation 2007]. A previous study of magnetic field modeling [Menart 1998] indicates that Maxwell-2D is an excellent software package for simulating two dimensional magnetic field problems. More discussion about the static magnetic field simulation can be found in the thesis work [Deshpande 2005].

3.1.3 Static Electric Fields

The static electric fields used in the PIC-MCC simulation are determined from electrical potential values. This is a convenient way to do this because electric potentials are scalar quantities and electric fields are vector quantities. In addition the boundary conditions on the discharge chamber are easily specified in terms of electrical potentials.

As stated in Chapter 2 there are three techniques utilized for determining the static electric potentials. Each of these techniques is applied to a separate region of the discharge chamber. These three regions are the near cathode region, the wall region, and the rest of the discharge chamber. These regions are clearly shown in Figure 2.3. The cathode region uses experimental results, the wall region is the sheath, and the bulk of the discharge chamber is at the floating potential of the

discharge.

As stated in Chapter 2 measured potentials are used to determine the potentials in the cathode region. In the bulk of the discharge the plasma potential is at a constant potential and set to float 3 volts above the discharge voltage. This is a reasonable number as the experimental investigations indicate [Herman 2005]. In the wall regions the electric potential is linearly interpolated from the wall value to the bulk plasma value. In order to do this the sheath thickness, t_s, is required. This is done using Equation (2.22). For xenon propellant, Equation (2.22) can be reduced to

$$t_s = 5.31\lambda_D \tag{3.5}$$

The Debye length values near the chamber walls using Equation (1.21) with a measured electron number density of $n_e = 1 \times 10^{15} m^{-3}$ and an electron temperature of $T_e = 3eV$ [Herman 2005; Sengupta et al. 2004] gives $4 \times 10^{-4} m$. Applying this Debye length value in Equation (3.5) gives a sheath thickness of $2.125 \times 10^{-3} m$. Since the electron number density at the walls varies greatly from one location to the next, and it is reported in [Herman 2005] that the experimentally measured electron number density values near the chamber walls are prone to have large errors, it is reasonable to use a sheath thickness that is somewhat different than this number. For this work the nominal value of the sheath thickness is taken to be $2.125 \times 10^{-3} m$. This varies a little depending on the griding.

A separate code, external to the PIC-MCC code, has been written to set up the static electric potential values for the entire discharge chamber. This code writes the static plasma potential values at the PIC-MCC cell nodes which can be read as an input to the PIC-MCC code.

3.2 Dynamic PIC-MCC simulation

Once the inputs are given, the PIC-MCC simulation cycle starts first by emitting particles into the discharge chamber based on the source rates specified at their locations. The hollow cathode emission of primary electrons, and neutrals and the main neutral supply are the two emission sources

for the discharge chamber. The forces are calculated at the particle locations which are determined using bilinear weighting of the electric and the magnetic fields at the grid points. Then the particles are advanced to new locations by calculating the velocities and positions based on the forces. During particles advance they are checked for crossing at the wall locations. Appropriate wall boundary conditions are applied to the particles that are crossing at the boundaries. Particles are then checked for collisions and the direction of travel for the colliding particles is calculated. The particle number density and charge density values at the grid locations are determined from the new particle positions. These values are then used to update the electric fields at the grid locations. This completes one simulation cycle. This simulation cycle is continued until the results reach a steady state or a desired time level. The steady state is determined based on the convergence of current and total particle results for the discharge chamber.

3.2.1 Dynamic Electric Field

As discussed in Chapter 2, the dynamic ES algorithm is appropriate and the least computational intensive technique for determining the dynamic electric potentials or equivalently the dynamic electric fields for an ion engine discharge chamber. For this situation the ES algorithm essentially reduces to solving Poisson's equation (see Equation (2.23) where the charge density changes as the charge particle distributions change. To solve the ES algorithm a parallel DADI (dynamic alternating direction implicit) Poisson solver has been developed as part of this work. The parallel DADI scheme is discussed in detail latter in this chapter; along with the parallel processing procedures used in this work.

Once the dynamic electric potential values are available, both static and dynamic electric potential values are summed to obtain the electric potential values inside the discharge chamber (see Equation 2.21). The electric potential values are computed at the cell nodes. Then the integral form of the axial and radial electric fields at the cell face-centers are calculated using

$$\tilde{E}_{z,i+1/2,j} = \phi_{i,j} - \phi_{i+1,j}, \tag{3.6}$$

and

$$\tilde{E}_{r,i,j+1/2} = \phi_{i,j} - \phi_{i,j+1}. \tag{3.7}$$

The electric field quantities $E_{z,i,j}$ and $E_{r,i,j}$ at any cell node can then be evaluated by interpolating the cell face-centered electric field values using the appropriate weighting functions. The axial electric field, $E_{z,i,j}$, at cell node (i,j) is given by

$$E_{z,i,j} = w_z^+ \left(\frac{\tilde{E}_{z,i+1/2,j}}{\triangle z_{i,j}} \right) + w_z^- \left(\frac{\tilde{E}_{z,i-1/2,j}}{\triangle z_{i-1,j}} \right) \tag{3.8}$$

where the weighting functions (w_z^+ and w_z^-) and the axial grid spacings ($\triangle z_{i,j}$ and $\triangle z_{i-1,j}$) are defined as

$$w_z^+ = \frac{\triangle z_{i-1,j}}{\triangle z_{i,j} + \triangle z_{i-1,j}}, \tag{3.9}$$

$$w_z^- = \frac{\triangle z_{i,j}}{\triangle z_{i,j} + \triangle z_{i-1,j}}, \tag{3.10}$$

$$\triangle z_{i,j} = z_{i+1,j} - z_{i,j}, \tag{3.11}$$

and

$$\triangle z_{i-1,j} = z_{i,j} - z_{i-1,j}. \tag{3.12}$$

Here $z_{i+1,j}$, $z_{i,j}$, and $z_{i-1,j}$ are the axial locations at cell nodes $(i+1,j)$, (i,j), and $(i-1,j)$ respectively.

Similarly the radial electric field, $E_{r,i,j}$, at cell node (i,j) is given by

$$E_{r,i,j} = w_r^+ \left(\frac{\tilde{E}_{r,i,j+1/2}}{\triangle r_{i,j}} \right) + w_r^- \left(\frac{\tilde{E}_{r,i,j-1/2}}{\triangle r_{i,j-1}} \right) \tag{3.13}$$

where the weighting functions (w_r^+ and w_r^-) and the radial grid spacings ($\triangle r_{i,j}$ and $\triangle r_{i,j-1}$) are defined as

$$w_r^+ = \frac{\triangle r_{i,j-1}}{\triangle r_{i,j} + \triangle r_{i,j-1}}, \tag{3.14}$$

$$w_r^- = \frac{\triangle r_{i,j}}{\triangle r_{i,j} + \triangle r_{i,j-1}}, \tag{3.15}$$

$$\triangle r_{i,j} = r_{i,j+1} - r_{i,j}, \tag{3.16}$$

and

$$\triangle r_{i,j-1} = r_{i,j} - r_{i,j-1}. \tag{3.17}$$

Here $r_{i,j+1}$, $r_{i,j}$, and $r_{i,j-1}$ are the radial locations at cell nodes $(i, j+1)$, (i, j), and $(i, j-1)$ respectively.

3.2.2 Particle Advance

Time integration of the equations of motion, Equation (2.30) and Equation (2.31), is done using a second order leap-frog scheme with a Boris advance to handle the magnetic field rotation. The time centered finite difference form of Equation (2.30) is given as [Birdsall and Langdon 1991]

$$\frac{\vec{v}_i^{n+1/2} - \vec{v}_i^{n-1/2}}{\triangle t} = \frac{q_i}{m_i}\left[\vec{E}^n + \frac{\vec{v}_i^{n+1/2} + \vec{v}_i^{n-1/2}}{2} \times \vec{B}^n\right] \tag{3.18}$$

where $\vec{v}_i$ is the particle velocity.

In the Boris advance technique the electric and magnetic forces are separated in the integration by substituting the relations

$$\vec{v}_i^{n-1/2} = \vec{v}_i^{-} - \frac{q_i \vec{E}^n \triangle t}{2m_i} \tag{3.19}$$

and

$$\vec{v}_i^{n+1/2} = \vec{v}_i^{+} + \frac{q_i \vec{E}^n \triangle t}{2m_i} \tag{3.20}$$

into Equation (3.18). This produces a new time integration equation which eliminates the electric field forces from (3.18),

$$\frac{\vec{v}_i^{+} - \vec{v}_i^{-}}{\triangle t} = \frac{q_i}{2m_i}\left(\vec{v}_i^{+} + \vec{v}_i^{-}\right) \times \vec{B}^n. \tag{3.21}$$

Equation (3.21) represents the rotation caused by magnetic field forces acting on the moving charged particle. The magnetic field rotation is handled by a Boris rotation which introduces another set of variables,

$$\vec{v}_i^{'} = \vec{v}_i^{-} + \vec{v}_i^{-} \times \vec{t}_i \tag{3.22}$$

and

$$\vec{v}_i^{+} = \vec{v}_i^{-} + \vec{v}_i^{'} \times \vec{s}_i \tag{3.23}$$

with

$$\vec{t_i} = \frac{q_i \vec{B}^n \triangle t}{2m_i} \tag{3.24}$$

and

$$\vec{s_i} = \frac{2\vec{t_i}}{1 + \vec{t_i^2}}. \tag{3.25}$$

The computational steps used to solve Equations (3.19) - (3.25) are: first compute the $\vec{v_i^-}$ velocity by adding half the electrical force to the known velocity $\vec{v}_i^{n-1/2}$ at time level $n-1/2$ using Equation (3.19). Then rotate the $\vec{v_i^-}$ velocity using Equations (3.22) - (3.25) for a full time step to calculate the $\vec{v_i^+}$ velocity and then add the remaining half electrical impulse, Equation (3.20), to obtain the new velocity, $\vec{v}_i^{n+1/2}$ at time level $n+1/2$. The particle positions are updated with the new velocity using

$$\vec{x}_i^{n+1} = \vec{x}_i^n + \vec{v}_i^{n+1/2} \triangle t. \tag{3.26}$$

3.2.2.1 Subcycling for heavy particles

Due to the high mass ratio of the heavy particles (ions and neutrals) compared to the electrons, the neutrals and ions always move at a much slower speed compared to the electrons. For xenon propellant, the mass ratio, $\frac{m_e}{m_{Xe}}$, is calculated to be $\sim 2.4 \times 10^5$. This means that the speeds of the heavy particles are more than two orders-of-magnitude smaller than the electron speeds. Moving the heavy particles using the same time step value as the electrons greatly increases the computational time. To handle the discrepancies in particle speeds, a subcycling procedure [Birdsall and Langdon 1991] is adopted. If subcycling is set to 100, the heavy particles use 100 times the time step that the electrons use. To keep the particles at the same time the electrons take 100 time steps for every heavy particle time step.

A subcycling procedure helps minimize the computational runtime. A drawback is that the subcycling procedure creates an issue in terms of handling the removal of heavy particles that have undergone inelastic collisions, such as ionizations and recombination collisions, in the MCC

simulation. These issues will be discussed in detail in the particle collision sequence section of this chapter.

3.2.3 Particle-Wall Interactions

At walls a number of things can happen to the particles: absorption, reflection, transmission, recombination, and secondary emission. What happens depends on the wall potential and the particle. These issues have all been discussed in Chapter 2. In this section some additional information will be presented on secondary electron emission and the transmission of particles through the screen grid.

At the screen grid plate at the end of the chamber, neutrals and ions have a chance of escaping the discharge chamber through the holes in the grid. The escaping of ions is what makes an ion engine work. As mentioned in Chapter 2 the probability of escaping is given by the transparency parameter. There is a separate transparency for neutrals φ_0 and ions φ_{ion}. Computationally the means used to determined which particles make it through the grid holes is determined by a random number. When a particle hits the grid a random number is generated. If the random number is less then or equal to the transparency, the particle exits the discharge chamber and is lost from the computation. If the random number is greater than the transparency, the particle is treated as hitting a solid cathode potential wall. From a computational perspective particles that leave the discharge chamber through the grid holes can be considered to be absorbed by the wall.

Secondary emission occurs when an ion hits a wall and drives a free electron back into the discharge chamber. The probability of this occurring is determined by the secondary electron emission rate coefficient. The secondary emission rate coefficient γ_i value is based on the work function, ϕ_{wf}, and the ionization potential (see Equation (2.38)). The ionization for a singly charged xenon ion, Xe^+, is 12.1 eV; and for doubly charged xenon, Xe^{++}, it is 33.3 eV. Using these ionization values, along with the ϕ_{wf} values, for different metals, a γ_i value can be determined for both hitting Xe^+ and Xe^{++} ions. The γ_i values for different wall materials for both incident Xe^+ and Xe^{++} are

tabulated in Table 3.1. The reference values for the ϕ_{wf} are obtained from the following references [Raizer 1991; Mura 1952].

Table 3.1: Secondary electron emission coefficient for different metals with incident Xe^{+} and Xe^{++} ions.

Metal Type	ϕ_{wf}	$\gamma_{i,Xe^{+}}$	$\gamma_{i,Xe^{++}}$
Aluminum	4.25	0.058	0.40
Titanium	4.11	0.062	0.39
Molybdenum	4.3	0.056	0.395

All wall boundaries are set to store the flux of particles that are collected during a specified time interval under each species category. These stored particle flux values are used for determining the current collected at the walls for each species type. The wall current, $I_{sp,wall}$, collected for a species type sp, during a specified time interval, $t_{interval}$, is given by

$$I_{sp,wall} = \frac{f_{x,wall}(sp) W_{macro} q_{sp}}{t_{interval}} \tag{3.27}$$

where

$$W_{macro} = \frac{N_{physical}}{N_{macro}} \tag{3.28}$$

where $N_{physical}$ is the total number of physical particles and N_{macro} is the total number of macro particles. A larger W_{macro} means that only a fewer number of macro particles are used in the simulation to represent the physical particles in the discharge chamber. In this work both macro particle and computer particle terminologies are used for referring the simulated computer particles. $f_{x,wall}(sp)$ is the sum of the total number of computer particles of species type sp collected at the walls during the time $t_{interval}$, q_{sp} is the charge value of the species type sp, $N_{physical}$ is the total number of physical particles, and N_{macro} is the total number of macro particles. In addition, at the wall boundaries the energy information of the lost particles is stored in separate bins which may be useful for diagnosing particle loss mechanisms at the walls.

3.2.4 Particle Collisions

All particle collisions are handled with an MCC algorithm using the null collision technique. A list of particle collisions considered in this work is tabulated in Table 3.2. This table does not include elastic collisions between charged particles. As mentioned in Chapter 2 this is handled by the dynamic electric field.

Table 3.2: Particle collisions considered in the MCC

Particle Interactions	electron-Xe collisions	electron-Xe^{+} collisions	electron-Xe^{++} collisions	Xe^{+}-Xe collisions	Xe^{++}-Xe collisions
Type of Collisions	Elastic	Excitation	Excitation	Elastic	Charge-Exchange
	Excitation	Ionization	Three-body Recombination	Charge-Exchange	
	Ionization	Three-body Recombination			

In a null collision procedure, the constant collision frequency is used for calculating the null collision probability. The constant collision frequency as given in Equation (2.40) is based on the maximum value of the target particle number density, n_t, the maximum value of the total collision cross section and the maximum incident particle speed. Equation (2.40) can be rewritten as

$$\nu_c = max(n_t)max(\sigma_T(\epsilon_{inc})|\vec{v}_{inc}|) = n_{t,max}max(\sigma_T(\epsilon_{inc})|\vec{v}_{inc}|). \tag{3.29}$$

Here $n_{t,max}$ is the target particle's maximum number density value and $\sigma_T(\epsilon_{inc})|\vec{v}_{inc}|$ is the maximum collision swept volumetric rate which is based on the incident particle energies. The maximum target particle number density is given by

$$n_{t,max} = \max\left(n_{t,i,j}\right) \quad \text{for} \quad i = 0, \cdots, N_z - 1, j = 0, \cdots, N_r - 1 \tag{3.30}$$

where (i, j) refers to the computational cell index and $n_{t,i,j}$ refers to the target particle number density value at the (i, j)th computational cell.

In a particle-particle collision, generally the slow moving heavy particle is treated as the target particle and the fast moving electron is taken as the incident particle. In electron-Xe, Xe^{+}-Xe and Xe^{++}-Xe collisions, Xe is treated as the target particle. In electron-ion collisions, the heavy ions are treated as the target particles. However, for the electron-ion-electron three body recombination collisions, both the ion and the electron are treated as the target particles. When an incident electron is treated for three body recombination, both ion and electron population at the incident electron needs to be known. Thus the MCC collision simulation requires particle number density distribution results for all particles inside the discharge chamber to properly handle the particle-particle collisions.

In typical PIC simulations, the chargeless neutrals are treated as a background gas. This means the neutral particle number density is treated as an input. Since neutral particles are being tracked inside the discharge chamber as part of this work, the neutral number density distribution varies in space and time. Similarly the ion and electron number density distributions also vary in space and time. Vahedi and Surendra's [1995] work suggests that the null collision technique can be adopted whether the particle distribution is constant or time varying. At each time step, the maximum number density values of all target particles are determined based on their particle distribution inside the discharge chamber using Equation (3.30).

3.2.4.1 Electron-Neutral Collisions

Reactions considered in the electron-Xe collision simulation are:

$$\begin{aligned} e + Xe &\longrightarrow e + Xe && \text{(elastic)}, \\ e + Xe &\longrightarrow e + Xe^{*} && \text{(excitation)}, \\ e + Xe &\longrightarrow e + e + Xe^{+} && \text{(ionization)}. \end{aligned} \tag{3.31}$$

Figure 3.4 shows the collision cross sections utilized for the electron-Xe collisions. The procedures followed for handling the electron-Xe I collision processes are:

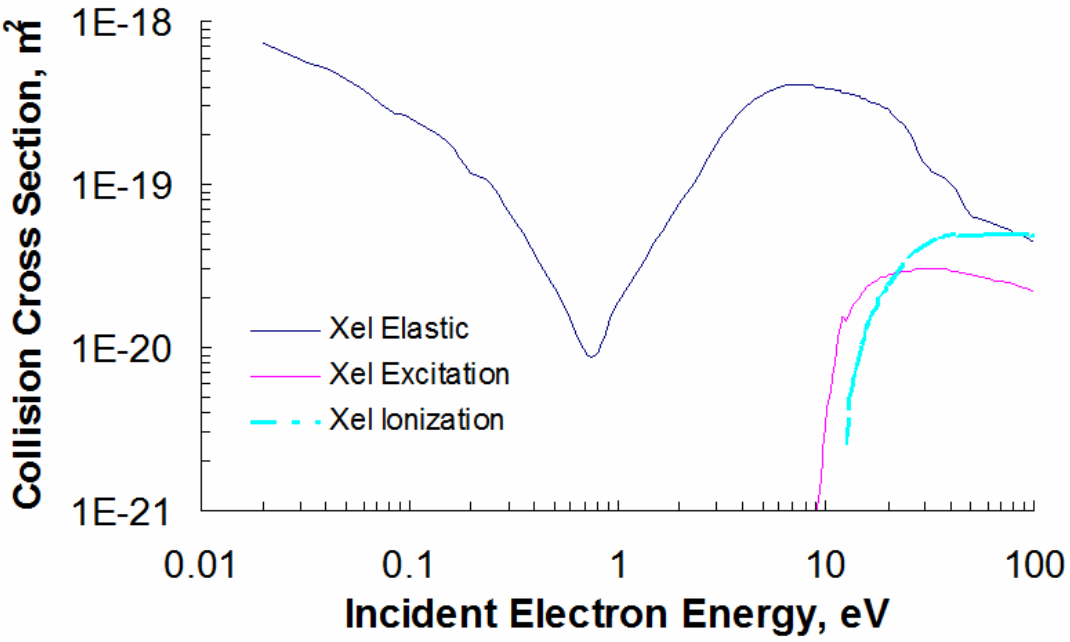

Figure 3.4: The electron-neutral collision cross sections in xenon.

1. Using Equations (2.41)-(2.42),the total electron-neutral collision cross section, $\sigma_{e0,T}(\epsilon_e)$,

$$\sigma_{e0,T}(\epsilon_e) = \sigma_{e0,el}(\epsilon_e) + \sigma_{e0,ex}(\epsilon_e) + \sigma_{e0,iz}(\epsilon_e) \tag{3.32}$$

and the incident electron speed, $|\vec{v}_e|$,

$$\vec{v}_e = \sqrt{\frac{2|e|\epsilon_e}{m_e}} \tag{3.33}$$

are calculated for a range of kinetic energies, ϵ_e, from 0 to 100 electron volts. From this range of particle kinetic energies, the maximum value of the collision swept volumetric rate is determined.

$$(\sigma_{e0,T}(\epsilon_e)|\vec{v}_e|)_{max} = \max\left(\sigma_{e0,T}(\epsilon_e)|\vec{v}_e|\right)_{\epsilon_e} \quad \text{for} \quad \epsilon_e = 0, 0.5, 1.0, \ldots, 100eV \tag{3.34}$$

Since this maximum collision volumetric rate is a constant value, it is computed only once at the beginning of the simulation.

2. Determine the maximum neutral number density, $n_{0,max}$, value using Equation (3.30)

3. Utilizing the maximum neutral number density and the maximum collision volume rate, the

constant collision frequency for electron-Xe collisions, $\nu_{e0,c}$, is obtained using Equation (3.29). It is given by

$$\nu_{e0,c} = n_{0,max}(\sigma_{e0,T}(\epsilon_e)|\vec{v}_e|)_{max}. \tag{3.35}$$

4. The probability of a null collision for electron-neutral collisions, $P_{e0,null}$, is calculated using a constant collision frequency and the electron time step $\triangle t_e$,

$$P_{e0,null} = 1 - \exp\left(-\nu_{e0,c}\Delta t_e\right). \tag{3.36}$$

5. The fraction of electron particles, $N_{e,coll}$, that undergo particle collisions is estimated using Equation (2.43).

6. Only this number of electrons are tested for collisions. The selection of which particles undergo a collision is done through a random process. In this process effort is made not to duplicate the same particle for another type of collision in a given time step.

7. The collision type for each colliding particle is tested using a random number, R, between 0 and 1 in the following manner,

$$0 \leq R \leq \nu_{e0,el}(\epsilon_e)/\nu_{e0,c} \quad \text{(elastic)}, \tag{3.37}$$

$$\nu_{e0,el}(\epsilon_e)/\nu_{e0,c} < R \leq (\nu_{e0,el}(\epsilon_e) + \nu_{e0,ex}(\epsilon_e))/\nu_{e0,c} \quad \text{(excitation)}, \tag{3.38}$$

$$(\nu_{e0,el}(\epsilon_e) + \nu_{e0,ex}(\epsilon_e))/\nu_{e0,c} < R \leq (\nu_{e0,el}(\epsilon_e) + \nu_{e0,ex}(\epsilon_e) + \nu_{e0,iz}(\epsilon_e))/\nu_{e0,c}\text{(ionization)}, \tag{3.39}$$

$$(\nu_{e0,el}(\epsilon_e) + \nu_{e0,ex}(\epsilon_e) + \nu_{e0,iz}(\epsilon_e))/\nu_{e0,c} < R \leq 1 \quad \text{(null)}. \tag{3.40}$$

Here $\nu_{e0,el}(\epsilon_{inc,e})$ is the electron-Xe elastic collision frequency, $\nu_{e0,ex}$, is the electron-Xe excitation collision frequency, and $\nu_{e0,iz}$ is the electron-Xe ionization collision frequency. These collision frequencies are determined using

$$\nu_{e0,j}(\epsilon_{inc,e}) = n_0\sigma_{e0,j}|\vec{v}_{inc,e}| \tag{3.41}$$

where the index j refers the jth type of electron-Xe collisions, n_0 is the neutral number density value at the incident electron location, and $\sigma_{e0,j}$ is the electron-Xe collision cross section for the j-th type of collision.

The above described collision process is performed in the same way for both primary and secondary electrons.

Elastic Collision In an elastic electron-Xe collision, the incident electron gets scattered and its direction of travel changes after the collision. The new path of this electron is determined using the two angles called the scattering angle and the azimuthal angle. The scattering angle, χ, is calculated using the relation given by Vahedi and Surendra [1995],

$$\cos\chi = \frac{2 + \epsilon_{inc,e} - 2(1 + \epsilon_{inc,e})^{R_1}}{\epsilon_{inc,e}} \tag{3.42}$$

where R_1 is a random number between 0 and 1. The azimuthal angle, ψ, can vary between 0 and 360. This angle is calculated by multiplying 360^o with another random number, R_2, which varies between 0 and 1. It is given by,

$$\psi = 2\pi R_2. \tag{3.43}$$

Once χ and ψ are known the scattered electron's velocity is calculated. This can be calculated by finding the scattered electron's energy first. The colliding electron loses a small amount of energy in an elastic collision and this energy needs to be removed from its kinetic energy. The scattered electron's energy is given by

$$\epsilon_{scat} = \epsilon_{inc}\left[1 - \frac{2m_e}{m_{Xe}}(1 - cos\chi)\right] \tag{3.44}$$

where m_{Xe} is the mass of a neutral atom. The energy lost by the colliding electron will be relatively small due to the low value of m_e/m_{Xe} . The scattered electron's speed, $|\vec{v}_{scat}|$ is then calculated using

$$|\vec{v}_{scat}| = \sqrt{\frac{2|e|\epsilon_{scat}}{m_e}}. \tag{3.45}$$

The elastic collision cross section data for Xe neutrals have been obtained from the following references [Lam 1982; Dababneh et al. 1980; Hayashi 1983]. The low energy electrons (for the range between 0.01 to 2.0 eV) elastic scattering cross section data are obtained from [Lam 1982]. For the electron energies ranging between 2.8 eV to 100 eV the cross sections are obtained from [Dababneh et al. 1980]. Reference [Raju 2006] compiles with all of the above reference elastic cross section data together. Figure 3.4 shows the curve fit of the elastic collision cross section data obtained from the above references.

Excitation Collision In an excitation collision, the incident electron loses the amount of the excitation threshold energy from its kinetic energy. The scattered electron energy is given by,

$$\epsilon_{scat,e} = \epsilon_{inc,e} - \epsilon_{ex} \tag{3.46}$$

where ϵ_{ex} is the excitation threshold energy which will be taken as 8.35 eV. After the collision the electron gets scattered and a new path of travel is determined in the same way as the elastic collisions of electrons and neutrals. The excited neutral in this collision process is assumed to deexcite instantaneously through radiative emission processes. The xenon excitation collision cross section data were obtained from [Hayashi 1983]. Figure 3.4 shows the curve fit of Hayashi's collision cross section data.

Ionization Collision In an ionization collision, the incident electron produces a positive ion and a secondary electron. The energy balance of this collision process is given by

$$\epsilon_{inc,e} + \epsilon_N = \epsilon_{scat,e} + \epsilon_{se} + \epsilon_{ion} + \epsilon_{ionz} \tag{3.47}$$

where ϵ_N is the energy of the neutral atom, $\epsilon_{scat,e}$ is the scattered electron energy, ϵ_{se} is the secondary electron energy, ϵ_{ion} is the energy of the positive ion, and ϵ_{ionz} is the ionization threshold energy. The ionization threshold energy required for xenon is 12.1 eV. The energy balance equation (3.47) can be simplified by assuming that the target neutral atom has higher momentum than the incident electron. This can be established because of the neutral's higher mass. In other words, the kinetic

energy of the created ion possesses the same kinetic energy as the target neutral atom. Thus the energy balance equation becomes

$$\epsilon_{inc,e} = \epsilon_{scat,e} + \epsilon_{se} + \epsilon_{ionz}, \tag{3.48}$$

and

$$\epsilon_N = \epsilon_{ion}. \tag{3.49}$$

The remaining energy of the incident electron has to be partitioned between the scattered electron and the secondary electron. The energy of the created secondary electron is calculated to be [Birdsall 1991; Vahedi and Surendra 1995],

$$\epsilon_{se} = B(\epsilon_{inc,e}) \tan\left[R_3 tan^{-1}\left(\frac{\epsilon_{inc,e} - \epsilon_{ionz}}{2B(\epsilon_{inc,e})}\right)\right] \tag{3.50}$$

where R_3 is a random number that varies between 0 and 1. This equation is obtained using a simplified form of the differential cross section between the incident electron and the secondary electron. Here B is a known function and it is set to a value of 10 eV [Birdsall 1991]. The energy of the scattered electron is simply calculated with

$$\epsilon_{scat,e} = \epsilon_{inc,e} - \epsilon_{se} - \epsilon_{ionz}. \tag{3.51}$$

Then both electrons are scattered by finding their angles χ and ψ using Equations (3.42) and (3.43) respectively. For the created ion, its velocity, $|\vec{v}_{ion}|$, is set by using the Maxwellian distribution function based on the neutral particle temperature, T_N. The average value of the speed of the ion is given by

$$|\vec{v}_{ion}| = \sqrt{\frac{2|e|T_N}{m_{Xe}}}. \tag{3.52}$$

The xenon ionization cross section data were obtained from [Rejoub et al. 2002]. Figure 3.6 shows the curve fit of Rejoub et al.'s ionization collision cross section data.

3.2.4.2 Ion-Neutral Collisions

The reactions simulated are:

$$\begin{aligned} Xe^+ + Xe &\longrightarrow Xe^+ + Xe \quad (\text{Xe}^+ \text{ elastic}), \\ Xe^+ + Xe &\longrightarrow Xe + Xe^+ \quad (\text{Xe}^+ \text{ charge-exchange}), \\ Xe^{++} + Xe &\longrightarrow Xe + Xe^{++} \quad (\text{Xe}^{++} \text{ charge-exchange}). \end{aligned} \tag{3.53}$$

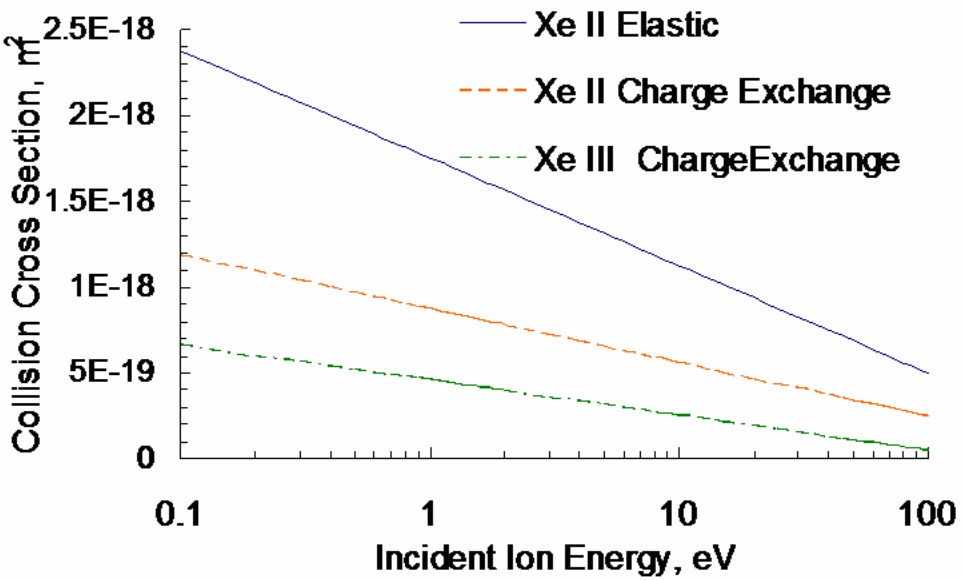

Figure 3.5: The ion-Xe I collision cross sections in xenon.

Elastic and charge-exchange type collisions are considered for the collisions between Xe^+ and Xe. Charge-exchange type collisions are considered for the collisions between Xe^{++} and Xe. Figure 3.5 shows the cross sections for ion-neutral collisions used in the MCC simulation [**?**]Miller:02.

The ion-neutral MCC simulation follows similar steps as used in the electron-neutral MCC simulation to determine the colliding ion and the type of collisions. The procedures followed in the singly charged ion Xe^+-neutral collision are:

1. Using Equations (2.41)-(2.42) the total ion-neutral collision cross section, $\sigma_{+0,T}(\epsilon_+)$, is

$$\sigma_{+0,T}(\epsilon_+) = \sigma_{+0,el}(\epsilon_+) + \sigma_{+0,cx}(\epsilon_+) \tag{3.54}$$

and the ion particle speed, $|\vec{v}_+|$, is

$$|\vec{v}_+| = \sqrt{\frac{2|e|\epsilon_+}{m_{Xe}}} \tag{3.55}$$

These quantities are computed for a range of ion kinetic energies, $\epsilon_{inc,+}$, from 0 to 100 electron volts. Then the maximum collision swept volumetric rate is calculated using

$$(\sigma_{+0,T}(\epsilon_+)|\vec{v}_+|)_{max} = \max\left(\sigma_{+0,T}(\epsilon_+)|\vec{v}_+|\right)_{\epsilon_+} \quad (\text{for})\epsilon_+ = 0\ldots 100eV \tag{3.56}$$

Since this maximum collision swept volumetric rate is constant, it is computed only once at the beginning of the simulation.

2. Determine the maximum neutral number density value, $n_{0,max}$ using Equation (3.30)

3. Using Equation (3.29) the constant collision frequency for ion-neutral collisions, $\nu_{+0,c}$,

$$\nu_{+0,c} = n_{0,max}(\sigma_{+0,T}(\epsilon_+)|\vec{v}_+|)_{max} \tag{3.57}$$

is obtained.

4. The probability of a null collision for an ion-neutral collision, $P_{+0,null}$, is calculated using a constant collision frequency and the ion time step $\triangle t_{ion}$. It is given by

$$P_{+0,null} = 1 - \exp(\nu_{+0,c}\Delta t_{ion}). \tag{3.58}$$

5. The fraction of ion particles, $N_{+,coll}$, that undergo particle collisions is estimated.

6. Only this number of ions are tested for collisions. The selection of which ions should have a collision is done through a random process. In this process effort is made not to duplicate the same particle for another type of collision in a given time step.

7. The collision type for each colliding particle is tested using a random number, R, between 0 and 1 in the following manner,

$$0 < R \leq \nu_{+0,el}(\epsilon_+)/\nu_{+0,c} \quad \text{(elastic)}, \tag{3.59}$$

$$\nu_{+0,el}(\epsilon_+)/\nu_{+0,c} < R \leq (\nu_{+0,el}(\epsilon_+) + \nu_{+0,cx}(\epsilon_+))/\nu_{+0,c} \quad \text{(charge-exchange)}, \tag{3.60}$$

$$(\nu_{+0,el}(\epsilon_+) + \nu_{+0,cx}(\epsilon_+))/\nu_{+0,c} < R \leq 1 \quad \text{(null)}. \tag{3.61}$$

Here $\nu_{+0,el}(\epsilon_+)$, is the Xe^+-Xe elastic collision frequency

$$\nu_{+0,el}(\epsilon_+) = n_0 \sigma_{+0,el}(\epsilon_+)|\vec{v}_+|, \tag{3.62}$$

and $\nu_{e0,cx}(\epsilon_+)$, is the Xe^+-Xe charge-exchange collision frequency

$$\nu_{+0,cx}(\epsilon_+) = n_0 \sigma_{+0,cx}(\epsilon_+)|\vec{v}_+|. \tag{3.63}$$

The collisions of Xe^{++} and Xe are handled in a similar way; however, in the Xe^{++} collision simulation, only the charge-exchange type collision is considered.

The collision of an ion with a neutral particle is handled differently from the electron-neutral collisions. In an electron-neutral collision the neutral atom is considered stationary, which makes simulating the electron-neutral collision simpler. In an ion-neutral collision, this assumption does not hold since the range of velocities of the neutrals and the ions are similar. In this PIC-MCC simulation the neutrals are maintained at a constant temperature and the neutral velocities are chosen from the Maxwellian distribution function based on this average neutral temperature. This approximation is made to avoid the search process to identify a colliding neutral particle within a computational cell. Also, the neutral particles followed in this work all have approximately the same temperature. By changing the reference frame to the center of mass frame, where the neutrals are assumed to have the same average velocities, the ion-neutral collisions can be handled easier. The ion particles are transferred to the center of mass frame to computationally handle their collisions with neutrals and then transferred back to the ion reference frame after the collision. In shifting from one reference frame to another, a neutral atom is selected randomly and its velocity is subtracted from the colliding ion velocity. After the collision, the same neutral velocity is added to the ion velocity.

Elastic Collision If an elastic collision of an ion with a neutral occurs, the collision is assumed to be between two hard spheres where the ion gets scattered and loses some of its kinetic energy after the collision. The energy of the scattered ion is given by

$$\epsilon_{scat,ion} = \epsilon_{ion} - \left(\frac{2m_{ion}m_{Xe}}{(m_{ion} + m_{Xe})^2}(1 - \cos\Theta) \right) \epsilon_{inc,ion} \tag{3.64}$$

where m_{ion} is the mass of the ion particle, Θ is the scattering angle in the center-of-mass reference frame, and the entire term inside the bracket is the energy loss factor, α_L . For $m_{ion} = m_{Xe}$

$$\Theta = 2\chi \tag{3.65}$$

where χ is the scattering angle in the reference frame. Substituting Equation (3.65) into the equation (3.64) and simplifying gives

$$\epsilon_{scat,ion} = \epsilon_{inc,ion} \cos^2\chi \tag{3.66}$$

Taking another random number R_4 which varies between 0 and 1 and assuming isotropic scattering gives

$$\cos\Theta = 1 - 2R_4. \tag{3.67}$$

Placing Equation (3.67) in Equation (3.65) gives the scattering angle ,

$$\cos\chi = \sqrt{1 - R_4}. \tag{3.68}$$

Similarly the azimuthal angle ψ is determined using Equation (3.43). The scattered ion velocity is then calculated using the scattered ion energy and its path is determined using these two angles.

Charge-Exchange Collision In a charge exchange collision an electron from the neutral is transferred to the incident ion. In this exchange the neutral becomes an ion and the ion turns to a neutral. The new ion leaves with the velocity of the incident neutral which normally would be slower than the incident ion's velocity.

3.2.4.3 Electron-Ion Collisions

Experimental measurements [Sengupta et al. 2004] made inside the NSTAR discharge chamber have found that the plasma is fully ionized (i.e., $n_{ions} \gg n_0$) along the centerline. The Extended Life Test [Sengupta et al. 2003] made on the NSTAR discharge chamber have found that the double to single ion ratio in the ion beam current is somewhere between 10 to 20 % for the throttle conditions that operate at higher discharge chamber propellant efficiencies. Also, the double to single ion ratio is observed to be larger along the thruster centerline than elsewhere in the discharge chamber [Milder 1962; Sovey 1984]. Thus inclusion of inelastic interactions between the electrons and xenon ions is necessary. The PIC-MCC code handles the electron-ion collisions using the same null collision technique as used for other types of collisions.

The reactions included in the electron-ion MCC simulation are:

$$\begin{aligned}
e + Xe^{+} &\longrightarrow Xe^{+*} + e && (\mathrm{Xe}^{+} \text{ excitation}),\\
e + Xe^{+} &\longrightarrow Xe^{++} + e + e && (\mathrm{Xe}^{+} \text{ ionization}),\\
e + Xe^{+} + e &\longrightarrow Xe + e && (\mathrm{Xe}^{+} \text{ three-body recombination}),\\
e + Xe^{++} &\longrightarrow Xe^{++*} + e && (\mathrm{Xe}^{++} \text{ excitation}),\\
e + Xe^{++} + e &\longrightarrow Xe^{+} + e && (\mathrm{Xe}^{++} \text{ three-body recombination}).
\end{aligned} \tag{3.69}$$

The procedures followed in the electron-Xe^{+} MCC collision simulation are similar to the procedures followed in the electron-Xe MCC simulation. These steps are explained below:

1. Using Equations (2.41)-(2.42), the total electron-Xe^{+}collision cross section, $\sigma_{e+,T}(\epsilon_e)$,

$$\sigma_{e+,T}(\epsilon_e) = \sigma_{e+,ex}(\epsilon_e) + \sigma_{e+,iz}(\epsilon_e) + \sigma_{ee+,r}(\epsilon_e) \tag{3.70}$$

and the electron particle speed, $|\vec{v}_e|$,

$$|\vec{v}_e| = \sqrt{\frac{2|e|\epsilon_e}{m_e}} \tag{3.71}$$

are computed for a range of kinetic energies, $\epsilon_{inc,e}$, from 0 to 100 electron volts. Then the

maximum value of the collision swept volumetric rate is calculated using

$$(\sigma_{e+,T}(\epsilon_e)|\vec{v}_e|)_{max} = \max\left(\sigma_{e+,T}(\epsilon_e)|\vec{v}_e|\right)_{\epsilon_e} \quad \text{for} \epsilon_e = 0, 0.5, 1, \ldots, 100eV. \tag{3.72}$$

Since this maximum collision swept volumetric rate is a constant value, it is computed only once at the beginning of the simulation.

2. Determine the maximum ion number density value, $n_{+,max}$ using Equation (3.30).

3. Calculate the constant collision frequency for electron-ion collisions, $\nu_{e+,c}$, using Equation (3.29),

$$\nu_{e+,c} = n_{+,max}(\sigma_{e+,T}(\epsilon_e)|\vec{v}_e|)_{max}. \tag{3.73}$$

4. The probability of a null collision for electron-ion interactions, $P_{e+,null}$ is calculated using the computed constant collision frequency and the electron time step $\triangle t_e$. It is given by

$$P_{e+,null} = 1 - \exp(\nu_{e+,c}\triangle t_e). \tag{3.74}$$

5. The fraction of electron particles, $N_{e,coll}$, that undergo particle collisions is estimated. Only this number of electrons are tested for collisions.

6. The selection of which electrons should have a collision is done through a random process. In this process effort is made not to duplicate the same electron for another type of collision in a given time step.

7. The collision type for each colliding particle is tested using a random number, R, between 0 and 1 in the following manner,

$$0 < R \leq \nu_{e+,ex}(\epsilon_e)/\nu_{e+,c} \quad \text{(excitation)}, \tag{3.75}$$

$$\nu_{e+,ex}(\epsilon_e)/\nu_{e+,c} > R \leq (\nu_{e+,ex}(\epsilon_e) + \nu_{e+,iz}(\epsilon_e))/\nu_{e+,c} \quad \text{(ionization)}, \tag{3.76}$$

$$(\nu_{e+,ex}(\epsilon_e) + \nu_{e+,iz}(\epsilon_e))/\nu_{e+,c} > R \leq (\nu_{e+,ex}(\epsilon_e) + \nu_{e+,iz}(\epsilon_e) + \nu_{ee+,r}(\epsilon_e))/\nu_{e+,c} \tag{3.77}$$

(recombination),

$$(\nu_{e+,ex}(\epsilon_e) + \nu_{e+,iz}(\epsilon_e) + \nu_{ee+,r}(\epsilon_e))/\nu_{e+,c} < R \leq 1 \quad \text{(null)}. \tag{3.78}$$

Here $\nu_{e+,ex}(\epsilon_e)$, is the electron-Xe^+ excitation collision frequency,

$$\nu_{e+,ex}(\epsilon_e) = n_+ \sigma_{e+,ex}(\epsilon_e)|\vec{v}_e| \tag{3.79}$$

$\nu_{e+,iz}(\epsilon_e)$, is the electron-Xe^+ ionization collision frequency,

$$\nu_{e+,iz}(\epsilon_e) = n_+ \sigma_{e+,iz}(\epsilon_e)|\vec{v}_e| \tag{3.80}$$

and $\nu_{ee+,r}(\epsilon_e)$, is the electron-Xe^+ three-body recombination collision frequency

$$\nu_{ee+,r}(\epsilon_e) = n_+ \sigma_{ee+,r}(\epsilon_e)|\vec{v}_e|. \tag{3.81}$$

The electron-Xe^{++} MCC simulation follows the above steps except this simulation does not include electron-Xe^{++} ionization collisions. Also the above collision process is the same for both primary and secondary electrons. Figure 3.6 shows the cross section data utilized for the electron-Xe^+ excitation and the electron-Xe^{++} ionization collisions.

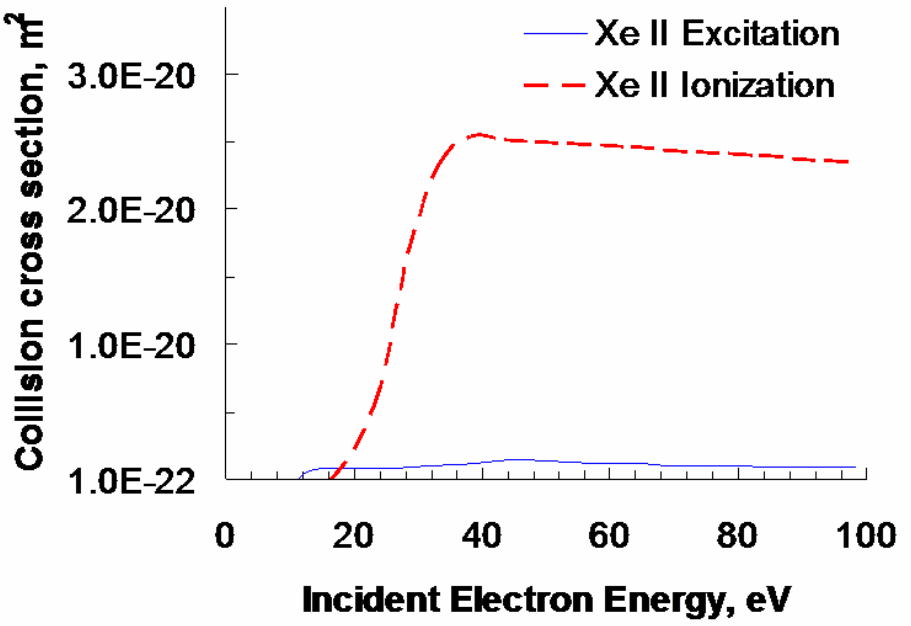

Figure 3.6: The electron-ion collision cross sections in xenon.

Excitation From a literature survey it was found that electron-impact excitation cross section data for both Xe^+ and Xe^{++} is sparse to nonexistent. For this reason the following approximations are made. A swarm analysis for Xe ion excitation [Strinic 2007] provides cross section data on electron-impact excitation collisions for the higher excitation levels of Xe^+ such as $6p^4D_{5/2}$ and $6p^4P_{3/2}$. For the plasma in the discharge chamber the most excitation collisions occur from the ground level of the ion to one of the first excited levels above that. Since no excitation cross section data for ground level excitation of Xe^+ could be found, we have approximated the ground level excitation cross section to be the same as an upper level ($6p^4D_{5/2}$) excitation for which results come from the swarm analysis of Strinic [2007]. The threshold energy for the Xe^+ excitation collision is estimated using information available from the NIST Atomic Spectra Database [Saloman 2004; NIST 2007]. There are many possible excitation transitions for Xe^+ from the ground state, we only look at one transition. This ground to the next excited level transition uses an average energy level value for upper state of the transition of $\epsilon_{ex,+} = 14.8eV$. In reference [VanNoord 2007], a value of 11.27 eV is used as the ion excitation threshold energy. Hence we utilize a minimum of the above two excitation threshold energies as the Xe^+ excitation threshold energy. The same procedure is followed for determining the excitation energy for the electron-impact excitation collisions of Xe^{++}, $\epsilon_{ex,++}$. Using the NIST Atomic Spectra Database, it was found that a value of 19.1 eV is a good excitation energy for an electron to excite Xe^{++}. Also, since information for the excitation cross section of Xe^{++} could not be found, we have used the Xe^+ excitation cross section data for Xe^{++} excitation collisions.

In an excitation collision, the incident electron loses the excitation threshold energy. Then the electron will get scattered and its new travel path is determined in the same way as the elastic scattering of electrons handled in the electron-neutral collisions. The excited ion in this collision process is not tracked further and it is assumed that the excited ion particle gets de-excited instantaneously through radiative emission process.

Ionization In an electron-impact ionization collision of Xe^+, the incident electron loses the ionization threshold energy of 21.2 eV to produce a Xe^{++} particle and a secondary electron. Ionization cross section data for electron-impact ionization of Xe^+ are obtained from reference [Bell et al. 1993]. The electron-impact ionization collisions of Xe^{++} are neglected in this work since the ionization threshold energy for these collisions is much larger than the discharge voltage used in ion thrusters. The energy and the direction of travel for both the scattered electron and the secondary electron are computed in a similar fashion to the electron-neutral ionization event.

Three-body Recombination Also included in this simulation are three-body electron-ion recombination processes. These inelastic collision processes [Fridman and Kennedy 2004; Raizer 1991] happen more frequently in high density plasmas with electron temperatures in the range of 1-2 eV, but they also occur in the ion engine discharge chamber plasma. The three-body electron-ion recombination rate coefficient for Xe^{++} is given by [Nedelea and Urbassek 2004]

$$\alpha_r^{ee++} = 9 \times 10^{-39} T_e^{-9/2} \quad \mathrm{m}^6/\mathrm{s}. \tag{3.82}$$

where T_e is the incident electron temperature in eV. From the literature search no recombination data could be found for xenon ions. However, there is recombination data available for molecular xenon ions. In reference [Nedelea and Urbassek 2004], the above recombination rate coefficient is used for the recombination of doubly charged aluminum ions. The same equation is used for the recombination rate for Xe^{++} ions. To obtain the Xe^{++} recombination cross section, $\sigma_{ee++,r}$, value the above equation needs to be divided by the electron number density and by the incident electron speed. It is given by

$$\sigma_{ee++,r} = \frac{\alpha_r^{ee++}}{n_e |\vec{v}_{inc,e}|}. \tag{3.83}$$

Since the recombination process has a strong dependence to the ion charge state, Z, the three-body electron-ion recombination rate coefficient for the Xe^+ is estimated to be [Nedelea and Urbassek 2004]

$$\alpha_r^{ee+} = \frac{\alpha_r^{ee++}}{Z^3}. \tag{3.84}$$

Taking the charge state Z value for Xe^{++} as 2 and substituting Equation (3.82) into Equation (3.84) gives the Xe^{+} recombination rate coefficient as

$$\alpha_r^{ee+} = 1.125 \times 10^{-39} T_e^{-9/2} \quad \mathrm{m}^6/\mathrm{s}. \tag{3.85}$$

The Xe^{+} recombination cross section can then be determined from

$$\sigma_{ee+,r} = \frac{\alpha_r^{ee+}}{n_e |\vec{v}_{inc,e}|}. \tag{3.86}$$

As mentioned in the beginning of this section, the total electron-ion collision cross-section such as $\sigma_{e+,T}(\epsilon_e)$ and $\sigma_{e++,T}(\epsilon_e)$ have to be evaluated first before performing the MCC collision. The $\sigma_{e+,T}(\epsilon_e)$ and $\sigma_{e++,T}(\epsilon_e)$ are the sum of collision cross-section value of each electron-ion collision event. Unlike the excitation and ionization cross-section which are coming from the experimental data, the three-body recombination cross section such as $\sigma_{ee+,r}(\epsilon_e)$ and $\sigma_{ee++,r}(\epsilon_e)$ have to be calculated using Equations (3.86) and (3.83). Both $\sigma_{ee+,r}(\epsilon_e)$ and $\sigma_{ee++,r}(\epsilon_e)$ values depend on the following:electron velocity, electron temperature and electron number density. The electron velocity can be computed based on the electron energy (i.e., electron temperature) but the electron number density is an unknown quantity at the beginning of the simulation. Hence an approximation has been made for the electron number density. A volume averaged electron number density value from the experimental data [Herman 2005] can be utilized. In this work, I have taken a value of $1{\times}10^{18}$ m^{-3} for the electron number density which is used both in Equations (3.86) and (3.83) to obtain the recombination cross section values for the calculation of total electron-ion collision cross sections.

3.2.5 Charge Density Calculations

The charge density and number density values at the computational grid points are updated after every time step before the next advance of the particles is undertaken. The charge density values are stored at the cell corner-nodes while the particle number density values are computed at the cell corner-nodes and at the cell centers. In this section the computation of charge density values at the

grid points are explained and in the following section the computation of particle number density values is discussed.

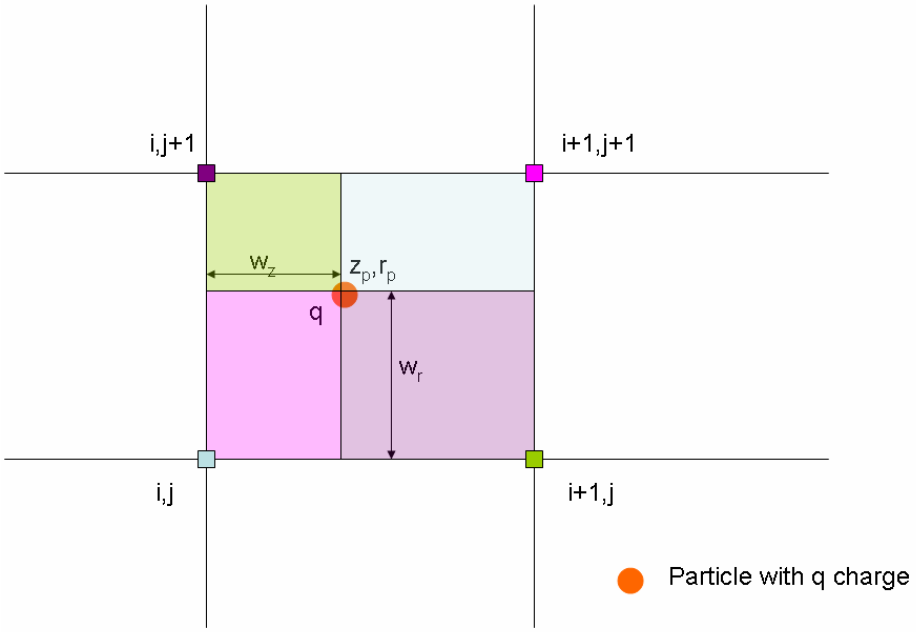

Figure 3.7: Bilinear interpolation of charge values at the particle locations to the charge density at the grid points.

The charge of the particles and their locations within a cell are used to compute the charge density at the full-cell corner-nodes. The charge values at the four corner-nodes of a cell are obtained by performing bilinear interpolation of charges present within that cell. This is done by calculating the fractional area weighting of charge values to the four cell nodes as shown in Figure 3.7. The fractions w_z and w_r are defined as

$$w_z = z_p - \eta_{i,j} \tag{3.87}$$

and

$$w_r = r_p - \xi_{i,j}, \tag{3.88}$$

where z_p and r_p represent the particle locations in grid units, in the z and r directions respectively; and $\eta_{i,j}$ and $\xi_{i,j}$ represent the lower left corner of the computational cell in grid units. The fractions

w_z and w_r have a value between 0 and 1. The charge values at the four cell corner nodes are given by [Birdsall and Langdon 1991]

$$Q_{i,j} = q(1 - w_z)(1 - w_r), \tag{3.89}$$

$$Q_{i+1,j} = qw_z(1 - w_r), \tag{3.90}$$

$$Q_{i,j+1} = q(1 - w_z)w_r, \tag{3.91}$$

and

$$Q_{i+1,j+1} = qw_z w_r, \tag{3.92}$$

where q is the charge of the particle.

This calculation is performed for all charge particles in each species group (i.e., primary electrons, secondary electrons, Xe^+, and Xe^{++}) to get each species charge value at all mesh points. Then the charge values are divided by their respective cell volume to get the charge density value. This is done with the equation

$$\rho_{sp,i,j} = \frac{1}{V_{1/2cell,i,j}} \sum_{Particle=1}^{N_{T,sp}} Q_{sp,i,j} \tag{3.93}$$

where $\rho_{sp,i,j}$, $V_{1/2cell,i,j}$, and $Q_{sp,i,j}$ are the species charge density, the half-cell volume associated with the full-cell corner grid point, and the species charge at the cell corner-node (i, j). Here $N_{T,sp}$ is the total number of particles present in the simulation for each species type. The subscript index *sp* is used on the above variables to identify them as based on species. Figure 3.2 shows the half and full-cell volumes surrounding the grid node (i,j). The half cell-volume at node (i,j) is computed using

$$V_{1/2cell,i,j} = \pi\big(r^2_{i,j+1/2} - r^2_{i,j-1/2}\big)(z_{i+1/2,j} - z_{i-1/2,j}). \tag{3.94}$$

Finally the charge density at any grid point is obtained by simply adding the charge density from of each species,

$$\rho_{i,j} = \sum_{sp=1}^{NchargeTypes} \rho_{sp,i,j} \tag{3.95}$$

where $\rho_{i,j}$ is the charge density at the cell node (i,j) and $NchargeTypes$ is the number of charge particle types. The charge densities at all of the cell nodes are calculated using Equation (3.95).

3.2.6 Number Density Calculations

The calculation of cell centered particle number densities are needed in the MCC collision simulation. These quantities are required to calculate the collision frequencies. Hence we need to know the particle number density values for all computational cells for all particle species inside the discharge chamber. The cell centered particle number density value for species type *sp*, for computational cell (i,j), $ncell_{sp,i,j}$, is calculated using

$$ncell_{sp,i,j} = \frac{W_{macro}(N_{T,sp})_{i,j}}{V_{cell,i,j}}. \tag{3.96}$$

Here W_{macro} is the computer particle weighting, $(N_{T,sp})_{i,j}$ is the total number of computer particles of species type *sp* present within grid node (i,j)'s full computational cell, and $V_{cell,i,j}$ is the full-cell volume for the computational cell (i,j). The full cell volume boundary is shown in Figure 3.2 and it is computed using

$$V_{cell,i,j} = \pi\big(r_{i,j+1}^2 - r_{i,j}^2\big)\big(z_{i+1,j} - z_{i,j}\big). \tag{3.97}$$

This cell volume has been written in terms of r and z locations because the cell volumes vary.

Instead of interpolating the cell particle number densities, $ncell_{sp,i,j}$, to the grid points the charge density, $\rho_{sp,i,j}$, values are used. Since the charge density values have already been determined at the grid points (see Equation 3.93), and they are directly related to the number density of particles present, they are a simple means to obtain the grid particle number densities, $ngrid_{sp,i,j}$. The particle number density of any particular species at any given grid point (i,j) is simply calculated by dividing the species charge density by its charge value, q_{sp},

$$n_{sp,i,j} = \frac{\rho_{sp,i,j}}{q_{sp}}. \tag{3.98}$$

For post processing purposes it is desired to transform the nonuniform particle results to a coarser, uniform grid. This is done using an equation similar to Equation 3.93, but a over the uniform grid. The cell centered particle number density, $ncell_{sp,iu,ju}$, at the uniform grid point (iu,ju) is given by

$$ncell_{sp,iu,ju} = \frac{W_{macro}(N_{T,sp})_{iu,ju}}{V_{ucell}} \tag{3.99}$$

where $(N_{T,sp})_{iu,ju}$ is the total number of particles of species type sp present within the computational cell (iu,ju), and V_{ucell} is the uniform grid cell volume . The uniform grid cell volume is computed using

$$V_{ucell} = \pi \Delta(r_u^2) \Delta z_u. \tag{3.100}$$

where Δz_u is the uniform grid spacing in the z direction, and $\Delta(r_u^2)$ is

$$\Delta(r_u^2) = \left(r_{i,j+1}^2 - r_{i,j}^2\right) \tag{3.101}$$

The symbol $\Delta(r_u^2)$ is used in Equation 3.100 to emphasis that a uniform spacing is used in the radial direction. The particle number density values at the uniform grid points, $ngrid_{sp,iu,ju}$ are computed using a bilinear interpolation of the cell centered particle number density values at the surrounding four cell centers.

3.3 Parallel Processing

Our initial simulation work on a 9.2 cm diameter discharge chamber showed that the simulation time to reach 1 μs is 30 days on a single processor [Mahalingam and Menart 2005]. This simulation used a 1000x500 uniform mesh, a time step value of 2×10^{-12}s, and 9 million computer particles. Millions of computer particles coupled with a large number of computational cells significantly increases the computer time needed to advance particles and fields for every time step. The computer time to finish a single time step steadily increases with time, because more particles are added into the discharge chamber as the plasma heads towards a steady state operating point. This occurs because more particles are emitted into the discharge chamber from the cathode, and particles are produced because of ionizing collisions. One month of computational time for 1 μs of plasma simulation time is unreasonable. For this reason parallel processing has to be enabled in this PIC-MCC simulation.

The parallel processing done in this work is done in the spatial realm. The computational domain is divided into a number of subdomains and each subdomain is assigned one processor to handle all computations for that subdomain. Here all computations refer both field calculations and particle

calculations within the subdomain. In parallelizing this PIC-MCC algorithm a number of issues need to be addressed. In this section two subsections are given; each dealing with a major issue of the parallelization of the PIC-MCC algorithm.

3.3.1 Parallel Domain Decompositions

The first major issue in applying a parallel algorithm to this PIC-MCC algorithm was dividing the overall computational domain into subdomains. In this work the computational domain is partitioned using a one-dimensional domain decomposition in the axial direction. This type of domain decomposition was chosen because the original XOOPIC code [Mardahl 2001; Mardahl and Verboncoeur 1998] has already been designed to handle parallel processing with the particle advancing using one-dimensional domain decomposition in the z-direction (i.e. columns). For the parallel Poisson solver routine, a separate domain decomposition which includes an overlapping region between subdomains has been developed as part of this work [Mahalingam and Menart 2006]. This domain decomposition is independent of the particle domain decomposition and is only used in the field solving routine. Both domain decompositions are discussed in this subsection.

The computational domain is partitioned in the axial direction by placing virtual boundaries known as *SpatialRegionBoundary* (SRB) [Mardahl 2001]. A SRB is a common boundary that is shared by two neighboring processors. This SRB boundary is used for handling the particle exchange between processors and to compute the field and charge density information at the partitioned boundary grid points correctly. The total number of SRBs required for a parallel run is based on the total number of processors employed and it is given by

$$N_{SRB} = N_{proc} - 1. \tag{3.102}$$

Figure 3.8 shows a sample partitioning of the computational domain using seven processors. The partition boundaries can be placed arbitrarily and each processor can have a different number of grid points. This feature allows better design of the decomposed domains for load balancing.

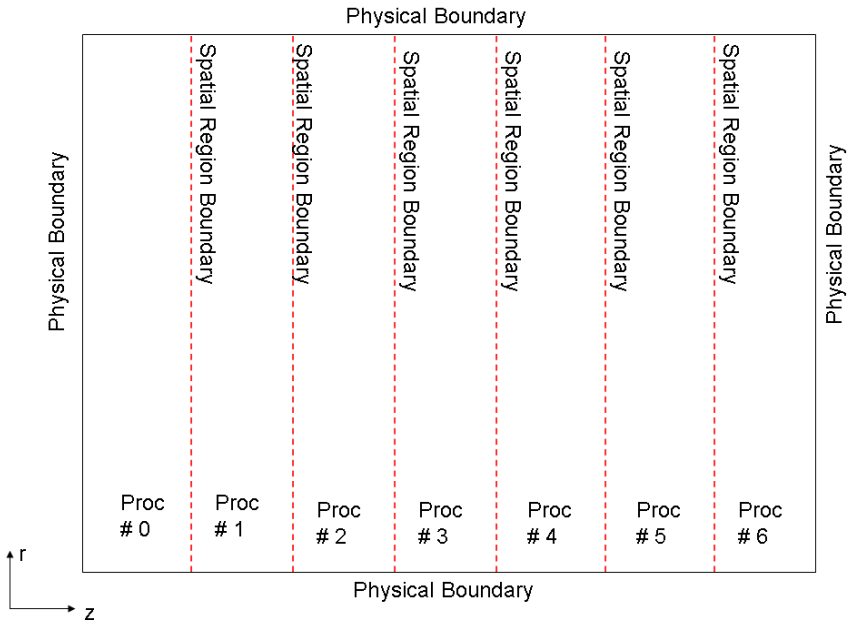

Figure 3.8: One dimensional domain decomposition for parallel particle advancing using seven processors.

In this work a parallelized DADI Poisson solver is written to handle the electric potential solving in parallel. For this Poisson solver, a slightly altered domain decomposition scheme is considered. This domain decomposition uses the same SRBs for partitioning the computational domain, but each processor's local domain is assigned extra columns at the SRB. These extra columns are the overlap or shadow regions of the adjacent processor's region. Since extra columns are attached to each SRB, all processors have extra columns where the decomposed domain interfaces with an adjacent decomposed domain. Figure 3.9 shows a sample partitioning of a discharge chamber using three processors with two extra columns at the SRB. Local regions of the first (Proc# 0) and last (Proc# 2) processors have only two extra columns since they share only one SRB with their neighboring processor (Proc# 1). The middle processor (Proc# 1) has four extra columns, since it has two SRBs. The choice of keeping a larger or smaller overlap at the SRBs depends on how quickly the information is passed, and the memory requirements [Sawdey and O'Keefe 1997]. Maintaining a

large overlap at the SRB tends to reduce the number of iterations required by the Poisson solver; however, the total computations performed for each iteration on each processor also increases and the memory requirement increase. With the global nature of the Poisson solver, large overlap results in better communication of information from one domain to another. This reduces the number of Poisson solver iterations required to reach a converged solution. Fewer Poisson solver iterations, require fewer computations in each processor, and fewer communications between processors. Large memory requirements due to a large overlap are not an important issue when the total computational domain is broken into small regions. The selection of overlapping is also essentially limited by the number of grid points considered in the neighboring processor. The overlapping region grid points should be less than the neighboring processor's local region grid points.

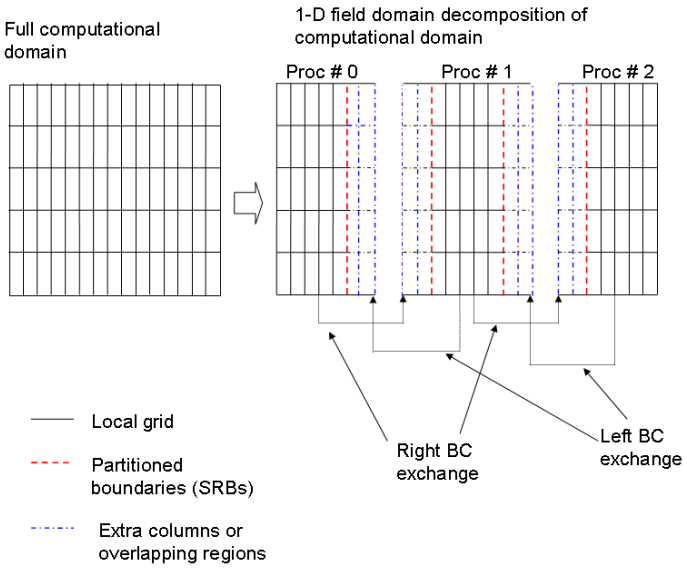

Figure 3.9: One dimensional domain decomposition for parallel DADI solver on three processors.

Since the computational domain is partitioned based on the total number of mesh points in the z-direction, the maximum number of processors that can be employed in the simulation is limited by the number of grid points. For example, if you consider 100 grid points in the axial direction,

then ideally the maximum number of processors that can be employed in parallel processing is 100. However, it is not possible to consider just one z-direction grid point for each processor because: 1) this does not allow for an overlap region between processors and 2) certain particles may completely jump over two grid points if their path of travel during a time step interval is larger than the width of two computational cells. This means crossing over a processor which would require additional computational overhead to handle. This work has chosen not to add the extra computational overhead to handle particle processer jumping and restricts the user to having more than one grid point per subdomain. From our current studies it is found that at least 3 to 5 grid points in each subdomain is required to allow simulations to run in parallel. Thus an overall computational domain that uses 100 axial grid points, is limited to 20 to 30 processors. Another issue in setting up the subdomains for each processor is that the SRBs should not divide the particle source regions at the cathode exit and the main neutral plenum.

3.3.2 Parallel Electrostatic Algorithm

Implementation of a parallel Poisson solver is a necessity to improve the computational performance of this PIC-MCC simulation. A number of mesh relaxation schemes [Hockney and Eastwood 1988] were studied on a two-dimensional mesh. Schemes that were studied include: pointwise Jacobi, pointwise Gauss-Siedel (GS), red-black GS scheme, line GS, alternating line GS, additive correction, and dynamic alternating direction implicit (DADI). Remarkably the DADI scheme [Doss and Miller 1979] was found to give converged solutions with the shortest run time. For a simple Dirichlet type boundary condition problem on a 200x200 uniform grid, the number of iterations taken by the DADI solver to reach a L_2 norm residual value of 0.001 was 15-20 iterations; while the best line Gauss-Seidel scheme required thousands of iterations to reach the same L_2 norm value. A single DADI iteration (as will be explained below) performs three ADI (alternating direction implicit) sweeps. Each ADI sweep uses two passes. This means a single DADI iteration solves the Poisson equation six times for every iteration. Even with these six inner iterations our tests of these different algorithms

show the DADI method to be more computationally efficient than other methods. Our observations are similar to the observations of Doss [1979]. Both the serial DADI and the inner ADI algorithm steps are provided in Appendix A.

3.3.2.1 Parallel DADI

The parallel DADI solver is performed with the computational mesh given in Figure 3.9. In this computational mesh each processor considers a local computational region along with the overlapping regions. The solver steps in the parallel DADI scheme are similar to the steps followed in the serial DADI scheme. The main differences between the serial DADI solver and the parallel DADI solver are the computational region and the boundary conditions. In a parallel DADI solver, each processor performs ADI sweeps within the local region and also in the overlapping region. Performing ADI sweeps in the overlapping region is a redundant computation with the adjacent DADI solver. Also the boundary conditions applied in the parallel ADI solver are different than the serial DADI solver. The serial DADI solver sees the entire computational domain as one piece. However computational domain is broken into individual regions with each region having its own processor, it is necessary to maintain the continuity of boundaries between the processors. By maintaining the continuity at the partition boundaries, it is ensured that the parallel DADI solves the same problem as serial DADI.

The parallel DADI solver needs four boundary conditions: left, right, top and bottom. Since the one-dimensional domain decomposition is performed in the z-direction, the bottom boundary condition (i.e. the axis of symmetry of the discharge chamber) and the top boundary condition (the side wall of the discharge chamber) will be the same for all processors. The left and right boundary conditions have to be exchanged between the processors. The left boundary condition for all processors, except the first processor, is set from the corresponding column points of the left neighbor processors computed electric potential values. Similarly the right boundary condition for all processors, except the last processor, is set to the corresponding column points of the right neighbor processors computed electric potential values. These boundary communications are indicated in

Fig. 3.9. The left boundary for the first processor and the right boundary for the last processor are the discharge chamber walls and the screen grid. The computation at the overlapping region mesh points is redundant, but necessary to obtain less disjoint between the two region's solutions as the DADI solver is approaching a converged solution.

Before performing the DADI solver, the primed coefficients ($a's$) of the Laplace operator given in Equation (A.7)-(A.12) are computed for the local region grid points. Each processor exchanges the computed primed coefficients and the grid spacing details at the overlapping region, to its neighboring processor. The exchange is performed at the beginning of the simulation. This information is necessary because each processor performs ADI sweeps for the entire subdomain comprised of the local region grid points and the overlap region grid points. Then each processor computes the initial fictitious time step size for the DADI iteration as given in Equation (A.26).

The iterative parallel DADI solver steps are:

1. Each processor exchanges the ϕ, and ρ values at the overlapping region mesh points to its neighboring processors.

2. The iteration index, k, is set to zero.

3. The DADI iteration begins by performing a single ADI sweep (comprised of 2 passes) using Δt_f^k to obtain solutions for $\phi_{i,j}^k$ to $\phi_{i,j}^{k+1/2}$

4. Each processor exchanges the computed electric potential values at the overlapping region mesh points to its neighboring processors. Then ϕ values at the overlapping region mesh points are averaged. The left and right overlapping regions of each processor are assigned with the averaged ϕ values. These ϕ exchange processes are indicated in Figure 3.10.

5. Another ADI sweep is performed using Δt_f^k to obtain solutions from $\phi_{i,j}^{k+1/2}$ to $\phi_{i,j}^{k+1}$.

6. Step 4 is repeated.

7. A single ADI sweep using a double $2\Delta t_f^k$ is performed to obtain solutions from $\phi_{i,j}^k$ to $\overline{\phi}_{i,j}^{k+1}$.

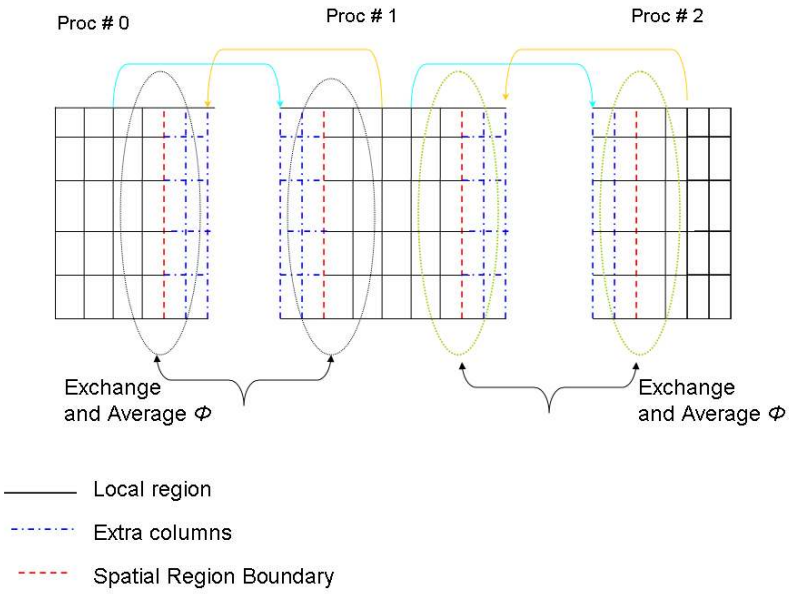

Figure 3.10: Inter processor communications shown for the overlapping regions and boundary condition assignments.

8. Step 4 is repeated.

9. The residual values of Poisson equation are calculated using the electric potential values at the $k+1^{th}$ iteration. For the residual calculation, each processor uses the local region points only. The localized residual in each processor is computed as:

$$Res_{local} = \|\nabla^2(\varepsilon_a \phi_{i,j}^{k+1}) + \rho_{i,j}\| \tag{3.103}$$

where the Laplace operator is expanded in the finite difference form using Equation (A.3). A global residue is obtained by summing the local residue values in each processor. It is given by

$$Res_{global} = \sum_{m=0}^{m=N_{proc}-1} Res_{local,m}. \tag{3.104}$$

Each processor exchanges their local residue value using MPI communication to determine the

global residue. Once the global residue is known it is normalized using

$$r_{global} = \frac{\sqrt{Res_{global}}}{\sqrt{\sum_{i=1}^{N_z}\sum_{j=1}^{N_r}\left[\rho_{i,j}\right]^2}} \tag{3.105}$$

This normalized global residue value is compared with a minimum tolerance value specified by the user. If the residual value falls below the tolerance limit, the solution is converged and a steady state has been reached; otherwise the DADI iterations are continued.

10. The fictitious time step for the next $k+1^{th}$ iteration is adjusted. The L_2norm of the computed ϕ solution of the two sets of ADI sweeps are used for this purpose. Each processor considers both the local region and the overlapping region mesh points for the computation of the L_2norm values. The L_2norm values are

$$L_{\phi diff,local} = \|\phi_{i,j}^{k+1} - \overline{\phi}_{i,j}^{k+1}\|, \tag{3.106}$$

$$L_{\phi error,local} = \|\phi_{i,j}^{k+1} - \phi_{i,j}^{k}\| \tag{3.107}$$

The global sum of the L_2 norm values are obtained by summing the L_2 norm results from each processor

$$L_{\phi diff,global} = \sum_{m=0}^{m=N_{proc}-1} L_{\phi diff,m}, \tag{3.108}$$

$$L_{\phi error,global} = \sum_{m=0}^{m=N_{proc}-1} L_{\phi error,m}, \tag{3.109}$$

Similar to Equation (A.30), the global test parameter ratio is computed as

$$TP_{global} = \frac{L_{\phi diff,global}}{L_{\phi error,global}}. \tag{3.110}$$

11. Based on TP_{global}, the time step multiplicative factor, f_w is obtained using Table 6. This f_w value and the current Δt_f^k are used in Equation (A.31) to compute the new Δt_f^{k+1}. Similar to the serial DADI solver, when the global test parameter value goes above 0.6, the computed ϕ solutions at the $k+1$ iteration are discarded and the ϕ values are reset to the initial ϕ values at k^{th} iteration.

12. The iteration counter k is set to k+1 and steps 3 through 11 are repeated until convergence.

3.3.2.2 Spatial Region Boundary Communications

Since the parallel PIC-MCC simulation uses the SRB to partition the computational domain, the field and particle information along the SRB grid points have to be handled correctly. The variables that require special handling are the electric field, charge density, number density, and the particles crossing between processors at the SRB grid points. Here the MPI commands are used for exchanging information from one processor to another.

After performing the parallel DADI solver, the electric potential, ϕ, results are available at the grid points in each processor. The electric field $\tilde{\vec{E}}$ values, which are stored at the cell face centers, are obtained using Equations (3.6) and (3.7). The electric field $\vec{E}$ results at the grid cell nodes and the cell face centered electric field results (see Equations (3.8) and (3.13)) are computed using the weighted interpolations based on the grid spacings. In each processor, the computation of electric fields at the interior grid points can be performed locally. However, the computations of the axial electric field values, E_z, at the SRB grid points in each processor require the cell face centered axial electric field and grid spacing information from the neighboring processor's interior grid points. Hence the two adjacent processors exchange this information to compute the axial electric field correctly. Since the grid spacing values are constant they are exchanged only once at the beginning of the simulation. Each processor stores the received grid spacing information from its neighbors, and uses them in the axial electric field calculations for the SRB grid cell nodes. Figure 3.11 shows the variables at the SRB grid points and the electric field exchange between the left and right processor. Once the values are communicated, the axial electric field values at the SRB grid points are evaluated as

$$E_{z,Nzl,j}^{Left} = E_{z,0,j}^{Right} = w_z^{+'}\left(\frac{\tilde{E}_{z,1/2,j}^{Right}}{\triangle z_{1,j}^{Right}}\right) + w_z^{-'}\left(\frac{\tilde{E}_{z,Nzl-1/2,j}^{Left}}{\triangle z_{Nzl,j}^{Left}}\right) \tag{3.111}$$

where

$$w_z^{+'} = \frac{\triangle z_{Nzl,j}^{Left}}{\triangle z_{1,j}^{Right} + \triangle z_{Nzl,j}^{Left}}, \tag{3.112}$$

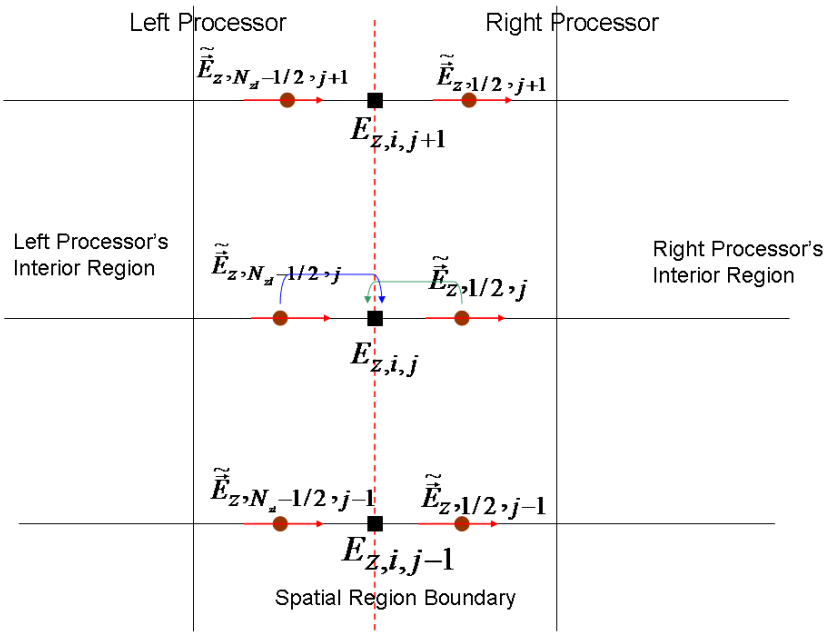

Figure 3.11: A plot of the grid points at the SRB which requires special handling.

$$w_z^{-'} = \frac{\triangle z_{1,j}^{Right}}{\triangle z_{i,j}^{Right} + \triangle z_{Nzl,j}^{Left}}, \tag{3.113}$$

$$\triangle z_{1,j}^{Right} = z_{1,j}^{Right} - z_{0,j}^{Right}, \tag{3.114}$$

and

$$\triangle z_{Nzl,j}^{Left} = z_{Nzl,j}^{Left} - z_{Nzl-1,j}^{Left}. \tag{3.115}$$

Here $\tilde{E}_{z,1/2,j}^{Right}$, $\triangle z_{1,j}^{Right}$, $z_{1,j}^{Right}$, and $z_{0,j}^{Right}$ are the right processor's cell-face centered axial electric field at location $(1/2, j)$, axial grid spacing of the computational cell (1,j), axial position at node (1,j), and axial position at node (0,j) respectively. Similarly the $\tilde{E}_{z,Nzl-1/2,j}^{Left}$, $\triangle z_{Nzl,j}^{Left}$, $z_{Nzl,j}^{Left}$, and $z_{Nzl-1,j}^{Left}$ are the left processor's cell-face centered axial electric field at location Nzl,j, axial grid spacing for grid cell Nzl,j, axial position at node Nzl,j, and axial position at node Nzl-1,j respectively. Also Nzl is the maximum number of axial grid points in the left processor.

The computation of charge density values at the SRB grid points have to be handled correctly also. The charge density values at the grid points are computed by simply adding the charge density

values of each species group at the grid point (see Equation (3.95)). At the SRB grid points, each processor will have the charge density values based on the sum of the local charges collected at that grid point. Since two processors share a same SRB, the correct charge density values for the grid points at the SRB is the sum of the local charge density values from each processor. The charge density value at the SRB grid point is given by

$$\rho_{Nzl,j}^{Left} = \rho_{0,j}^{Right} = \rho_{Nzl,j}^{local,Left} + \rho_{0,j}^{local,Right} \tag{3.116}$$

where $\rho_{Nzl,j}^{local,Left}$ is the left processor's locally computed charge density at the SRB grid point (Nzl,j) and $\rho_{0,j}^{local,Right}$ is the right processor's locally computed charge density at the SRB grid point (0,j).

The particle number density given in Equation (3.96) is the computational cell averaged value, there is no need to exchange this particle number density information between processors. When computing the particle number density values in the uniform computational mesh, it is necessary to exchange the number density information between processors. Even though each processor performs computations only within the local regions assigned by the SRBs, the entire uniform computational mesh is made known to all processors. This is done because the uniform grid points may not match with the nonuniform grid points, and dividing the uniform grid with the same number of processors as used in the non-uniform grid would require another domain decomposition. Each processor computes particle number density calculations on the entire computational domain of the uniform grid using Equation (3.99). Finally a global summation of particle number density is done. Results from each processor are summed to obtain the particle number density results for the entire computational domain. This summation is given by

$$n_{sp,iu,ju} = \sum_{m=0}^{m=N_{proc}-1} n_{sp,iu,ju,m} \tag{3.117}$$

where $n_{sp,iu,ju,m}$ is the particle number density value of species type sp at the computational cell (iu,ju) for processor m. The above equation is performed using MPI commands which does the summation of the particle number density results obtained in each processor.

Using the same uniform grid, the average particle kinetic energy results for species type sp at

the computational cell (iu,ju), $KEavg_{sp,iu,ju}$ is calculated as below:

$$KEavg_{sp,iu,ju} = \frac{\sum_{m=0}^{m=N_{proc}-1} KElocal_{sp,iu,ju,m}}{\sum_{m=0}^{m=N_{proc}-1} N_{sp,iu,ju,m}} \tag{3.118}$$

where $KElocal_{sp,iu,ju,m}$ is the m^{th} processor's total sum of the kinetic energies of particles of species type sp present in the computational cell (iu,ju), and $N_{sp,iu,ju,m}$ is the total number of computer particles of species type sp present within the computational cell (iu,ju) in the m^{th} processor. The $KElocal_{sp,iu,ju,m}$ is computed using

$$KElocal_{sp,iu,ju,m} = \sum_{n=0}^{n=N_{sp,iu,ju,m}-1} \frac{1}{2} m_{sp} |\vec{v}_n|^2. \tag{3.119}$$

The above equation and $N_{sp,iu,ju,m}$ computations are local to each processor. Once all processors complete these local computations then Equation (3.118) is solved. Both the numerator and denominator of Equation (3.118) are obtained using the MPI command which performs the summations of the local quantities obtained in each processor.

The handling of particles crossing the SRBs are described in [Mardahl 2001]. During every particle advance function, the crossing charge particles are collected at the SRBs. At the end of the particle advance, these collected particles are sent to the neighboring processor. From our parallel PIC-MCC simulations, we have found limitations on the communication buffer size with the message passing interface (MPI) routines such as the MPI_Send and MPI_Recv commands. When a particle is being exchanged across the partitioned boundary, 10 floating point numbers (8 bytes each) for each particle are being communicated between the processors: 3-components of the particle velocity, the particle r-location at the partitioned boundary, the particle type, the particle weighting, the factor for particle weighting, and 3-components of the remaining distance that the particle has to travel in the neighboring processor. In total, 80 bytes of floating information are exchanged during a single particle crossing. Each processor's partitioned boundary performs a MPI_Send command to send particles to its neighboring processor. In the same way each processor's partitioned boundary does perform MPI_Receive commands to receive particles that are being sent from its neighboring processor. We have observed that the communication buffer for these two commands combined

together can handle only 512 kb of particle information, i.e., exactly 6400 crossing particles in a single time step. If the number of crossing particles at the partitioned boundary exceeds this buffer limit, it causes a problem in the MPI routines and hangs-up the parallel run. This subtle problem with the communication buffer limit was found when we enabled the tracking of neutrals. Now I are handling the communication buffer problem by dividing the number of crossing particles in to two sets; this way the single MPI_Send and MPI_Recv commands are now broken down into double MPI_Send and MPI_Recv commands.

3.3.2.3 Parallel Solver Verification

The parallel Poisson equation algorithm developed as part of this work is verified on a small chamber case before applying it to an ion engine discharge chamber. This verification is done by checking the single processor results against the parallel processor results. Comparisons of total particle results and the electric potential results between the single processor case and the 2-processor, parallel case show excellent agreement. Less than 2% difference is seen in the results which could be attributed to the randomness of the particle collision events. A speed up of 1.53 is obtained by using two processors instead of one processor. Ideally a speed-up of 2 is expected; however, the parallel simulation is slowed for a number of reasons. The exchange of information between the processors takes time and typically the load between the two processors is not balanced. If the loads are imbalanced one processor has to wait on the other processor. An imbalance of particles in the two regions plays a major role in causing one processor to run longer than the other.

The *Numerical Recipes* book [Press 1992] states that certain random number generators have serial correlations and other errors when more than 100 million random numbers are generated in a single simulation. For this reason a random number generator called RAN2 [Press 1992] is used in this work and is recommended for parallel computations.

3.3.3 The Parallel PIC-MCC Simulation sequence

Figure 3.12 shows the flow path of particle and field solver routines in parallel processing. In a parallel run, all processors have to wait for the completion of the following four messages. In msg # 1 all processors wait for the completion of the particle advances and to send and receive the crossing particles between the processors. This waiting can be significant if imbalance of particles is present between different processors. In msg # 2 the charge density values are updated at the SRB grid points. In this step all processors have to wait until all charge particles are weighted to the grid points, the density for different species are computed, and the exchange of charge density at the SRB grid points is done. In msg # 3 all processors perform exchange of ϕ information during the DADI iteration and wait for the completion of the parallel DADI solver. This can significantly slow down the advancing of the computations, since all processors perform the field solver iterations simultaneously. During a single DADI iteration step, there are three sets of communications that are passed between processors for the ϕ values at the overlapping regions. The number of messages communicated during a DADI solver step depends on the total number of grid points in the overlapping region and the number of iterations taken by the DADI solver to obtain convergence. If the communications are large, processors can get slowed down in trying to reach the correct ϕ values. If an imbalance in the number of grid points between processors exists, it could significantly slow down the parallel run. In msg # 4, the electric fields at the SRB grid nodes are computed by exchanging field information between processors. Messages # 1 and # 3 are the critical components that can decrease the performance of parallel processing.

3.3.3.1 Particle Advancing Sequence

In this PIC-MCC simulation different time step sizes are used for simulating the lighter electron particles than the heavier particles such as ions and neutrals. This is done because of the two order magnitude difference between the speed of the electrons and the speed of the heavier particles. The

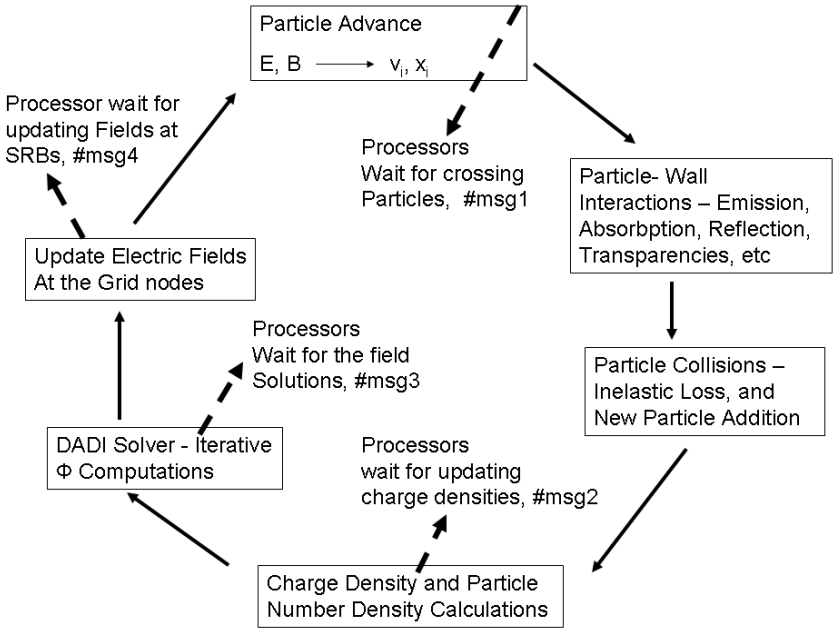

Figure 3.12: A flow chart of the PIC-MCC simulation sequence in parallel processing.

relative time step values between the electrons and heavier particles are

$$\Delta t_e < \Delta t_{ion} < \Delta t_{Xe} \tag{3.120}$$

where Δt_e is the electron's time step, Δt_{ion} is the ion's time step, and Δt_{Xe} is the neutral's time step. Because of the different time step sizes, handling the total particles and the particle's number density values require special treatment. This section explains the sequence of operations followed during each particle advance.

During one electron time step the following steps are performed:

1. The electrons are advanced using the Newton-Lorentz equation of motion. During an electron advance, the electron path is checked for crossing the boundaries. If the electron is found to have crossed a boundary, appropriate boundary conditions are applied. In addition, the advance of the remaining electrons are handled. If the electron moves out of one processor to another, the remaining advance of the electron is handled by the neighboring processor.

2. Primary electrons are emitted from the cathode source.

3. Electron collisions with heavy particles, neutrals and ions, as well as elastic and inelastic collisions are considered. If a primary electron is involved in an inelastic collision, the primary electron's final energy is compared with a value of 4 eV. If the primary electron's energy is below 4 eV, the primary electron is moved into the secondary electron group.

   For every e-Xe ionization collision event, the following steps need to be performed: 1) a neutral particle needs to be removed from the neutral particle list, 2) a new Xe^+ and secondary electron need to be added to their respective lists, 3) the neutral number density at the ionization location needs to be adjusted, and 4) the density of Xe^+ particles and secondary electrons needs to be adjusted. Even though subcycling is used for the neutrals and ions, the recalculation of the neutral and Xe^+ number densities needs to be done for every electron iteration. The grid cell locations (both z and r indices) where the ionization event occurred are stored at the time they occur. Later, during the neutral particle's advance, the neutral particles are removed from the neutral list and the remaining neutrals are advanced using the equation of motion. Unlike the neutrals, Xe^+ particles are added to the Xe^+ list immediately. Any particle can easily be added to its list during electron iterations, but deletion of heavy particles have to wait until the next subcycle process. Proper determination of the neutral number density and Xe^+ number density throughout the discharge chamber, at every electron time step, is necessary because these particles are utilized in the MCC routine to determine the total number of electron-neutral collisions. The adjustment of the electron number density because of an ionization collision event is easily handled before the next electron advance iteration.

   For every e-Xe^+ ionization collision event, the following steps need to be performed: 1) Xe^+ needs to be removed from the Xe^+ particle list, 2) a new Xe^{++} and secondary electron need to be created and 3) the Xe^+ and Xe^{++} number density at the ionization location needs to be adjusted. Because of the subcycling used for the ions, the removal of ionized Xe^+ is handled in

a similar manner as was done for the removal of Xe during an e-Xe ionization event.

For every e-Xe^+-e recombination event, the following steps need to be performed: 1) one Xe^+ and one electron need to be removed from there respective particle lists, 2) a new neutral is created and 3) the e, Xe^+, and Xe number density values at the recombination location need to adjusted. The correction of e, Xe^+, and Xe number densities and the removal of a recombined Xe^+ are handled in the similar manner as was done for the alteration of Xe and Xe^+ number densities. The recombination event of e-Xe^{++}-e is handled in a similar fashion.

4. After handling the electron collisions, the charge density values at the grid points are calculated based on the charge particle distribution. Also the electron number density values at the cell centers are computed using both primary and secondary electron particle distributions.

5. The electric potential values at the grid points are solved in the parallel DADI solver using the computed charge density values. This completes one electron cycle and the above steps are shown in flow chart form in Figure 3.13.

During one ion time step, the following steps are performed.

1. For e-Xe^+-e recombination reactions a Xe^+ is removed from its list. Likewise a Xe^{++} is removed from its list for each e-Xe^{++}-e recombination reaction. For each Xe^+-e ionizing reaction a Xe^+ is removed from its list. A search algorithm has been developed in which the whole particle list is traversed until all colliding particles are identified. The grid cell indices which are stored during the MCC simulation are utilized in identifying the particles. The selection of which particles within the computational cell are removed is arbitrary. The first particle found in the computational cell during the search is removed from the particle list.

2. All ions are advanced using the Newton-Lorentz equation of motion. During an ion advance, the ion path is checked for boundary crossings. If crossing is found, the appropriate wall boundary conditions are applied and the remaining ion advance is carried out. If the ion causes secondary

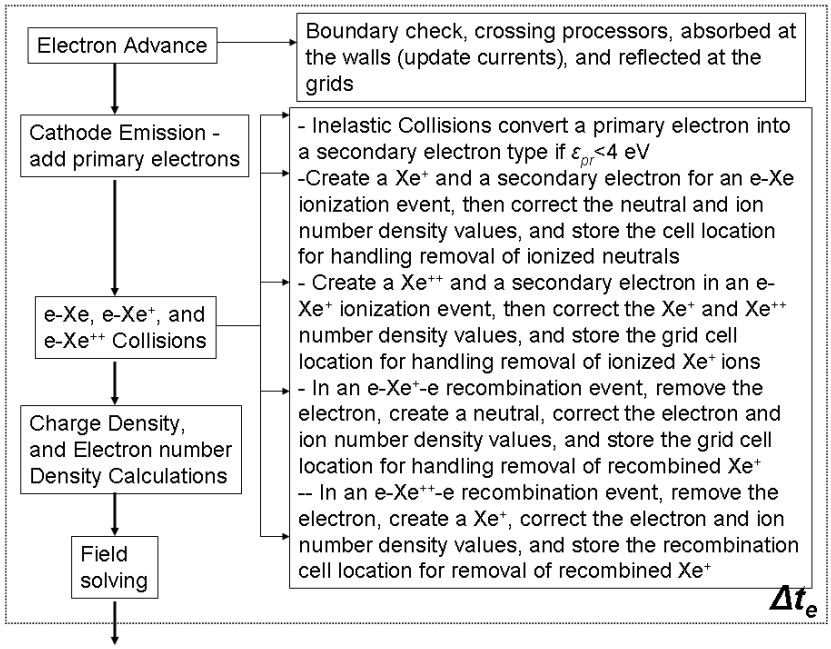

Figure 3.13: A flow chart shows the PIC-MCC steps followed during one electron time step.

emission at the wall, a secondary electron is introduced into the computational domain. If an ion moves across the processor, the remaining advance of the ion is handled by the neighboring processor.

3. Ion collisions with heavy particles (neutrals and ions), both elastic and inelastic, are determined. During a charge-exchange collision a faster ion takes on the velocity of the slower neutral.

4. The ion number density values at the cell centers for both Xe^+ and Xe^{++} are computed.

This completes one ion time step cycle and the above steps are shown in a flow chart form in Figure 3.14.

The steps followed during one neutral time step are:

1. One Xe is removed from the Xe particle list for every Xe-e ionization reaction. A search algorithm is utilized in which the whole particle list is traversed until all colliding neutrals are identified. The grid cell indices which are stored during the MCC simulation are utilized to identify the

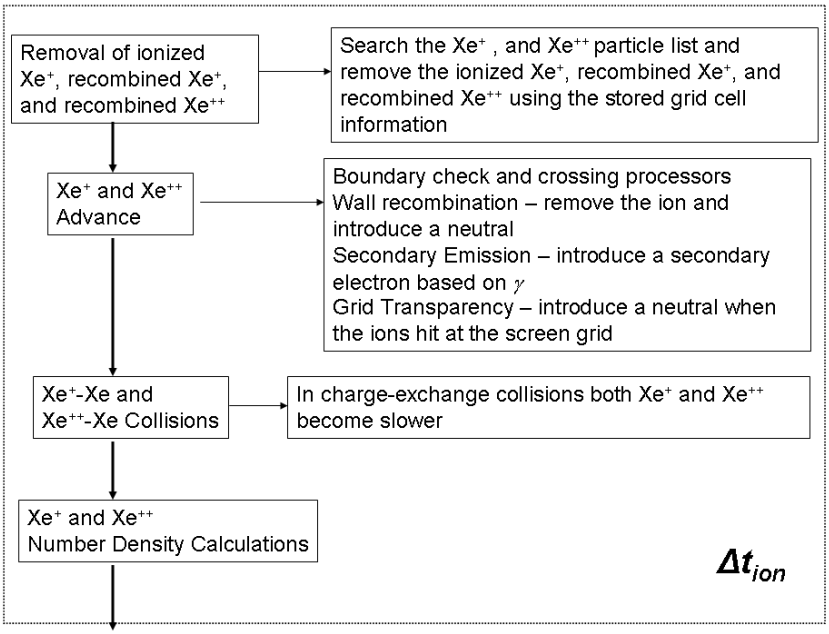

Figure 3.14: Flow chart showing the PIC-MCC steps followed during one ion time step.

particles. The selection of which particles within the computational cell are removed is arbitrary. The first particle found for the computational cell during the search is selected and gets removed from the particle list.

2. The neutrals are advanced using the equation of motion. During a neutral advance, the neutral path is checked for crossing at the boundaries. If found to cross, appropriate wall boundary conditions are applied along with the remaining neutral advance.

3. The neutral number density values at the cell centers are computed.

This completes one neutral time step cycle and the above steps are shown in a flow chart form in Figure 3.15.

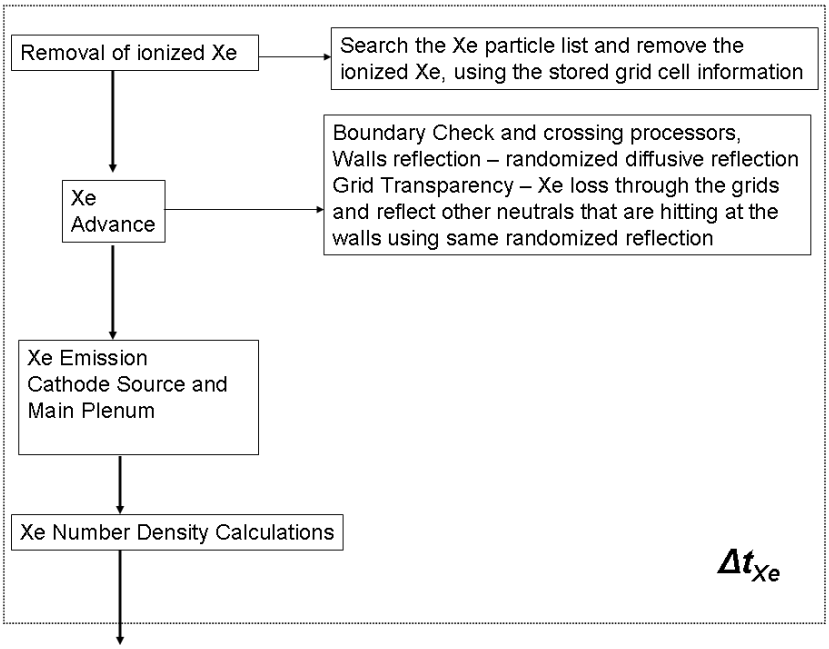

Figure 3.15: A flow chart shows the PIC-MCC steps for neutrals during the neutral time step.

3.4 Numerical Stability Criteria

The numerical techniques used in the PIC-MCC algorithm are affected by instability and noise problems. The numerical instability problems arise due to errors introduced from the discrete simulation of the fields and particle motion. The discrete nature in the computer simulation is given by the finite grid spacing, finite time step size, and finite number of computational particles used. The numerical parameters such as the grid spacing and time step need to capture the Debye length and plasma frequency. If these two scales are not resolved well instability problems results, for example numerical heating. Numerical heating causes a nonphysical energy growth in the electrons [Birdsall and Langdon 1991]. This can change the numerical results significantly and the real instabilities in the problem can not be distinguished from the numerical instabilities. In the following paragraphs numerical stability criteria associated with the numerical techniques used in the PIC-MCC simulation are given.

The ES algorithm solves the dynamic electric fields using Poisson's equation. An explicit leap-frog

scheme is adopted for the particle advancing. This explicit schemes has limitations on grid spacing size, Δz and Δr, and the time step size, Δt_e. The explicit particle advancing scheme (Birdsall, 1991) is limited by the following constraint on the time step size,

$$\omega_{pe}\Delta t_e \leq 2, \tag{3.121}$$

and for high accuracy

$$\omega_{pe}\Delta t_e \approx 0.2 \tag{3.122}$$

where ω_{pe} is given in Equation (1.22).

The constraint for grid spacing is given as [Birdsall and Langdon 1991],

$$\frac{\lambda_D}{\tilde{\Delta}} \geq 0.3 \tag{3.123}$$

where λ_D is the Debye length given in Equation (1.21) and $\tilde{\Delta}$ is the 2-D characteristic grid spacing given by

$$\tilde{\Delta} = \left[\sqrt{\frac{1}{\Delta z^2} + \frac{1}{\Delta r^2}}\right]^{-1}. \tag{3.124}$$

The constraint on grid spacing is required to control plasma heating [Birdsall and Langdon 1991]. The plasma frequency and the Debye length are proportional to the particle number density values (see Equations (1.22) and (1.21)). If a high plasma density problem is encountered, the simulation needs to deal with a high plasma frequency and a small Debye length. This demands smaller time steps to reduce the plasma oscillations and a much finer mesh to resolve the Debye length. Both of these factors result in an exponential growth computational times (estimated year long computational run time to reach steady state) and along with larger computational resources [Mahalingam and Menart 2006].

At this point in time, given the speed of computers, it is not practical to perform a discharge chamber sized PIC-MCC simulation of a plasma that has densities over $10^{13} cm^{-3}$. This is the reason that input electric fields along with an inflated permittivity constant are used in this work. Increasing the plasma permittivity to 1.08×10^{-5} allows the grid size to be increased by a factor of 1100. This is

the difference between obtaining a solution in a month as opposed to years. The inflated permittivity affects only on the part of dynamic electric field calculations. As mentioned in Chapter 2 (see Section 2.3.1), the inflated permittivity presents only on the Poisson equation given for the dynamic electric fields (see Equation 2.25). The imposed static electric field based on the experimental measured plasma potential helps maintaining the electric field inside the discharge chamber closer to the experiments. In other parts of the PIC-MCC calculations, the inflated permittivity value will not be used and hence won't affect. This helps immensely in this project to perform a fully particle based plasma simulation for modeling the ion engine discharge chamber.

Combining the spatial grid constraint and the plasma frequency condition a thermal speed stability condition is formed [Bowers 2001]

$$\frac{v_{te}\Delta t_e}{\tilde{\Delta}} \sim 0.2 \tag{3.125}$$

where v_{te} is the thermal speed of electrons given by

$$v_{te} = \omega_{pe}\lambda_D = \sqrt{\frac{k_B T_e}{m_e}}. \tag{3.126}$$

This stability condition ensures that the plasma electrons do not cross more than one cell in a single time step. The time step Δt_e value is also restricted by the MCC accuracy condition. It is given by [Verboncoeur et al. 1996]

$$P \sim \left(n_t \sigma(v_{te}) v_{te} \Delta t_e\right)^2 \ll 1 \tag{3.127}$$

where P is the probability, n_t is the target particle number density, and $\sigma(v_{te})$ is the total collision cross section. This MCC accuracy condition eliminates missing collisions in one time step.

The particle grouping is also a factor in maintaining the stability of the PIC-MCC simulations. Numerical noise caused by particle grouping [Mardahl 2001] is proportional to $\sqrt{1/N_{cp}}$, where N_{cp} is the number of macro particles in the simulation. A macro particle is a computational particle that represents a large group of real particles. Weighting each particle with fewer physical particles reduces the numerical noise. In general too few particles can result in numerical heating. Also the

interpolation techniques used in the calculation of the charge density at the grid points is based on charge values at the particle positions. In turn the charge densities determine the electrical forces at a point, which determine the forces acting on a particle. This influences the numerical stability [Mardahl 2001]. The interpolation of particle charge to the mesh points is often referred to as the particle shape (see [Birdsall and Langdon 1991]). There are different particle shapes used PIC simulations, such as zero order, first order, second order, and third order schemes. In this PIC-MCC simulation a first-order particle shape is used with bilinear interpolation. From Mardahl's 1-D PIC simulation analysis, it was shown that a PIC simulation with a first order particle shape provides a longer heating time than the zero-order NGP (Nearest Grid Point) method. A longer numerical heating time signifies a stable numerical scheme with less numerical errors. Mardahl's study has shown that PIC simulations that use higher order weighting, such as quadratic and cubic spline interpolations, do not increase the heating times significantly.

4

Numerical Parameters

Convergence Study

Each of the numerical techniques used in the PIC-MCC simulation discussed in Chapter 3 has a numerical parameter associated with it. These numerical parameters need to be converged. In a PIC-MCC simulation convergence is a difficult task. The numerical parameters utilized by a PIC-MCC simulation are: the number of iterations used, the number of particles used, the time step size used, and the grid size used. Convergence of these four parameters will be discussed in this chapter. In addition, the initial guess at the particle distributions in the discharge chamber will be addressed. All of the convergence studies shown in this chapter are performed on the 3-ring NSTAR (NASA Solar Electric Propulsion Technology Application Readiness) ion engine discharge chamber. Before presenting any convergence studies, the details of the NSTAR discharge chamber will be given. A short history of the NSTAR ion engine and its monumental Deep Space 1 mission (DS1) are given in Appendix B.

4.1 NSTAR Ion Engine

The details of the NSTAR ion engine presented here are obtained from the following papers and reports: NSTAR ion engine technology validation studies [Brophy et al. 2000; Polk et al. 1999], in-flight performance studies [Polk et al. 2000], hyper-extended in-flight ion thruster performance studies [Brophy et al. 2002], long duration and extended life test studies [Polk et al. 1997; Anderson et al. 1999; Anderson et al. 2000; Sengupta et al. 2002; Sengupta et al. 2003], laboratory model NSTAR type ion thruster experimental studies [Williams 2000; Herman and Gallimore 2004a; 2004b; Herman 2005; Sengupta et al. 2004; Sengupta 2005], and computational studies [Wirz and Katz 2005].

NASA's NSTAR discharge chamber is shown in Figure 4.1. Both axial and radial dimensions of the NSTAR discharge chamber are shown in nondimensional units. The discharge chamber length was used for nondimensionalizing the axial and radial directions. In this dissertation all discharge chamber plots are given in nondimensional units to comply with ITAR requirements though all computations are performed in dimensional units. Most of the NSTAR discharge chamber geometric details were obtained from the dissertation report of Wirz [2005a]. The NSTAR hollow cathode dimensions were obtained from Mikellides et al. [2007] and the discharge chamber length was obtained from Sengupta et al. [2004]. The discharge chamber wall materials are aluminum and titanium. The flight thrusters (FT) were fabricated with titanium, while the engineering model thrusters (EMT) were fabricated with a combination of aluminum and titanium. The wall material for the fight model thruster (FMT) discharge chamber was made of aluminum. The propellant used is xenon.

In this work we utilize the experimentally measured plasma potential mapping results obtained from the work of Herman [2005]. Herman performed NSTAR investigations using the FMT. Hence, in our discharge chamber model aluminum is taken as the wall material. The permanent magnets on the discharge chamber walls are made of samarium cobalt. The discharge chamber cathode assembly

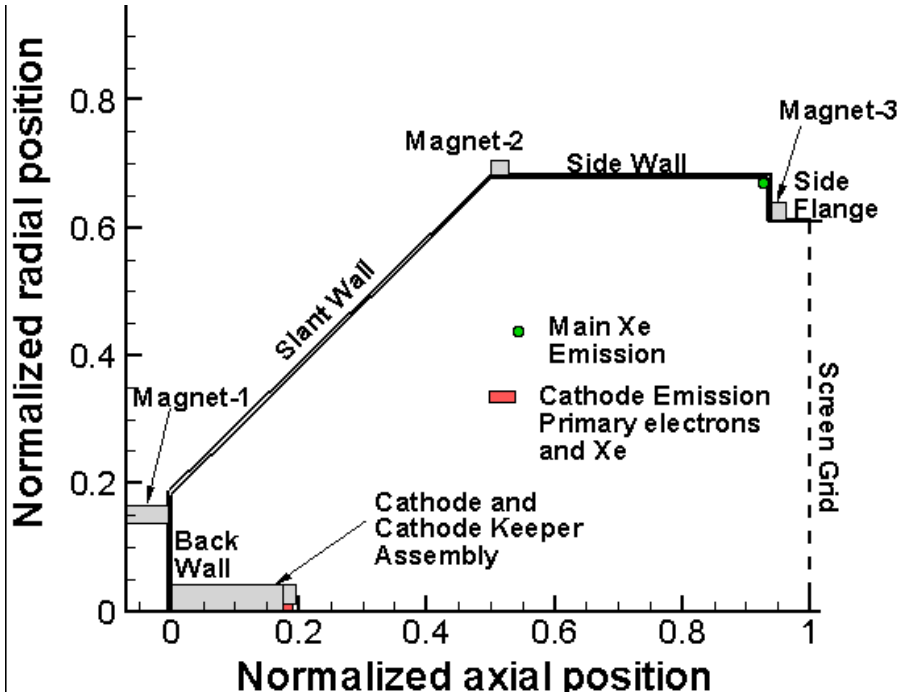

Figure 4.1: A schematic of the NSTAR 30-cm diameter discharge chamber.

includes both the hollow cathode and the cathode keeper enclosure. A small primary electron source is placed at the exit of the hollow cathode orifice. The same source is utilized to model the neutral xenon flow through the cathode. Both primary electron and neutral emission sources have a 30 degree full-angle flow stream directed towards the screen grid. This angular distribution of emission seems reasonable given the chamfered edges of the cathode orifice plate as used in the NSTAR discharge chamber. The main neutral xenon injection site is located in the corner along the side wall and front flange. The neutral propellant from this source also has a 30 degree angular distribution. The molybdenum screen and accelerator grid plates used on the NSTAR discharge chamber are circular disks that have been concaved slightly to reduce thermal buckling problems. In this work only the screen grid is modeled, and it is taken as being flat for simplicity's sake. All three magnets, the cathode source, the main neutral xenon emission location, the discharge chamber walls, and the screen grid are labeled in Figure 4.1.

Different throttle levels have been experimentally investigated for the NSTAR thruster for the

Table 4.1: NSTAR TH-15 Operating Conditions and Input Parameters.

Description	TH-15
P_{IN}	2.29 kW
T	92.4 mN
I_{sp}	3120 s
η_t	0.618 s
V_D	25.14 V
I_D	14.9 A
$\dot{m}_{main}$	23.43 sccm
$\dot{m}_{cathode}$	3.70 sccm
I_E	12.7 A
I_B	1.76 A
V_B	1100 V
V_{Acc}	-180 V
η_{prop}	90 %
φ_{ion}	0.84
φ_0	0.13
V_{bulk}	28 V
V_{cTip}	2 V
$T_{pe,init}$	2 eV
T_0	0.0365 eV
t_s^*	0.01391

Deep Space 1 mission (see Appendix B). However, the majority of wear and life tests were conducted on the NSTAR thruster when operated at its full power level. This throttle condition is called TH-15. In addition, the spare flight thruster which is identical to the one used in the NSTAR mission was operated at the TH-15 condition for a long duration test. In this work the NSTAR TH-15 throttle level is taken as the operating condition for all PIC-MCC simulation cases, except the two cases where the effect of emission current is studied. In an earlier work by Mahalingam and Menart [2007] the TH-12 throttle level was used (see Appendix B). Table 4.1 lists the TH-15 operating conditions and performance parameters.

Figure 4.2 shows the static electric potential mapping utilized for the TH-15 operating condition. This electric potential mapping uses the experimental measurements of made in reference [Herman and Gallimore 2004a]. Herman and Gallimore made these measurements for locations near the cathode keeper to 0.56 nondimensional units upstream of the back wall and radially traversing from thruster centerline to the slant wall. Herman and Gallimore's measurements indicate that

the bulk of the discharge chamber plasma potential is at 28 volts (for radial locations greater than 0.12 nondimensional units). This is what is used in this work. Herman and Gallimore's data are considered for the region axially between 0.2 to 0.5 nondimensional units from the back wall and radially from thruster centerline to 0.1 nondimensional units. The electric potential values for the region axially between 0.5 to 0.55 nondimensional units and radially between 0.1 to 0.12 nondimensional units are interpolated to have a smooth transition of electric potential values from the region which utilizes the experimental data to the bulk plasma. All discharge chamber walls are covered with a sheath that has a thickness of 3.2 mm, in which the 28 volt bulk plasma potential drops to the 25.14 volt wall potential. Since the bulk plasma potential is maintained at 28 volts and the cathode source is maintained at 2 volts, there is a 26 volt rise from the cathode to the bulk plasma. The initial primary electron kinetic energy from the cathode tip is set to 2 eV [Mikellides et al. 2005a] and the neutral particle kinetic energy is set to 0.0365 eV. The sum of the 2 eV primary electron's initial kinetic energy and the 26 eV potential energy provides an energy input for the primary electrons of 28 eV, the plasma potential value. The cathode keeper is maintained at 6 volts positive to the cathode and the screen grid is maintained at 0 volts.

Figure 4.3 shows the static magnetic field inside the NSTAR discharge chamber. A high magnetic flux density of 1000 gauss is observed close to the magnets. In the axial direction the magnetic flux density values are low for a region from 0.25 nondimensional units downstream of the cathode keeper to the screen grid. In the radial direction the magnetic flux density values are low from the thruster centerline to a radius of 0.45 nondimensional units. This can be looked at as a field free region. In Figure 4.3 the magnetic vector potential contour lines (magnetic field lines) are superimposed on the flux density contour plot. The magnetic vector potential lines run between the cusp regions of the magnets. The slanted wall of the discharge chamber is covered by the 100 gauss-cm magnetic vector potential line running between magnet-1 and magnet-2. This 100 gauss-cm line leans towards the slanted wall at an axial position between 0.3 to 0.42 nondimensional units and a radial position between 0.25 to 0.5 nondimensional units. This wall region is highlighted because this is a weak spot

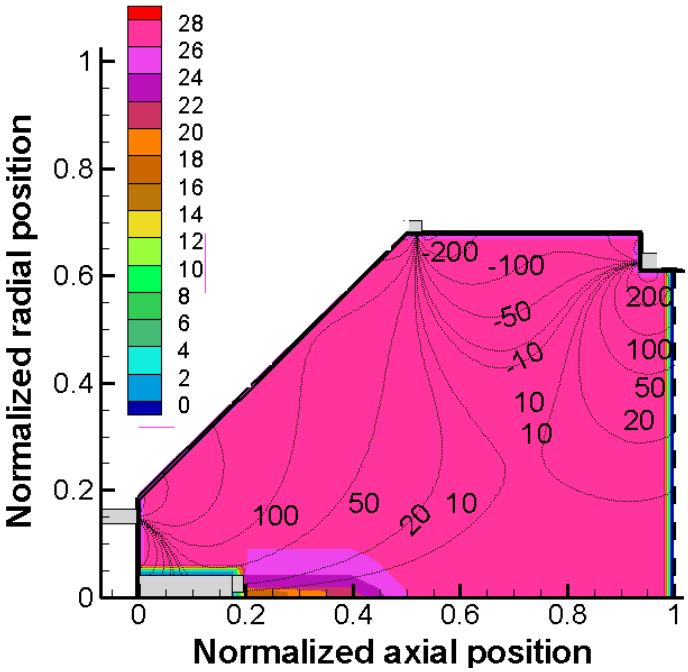

Figure 4.2: Input static electric potential contours in volts for NSTAR TH-15 operating condition.

in the confining magnetic field and it is believed that this effects the NSTAR performance. More will be said about this in Chapter 5.

4.2 Convergence Studies

In similar particle based plasma simulations investigators [Kolev et al. 2005; Parker 2002] have used a single computed output parameter for determining convergence. In this work the following output parameters are utilized: the beam current, the discharge current, and the particle number density distribution. Local convergence in terms of particle number density distributions are difficult to achieve with a PIC-MCC simulation. The volume of the NSTAR ion thruster discharge chamber is about 12,500 cubic centimeters. This volume is one of the major factors that make these calculations so difficult. Larger volumes mean more computational particles are required, more grid points are required, and more iterations are required to reach a steady state solution. To obtain convergence to engineering accuracy (2%), for all parameters, at all locations in the discharge chamber, is not

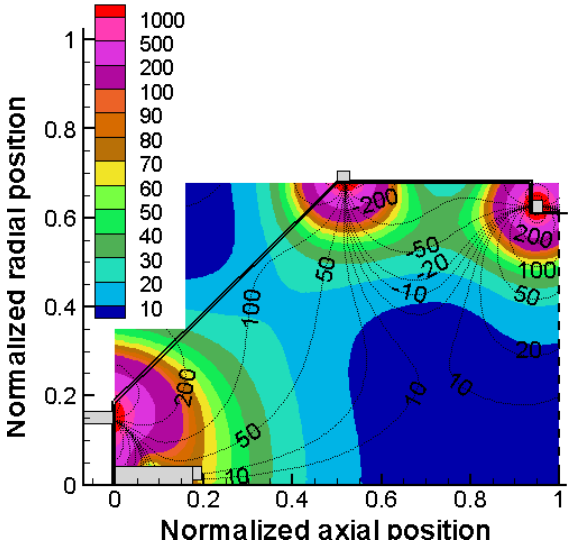

Figure 4.3: Magnetic flux density contours in gauss for the NSTAR discharge chamber. Magnetic vector potential values in gauss-cm are also shown as line contours in this plot.

practical. Better convergence can be purchased at the price of more computational time; however, it must be realized that the computational times being used in this work are measured in days and weeks. For the most part the global parameters studied are converged within 5 to 10% when compared against the finest value tested. The local parameters have more deviation than this at certain locations. This is understandable because certain locations in the discharge chamber have few particles. It would take months of computational time to converge all locations of the discharge chamber within 5 to 10%.

The computational mesh used for most of the convergence studies shown in this chapter is shown in Figure 4.4. Variations of this computational mesh are considered in the grid convergence study. This nonuniform mesh is selected such that a fine mesh is applied in the wall-sheaths, at the magnetic cusps, and at the cathode source. The number of grid points in the axial direction is 100 and the number of grid points in the radial direction in 82. The minimum two-dimensional grid spacing value is 0.002 nondimensional units and the maximum two-dimensional grid spacing value is 0.016 nondimensional units. Figure 4.4 shows the one dimensional domain decomposition utilized in this work. The boundaries between the ten different processor domains are shown as dotted lines.

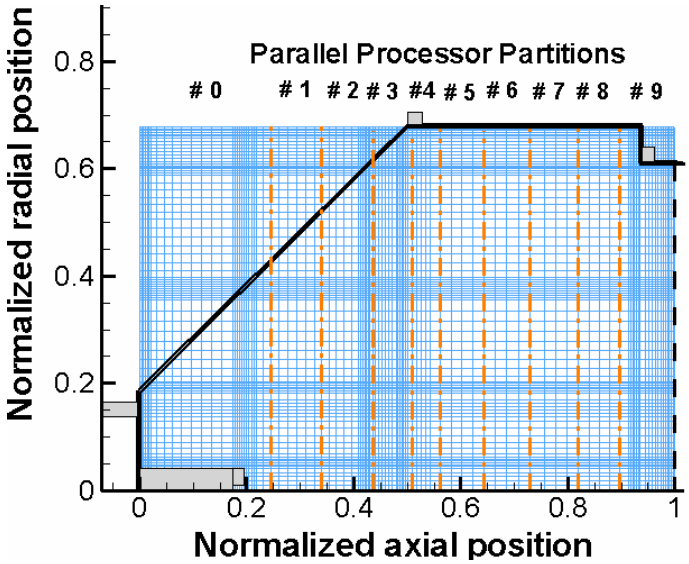

Figure 4.4: Non-uniform computational mesh for the NSTAR discharge chamber.

The partition boundaries are selected to maintain load balancing between the processors as much as possible. This is a problem because the number of particles in each region is changing as the computation progresses. Dynamic load balancing is not used in this work. Also, the partitioning boundary selection is limited by the requirement of 5 axial grid points in any processor region.

Figure 4.5 shows the uniform computational mesh considered for postprocessing of the particle distribution results. The number of grid points in the axial direction is 50 and the number of grid points in the radial direction is 30. All cases considered during the convergence study utilize this uniform computational mesh to obtain post processed particle number density results.

It should be mentioned that the convergence of one numerical parameter is not independent of the other numerical parameters. There are some coupling between W_{macro} and $\tilde{\Delta}$, and between Δt and $\tilde{\Delta}$. For this reason an iterative procedure was used to zero in on reasonable values for W_{macro}, Δt, and $\tilde{\Delta}$. The fourth numerical parameter, the number of iterations required to obtain a converged solution, can be looked at as being independent of the other three numerical parameters. Convergence of this numerical parameter can be determined by looking at a plot of the beam or discharge current as a function of the iteration number. When the beam current is determined

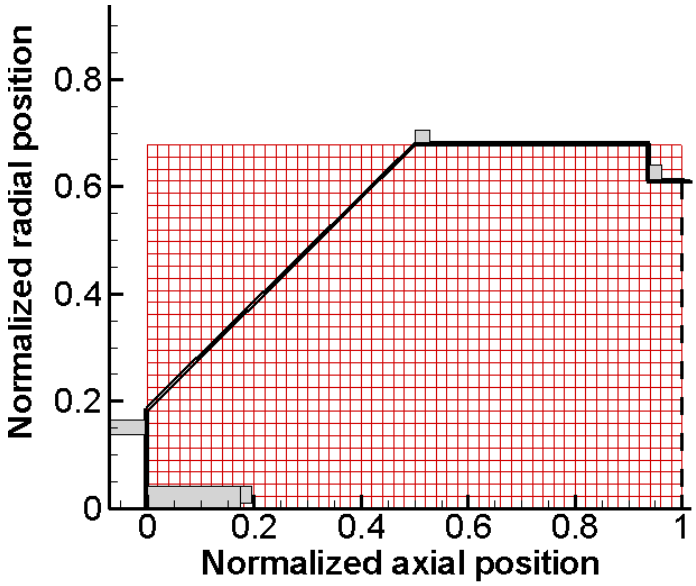

Figure 4.5: Uniform computational mesh considered for computing the particle number density results.

to be relatively constant with iteration number, the solution is declared converged regards to this numerical parameter. So that the reader can make better decisions regards to the convergence study done, the chosen converged values for W_{macro}, Δt, and $\tilde{\Delta}$ are given here:

N_{grid}=8383,

W_{macro}=1.25×10^{11}, and

Δt_e=5×10^{-10} s.

A value is not given for the number of iterations numerical parameter in the above list because this number is a function of the initial particle distribution profile used in the PIC-MCC simulation. A ballpark number can be taken to be 5 million iterations. Before talking about the number of iterations convergence parameter, the initial guesses at the particle distributions are discussed.

4.2.1 Different Starting Points

In the particle based simulations, the convergence of a simulation can be accelerated to reach steady state if the discharge chamber computational domain is initialized with a distribution of particles. This initial particle distribution can be in any one of the following cases:

1. a precomputed distribution is used for the neutral particles, while all other particles have a number density of zero throughout the discharge chamber,
2. a uniform distribution of all particles (electrons, ions and neutrals) throughout the discharge chamber, or
3. a particle distribution can be taken from a previous run of the PIC-MCC simulation.

This is not a complete list of possible initial guesses of particle distributions, but it does provide three viable options.

No matter what initial particle distributions are chosen for the PIC-MCC simulation, the final steady state solution should be the same. Because of the possibilities of different initial particle distributions, steady state results are the focus of this work. The transient results from this PIC-MCC simulation are a function of the starting point. Of the 3 initial starting points listed above the first is the most realistic. All three of these initial distribution have been used in this work and the PIC-MCC simulation has marched towards the same steady state solution for all three cases. The third case listed above is the one used the most often in this work.

For initial starting condition case one listed above a stand alone neutral particle simulation is required. This can be done with the PIC-MCC simulation developed for this work. These results are shown in Figure 4.6. This plot shows the convergence of the total neutral particles with respect to the simulation time. Both axes in Figure 4.6 are given in logarithmic scales. A particle's transit time inside the discharge chamber is defined as the life time of the particle from its creation to its destruction. The neutral transit time inside the discharge chamber is longer when compared to the transit time of other particles due to its zero charge and heavier mass. Figure 4.6 shows the

long neutral transit time to reach a steady state solution. The steady state solution of a neutral particle is observed when the simulation is at > 0.1 s where the solution is converged within 2%. The number of iterations to reach a simulation time of 0.1 s using $\Delta t_{Xe} = 5 \times 10^{-6}$ s is 20,000 and the required CPU time for this simulation is less than 1 hr on a single processor. If this is compared to a full particle simulation with $\Delta t_e = 5 \times 10^{-10}$ s, then the total number of iterations required for convergence becomes 200×10^6. The CPU time required in a full particle simulation to reach 5×10^6 iterations for a particle weight of 1.25×10^{11} is 91 hours on ten processors. At this rate, the CPU time to perform 200×10^6 iterations is upward of a half a year on ten processors. This is a very long computational time and is not practical.

A larger neutral time step value, $\Delta t_{Xe} = 5 \times 10^{-6}$ s, is selected for the neutral alone simulation to reduce the computational time. This neutral time step is 50 times bigger than the neutral time step applied during the full particle discharge chamber simulation. The neutral alone particle simulation can adapt to a large time step, because there are no particle kinetics inside the discharge chamber. From experience [Mahalingam and Menart 2007b], the pure neutral solution uses a 25% flow rate instead of a 100% or a 50%. It was found that 25% neutral flow rate provides a better initial neutral particle distribution for the full particle simulations as compared to a 100% or a 50% neutral flow. This happens because more neutrals make more ions and which makes the steady state solution of the simulation to be longer.

Two different initial points are considered in this study; that is case 1 and case 3 listed above. Case 1 will be referred to as the SP1 case (Starting Point One case) and case 3 will be referred to as the SP2 case (Starting Point 2 case) The initial particle distribution in the SP1 case is taken to be neutral particles only. The initial distribution in SP1 is obtained by simulating neutrals alone in the discharge chamber at 25% of the NSTAR TH15 flow rate. In the SP2 case the initial particle distribution is taken from the steady state solution obtained from a PIC-MCC simulation and contains initial distributions of all particles. In the SP2 case the discharge chamber domain is initiated with all plasma particle types. Table 4.2 gives the numerical parameters considered in

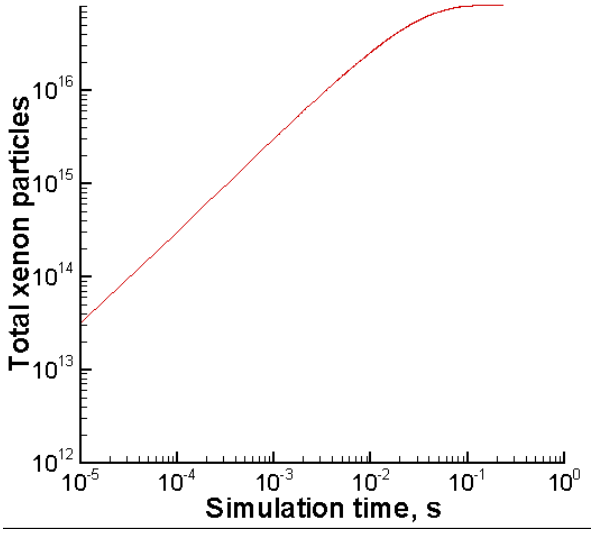

Figure 4.6: Total xenon particle results inside the NSTAR discharge chamber under TH-15 operating condition by assuming neutrals alone in the discharge chamber. Here the neutral flow rate is 25% of the actual flow rate.

the SP1 and SP2 simulations. A subcycling value of 100 is used for advancing Xe^{+} and Xe^{++}, and a subcycling value of 200 is used for advancing the neutral xenon particles. The simulations were performed in parallel on ten processors.

Results showing the independence of the steady state solution from the chosen starting point are shown in Figure 4.7. The horizontal axis shows the number of iterations used, the vertical axis on the left is the beam current, and the vertical axis on the right is the discharge current. Both SP1 and SP2 results converge to the same steady state solution. Less than 2% difference is observed in the results from the two cases. The SP1 case took nearly 3×10^6 iterations to reach convergence in both beam current and discharge current; while the SP2 case has taken less than 0.5×10^6 iterations to reach the same steady state point in beam ion current and discharge current convergence. These results show the independence of starting point on the final results and they show that the number of iterations required to achieve convergence is a function of the initial guess of particle distributions.

Table 4.2: Numerical Parameters considered in the validation of two different starting points.

Description	Details
Computational Mesh	$N_{grid} = 8383$, $N_{cell} = 8200$ (see Figure 4.4)
Δt_e	5×10^{-10} s
Δt_{ion}	5×10^{-8} s
Δt_{Xe}	1×10^{-7} s
W_{macro}	$1{\times}10^{12}$ physical particles
Parallel Processing	Ten processors

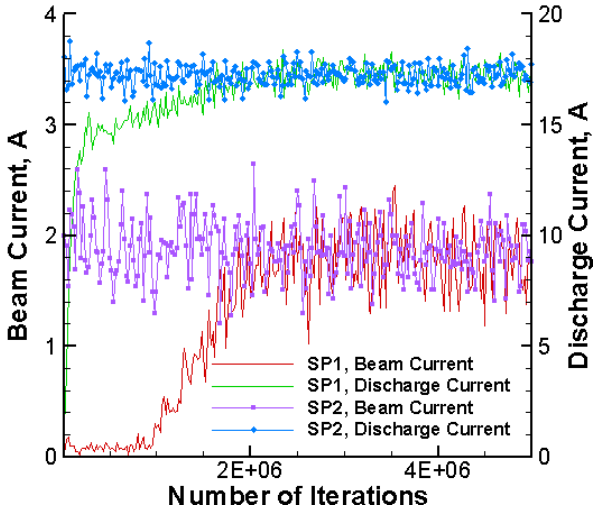

Figure 4.7: Comparisons of beam and discharge current results vs number of iterations for the two different starting point cases.

4.2.2 Iteration Convergence

In this section the following results are plotted versus iteration number to demonstrate a converged or steady state solution of the NSTAR, for the TH-15 operating condition: total particles inside the discharge chamber, average kinetic energy of the plasma particles, discharge current, beam current, and propellant utilization efficiency. This simulation is called the base case of this work. The numerical parameters used in this simulation are the chosen values shown at the introduction of this section. More detailed results for the base case are presented in the next chapter.

Figure 4.8(a) shows the total number of Xe, Xe^{+}, Xe^{++}, primary electrons, and secondary electrons in the discharge chamber as a function of the number of iterations used by the PIC-MCC

simulation. A previous PIC-MCC solution is used as an initial guess of the particle distributions for this case. From Figure 4.8(a) it can be seen that the simulation has achieved a steady state condition in which the solution converged within 5%. All the charge particles plotted in Figure 4.8(a) show this. The total number of iterations for which the particles are tracked is about 100 million.

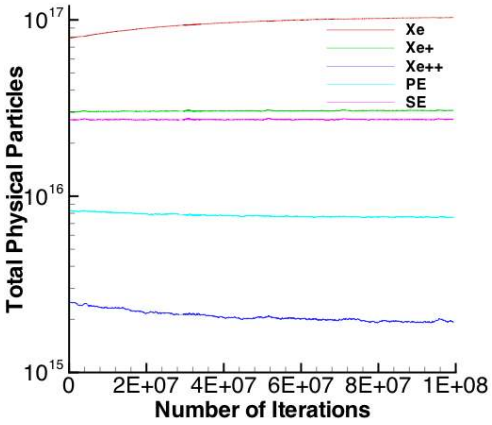

(a) Total physical particles.

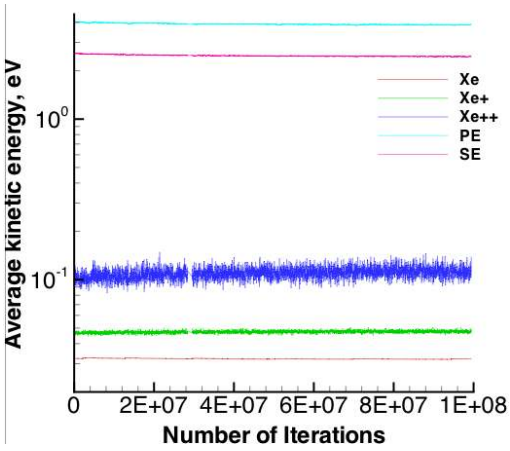

(b) Average kinetic energy.

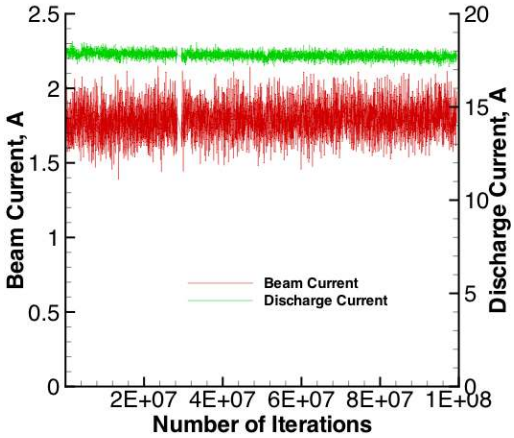

(c) Beam current and discharge current.

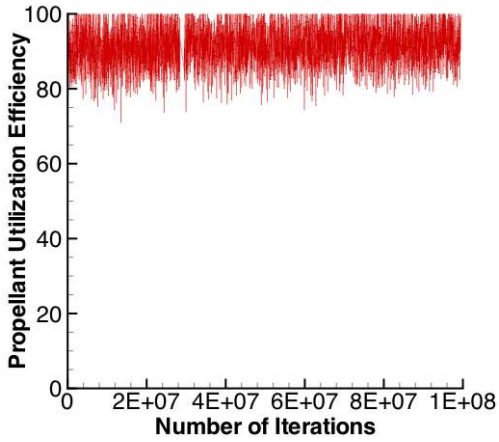

(d) Propellant utilization efficiency.

Figure 4.8: Iteration convergence of NSTAR discharge chamber operating under TH-15 throttle level.

The results in Figure 4.8(a) indicate that all charge particles require about 5 million iterations to reach a steady state condition. The high energy primary electrons are the first to reach convergence. The heavier ion particles and the secondary electrons take a long time to reach convergence com-

pared to the primary electrons. The ions and secondary electrons are produced inside the discharge chamber from the ionization collisions of high energy electrons. At every ionization location both species are produced. The results of the secondary electrons and ions are somewhat coupled because the bulk of the secondary electrons in the discharge chamber come from ionization events. The dynamic electric fields also couple the two particle types together. The secondary electrons move faster because of their lower mass and try to move away from the ions. However the dynamic electric field effect pulls the secondary electrons to the ion locations to balance the charge difference. Thus the heavier ions tug on the secondary electrons trying to bring them together.

The neutral particles shown in Figure 4.8(a) takes really many iterations ($\sim$ 80 million) to reach convergence than the number of iterations required for the charge particles to reach converged state. A couple of reasons for this are that the neutrals move slower than the ions and ions tend to be created at many different positions throughout the discharge chamber. On the other hand the bulk of the neutrals have to travel from their source points (emission locations) to the location where a steady state distribution is maintained in the bulk of the discharge chamber. The small changes seen in the neutrals as a function of time is difficult to eliminate. It can be seen that to get the neutral particles to full convergence about 100 million iterations, i.e., 50 milliseconds, is required. The neutral only simulation shown in Figure 4.6 indicates that neutral particles reach convergence in 100 milliseconds. Since the full particle simulations use an initial neutral distribution, steady state is obtained sooner than this. The CPU time taken for the simulation to perform 100 million iterations is nearly 2.5 months.

Figure 4.8(b) shows the average kinetic energy results for all plasma particles inside the discharge chamber as a function of the number of iterations taken by the simulation. All particles show convergence of their average kinetic energy over the entire discharge chamber. As expected the primary electrons have the highest kinetic energy, the secondary electrons the next highest, then Xe^{++}, Xe^{+}, and Xe. Notice that oscillations are seen on the Xe^{++} average kinetic energy results. This is due to the number of computer particles used.

Figure 4.8(c) shows the beam current and discharge current results for the discharge chamber as a function of the number of iterations. Both current results indicate that the simulation has reached steady state. Oscillations can be seen in both current results, but this is due to the number of computational particles used in the simulation. This will be discussed with the particle weight survey results in the next subsection. Figure 4.8(d) shows the discharge chamber propellant utilization efficiency results for the NSTAR discharge chamber as a function of the number of iterations taken by the simulation. The propellant utilization efficiency results show similar behavior as observed in the beam current results shown in Figure 4.8(c).

The iteration convergence criteria used in the PIC-MCC simulations are further illustrated with the comparison of results between two different PIC-MCC simulation cases as given in Figures 4.9(a) - 4.9(d). Figure 4.9 compare the total particles, beam current and discharge current results between the base case and the no Xe excitation case. In the no xe excitation case, the excitation collision between the electron and xenon particles are turned off. More details about the no Xe excitation simulation are given in the next chapter.

Both simulations are initiated from the same starting points and are run until each case reaches it's steady state condition. Figure 4.9(a) shows the iteration convergence for both Xe^{+} and Xe^{++} particles. Unlike the base case, the no Xe excitation case's ion particles convergence require a large number of iterations ($\sim$ 50 million) to achieve a steady state condition. The total Xe^{+} particles in the discharge chamber for the no Xe excitation case rises initially compare to the base case's total Xe^{+} particles during the first 10 million iterations. However this increasing trend of Xe^{+} particles in the no Xe excitation simulation is a transient behavior and the total Xe^{+} particle result changes after 10 million iterations. This happens because of the increased rate of production of Xe^{++} particles in the discharge chamber for the no Xe excitation case. Similarly the iteration convergence results comparison for the total electron particles are given in Figure 4.9(b). The total secondary electron particles convergence has similar trend as observed in the total Xe^{+} ion particle result. Figure 4.9(c) shows the comparison of total Xe particles between the base and the no Xe excitation cases. The

xenon neutrals in the discharge chamber for the no Xe excitation simulation drops more steep for the first 30 million iterations and then the total Xe particles are reaching a steady state condition.

Figure 4.9(d) shows the comparison of discharge and beam current results between the base case and the no Xe excitation case. The convergence of current results for the base case happens within a few million iterations. But the no Xe excitation case's current results trend differs from the base case and the steady state condition can be seen only after 40 million iterations.

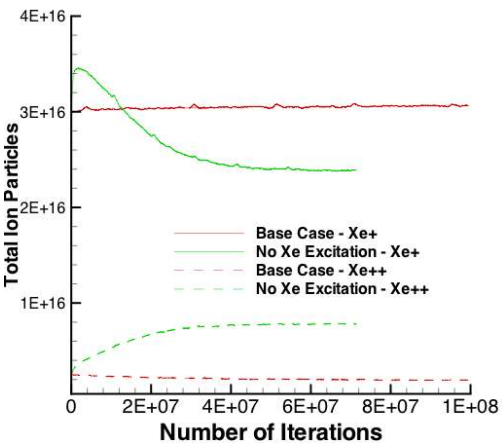

(a) Total ion particles.

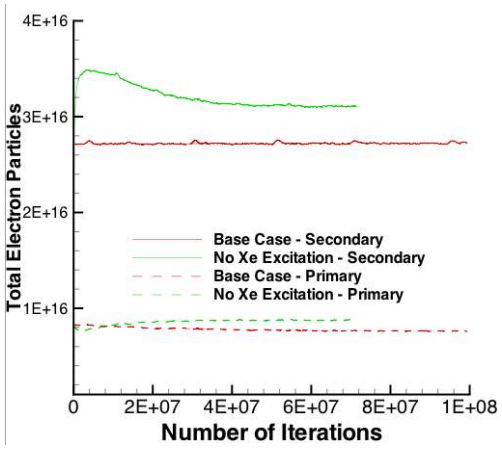

(b) Total electron particles.

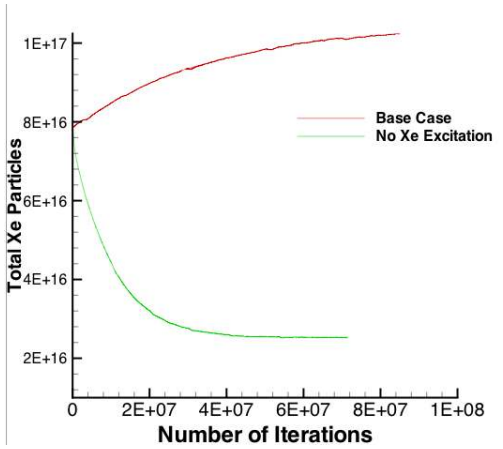

(c) Total xenon particles.

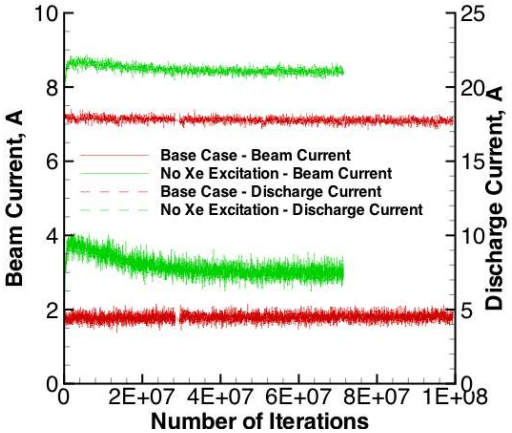

(d) Beam current and discharge current.

Figure 4.9: Comparison results of iteration convergence for two different NSTAR discharge chamber simulations.

4.2.3 Computer Particle Weight

The computer particle weight is a critical parameter in a PIC-MCC simulation. The weight assignment to each particle type determines the number of computer particles used in the simulation. A statistically large number of computer particles has to be used in the simulation to minimize variations in the results. These variations have been seen in prior results presented in this section, see Figure 4.7, Figure 4.8(b), Figure 4.8(c), and Figure 4.8(d). The problem with using too many computer particles in the simulation is the increased computational time.

The statistical noise due to under sampling of the real plasma is an inherent problem in a particle based simulation. The statistical noise scales inversely with the square root of the number of computer particles employed in the simulation [Mardahl 2001]. The statistical noise in the numerical solution produces oscillatory results and a poor representation of the plasma characteristics. In this work a computer particle weight survey is conducted in order to obtain statistically invariant results with particle weighting.

Since all species of particles tracked in this PIC-MCC simulation are assigned the same particle weight only one particle weight needs to be specified in this study. The primary electrons have the same particle weighting as the neutrals which have the same particle weighting as the secondary electrons, the first ions, and the second ions. This simplifies the tracking of the computer particles inside the discharge chamber; especially the handling of the removal of heavy particles and electrons because of inelastic collision processes.

Another means used to quantify the statistical nature of the number of computational particles used in the simulation is the average number of computer electron particles per computational cell, $N_{e,cell}$. The value of $N_{e,cell}$ is given by the ratio of the total number of computer electron particles to the total number of computational cells. A larger particle weight reduces the total number of computer electron particles in the simulation, and also reduces the $N_{e,cell}$ value. A smaller $N_{e,cell}$ increases numerical heating effects. To reduce numerical heating, a $N_{e,cell}$ value of 25-100

[Bruhwiler 2005] is recommended. The two-dimensional PIC simulation study performed by Marek et al.[2005] on a DC magnetron suggests that 10-50 computer particles per cell are required to obtain a statistically invariant result. In this work, along with the survey of the computer particle weight, the $N_{e,cell}$ value is presented.

In the particle weighting survey it is desired to study the computational particle weight assignment from a larger value to a smaller value until a statistically invariant result is observed. In a DC Magnetron, PIC simulations done by Kolev et al. [2005] have considered doubling the number of computer particles to control the statistical noise. They did not show more than two particle weightings. In this work six particle weighting cases are tested and presented. Both global current quantities and particle distribution plots are presented. The six cases show the particle weighting being continually doublw10wed. The convergence of the current results with an increasing number of computer particles is shown. This process is performed iteratively with a smaller weighting in each subsequent step. The steps followed in the particle weighting survey are:

1. The process is begun by considering a simulation with a large particle weight value, 4×10^{12}. The starting point for this weighting value is an initial distribution of neutrals in the discharge chamber.

2. Using this initial neutral distribution, the discharge chamber simulation is performed until a steady state solution is found. The steady state solution is determined based on the iterative convergence of the beam current and discharge current. Once a steady state solution is found, the simulation is stopped. A minimum of 2.5×10^{6} iterations is used in every run.

3. At steady state value of the beam current and the discharge current are obtained. The computed beam current and discharge current results oscillate with respect to the number of iterations so an average value over several iterations in the steady state realm is obtained.

4. The converged results from the higher particle weighting case are used as inputs to the next lower particle weighting case. To cut the computational particle weighting each computer particle in

the discharge chamber is assigned $\frac{1}{2}$ of its particle weight.

5. The discharge chamber simulation is performed again using this new particle distribution with a lower particle weight. The simulation is conducted until iterative convergence of the beam and discharge current is obtained.

6. Steps 3 to 5 are repeated until convergence of the current results are found with respect to a shrinking particle weight value.

The numerical parameters utilized in the particle weight survey are given in Table 4.2. A computer particle weight value of 4×10^{12} is taken as the initial choice of W_{macro}. Considering larger weight values like 8×10^{12} and 16×10^{12} was found to be problematic as excessive depletion of the neutrals occurred. For larger weight assignments, the $N_{e,cell}$ value is small.

The steady state neutral particle distribution of $W_{macro} = 4\times10^{12}$ shown in Figure 4.10 is utilized as the starting point of the particle weight survey. This distribution has a maximum neutral particle number density value of ($> 5\times10^{19}$ m^{-3}) at the cathode exit. The bulk of the discharge chamber neutral number density is found to be greater than 5×10^{18} m^{-3}. Along the thruster centerline the number density values are found to be high compared to the bulk of the discharge chamber. This is mainly because of the axial flow of neutrals through the cathode supply and also due to the higher noise near the axis of symmetry [Verboncoeur 2001]. The volume averaged neutral number density is calculated to be 6.64×10^{18} m^{-3}.

Steps 2 through 6 of the particle weight survey are performed with the following particle weight values : 4×10^{12}, 2×10^{12}, 1×10^{12}, 5×10^{11}, 2.5×10^{11}, and 1.25×10^{11}. Figure 4.11 shows both the steady state averaged beam current and discharge current results for the six different particle weighting cases. The beam current results show a clear convergence with successive test cases when the particle weight is lowered below 1×10^{12}; the discharge current shows a small dip and rise with respect to lowering the particle weight. The discharge current results are found to have a 1% difference between two successive particle weight values for the particle weight below 1×10^{12}.

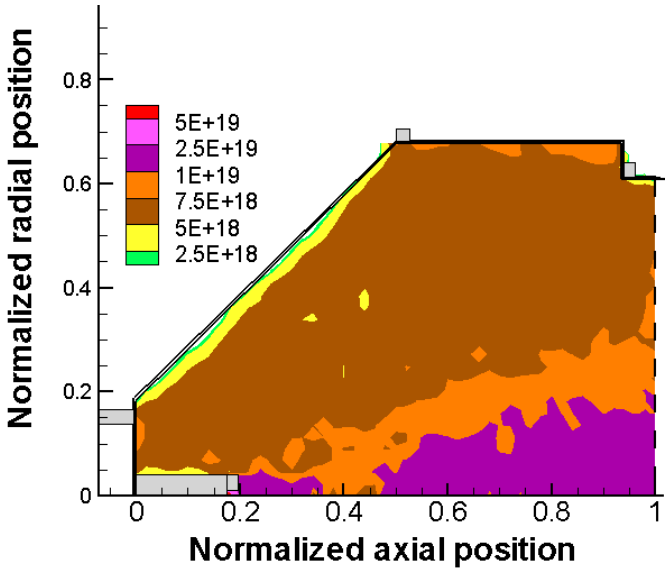

Figure 4.10: The neutral xenon number density contours in m^{-3} at steady state for the NSTAR discharge chamber under TH-15 operating condition. Here the simulation considered neutrals alone in the discharge chamber.

Besides convergence of the beam and discharge currents as a function of particle weight, it is also desired to minimize the numerical noise in the final results. This can be studied by looking at the standard deviation of the current results for the different particle weight cases. The standard deviation of the current indicates the magnitude of the oscillations in the steady state current data. Figure 4.12 shows the standard deviation results with different particle weight values for both the beam current and discharge current. Both of these currents show a clear reduction in the standard deviation with decreasing particle weight. Figure 4.12 is a clear indication of improvement in the solutions when the number of computer particles is increased. In Mardahl's PIC convergence study on a one-dimensional problem [2001] it is stated that the numerical noise scales inversely with the square root of the number of computer particles employed in the simulation:

$$Noise = \frac{Noise_c}{\sqrt{N_{cp}}}. \tag{4.1}$$

where $Noise_c$ is a constant of proportionality. The standard deviation results can be viewed as the quantitative representation of the statistical noise in the solution. Hence we can make use of the

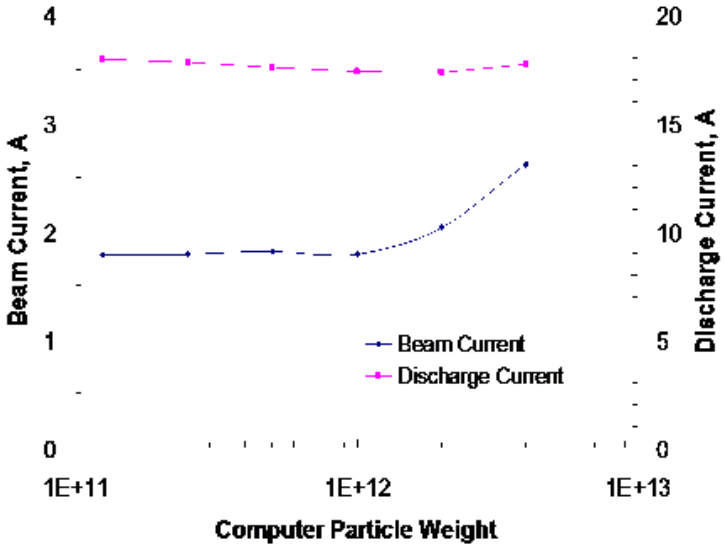

Figure 4.11: Particle Weight Convergence.

computed standard deviation results to validate the above statistical noise equation. Since the total number of computer particles in this particle survey is doubled in sequence, the standard deviation at each lower particle weighting should be reduced by a factor of 1 over the $\sqrt{2}$. This is what is done in Figure 4.12. The results from Equation (4.1)are plotted as dashed lines in Figure 4.12. These dashed lines show excellent agreement with the PIC-MCC simulation results. The particle weight results presented here agree with the statistical noise equation.

The convergence of particle weight is further demonstrated by comparing the particle distribution results for the six particle weight cases. Figures 4.13-4.17 show the particle number density distribution results at the steady state condition for the particle weights 4×10^{12}, 2×10^{12}, 1×10^{12}, 5×10^{11}, 2.5×10^{11}, and 1.25×10^{11}. The particle number density results are given in the units of m^{-3}. In all particle number density distribution results, the magnetic vector potential contour lines are superimposed to show the magnetic field.

By comparing the Xe^+ number density results given in Figures 4.13(a)-4.13(f), it can be seen that the number density fluctuations become less with decreasing particle weighting. The Xe^+

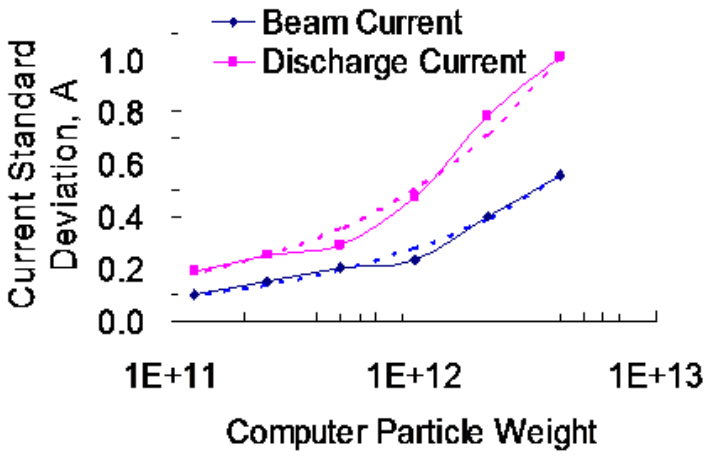

Figure 4.12: Standard deviation results vs particle weight for both beam current and discharge current. The dashed lines on this plot represents the $1/\sqrt{N_{cp}}$ curve.

number density contour lines for the particle weight 1.25×10^{11} are found to be much smoother and continuous than a particle weighting of 4×10^{12}. Near thruster centerline the Xe^{+} number density values are found to be fluctuating for all particle weight cases. Along thruster the centerline the control volume size shrinks because of the smaller r values at the centerline of a cylindrical coordinate system. This shrinking in cell size results in fewer computational particles per cell. In addition first ions are depleted because they are being turned into second ions. Fewer first ions along the centerline means more statistical noise in the first ion number density results.

Comparisons of Xe^{++} number density results are given in Figures 4.14(a)-4.14(f). At the largest particle weight, 4×10^{12}, the Xe^{++} particle is found to be greatly under represented. Figure 4.14(a) shows the sparse representation of the Xe^{++} number density results at a particle weight of 4×10^{12}. The sparse distribution of Xe^{++} number density results can also be seen for the next three lower particle weights such as 2×10^{12}, 1×10^{12}, and 5×10^{11}. Even though the first two particle weight cases show the higher Xe^{++} number density regions along the thruster centerline and at the exit

of the cathode keeper assembly (see Figures 4.14(a)-4.14(b)) a much better representation of these regions can be seen when the particle weight is lowered below 2×10^{12}. Since the Xe^{++} particle is the least populated species inside the discharge chamber it is difficult to obtain a smooth density distribution. The Xe^{++} number density contour lines for the particle weight 1.25×10^{11} case are good at most locations.

The primary electron number density results for the six different particle weight cases are given in Figures 4.15(a)-4.15(f). Followed by the Xe^{++}, the primary electrons are the next least populated species inside the discharge chamber. Thus a better representation of the primary electron number density results can be seen at the smallest particle weighting cases. Large number density fluctuations and sparse representation of the primary electron distribution can be seen at the particle weights 4×10^{12} and 2×10^{12}. The primary electron number density contour lines get smoother and smoother with increasing number of computer particles (i.e., by reducing the particle weight). Next to the slanted wall, near the back wall magnet the primary electron number density values are below 1×10^{16} m^{-3}. This occurs because the strong magnetic field lines do not allow electrons into this region. Even with the lowest particle weighting used, 1.25×10^{11}, these regions can not be resolved. To capture details at such small particle densities, a much smaller particle weighting has to be used. CPU time restricts this from happening.

The contour plot of secondary electrons given in Figures 4.16(a)-4.16(f) show similar convergence trends as Xe^{+} (note different scales are used on the secondary electron plots and the Xe^{+} plots). As with all the charge particle density results, the results get much smoother when the particle weight is reduced from 4×10^{12} to 1.25×10^{11} with the 1.25×10^{11} weighting results looking quite good. The comparisons between the 2.5×10^{11} to 1.25×10^{11} results are basically similar.

Comparisons of the neutral xenon number density results are given in Figures 4.17(a)-4.17(f). As with the charge particle plots, neutral xenon also exhibits that the number density fluctuations become less with lower particle weights. For larger particle weights, 4×10^{12} and 2×10^{12}, the neutrals are found to be depleted along the thruster centerline. This depletion reduces with decreasing particle

weighting. The number density results of the 2.5×10^{11} and 1.25×10^{11} cases appear to be similar, except the number density contour lines look smoother at the 1.25×10^{11} particle weighting case.

Figure 4.18 compares the heavy particle distributions, Xe^{+}, Xe^{++}, and Xe, at the steady state condition for the largest particle weight 4×10^{12} and the smallest particle weight 1.25×10^{11}. Similarly the comparisons of electron particle distributions for the largest and the smallest particle weight cases are given in Figure 4.19. All dots shown in Figures 4.18 and 4.19 represent one computer particle. The total number of computer particles present inside the discharge chamber for both particle weight cases at the steady state condition are listed in Table 4.3. The dot plots and tabulated results give a dramatic demonstration of the differences in particles between the 4×10^{12} and the 1.25×10^{11} weighting case. They also emphasize that even with the smallest particle weight there are some regions, such as the high magnetic field, near the wall sheath, and grid sheath where the charge particles are found to be under represented. Because these regions are found to be less populated, and the difference in number density values in these regions could be 3 to 4 orders of magnitude smaller than the number density values observed for the bulk plasma inside the discharge chamber, there is more noise. This is quantitatively demonstrated in the particle number density plots displayed earlier; however, Figures 4.18 and 4.19 and Table 4.3 provide a computational particle perspective.

Figure 4.18(f) shows that the neutrals are found to be sparse along the thruster centerline, even with the lowest particle weight case. Experimental measurements indicate that the relative neutral number density values near the thruster centerline are two orders magnitude less than the interior of the discharge chamber (for radial locations greater than 0.13 nondimensional units) [Sengupta et al. 2006; Sengupta et al. 2004]. Along the thruster centerline a higher rate of ionizing collisions of neutrals occurs because of the high energy primary electrons emitted from the cathode tip. The PIC-MCC model is predicting that the centerline region is deficient in neutral particles.

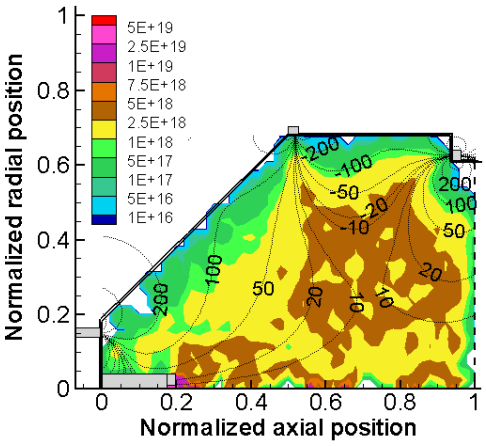

(a) Weight=4×10^{12}.

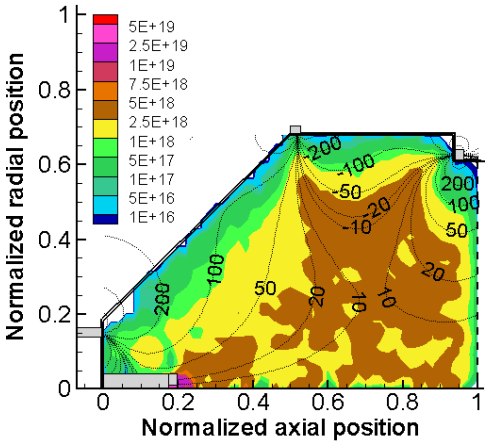

(b) Weight=2×10^{12}.

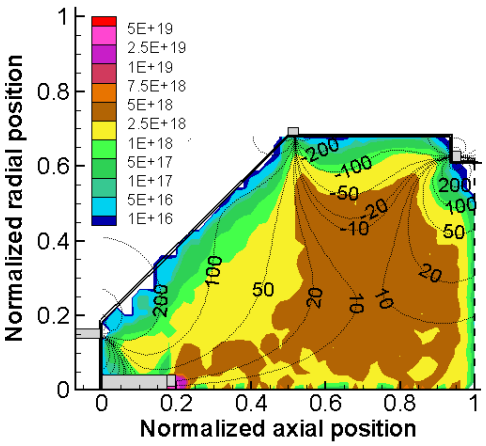

(c) Weight=1×10^{12}.

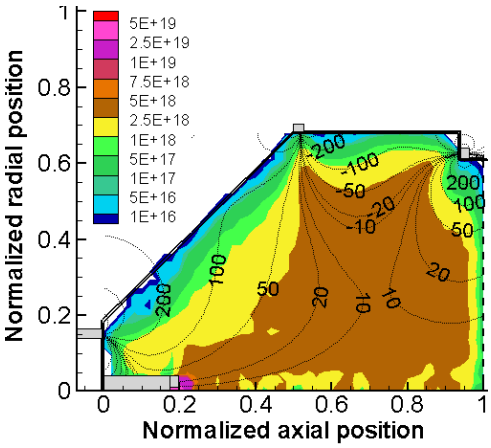

(d) Weight=5×10^{11}.

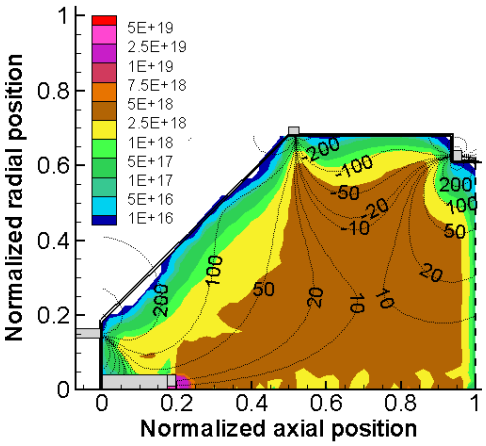

(e) Weight=2.5×10^{11}.

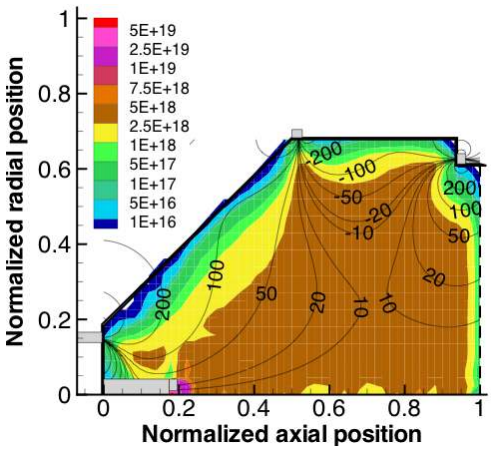

(f) Weight=1.25×10^{11}.

Figure 4.13: Comparisons of Xe^+ particle number density results in m^{-3} for the six different particle weight cases.

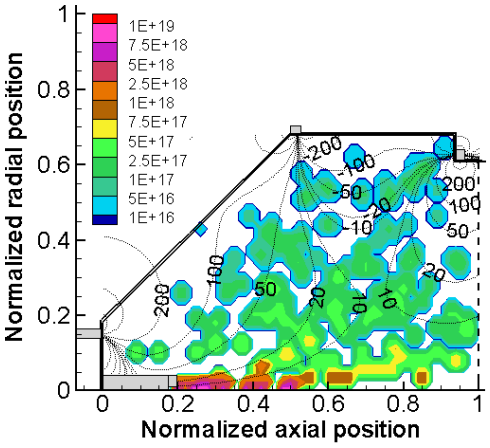

(a) Weight=4×10^{12}.

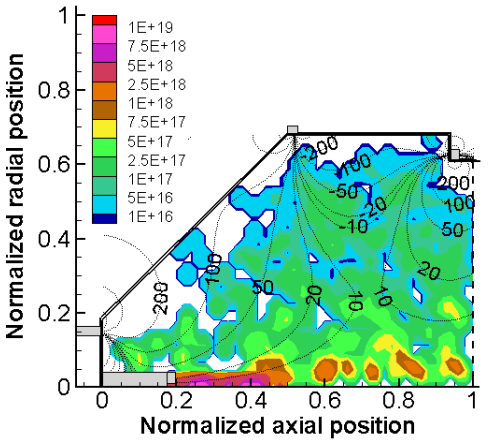

(b) Weight=2×10^{12}.

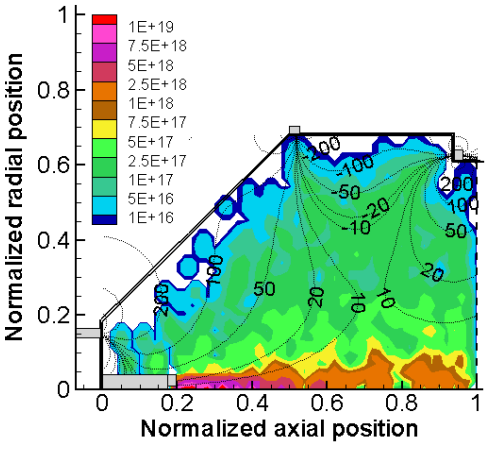

(c) Weight=1×10^{12}.

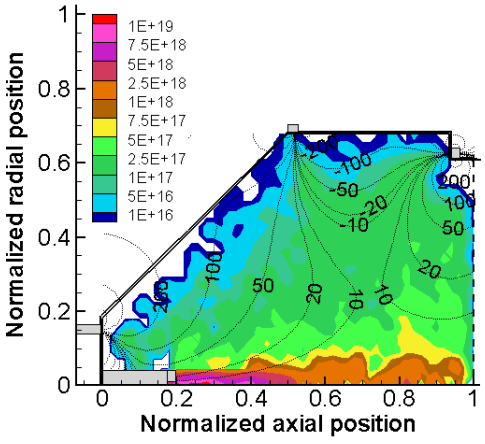

(d) Weight=5×10^{11}.

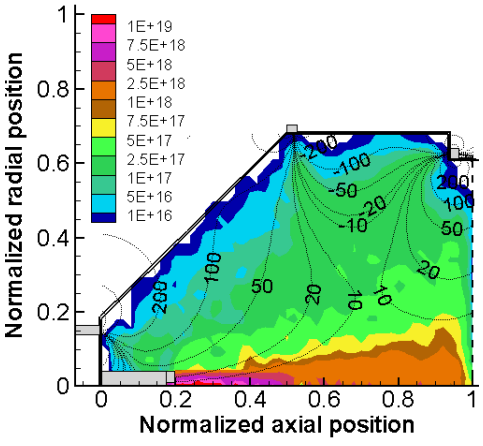

(e) Weight=2.5×10^{11}.

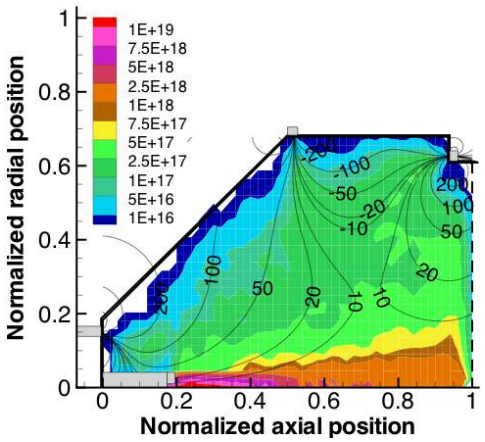

(f) Weight=1.25×10^{11}.

Figure 4.14: Comparisons of Xe^{++} particle number density in m^{-3} for the six different particle weight cases.

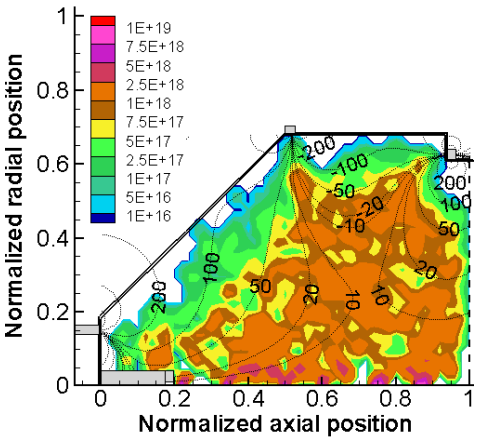

(a) Weight=4×10^{12}.

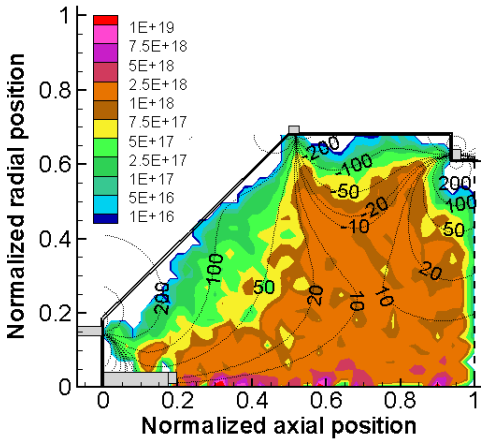

(b) Weight=2×10^{12}.

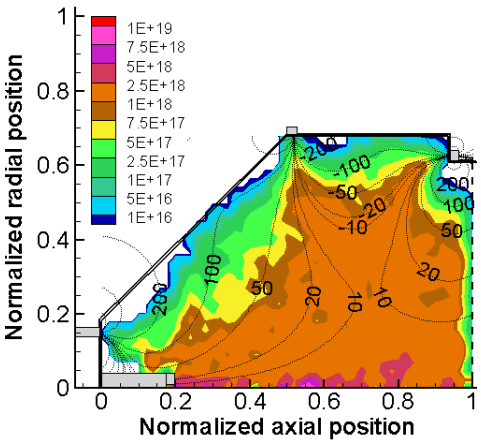

(c) Weight=1×10^{12}.

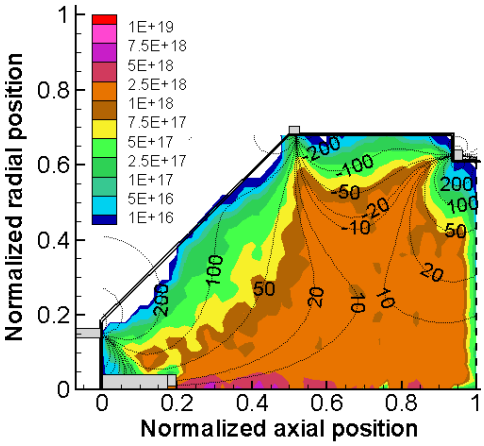

(d) Weight=5×10^{11}.

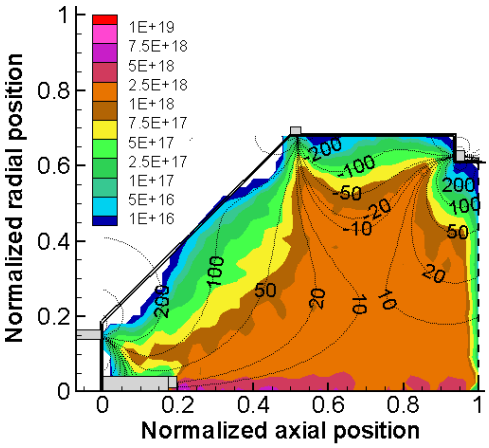

(e) Weight=2.5×10^{11}.

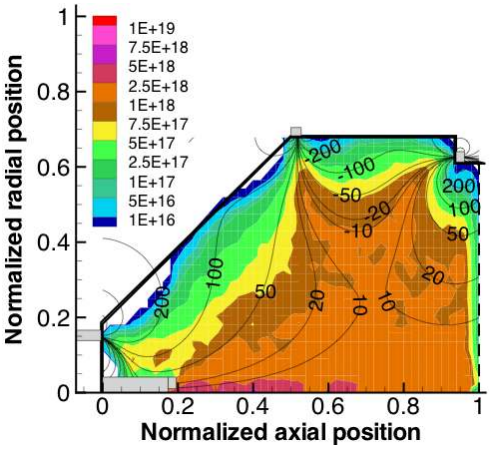

(f) Weight=1.25×10^{11}.

Figure 4.15: Comparisons of primary electron particle number density in m^{-3} for the six different particle weight cases.

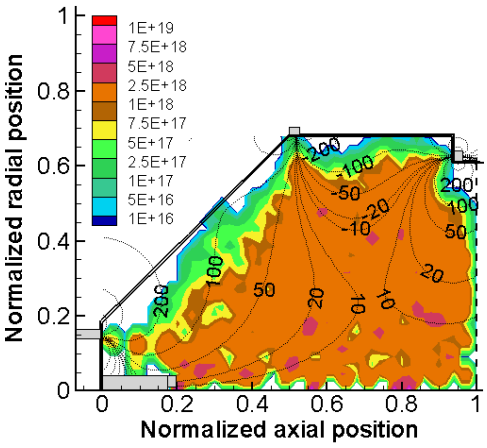

(a) Weight=4×10^{12}.

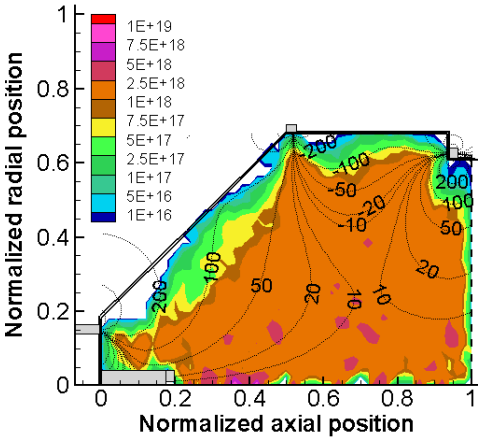

(b) Weight=2×10^{12}.

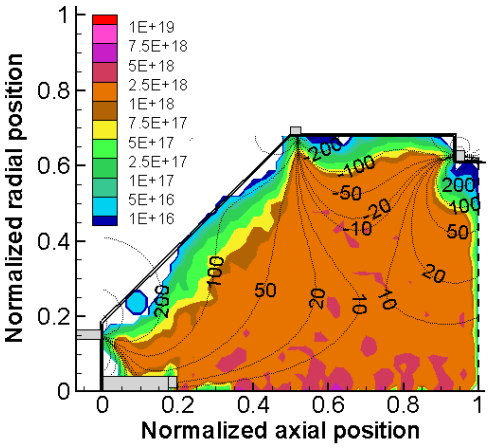

(c) Weight=1×10^{12}.

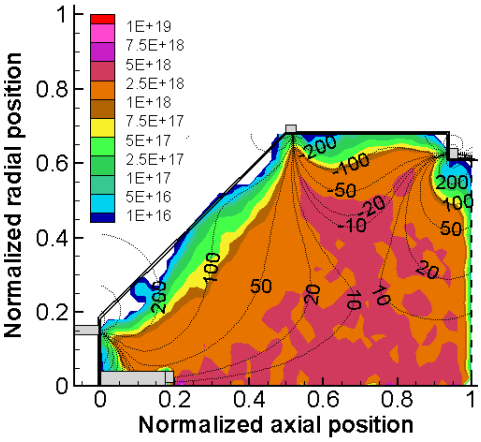

(d) Weight=5×10^{11}.

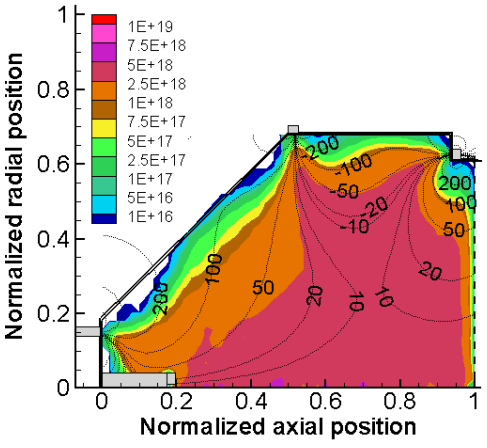

(e) Weight=2.5×10^{11}.

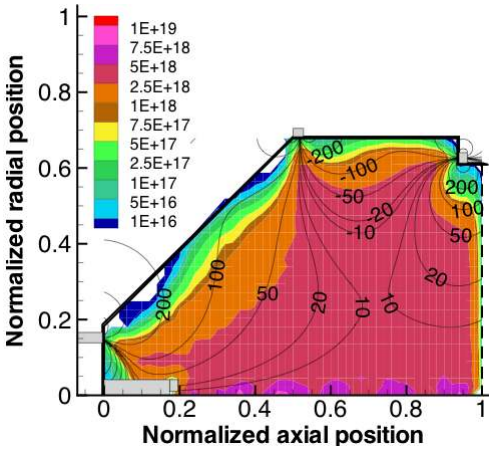

(f) Weight=1.25×10^{11}.

Figure 4.16: Comparisons of secondary electron particle number density in m^{-3} for the six different particle weight cases.

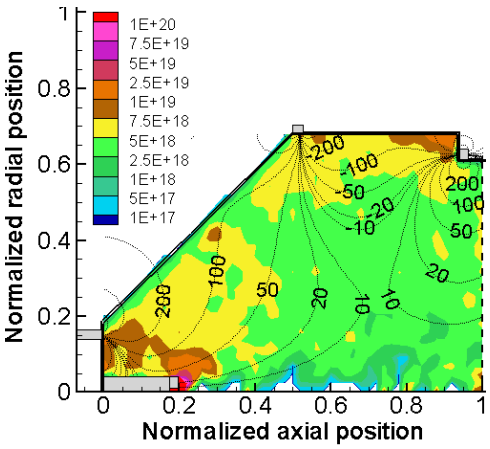

(a) Weight = 4×10^{12}.

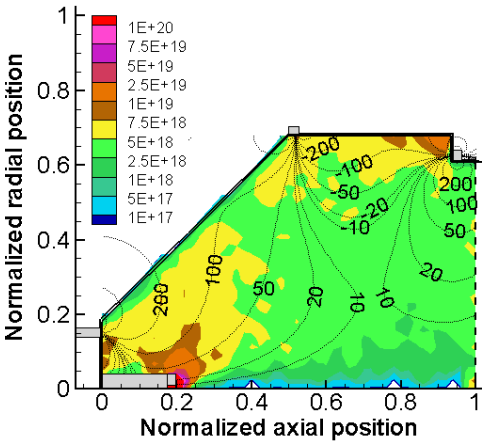

(b) Weight = 2×10^{12}.

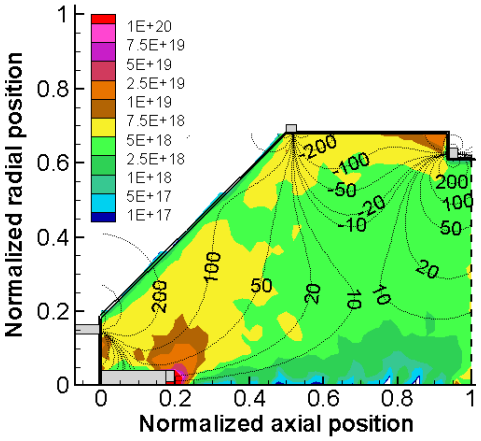

(c) Weight = 1×10^{12}.

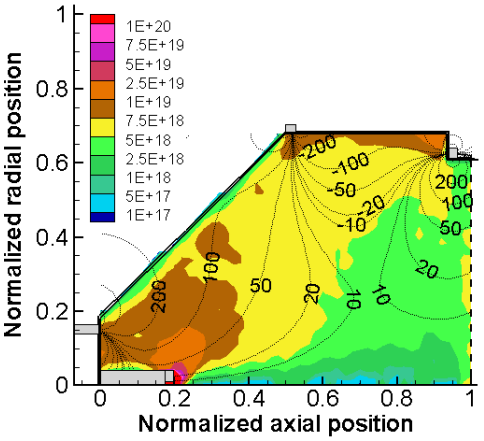

(d) Weight = 5×10^{11}.

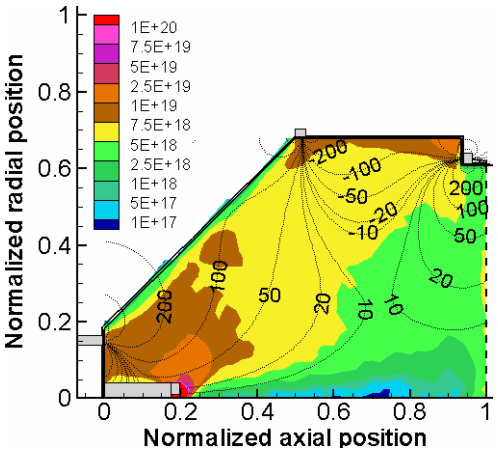

(e) Weight = 2.5×10^{11}.

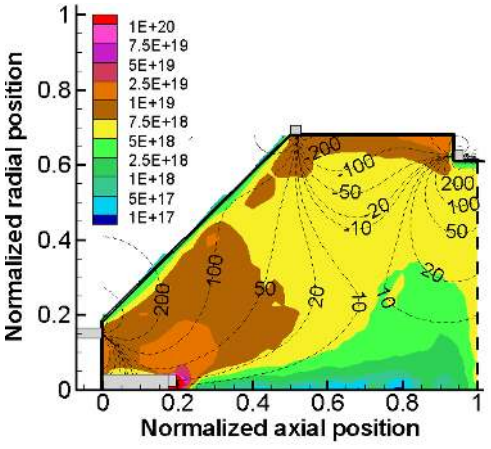

(f) Weight = 1.25×10^{11}.

Figure 4.17: Comparisons of Xe particle number density in m^{-3} for the six different particle weight cases. Figure (f) plot is taken many iterations before its steady state condition and this is followed for matching all particle weight cases Xe density plots to be compared at the same iteration level.

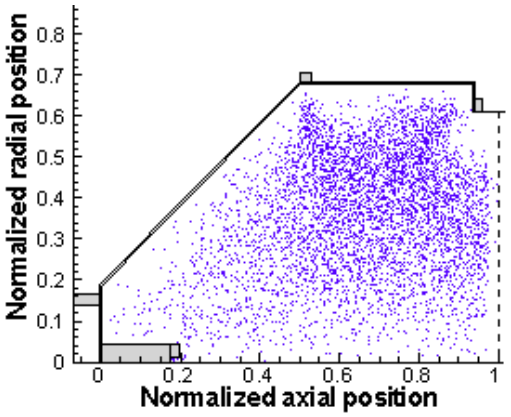

(a) Weight = 4×10^{12}, Xe^{+}.

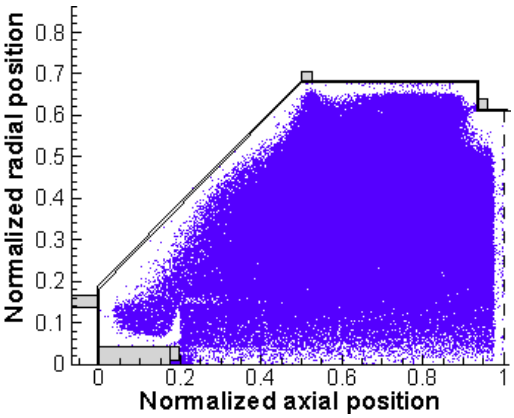

(b) Weight = 1.25×10^{11}, Xe^{+}.

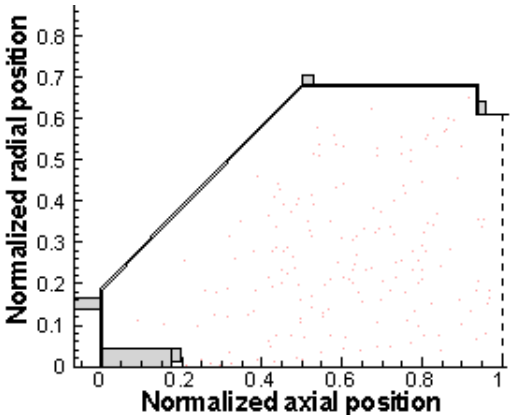

(c) Weight = 4×10^{12}, Xe^{++}.

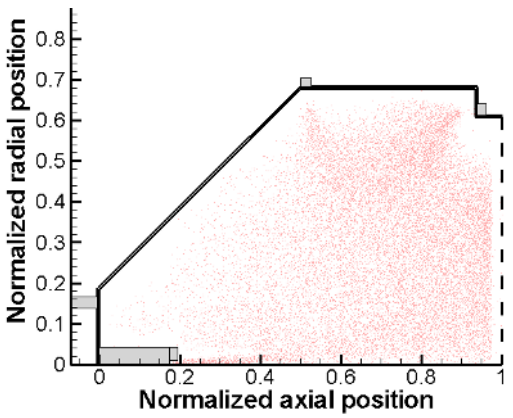

(d) Weight = 1.25×10^{11}, Xe^{++}.

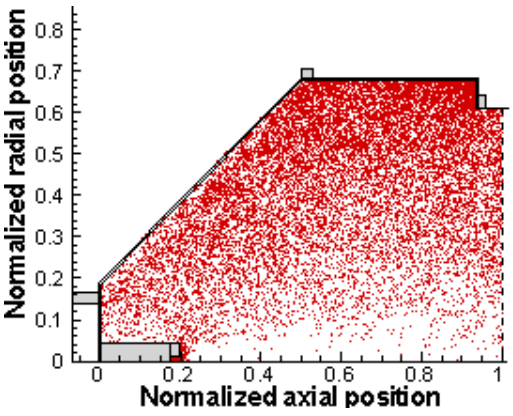

(e) Weight = 4×10^{12}, Xe.

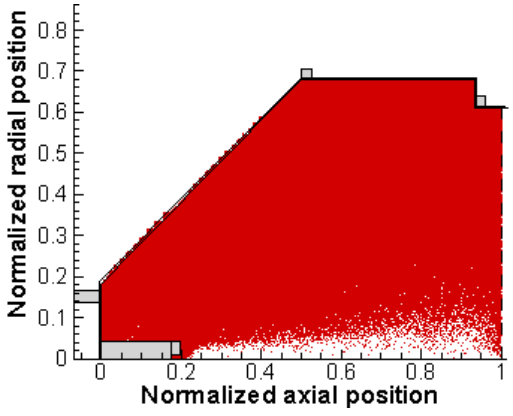

(f) Weight = 1.25×10^{11}, Xe.

Figure 4.18: Comparisons of the heavy particle dot plots for the particle weighting cases of $4{\times}10^{12}$ and $1.25{\times}10^{11}$.

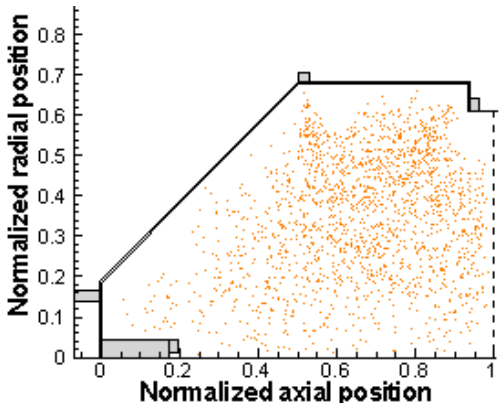

(a) Weight = 4×10^{12}, primary electrons.

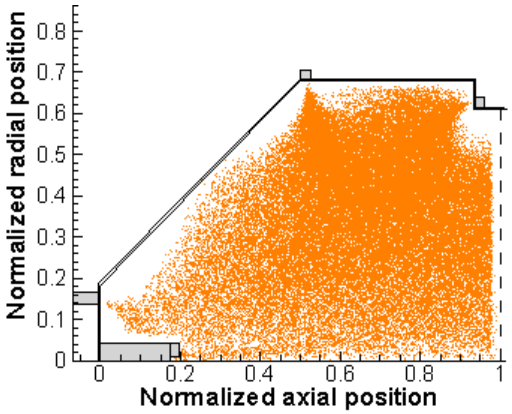

(b) Weight = 1.25×10^{11}, primary electrons.

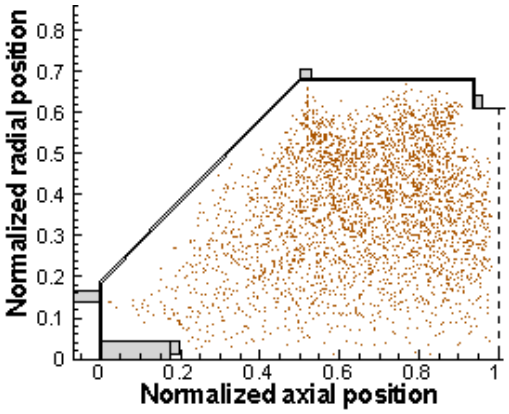

(c) Weight = 4×10^{12}, secondary electrons.

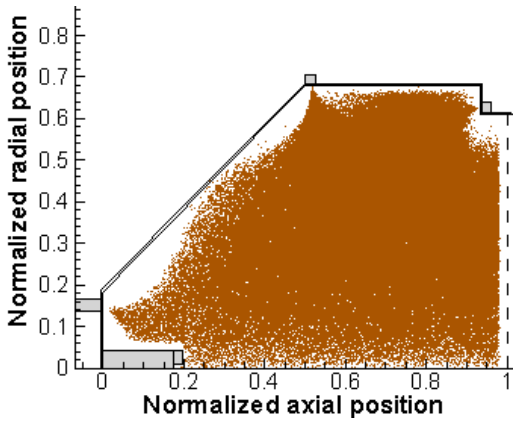

(d) Weight = 1.25×10^{11}, secondary electrons.

Figure 4.19: Comparisons of the electron particle dot plots for the particle weighting cases of $4{\times}10^{12}$ and $1.25{\times}10^{11}$.

Generally in an ion engine discharge chamber, the Xe^{++} and the primary electrons are the least populated species. The use of a larger particle weight for representing these particles poorly samples their distribution inside the discharge chamber. The Xe^{++} particle distribution for the largest particle weight case shows the poorest distribution (see Figure 4.18(c)). This is evident from the total Xe^{++} particle comparisons given in Table 4.3. Two orders of magnitude difference is seen between the total Xe^{++} computer particle results between the largest particle weight case and the smallest particle weight case, even though the particle weight ratio differs by 32. The reason for this large difference in the total number of computer Xe^{++} particles is the larger particle weight

Table 4.3: Total number of computer particles in the discharge chamber at the steady state condition for the particle weight cases of $W_{macro} = 4 \times 10^{12}$ and $W_{macro} = 1.25 \times 10^{11}$.

W_{macro}	Xe^{+}	Xe^{++}	Xe	Primary electrons	Secondary electrons	Total
4×10^{12}	4,742	175	15,894	1,796	3,264	21,987
1.25×10^{11}	243,179	17,487	725,450	63,320	217,666	1,267,102

assignment of the primary electrons. The electron threshold energy required to produce a Xe^{++} from a single Xe^{+} is 21.2 eV. The primary electrons are the ones that possess high enough energy to cause these reactions. Using a larger particle weight under samples these high energy electrons. In the smallest particle weight case the number of high energy primary electrons are increased by a factor of 32. This allows much better sampling of high energy electrons. Thus the total number of double ionization reactions increases in the smallest particle weight case causing the population of Xe^{++} to go up.

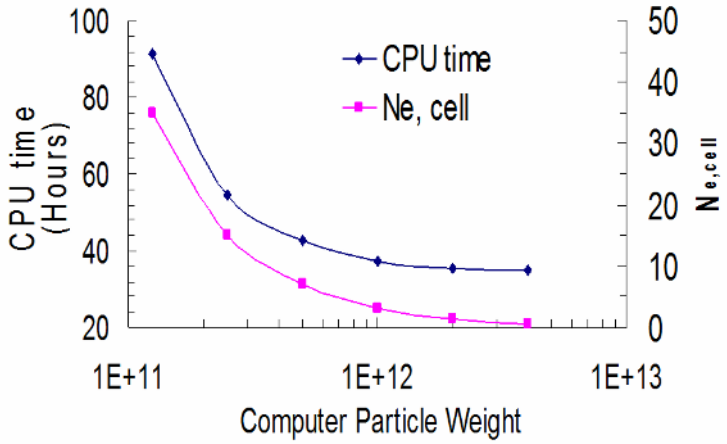

Figure 4.20: The computational run time and the average number of electrons per computational cell results are shown for different particle weight cases. Here the CPU time is the total time taken by the parallel run to finish 5×10^{6} iterations.

Figure 4.20 shows the average number of electrons per computational cell, $N_{e,cell}$, inside the discharge chamber for the six different particle weight cases. The non-uniform mesh used in this simulation has 8200 computational cells. As discussed earlier, to minimize the statistical noise at least 10-50 computer particles per cell are desired. In Figure 4.20, the $N_{e,cell}$ values of the particle

weight cases 4×10^{12}, 2×10^{12}, 1×10^{12}, and 5×10^{11} are found to be less than 10 electron particles per cell. The value of $N_{e,cell}$ for the particle weight 2.5×10^{11} is found to be 15, which is more than twice the $N_{e,cell}$ value of 7.0 for the particle weight 5×10^{11}. At the lowest particle weight, 1.25×10^{11}, the value of $N_{e,cell}$ is found to be $\sim$35. The $N_{e,cell}$ values of both particle weight cases, 2.5×10^{11} and 1.25×10^{11}, satisfy the required number of computer particles per cell in the discharge chamber.

Also shown in Figure 4.20 is the CPU time taken to perform the 5×10^{6} iterations on ten processors. The first three particle weight cases show no significant increase ($< 6\%$) in the computational run time, even when the number of computer particles in the simulation is quadrupled. In a PIC-MCC plasma simulation the computational time is primarily expended in the following two portions of the simulation: particle advance routine and electric field solver. It can be deduced from the comparison of the CPU times for the first 3 particle weight cases that most of the computational time is being spent on the electric field solver. At first three particle weight cases the computation time consumed by the electric field solver is larger than the time spent on the particle advance routine. This is why the CPU time does not change much as the number of computer particles is increased from 50,000 ($W_{macro} = 2 \times 10^{12}$) to 100,000 ($W_{macro} = 1 \times 10^{12}$). This doubling of particles only increases the CPU time by 5.7%. A 14% increase in computational time is observed when the particle weight is changed from 1×10^{12} to 5×10^{11}; and a 28% increase in CPU time is observed when the particle weight is changed from 5×10^{11} to 2.5×10^{11}. The CPU times shown in Figure 4.20 indicates the particle advancing portion of the simulation is becoming more important as the particle weighting decreases.

It is found that with subsequently lower particle weights the computational time rises sharply. A 67% increase in CPU time is found when the particle weight is decreased from 2.5×10^{11} to 1.25×10^{11}. In the 1.25×10^{11} particle weight case, the simulation handles nearly 1.1×10^{6} computer particles. The computational run time to perform 5×10^{6} iterations of the 1.1×10^{6} computer particles is nearly 4 days. This makes the total CPU time for the 1.25×10^{11} particle weight case to be one week on ten processors. The CPU time for the next two lower particle weights not performed in this work,

6.25×10^{10} and 3.125×10^{10}, are estimated to be 2 and 4 weeks respectively.

Based on computer particle convergence study done in this section and the CPU requirement for each particle weighting, a value of 1.25×10^{11} is used as the converged particle weight value in this work.

4.2.4 Time Step Size

The time step size is also found to be a difficult numerical parameter to get converged. Next to the particle weight, a good deal of computational effort was spent on determining the converged time step value. Here the time step refers to Δt_e,the time step used in the electron advancing routine. Since the electrons are the fast moving particles, the selected time step has to resolve the path of the electron travel. In addition, the selected electron time step should ensure that the bulk of the electrons do not cross more than one computational cell in one time step. The ion time step Δt_{ion} and the neutral time step Δt_{Xe} are much bigger than the electron time step size. Ions are subject to the same stability criteria as the electrons; however, because they are much slower the values that come out of the stability criteria for ions are much less severe. Neutral particles on the other hand, are not subject to the same stability criteria as the charge particles. Because of the subcycling, all particle types are in time sync with one another.

Table 4.4 lists the numerical parameters considered in the time step convergence study. Four test cases of electron time steps, 5×10^{-9} s, 1×10^{-9} s, 5×10^{-10} s, 1×10^{-10} s, are considered. Extremely long computational times make it difficult to consider more test cases with time steps below 1×10^{-10} s. The ion and neutral time step sizes are maintained at the same value in these four test cases. Quick convergence studies on these times indicate they are sufficient. A non-uniform computational mesh given in Figure 4.4 is considered for these studies. Each computer particle is set to represent 1×10^{12} physical particles. This particle weight value is larger than our converged particle weight value 1.25×10^{11}. The simulation run time for the lower particle weight case,(1.25×10^{11}), increases computational time by a factor of 3 when compared to the simulation run time for the larger particle

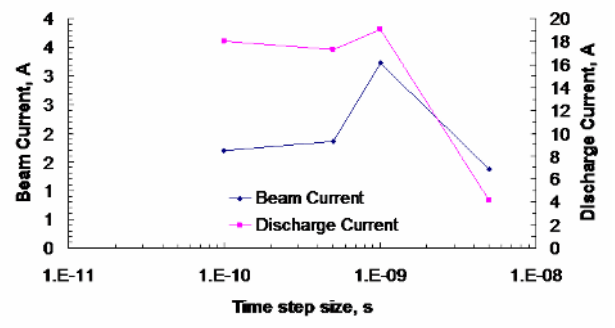

Figure 4.21: Time step convergence.

weight case(see Figure 4.20). To minimize the overall computational run time a compromise is made by using a larger particle weight in the time step study. Since the coupling between the time step size and the particle weight is weak (known from prior particle simulations), there should not be any significant effect on the determination of time step size convergence.

Table 4.4: Numerical parameters used for the different test points considered in the time step convergence study.

Details	Numerical parameter value
Case 1, Δt_e	$5{\times}10^{-9}$ s
Case 2, Δt_e	$1{\times}10^{-9}$ s
Case 3, Δt_e	$5{\times}10^{-10}$ s
Case 4, Δt_e	$1{\times}10^{-10}$ s
Δt_{ion}	$5{\times}10^{-8}$ s
Δt_{Xe}	$1{\times}10^{-7}$ s
Computational Mesh	100x82 Non uniform mesh
W_{macro}	1×10^{12} physical particles

All the cases presented in the time step study are initiated with a predistribution of particles from another simulation. All four time steps tested are initiated with the same starting point. Each test case is run until the simulation reaches a steady state condition. At this point, a steady state, iteration averaged time beam current and discharge current are determined.

Figure 4.21 shows the time step convergence of the steady state beam current and the discharge current. The current results at $\Delta t_e = 5 \times 10^{-9}$ s are found to be off from the actual beam and

discharge current values. The current results show a larger difference between the time steps 5×10^{-9} s and 1×10^{-9} s. The beam current for the time step size 1×10^{-9} s is nearly double that for time step size 5×10^{-9} s. Then the beam current value drops by 42% at the electron time step size 5×10^{-10} s. Further lowering of the time step to 1×10^{-10} shows a drop in the beam current of 8%. These results indicate that the time step size 5×10^{-10} has converged to within about 10%. The discharge current results are found to be oscillatory and the fluctuations become smaller with smaller time step sizes. Due to the long computational times, further validation of the effect of lowering the time step size could not be undertaken. A smaller discharge current is observed for the bigger time step 5×10^{-9} s case due to the increased ion losses to the chamber walls. The average kinetic energy of both Xe^{+} and Xe^{++} are found to be much higher in the bigger time step case, than in the other time step cases.

The thermal speed stability criterion given in Equation (3.125) is applied to the four time steps used in this convergence study. In Equation (3.125) the grid spacing is required to check for the satisfaction of the stability condition. The minimum grid spacing value on the non-uniform computational mesh is 1 mm in the following areas of the discharge chamber: near the wall sheath regions, the cathode source, and at the magnet cusp locations. The bigger electron time step value of 5×10^{-9} s violates Equation (3.125) at these locations for any electron which possess energy above 0.2 eV. The average electron energy in the discharge chamber is experimentally measured to be 2 - 4 eVs. This is close to what is determined in this work as well. Thus the time step value of 5×10^{-9} s will not satisfy the thermal speed criterion for most of the electrons in the discharge chamber. The current results obtained for this time step illustrate this nonobservance of stability condition. The next time step value 1×10^{-9} s is found to be violating the thermal speed criterion in the smaller grid spacing region for any electron that possess more energy than 6 eV. This time step works fine for other regions where the grid spacing is larger. The time step value of 5×10^{-10} s satisfies the thermal speed stability condition over the bulk of the discharge chamber and in the fine grid spacing regions. This time step value becomes a problem in the fine grid spacing region for electrons that

possess energy greater than or equal to 27 eV. The smallest time step value, 1×10^{-10} s, is found to satisfy the thermal speed criteria throughout the discharge chamber for electron energies up to 30 eV.

In addition to current results, the particle number density results are compared as part of the time step convergence study. Figures 4.22-4.26 show the comparisons of the steady state number density results of Xe^{+}, Xe^{++}, primary electrons, secondary electrons, and Xe particles for the four time step cases: 5×10^{-9} s, 1×10^{-9} s, 5×10^{-10} s, and 1×10^{-10} s.

Figure 4.22(a) shows that the bulk of the discharge chamber's ion number density is found to be between 1×10^{17} - 5×10^{17} m^{-3} for the time step case 5×10^{-9} s. This is an order of magnitude lower than the bulk ion number density results seen for the other time step cases. This large depletion of ions happens due to the increased loss of ion particles to the chamber walls. Most of the ion losses are observed at the slanted wall and the side wall of the discharge chamber. The ion number density fluctuations become smoother with smaller electron time step sizes (see Figures 4.22(c) and 4.22(d)).

Figures 4.23(a)-4.23(d) show the comparisons of Xe^{++} number density results for the four different time step cases. A sparse Xe^{++} population is observed in the bigger time step 5×10^{-9} s case. The sparse distribution in Xe^{++} improves with smaller time step sizes. As discussed in the particle weight section, the least populated Xe^{++} requires a much smaller weighting than what we have used in this study. Hence the Xe^{++} particle distributions cannot be expected to be smooth for the particle weight used in this study, 1×10^{12}.

Figures 4.24(a)-4.24(d) show the results of primary electron number density values for the four time step cases. Similarly to the Xe^{++} results, a sparse distribution of primary electrons is observed at the 5×10^{-9} s case. The primary electron number density results at the 1×10^{-9} s case is found to be jagged. The number density fluctuations in the primary electron distribution improve with smaller time step sizes.

Figures 4.25(a)-4.25(d) show comparisons of the secondary electron number density results. Like

other particles, fluctuations in the number density contours are reduced with smaller electron time step sizes. The secondary electron number density results for the time step cases 1×10^{-9} s, 5×10^{-10}, s and 1×10^{-10} s look similar.

Finally comparisons of Xe particle number density results are made in Figures 4.26(a)-4.26(d). The Xe number density values near the slanted wall and side wall regions for the bigger time step case are found to be larger (see Figure 4.26(a)). This happens because of the higher ion recombination at the walls. The neutral depletion has increased inside the discharge chamber for the 1×10^{-9} s case (compare Figures 4.26(b)-4.26(d)). No significant difference is seen between the neutral distribution of the 5×10^{-10} s and the 1×10^{-10} s cases. The thruster centerline neutral number density values for the 1×10^{-10} s case is found to be slightly larger than the 5×10^{-10} s case.

The current and particle distribution comparisons (see Figures 4.21 - 4.26) show no significant difference between the time step size cases 5×10^{-10} s and 1×10^{-10} s. Hence, in this work the 5×10^{-10} s time step is taken as the time step of choice for all of the simulation results shown in the Results section. Selecting a larger time step size helps in terms of the computational run time. This is evident from the comparison of the CPU times for the different time step cases. Figure 4.27 shows the CPU time taken for the four different time step cases to reach a simulation time of 2.5 milliseconds. The bigger time step size of 5×10^{-9} s requires only 0.5×10^{6} iterations to reach the simulation time limit of 2.5 milliseconds. The CPU time for the 5×10^{-9} s case is only 7.5 hours. The next time step, 1×10^{-9} s, takes 20 hours to perform 2.5×10^{6} electron iterations. The 5×10^{-10} s case takes 36.2 hours to perform for 5×10^{6} electron iterations. The CPU time increases nearly twice over that of the case with the time step size lowered by a factor of two. The CPU time for the last test case uses a time step value of 1×10^{-10} s and requires nearly 4.5 times the CPU time as for the 5×10^{-10} s case. It corresponds to 170 hours (>7 days), which is a long computational run time compared to the 36.2 hours run time taken by the 5×10^{-10} s case.

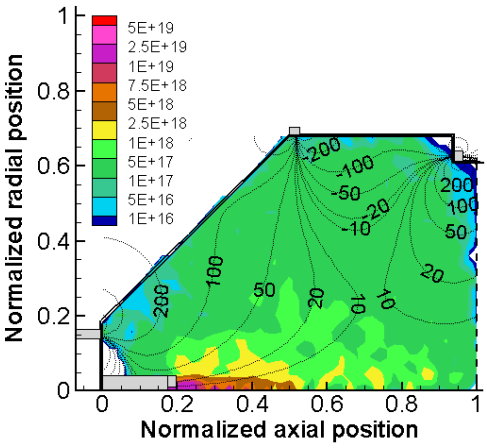

(a) Δt=5 $\times$ 10^{-9} s.

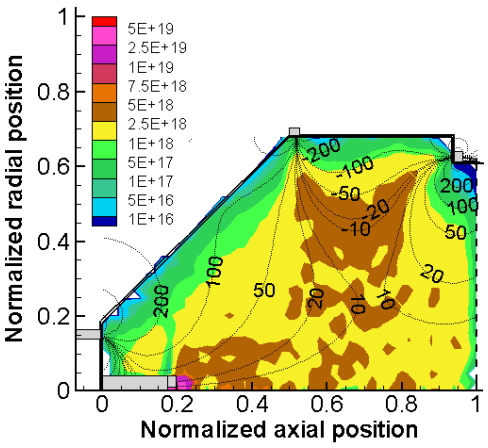

(b) Δt=1 $\times$ 10^{-9} s.

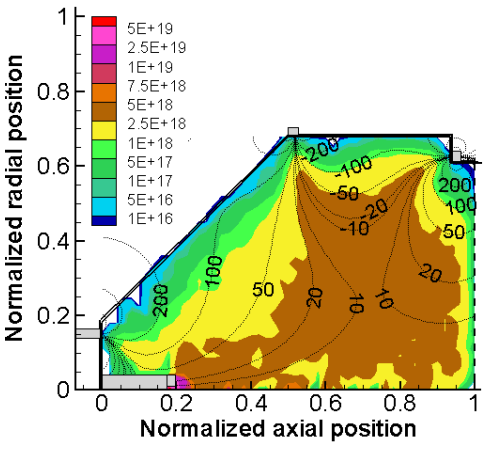

(c) Δt=5 $\times$ 10^{-10} s.

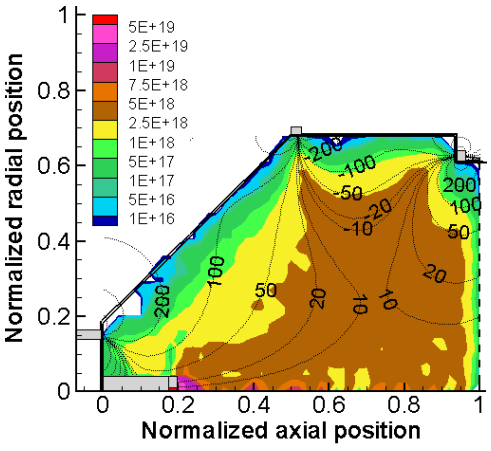

(d) Δt=1 $\times$ 10^{-10} s.

Figure 4.22: Comparisons of Xe^{+} number density results in m^{-3} for the four different electron time step cases.

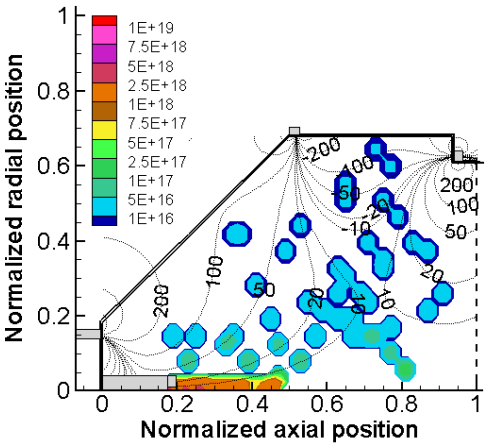

(a) Δt=5 $\times$ 10^{-9} s.

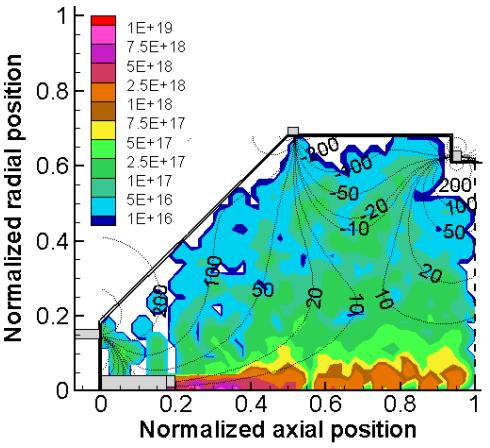

(b) Δt=1 $\times$ 10^{-9} s.

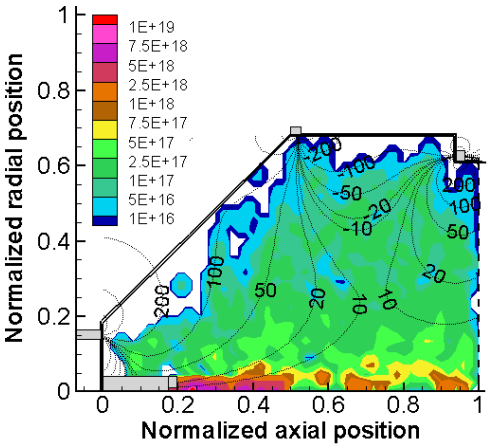

(c) Δt=5 $\times$ 10^{-10} s.

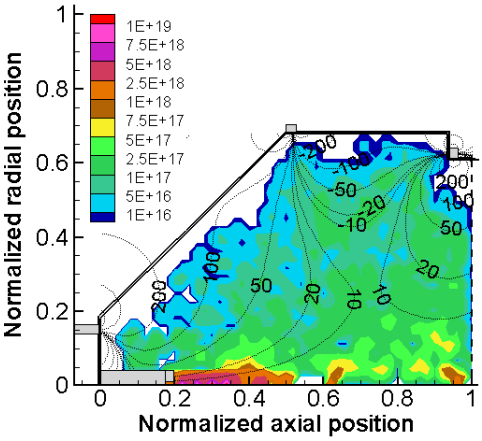

(d) Δt=1 $\times$ 10^{-10} s.

Figure 4.23: Comparisons of Xe^{++} number density results in m^{-3} for the four different electron time step cases.

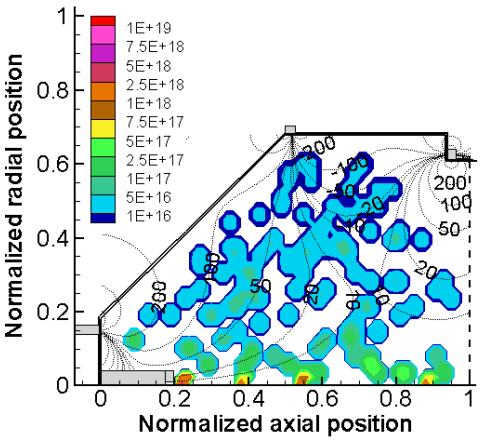

(a) Δt=5 $\times$ 10^{-9} s.

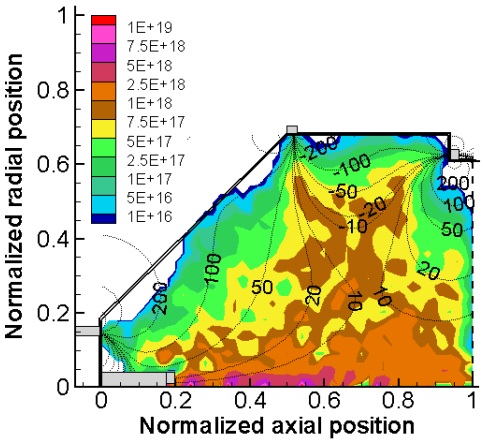

(b) Δt=1 $\times$ 10^{-9} s.

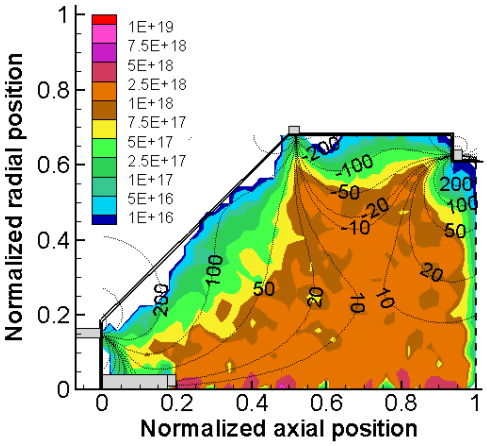

(c) Δt=5 $\times$ 10^{-10} s.

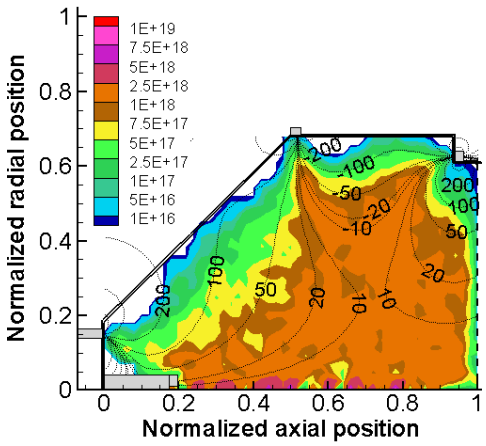

(d) Δt=1 $\times$ 10^{-10} s.

Figure 4.24: Comparisons of primary electron number density results in m^{-3} for the four different electron time step cases.

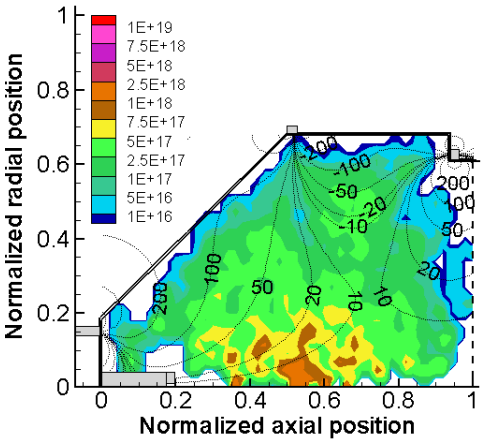

(a) Δt=5 $\times$ 10^{-9} s.

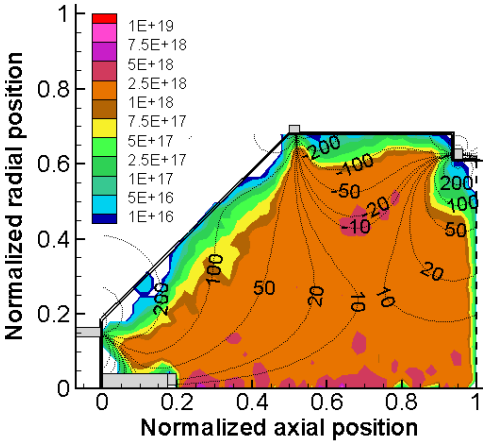

(b) Δt=1 $\times$ 10^{-9} s.

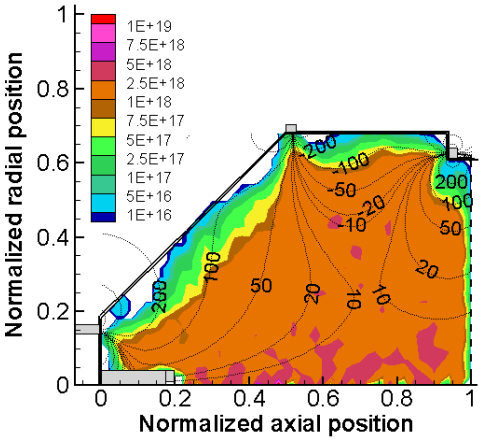

(c) Δt=5 $\times$ 10^{-10} s.

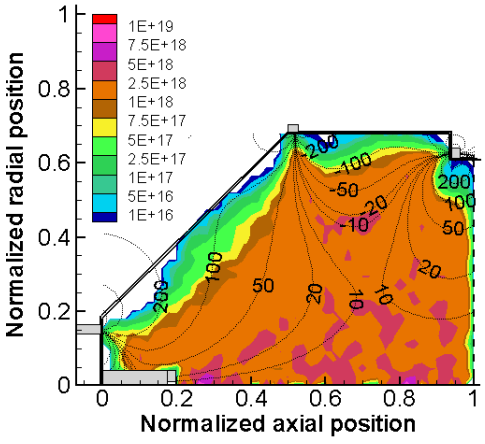

(d) Δt=1 $\times$ 10^{-10} s.

Figure 4.25: Comparisons of secondary electron number density results in m^{-3} for the four different electron time step cases.

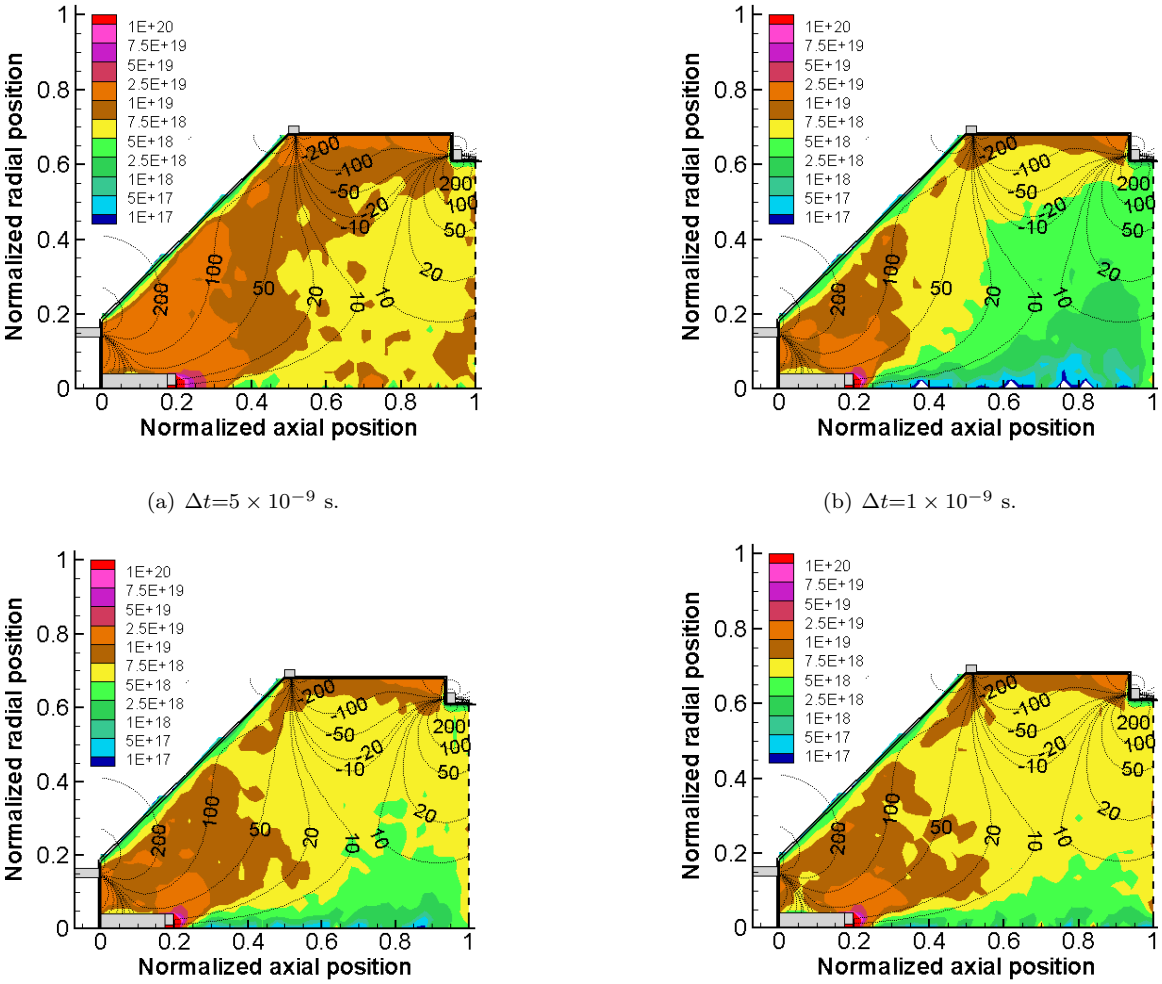

(a) Δt=5 × 10^{-9} s.

(b) Δt=1 × 10^{-9} s.

(c) Δt=5 × 10^{-10} s.

(d) Δt=1 × 10^{-10} s.

Figure 4.26: Comparisons of Xe number density results in m^{-3} for the four different electron time step cases.

It should be reiterated here that the time step study is performed using an 8 times bigger particle weight ($W_{macro} = 1 \times 10^{12}$) than the converged particle weight result ($W_{macro} = 1.25 \times 10^{11}$). If the above CPU hours are interpreted based on a particle weight of ($W_{macro} = 1.25 \times 10^{11}$) then the CPU times will increase by a factor of 3. This means the time step case of (1×10^{-10} s) would require 510 hours (3 weeks) of CPU time to reach 2.5 milliseconds of simulation time. Hence the 5×10^{-10} s case is selected as our converged time step value.

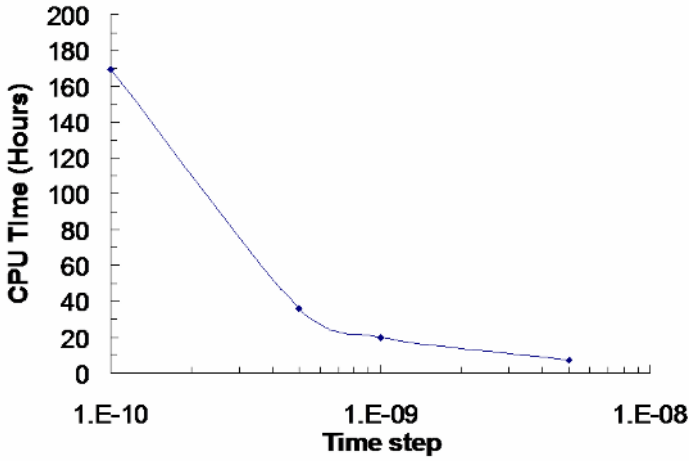

Figure 4.27: The CPU run time vs electron time step results are given for the four electron time step values.

4.2.5 Grid Spacing

Non-uniform grids are adopted in this work In this subsection three different nonuniform grids are studied with different refinements: coarse, medium, and fine. The computational mesh given in Figure 4.4 is taken as the fine mesh and this nonuniform grid is made coarser in two levels to create the medium and the coarse grids. The finer mesh has 100 grid points in the axial direction and has 82 grid points in the radial direction. The medium grid is obtained by reducing the number of grid points in the finer mesh by half in each direction. Thus the medium grid has 50 grid points in the axial direction and 43 grid points in the radial direction. This grid was obtained by taking out every other grid row and column on the fine mesh. The coarse grid has 29 grid points in the axial direction and 25 grid points in the radial direction. This mesh was created by taking out every other row and column from the medium mesh. Figure 4.28 compares the three computational meshes used in the grid spacing study. Figure 4.28 also shows the parallel partitions employed on each grid. A different number of processors are considered for each computational mesh. It was not possible to adopt ten processor partitions on the medium and coarse grid because of the restriction of using a minimum of 5 grid points in each processor and partitioning was not allowed to divide the source

region. Hence a seven processor partition is considered for the medium grid and a three processor partition is considered for the coarse grid.

Table 4.5 lists the number of computer particles per cell actually obtained for each grid used in this study. The computer particle weight is altered for each grid, so that an approximately equal number of computer particles per grid cell are used. The number of computational cells on the coarse and medium grids is different by a factor of 3. Similarly the number of computational cells on the medium and fine grid differ by close to a factor of 4. To maintain uniformity in the cell particle weight, the particle weight used with the coarse grid is 4×10^{12}, the particle weight used with the medium grid is 1×10^{12}, and the particle weight used with the fine grid is 5×10^{11}. As shown in Table 4.5 the cell particle weight for the coarse grid fell slightly below that obtained with the other two grids. This occurs because more particles are lost in the coarse grid case. The time step used for the electrons for all grids is 5×10^{-10}.

Different starting points are used for each grid. The coarse grid's initial particle distribution is obtained from the steady state results of a 4×10^{12} particle weight simulation performed for the particle weight convergence study. The medium grid's initial particle distribution is obtained from the steady state results of a 1×10^{12} particle weight simulation performed for the time step convergence study. Since the fine grid was used in the rest of the numerical parameter studies shown in this chapter, the 2.5×10^{11} particle weight study results are the fine grid results presented in this subsection. All the grid simulations are performed until a steady state solution is obtained. At this point an iteration averaged beam current and discharge current are obtained.

Table 4.5: Numerical parameters used for the different test points considered in the grid spacing convergence study. The tabulated cases use following common parameters: $\Delta t_e = 5 \times 10^{-10}$ s, $\Delta t_{ion} = 5 \times 10^{-8}$ s and $\Delta t_{Xe} = 1 \times 10^{-7}$ s.

Grid Spacing	N_{grid}	N_{cell}	W_{macro}	Number of CPUs
Coarse	780	725	4×10^{12}	3
Medium	2244	2150	1×10^{12}	7
Fine	8383	8200	2.5×10^{11}	10

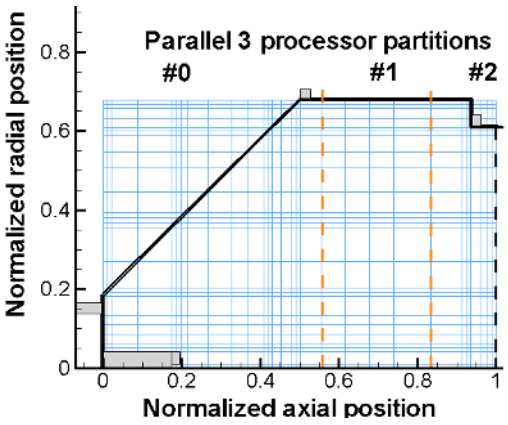

(a) Mesh 29×25.

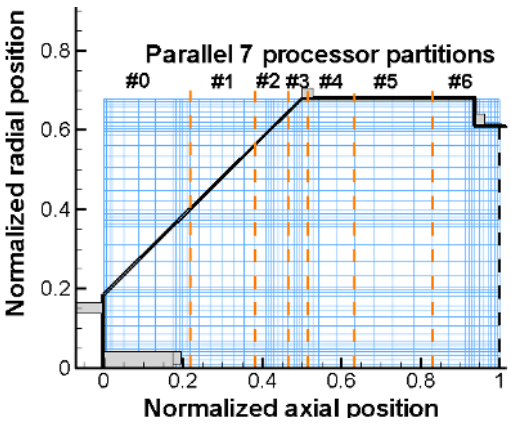

(b) Mesh 50×43.

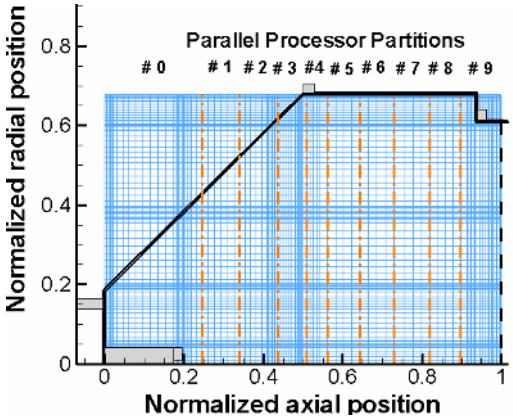

(c) Mesh 100×82.

Figure 4.28: Three computational meshes considered for the grid spacing convergence study. The dotted lines represent the partition boundaries considered for the parallel processing

Figure 4.29 shows the steady state beam current and discharge current results for the three grid spacing cases. A larger beam current of 3.13 amps is observed for the coarser grid. The medium and finer grid beam current results are found to be within 2% of one another. Similarly a larger discharge current is observed for the coarse grid spacing. This is mainly due to the increased electron losses to the chamber walls. The magnetic cusp regions and the strong magnetic field regions are not resolved well with the coarse grid (see the grid refinement near the side wall magnet and near the back wall magnet in Figure 4.28(a)). Less than 2% difference is observed between the discharge current results of the medium grid and fine grid. Figure 4.29 shows the calculated currents converging with fine

and medium grid spacings. In this work the fine grid is utilized.

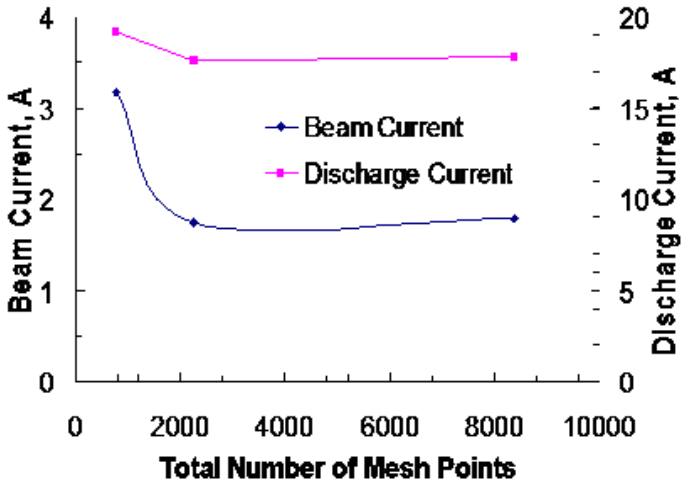

Figure 4.29: Grid spacing convergence.

Table 4.6: The average number of electron computer particles per cell for the three different grid spacing cases.

Grid Spacing	$N_{e,cell}$
Coarse	7.5
Medium	13.5
Fine	14.6

Figures 4.30-4.34 show the particle number density results at the steady state condition for the three grids. Comparisons of the particle number density contour plots indicate that the number density fluctuations are reduced as the mesh is refined. The coarse grid particle number density results are found to have significantly more statistical noise than the medium or fine grid; especially the Xe^{++} and primary electron number density results (see Figures 4.31(a) and 4.32(a)). When looking at these results it must be remembered that different particle weightings are used to try and maintain similar numbers of computer particles per cell. As shown in Table 4.5 the coarse grid ended up with a 37% smaller cell weighting than the medium grid. The cell weightings are similar for the

medium and fine grids. The numerical noise observed with the coarse mesh is being influenced by the by the lower number of computer particles maintained in the discharge chamber.

From the particle weight survey results the highest statistical noise is recorded for a particle weight of 4×10^{12} using the fine non-uniform grid (see Figures 4.13(a), 4.14(a), 4.15(a), 4.16(a) and 4.17(a)). This is the particle weight used by the coarse grid in the grid study. For a fine grid a particle weight of 4×10^{12} only gives 0.62 particles per cell, while for the coarse grid this particle weight provides 7.5 particles per cell. The coarse grid results with a particle per cell number of 7.5 seem to have less statistical noise than the fine grid results using the same particle weighting shown in the particle weighting study. The number of computational cells on the coarse grid is nearly $1/10^{th}$ the number of computational cells on the fine grid. Thus the average number of computer particles per cell should be about 6.2 which is ten times higher than the value of the number of computer particles per cell found on the fine grid. The coarse grid actually had 7.5 particles per cell. From Figure 4.20, the number of computer particles per cell result at a particle weight value of 5×10^{11} matches closer to the number of computer particles per cell observed with the coarse mesh using a particle weight value of 4×10^{12}. However, the particle number density results of the fine grid with a 5×10^{11} particle weight (see Figures 4.13(d), 4.14(d), 4.15(d), 4.16(d), and 4.17(d)) are found to be much smoother than the particle number density results of the coarse grid (see Figures 4.30(a), 4.31(a), 4.32(a), 4.33(a), and 4.34(a)). This may be because fewer total computer particles are used in the coarse grid simulation.

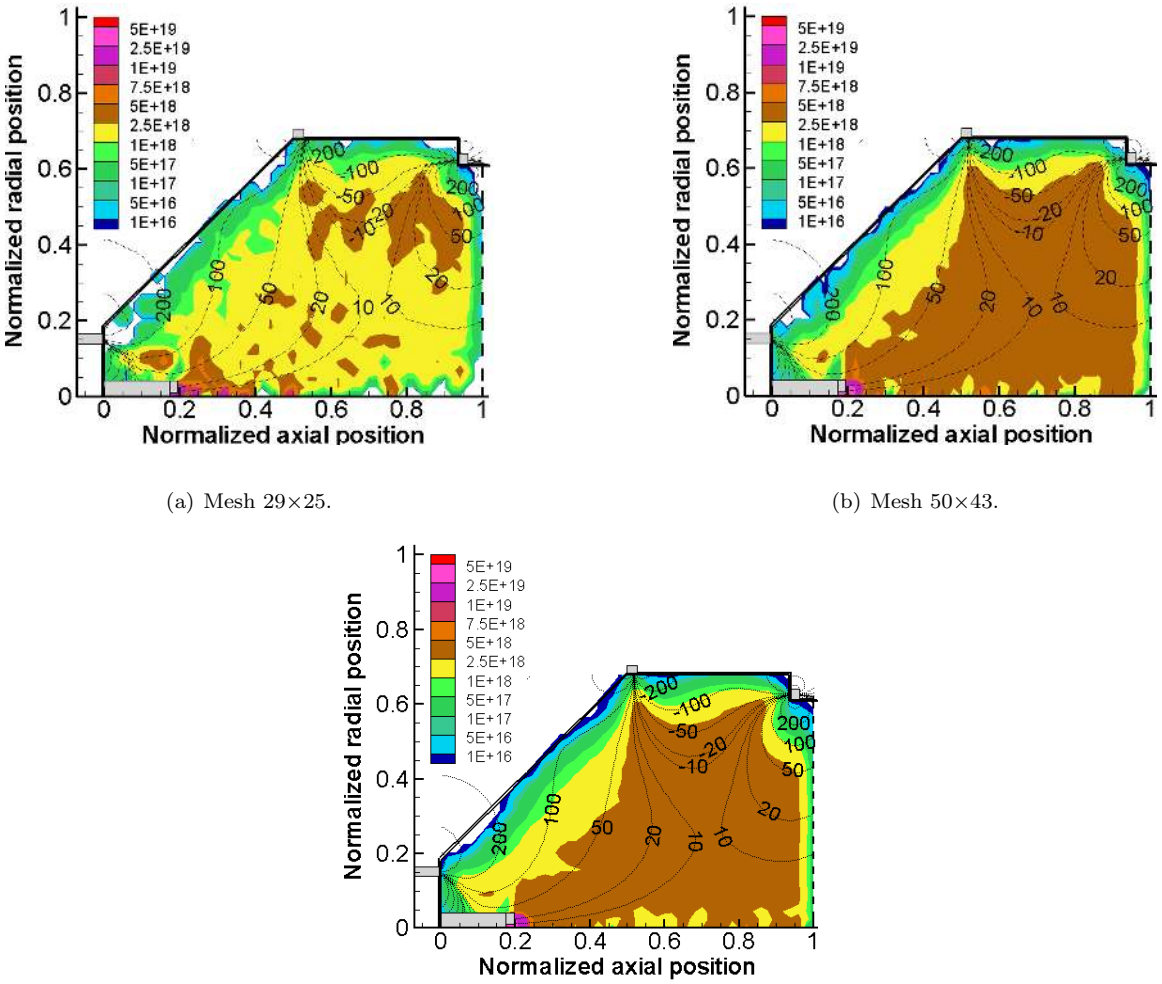

(a) Mesh 29×25.

(b) Mesh 50×43.

(c) Mesh 100×82.

Figure 4.30: Comparisons of Xe^+ particle number density results in m^{-3} for three different grid spacing cases.

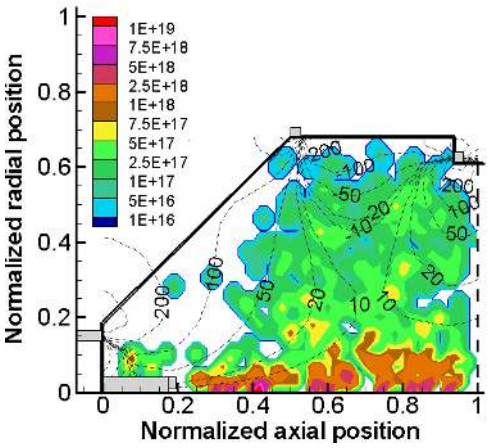

(a) Mesh 29×25.

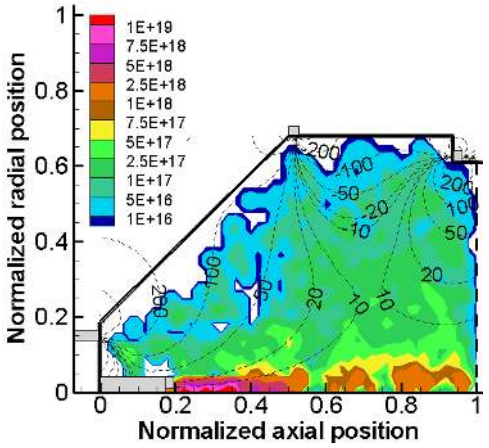

(b) Mesh 50×43.

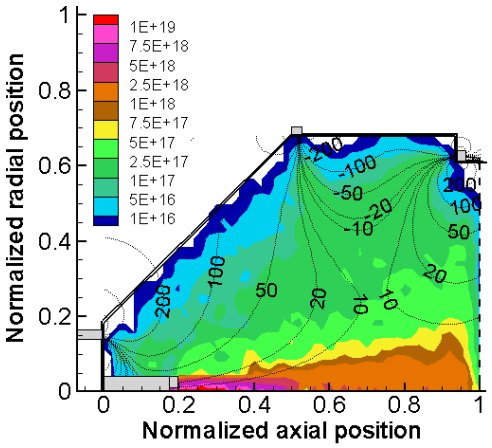

(c) Mesh 100×82.

Figure 4.31: Comparisons of Xe^{++} particle number density results in m^{-3} for three different grid spacing cases.

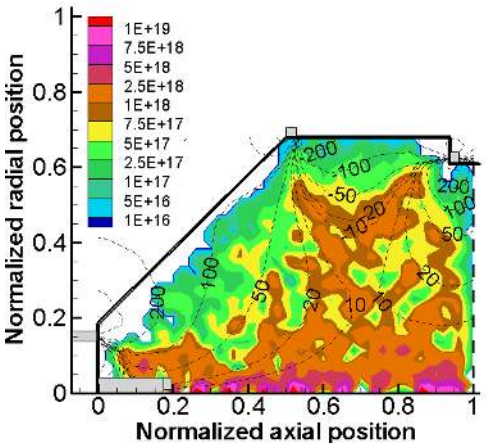

(a) Mesh 29×25.

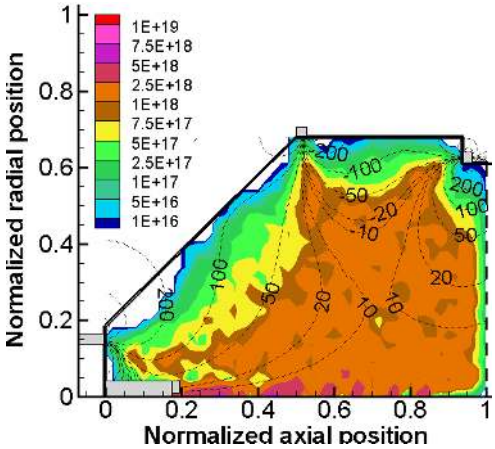

(b) Mesh 50×43.

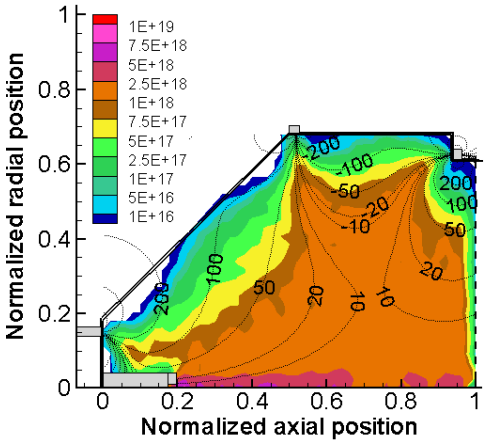

(c) Mesh 100×82.

Figure 4.32: Comparisons of primary electron particle number density results in m^{-3} for three different grid spacing cases.

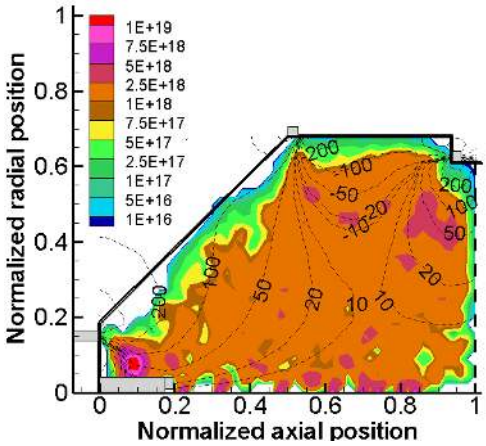

(a) Mesh 29×25.

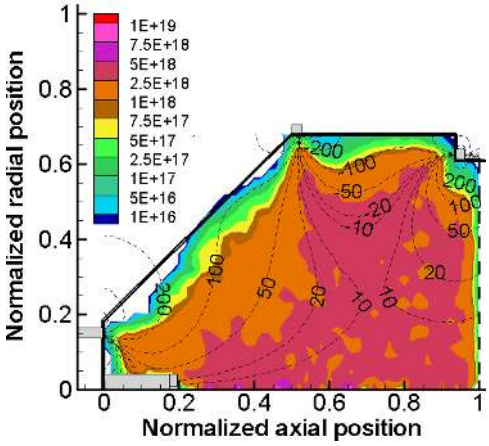

(b) Mesh 50×43.

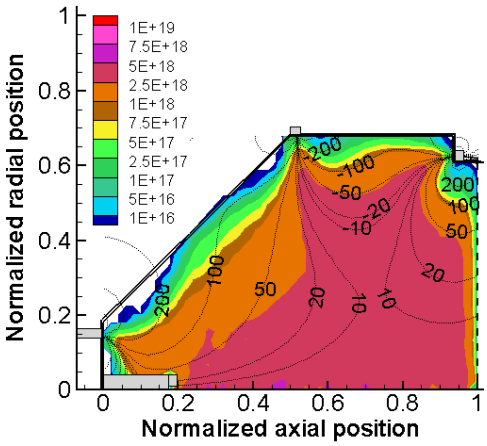

(c) Mesh 100×82.

Figure 4.33: Comparisons of secondary electron particle number density results in m^{-3} for three different grid spacing cases.

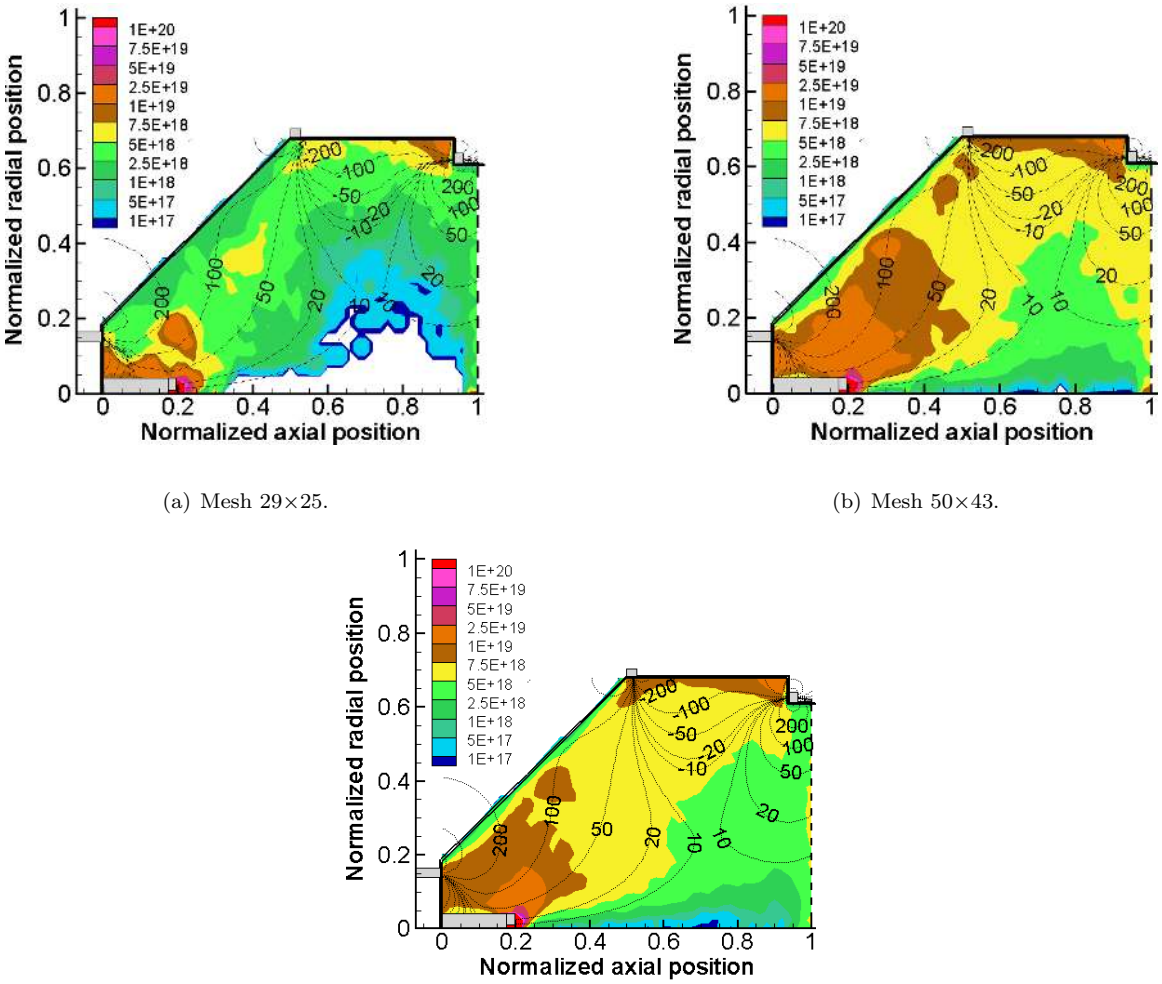

(a) Mesh 29×25.

(b) Mesh 50×43.

(c) Mesh 100×82.

Figure 4.34: Comparisons of Xe particle number density results in m^{-3} for three different grid spacing cases.

The comparisons between the medium and the fine grid particle number density results indicate that fluctuations become smoother with the finer grid. The difference between the number of computer particles per cell for the medium and fine grid is small (see Table 4.6); however, the total number of computer particles in the fine grid is 4 times larger than the number of computer particles considered in the medium grid. Though both number of computer particles and the number of particles per cell are used to quantify the statistical noise, our results indicate that priority should be on increasing the number of computer particles. The total number of computer particles in the

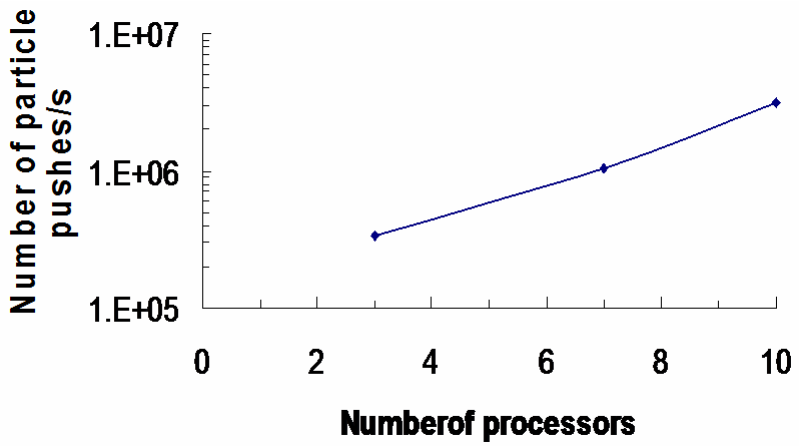

Figure 4.35: Parallel performance of the PIC-MCC scheme with number of processors.

simulation is a critical parameter.

The grid spacing study results also help in assessing the performance of parallel processing. Since each grid spacing case has employed a different number of processors, the CPU performance of changing the number of processors can be determined. The number of processors used on each computational grid is listed in Table 4.5. The parallel partitions considered in each grid are made to maintain load balancing between the processors as best as possible. Figure 4.35 shows number of particle pushes per second with the 3, 7, and 10 processor cases. The results indicate a near linear scale up of the performance of the PIC-MCC scheme with the number of processors. In the parallel PIC code development by Mardahl [2001], a similar linear scale up is shown. Mardahl's parallel code used the electromagnetic (EM) algorithm, and in this work the electrostatic (ES) algorithm is used. In Mardahl's dissertation report, he conducted this study on a perfectly load balanced parallel problem. He reported performance scale up for up to 8 processors using different compilers and different CPU configurations. The maximum performance reported was 2.1×10^6 particle pushes per second on an 8 processor case. Our parallel simulations have shown a maximum performance of 3.13×10^6 particle pushes per second with ten processors. The linear scale up of performance shown in Figure 4.35 indicates that this PIC-MCC simulation can benefit from more processors. However,

due to the limitations of maintaining a minimum of 5 axial grid points in each region and the way the particles cluster in certain regions, this linear scale will not continue. Because of the need to maintain 5 axial grid points in each processor, the maximum number of processors that can be employed with the fine grid is 20. Because of the way the particles are distributed throughout the discharge chamber, increased performance will level out before 20 processors. Adding more axial grid points allows more processors to be used; however it should be realized that when the number of grid points is increased, the number of computer particles have to be increased to maintain a optimal number of particles per cell. This is detrimental to the overall run time. In Chapter 6, recommendations are suggested for improving the performance of the parallel scheme used on this PIC-MCC model.

5

Results

A number of results from the PIC-MCC simulation are presented in this chapter. The primary results presented are those for the TH15 operating condition of NASA's NSTAR ion engine. The NSTAR engine and the TH15 operating condition were described in Chapter 4. In this work the TH15 operating condition is considered the base case. Base case results serve three important functions. First, they are used as a means of validating the plasma model and PIC-MCC simulation developed as part of this work. Secondly, the base case serves as a set of results to which other cases can be compared. Lastly, the base case results are interesting in and of themselves. Information on the operation of the plasma in the discharge chamber is presented at three different levels: the global level, the intermediate level, and the local level. These three levels refer to the spatial region which is described by a particular result. Local level results are the most detailed and provide information on a quantity as a function of position. Examples of a local level results are the number density distribution of a particle species throughout the discharge chamber and current density distributions along the discharge chamber walls and grids. Global level results are usually single numbers that describe the plasma as a whole. Parameters that fall into this category include the beam ion production cost, total currents, total particles, and average energy of each particle species in the discharge chamber. Intermediate level results describe the plasma at a level between the

local and global levels. Intermediate level information includes quantities that average local results over some area or some region of the discharge chamber. Examples of these types of results include currents lost to each of the walls of the discharge chamber. The fact that a PIC-MCC simulation can produce results at the local, intermediate, and global levels is a very desirable aspect of the work presented in this dissertation.

After the base case results are presented a parametric study of a number of the physical aspects of the plasma discharge chamber model are studied. Five different physical processes are studied to determine how they influence the results produced by the plasma discharge chamber model. These parametric studies are conducted using the same NSTAR discharge chamber used for the base case. A desirable aspect of numerical simulations is that different aspects of the physics in the model can be turned on and off at will. This can not be done easily, or at all in an experimental investigation. In the PIC-MCC simulation different types of collisions are disabled from the base case results to study their influence on the operation of the plasma. This technique can also be used to analyze the effect of some of the assumptions made in the PIC-MCC simulation. An important assumption made in this work is the manner in which the electric field is handled. In this work an input electric field is used with an electric field that depends on the particle position superimposed on the input electric field. Results will be presented that give some insights into the effects of this assumption.

To close out the chapter a small design change that has been recommended by another investigator in the ion engine modeling community is studied. It has been suggested that increasing the strength of the middle magnet on the NSTAR ion engine will improve performance. The PIC-MCC simulation developed as part of this work is used to check this claim. In this chapter the strength of the middle magnetic ring is doubled and the performance results are compared to the base case NSTAR discharge chamber results.

5.1 Base Case Results

The base case simulation begins with an initial distribution of plasma particles obtained from the steady state results using a higher particle weighting of 2.5×10^{11}. The results presented in this chapter use a particle weighting of 1.25×10^{11}. The simulation is performed until the numerical solution reaches a steady state condition. The iterative convergence of the numerical results is given in a previous chapter. The total number of iterations for which the plasma particles are tracked with a particle weighting of 1.25×10^{11} is close to 100 million and corresponds to a simulation time of 50 milliseconds. The initial distributions used as a starting point for the base case results came from a computation history that has accumulated nearly 40.9 million iterations from the neutral alone particle distribution results. This means the base case results presented in this chapter have a computational history of 141 million iterations which corresponds to a simulation time of 70.5 milliseconds. As discussed in the last Chapter, this long simulation time is due to the slow movement of the heavy neutrals. The total computer run time to perform the base case computation from the neutral alone distribution to steady state is nearly 3 months using ten processors.

In the following subsections the steady state results of the base case computation are described. In this discussion the first half of the discharge chamber, axially between 0 and 0.5 nondimensional units, is called the conical section and the second half of the discharge chamber, axially between 0.5 and 1 nondimensional units, is called the cylindrical section. The conical section is where the cathode is located and the screen grid is located at the end of the cylindrical section.

5.1.1 Comparisons to Experimental Results

In this section the numerical results from the base case are compared with experimentally measured data. The experimental data for the NSTAR TH-15 condition are obtained from a number of references [Brophy et al. 2000; Brophy 2002; Brophy et al. 2002; Polk et al. 1997; Polk et al. 1999; Foster et al. 2000].

Current comparisons are given in Table 5.1. The beam current, I_B, and the propellant utilization efficiency, η_{prop} results are found to be in very good agreement with the experimental data. The beam current ([Polk et al. 1999; Brophy 2002]) and the propellant efficiency compare within 2%. This is an extremely good comparison for any type of plasma work. These comparisons are probably a little deceiving as to the accuracy of the plasma model developed in this work. If one looks at the comparisons of the ratio of double ion current to single ion current, I_B^{++}/I_B^{+}, it can be seen that the plasma model developed in this work is not predicting the performance of the NSTAR ion engine quite that well. The I_B^{++}/I_B^{+} ratio differs from the maximum experimental results [Brophy et al. 2002] by 63%. The maximum double-to-single ion ratio was measured by Brophy [2002b] along the engine centerline of an engineering model thruster at JPL. In other experimental studies the ratio of double-to-single ion current in the beam was reported in the range of 0.1-0.25. The double ion comparison indicates that the current plasma model is over predicting the number of double ions in the beam current. It is quite possible that it is overprediciting the number of double ions inside the discharge chamber as well. It is felt that a better estimate of the accuracy of the model presented in this dissertation is given by the discharge current, I_D. The calculated discharge current differs from the measured value by 19%. Since discharge currents can be measured with a high degree of accuracy, and there are many difficulties involved in measuring double and single ion currents, it is felt that the comparison to the discharge current is the best one number to obtain a global idea of the accuracy of the results produced by this plasma model. While 19% may seem like a large amount of error, for this type of modeling work this should be considered good.

Table 5.1: Comparisons of numerical discharge chamber current results with experimental measurements for the TH-15 operating condition.

Discharge Parameters	I_B	I_B^{++}/I_B^{+}	η_{prop}	I_{SG}	I_D
Units	A		%	A	A
Numerical Results	1.78	0.44	91.4	0.33	17.8
Experimental Data	1.76	0.1-0.27	90	0.37-0.43	14.9

The discharge current value is based on the difference between the rate of electrons collected at

the anode biased walls and the rate of ions collected at the anode biased walls. From the plasma model the total ion current collected at the chamber walls is 0.78 A. The experimentally estimated ion currents to the anode and screen grid on an NSTAR type ion thruster ([Foster et al. 2000]) is 2.5 A. An estimate of the anode biased wall ion current can be obtained by subtracting an average experimentally determined screen grid ion current (0.40 A) from the 2.5 A anode and grid current. This gives an anode biased wall ion current of 2.1 A. This is significantly higher than the 0.78 A predicted by this model. It is believed the reason for this difference is the electrical potential distribution used. The electric potential field used in this work does not produce any significant gradients except in small regions close to the walls mimicking sheaths and in the cathode region. Important potential gradients controlling ion flow to the walls would be a presheath region. A presheath region would accelerate ions out of the plasma into the anode biased walls. When ions hit the anode biased walls the discharge current is reduced. A presheath region would also hinder the flow of electrons to the anode biased walls. This also would lower the discharge current. Future work should look into applying a presheath potential in regions close to anode biased walls. The presheath region electric potential value should have a gradient of about 1-2 volts below the bulk plasma potential and it should be set between the sheath and bulk plasma regions inside the discharge chamber.

The plasma ion production cost, ϵ_p, is computed using Equation (1.14) which is based on the total ion production current inside the discharge chamber. The total ion production current in the discharge chamber is based on the total ion currents collected at the various chamber walls and the ion currents to the beam. The ion production current as given by Brophy [1985] and Foster [2000] is

$$I_P = I_A + I_B + I_C + I_{SG}. \tag{5.1}$$

where I_A is the ion current to the anode walls, I_C is the cathode ion current, and I_{SG} is the ion current lost to the solid portion of the grid. This computed total ion production current is found to be 5.74 A. Using the computed I_B and I_P in Equation (1.17) gives a ion beam fraction of 0.31.

Similarly the computed I_D, I_P, and the input discharge voltage in Equation (1.14) gives a plasma ion production cost of 77.8 W/A. The beam ion production cost, ϵ_B, is computed using Equation (1.15) based on the computed discharge current and beam current. The beam ion production is calculated to be 226 W/A. The computed plasma ion production cost and beam ion production cost, as well as other global performance parameters, are compared to experimental values ([Foster et al. 2000; Polk et al. 1997; Polk et al. 1999]) in Table 5.2. The plasma ion production cost compares within 3% and the beam ion production cost compares within 16% of the average experimental values.

Table 5.2: Comparisons of numerical results with experimental measurements for the discharge chamber performance parameters of TH-15 operating condition.

Discharge Parameters	ϵ_p	ϵ_B	T_{actual}	I_{sp}	η_t
Units	W/A	W/A	mN	s	%
Numerical Results	77.8	226	87.0	2930	0.55
Experimental Results	76	190-200	92.4	3120	0.618

The ideal thrust produced by the ion engine discharge chamber is computed using Equation (1.6) which depends on the beam current and the beam supply voltage. The computed beam current is 1.78 A and from the NSTAR throttle table (see Table 4.1) the beam supply voltage, V_B for the TH-15 throttle condition is found to be 1100 V. This quantity is not predicted by the plasma model because the region where this is applied is outside the discharge chamber computational domain. Substituting these values into Equation (1.6) gives an ideal thrust value of 97.5 mN. However, the actual thrust produced in the ion engine discharge chamber, as given in Equation (1.7), is affected by the presence of double ions in the beam and the beam divergence factor. Hence the computed ideal thrust value should be lowered to account for these phenomena. The double ion correction factor, α, as given by Equation (1.8) is based on the ratio of double-to-single ion current in the beam current. The computed α value is found to be 0.91. Substituting this α result, the beam divergence factor of $F_t = 0.98$ obtained from experiments, and the ideal thrust result into Equation (1.7) gives a thrust value of 87 mN. The directly measured result is 92.4 mN.

The specific impulse of the ion engine discharge chamber is computed using Equation (1.11)

which is based on the actual thrust value and the total propellant mass flow rate value. The total propellant mass flow rate for the discharge chamber is based on the sum of the neutral flow rate through the cathode, the main plenum, and the neutralizer cathode. The total flow rate for the NSTAR TH-15 throttle condition is found to be 3.02×10^{-6} kg/s. Substituting the computed actual thrust of 87 mN and the total mass flow rate of 3.02×10^{-6} kg/s into Equation (1.11) gives a specific impulse of 2930 s. Once the values of T_{actual} and I_{sp} are known, the overall thruster efficiency, η_t is computed using Equation (1.18). The input power value for the calculation of η_t is taken from the NSTAR throttle table (see Table 4.1). The overall thruster efficiency is computed to be 55%.

Next a comparison between the beam profile results obtained from the numerical simulation and from experiments is made. The numerical beam current density results are presented in two forms following the technique used by Wirz [2005a]. In the first form, the beam current density called $jB++$ is computed by summing the ion current due to singly charged ions (Xe^{+}) and doubly charged ions (Xe^{++}). In the second form, the beam ion current is called $jB+$, and is computed by summing the value of the single ion current and half the value of the double ion current. The first form looks at the beam current as the number of unit charges leaving the grid. This is the physically correct way to look at the beam current. The second form looks at the beam current as the number of positively charged particles leaving the grid. The second form is useful for studying the relative contribution of double ion current to the total beam current.

Figure 5.1 shows the beam current density values obtained from the numerical simulation and from measured data taken during an NSTAR wear test [Polk et al. 1999]. The computed beam current density results are obtained right at the screen grid location, while the experimental data is obtained 2.5 cm downstream of the accelerator grid [Polk et al. 1999]. Both numerical beam profiles $jB++$ and $jB+$ are found to be in qualitative agreement with the experimental beam profile. The profile which should be compared to the experimental results is $jB++$. Note that the $jB+$ profile compares better to the experimental results. This result also explain about the observation in the numerical simulation about the production of too many double ions. The computed beam current

density values are found to peak close to the centerline and this is not seen in the experimental results. The experimental values may have been more peaked at the centerline if they were taken at the screen grid exit location at which the numerical results were taken. Measuring the beam current density downstream of the accelerator grid may reduce the peak. In addition, charge-exchange collision processes between ions and neutrals after the screen grid exit may lower the number of ions reaching the 2.5 cm location where the experimental data is measured. Another difference between the calculated and experimental beam current profiles is the experimental results come form a screen grid that has a slight curvature. This curvature is not included in the grid boundary condition used in the modeling work. The oscillations seen in the calculated results are due to statistical variations present in the PIC-MCC simulation. These are reducible by using a lower particle weighting.

The other performance parameter that is used for describing the beam profile is the beam flatness parameter, F_B. It is defined as the ratio of the average beam current density to the peak beam current density. A larger value of F_B signifies a less peaked beam profile. In our numerical simulation, the F_B value for the $jB++$ beam current density profile is found to be 0.39 and the F_B value for the $jB+$ beam current density profile is found to be 0.44. The experimentally reported F_B value is 0.46 for the TH-15 operating condition [Polk et al. 1999].

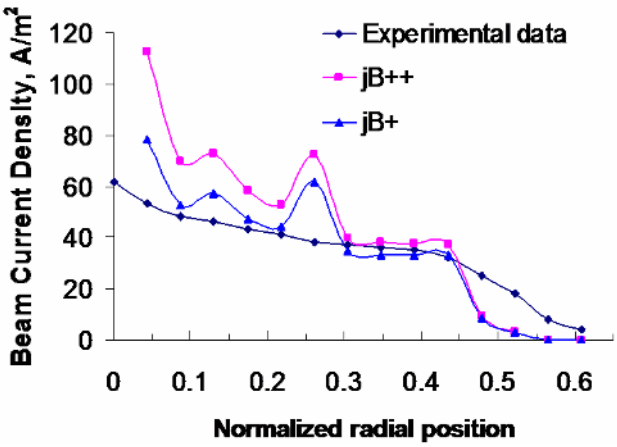

Figure 5.1: Beam profile for the NSTAR TH-15 operating condition. Comparison between the numerical results and the experimental data are also shown in this plot.

5.1.2 Total Particle and Current Results

Table 5.3 shows the steady state results for the total number of each type of particle, N_{phys}, present inside the discharge chamber for each species. These results indicate that the ionization fraction of the plasma is 26% and the ratio of the total number of double ions (Xe^{++}) to single ions (Xe^{+}) is 0.064. This is much lower than the double to single ion current ratio, 0.44, obtained at the grid. The total number of primary electrons is 23% of the total number of electrons. These total particle results also indicate that the total number of negative charges (sum of primary and secondary electrons) are nearly equal to the total number of positive charges (sum of Xe^{+} and twice Xe^{++}). The ratio of the negative charges to the positive charges is 1.01. This corresponds to a net negative coulomb charge of -5.4×10^{-5} C or 3.4×10^{14} electrons. This is less than 1% of the total electron particles in the discharge chamber. This is a strong indication that the dynamic electric field solver with an inflated plasma permittivity is performing the function it was intended to do, maintain an overall plasma charge of zero.

Table 5.3 also shows the steady state volume averaged particle number densities and kinetic energy results for each species. As expected the primary electrons have the highest energy, the secondary electrons the next highest, then Xe^{++}, Xe^{+}, and Xe.

Table 5.3: Total particle results at steady state for the NSTAR discharge chamber at TH-15 operating condition.

Steady State Results	Xe	Xe^{+}	Xe^{++}	Primary	Secondary
N_{phys}	10.3×10^{16}	3.06×10^{16}	0.196×10^{16}	0.76×10^{16}	2.72×10^{16}
$\overline{n}$ in m^{-3}	8.25×10^{18}	2.46×10^{18}	0.16×10^{18}	0.61×10^{18}	2.18×10^{18}
T_{avg} in eV	0.0324	0.047	0.104	3.90	2.45

5.1.3 Particle Distribution Results

In this section the steady state plasma particle number density results for the base case are given. Also the cell averaged kinetic energy results are given for Xe^{+}, primary electrons, and the secondary

electrons. All particle distribution plots have the magnetic vector potential lines superimposed on them so the reader can judge the effects of the magnet field on the particles. Comparisons of the particle number density results are made with the experimental results obtained by Herman [2005] and Sengupta et al. [2004, 2006] on the NSTAR thruster.

Figure 5.2 shows the steady state neutral gas number density results. The maximum neutral number density value is observed near the cathode keeper exit, ($\sim 1 \times 10^{20}$ m^{-3}), where the cathode neutral particle source is located. This number density result is higher than the neutral number density result observed at the main plenum source for neutrals ($\sim 2.0 \times 10^{19}$ m^{-3}). One reason for this higher number density is the small emission volume at the cathode as compared to the main plenum emission. In an axisymmetric, cylindrical coordinate system the volume at a given radial location is proportional to r. The cathode emission is focused while the main plenum emission is more diffuse. Another reason for getting a peak number density value at the cathode exit is because of ion recombination at the cathode wall surfaces. Ions made in the plasma close to the cathode emission source have a propensity to travel back towards the cathode, because of its lower electrical potential. This increases the number of neutral particles present in this region. High neutral number densities are also observed in the back part of the conical section and near the side wall. The neutral number density values in the cylindrical section increase sharply in the radial direction after 0.05 nondimensional units. The side wall region has a neutral number density of 1×10^{19} m^{-3}, because there are few high energy electrons in this region and also due to wall recombination of ions. The high side wall neutral number densities are also the result of the neutrals coming from the main plenum source.

The most interesting aspect of the neutral number density distribution results is the depletion of neutrals along the centerline of the discharge chamber. Most of the plasma along the centerline is more than 90% ionized. This neutral particle depletion is reported in a study done by Sengupta et al. [2006]. Sengupta et al. [2006] only report relative neutral number density results so quantitative comparisons can not be made. The minimum neutral number densities in the discharge chamber are

found along the centerline; (1×10^{17} - 5×10^{17} m^{-3}) for the region between 0.25 nondimensional units and just upstream of the screen grid in the axial direction and radially from the centerline to 0.05 nondimensional units. This depletion occurs because of the high energy primary electrons coming from the cathode. The magnetic field enhances this problem by keeping electrons confined to the centerline region. If these electrons could be forced off the centerline quicker, a better performing ion engine would be the result.

Figure 5.3 shows the steady state Xe^+ number density results. At the cathode source a maximum Xe^+ number density value of $\sim 5 \times 10^{19}$ m^{-3} is observed. At the exit of the cathode keeper the number density value is observed to be 1×10^{19} m^{-3} which is in agreement with plasma number density results given by Herman [2005]. The experimental measurements by Herman [2005] show a sharp decrease in the number density values in the conical section while our Xe^+ number density results show no decrease in number density values in the radial direction until after 0.16 nondimensional units. Our number density results are in agreement with the electron number density results given by Sengupta et al [2004] who had made a similar measurement in the conical section of an NSTAR type thruster. The number density values decrease rapidly, by two orders of magnitude, in the region between axial positions of 0.2 - 0.5 nondimensional units and radially in the conical section after 0.16 nondimensional units. The minimum Xe^+ number density value in the slanted wall region is observed to be 1×10^{16} m^{-3}. This result is in agreement with experimental studies [Foster et al. 2000; Herman 2005; Sengupta et al. 2004; Sengupta et al. 2006]. In the cylindrical section, the Xe^+ number density values are found to be in the range between 2.5×10^{18} m^{-3} and 5×10^{18} m^{-3}. The Xe^+ number density values in the cylindrical section decreases after 0.58 nondimensional radial units and show an order of magnitude decrease in the number density values near the side wall region. The minimum Xe^+ number density value in the side wall region is observed to be 2.5×10^{17} m^{-3}. At the screen grid, the ion number density values are observed to be smaller. This is mainly because the ions are accelerated to a high speed by the presence of large electric fields in the screen grid sheath. The white regions inside the discharge chamber boundaries are regions where no

computational particles exist. This does not mean there are no real particles present here; however, it does mean that the number of real particles present is extremely small.

Figure 5.4 shows the steady state average kinetic energy results for Xe^{+}. Near the back wall sheath and at the magnetic cusp region-1 the average ion energy value is found to be 1-2.5 eV. The ion energy drops for the region axially downstream of the back wall. Near the cathode source the average kinetic energy of Xe^{+} is found to be 1-2.5 eV. At the cathode keeper top surface sheath, the Xe^{+} kinetic energy is found to be between 2.5-10 eV due to the large electric field presence in this sheath. The average kinetic energy value decreases axially away from the cathode keeper. The average Xe^{+} kinetic energy for the bulk of the cylindrical section is 0.03-0.05 eV. Closer to the side wall sheath, the Xe^{+} average kinetic energy is found to increase again because of the acceleration provided by the side wall sheath. At the side wall magnetic cusp region the average Xe^{+} energy 1-2.5 eV. The average Xe^{+} energy at the screen grid is found to be between 2.5-10 eV as a results of the grid sheath.

Figure 5.5 shows the steady state Xe^{++} number density results. Xe^{++} has its highest number densities ($\sim 1.25 \times 10^{19}$ m^{-3}) between the cathode keeper and 0.15 nondimensional units axially downstream of the cathode keeper. These number densities may increase the erosion of the cathode and cathode keeper walls as discussed by Williams [2000]. The Xe^{++} number density values decrease sharply in the radial direction. In the conical section the Xe^{++} number densities decrease rapidly in the radial direction which indicates fewer double ionization events compared to the cylindrical section. In the cylindrical section axially between 0.5 to 0.9 nondimensional units and radially from the thruster centerline to 0.12 nondimensional units, the Xe^{++} number density values are found to be in the range between 1×10^{18} m^{-3} and 2.5×10^{18} m^{-3} which is about 0.3-0.8 times of the Xe^{+} number density values in these locations. These high Xe^{++} number density values radially near the thruster centerline and axially a few centimeters upstream of the screen grid indicates that the beam current density along the thruster centerline is peaked by the Xe^{++} ions. The formation of such a large Xe^{++} number density along the thruster centerline is due to high energy primary electrons

concentrated along the thruster centerline. This along with the neutral number density depletion increases the chances of Xe^{++} production along the centerline than the Xe^{+}. In the bulk of the discharge chamber, the Xe^{++} number density values are in the range of $1/3^{rd}$ to $1/25^{th}$ that of the Xe^{+} ion number density values.

The average kinetic energy results of Xe^{++} are found to be similar, but slightly higher, than the Xe^{+} kinetic energy results. The bulk of the ions are at low energy, while their energy in the sheath regions is much higher. In the grid sheath region, Xe^{++} is found to peak more than 25 eV at the centerline.

Figure 5.6 shows the steady state primary electron number density results. Maximum primary electron number densities are observed near the cathode keeper exit, $\sim 7.5 \times 10^{18}$ m^{-3}. The primary electron number densities along the thruster centerline are observed to be $5{\times}10^{18}$ - $2.5{\times}10^{18}$ m^{-3}. The primary electron distribution results in Figure 5.6 indicate that the primary electrons are mostly confined by the magnetic field lines. In the conical section the primary electron number density values decrease rapidly due to the confinement of electrons with the higher magnetic field lines (above 50 gauss-cm) running between the cusps of magnet-1 and magnet-2. One problem in the magnetic field is in the middle of the slanted wall. The 100 gauss-cm magnetic vector potential line leans into the wall. Primary electron number densities also bow into the wall close to this point. As will be shown latter, this leads to an increased flux of primary electrons to the slanted wall. This region in the magnetic field is called a hole by Bennett et al [2007]. In the cylindrical section the primary electron number density values are found to decrease radially after 0.5 nondimensional units where the 50 gauss-cm magnetic vector potential line runs between the cusp regions of magnet-2 and magnet-3.

Figure 5.7 shows the steady state primary electron average kinetic energy results. The maximum local average primary electron kinetic energy values of 12.5-15 eV are found axially between the cathode keeper exit and 0.15 nondimensional units downstream of the cathode keeper. The radial extent of these energies is from the thruster centerline out to 0.05 nondimensional units. The high energy primary electrons in this region are responsible for the higher Xe^{++} number densities (see

Figure 5.5) and the depleted neutral particle number densities (see Figure 5.2). The kinetic energy values sharply drop in the radial direction to 5 eV at 0.08 nondimensional units. The bulk of the primary electron average kinetic energies are found to be between 3.5-4 eV. Both conical and cylindrical sections exhibit similar primary electron energy variations. Near the chamber walls the average kinetic energy value is found to be on the order of 1-2.5 eV. As started earlier, primary electrons are converted into secondary electrons after their energy drops below 4 eV. It was also stated that this is only done after the primary electrons undergo an inelastic collision. As Figure 5.7 shows a large number of primary electrons are decelerated by the electric fields to values below 4 eV before they are converted to secondary electrons. As expected, this is especially true in the sheath regions. The PIC-MCC simulation also includes long range coulomb collisions between electrons and ions. These collisions will remove energy from the electrons and transfer it to the ions. More will be said about this latter.

Figure 5.8 shows the steady state secondary electron number density results. High secondary electron number density values of 5×10^{18} m^{-3} are found for the axial positions between 0.3 to 0.8 nondimensional units and close to the thruster centerline in the radial direction. Near the cathode source region, the secondary electron number density values are found to be between 2×10^{18} m^{-3} and 4×10^{18} m^{-3}. The secondary electron distribution results in Figure 5.8 indicates that the secondary electrons are confined by the magnetic field lines. In the conical section, the number density values drop radially after 0.2 nondimensional units indicating the presence of strong magnetic field lines. The minimum secondary electron number density value near the slanted wall is found to be in the range of 5×10^{16} m^{-3}, which is in agreement with experimental measurements by Herman [2005]. In the cylindrical section for the regions axially between 0.5 to 0.9 nondimensional units and radially between 0.05 to 0.58 nondimensional units, the secondary electron number density values are found to be in the range of 3×10^{18} m^{-3} - 4×10^{18} m^{-3}. The secondary electron number density values decrease for regions radially after 0.58 nondimensional units because of confinement by the strong magnetic field lines. At the side wall the secondary electron number density values are found to be

in the range of 1×10^{17} m^{-3} - 3×10^{17} m^{-3}. These results qualitatively agree with the experimental measurements made by Sengupta et al [2006]. In the bulk of the discharge chamber the calculated secondary electron number density results are higher than the experimental values.

Figure 5.9 shows the steady state secondary electron average kinetic energy results. The maximum secondary electron average kinetic energy values are found to be along the thruster centerline varying between 3-5 eV. In the bulk of the conical and cylindrical section, the secondary electron energy is found to be in the range between 2-3 eV. In the conical section the minimum secondary electron energy of 0.8 eV is found near the slanted wall. In the cylindrical section the minimum secondary electron energy of 1.3 eV is found near the side wall.

It is interesting to study the population fraction of electron energies inside the discharge chamber for both the high energy primary electrons and the low energy secondary electrons. Before discussing the electron energy distribution results, let us first look at the maximum energy that the PIC-MCC simulation allows the electrons to obtain. From the input static electric field, the maximum kinetic energy possible for the primary electrons would be 28 eV. This maximum kinetic energy is estimated based on the net total of a 2 eV input kinetic energy at the source and the 26 volt rise from the cathode potential, 2 volts, to the bulk plasma potential, 28 volts. The electric potential results from the dynamic electric field solver have shown an increase in the bulk plasma potential from 28 volts to 30 volts. Thus, the primary electron energy values can go above the 28 eV limit to a maximum of about 30 eV. The secondary electrons which are produced inside the discharge chamber, generally do not achieve the energies that primary electrons do. Only primary electrons created in the low voltage regions can gain maximum energies comparable to the maximum energies of the primaries. For example, a secondary electron produced from secondary emission at the grid wall can gain electron energy of 30 eV. In a real thruster, electrons can pick up energy through elastic collisions with other electrons. In this work, elastic electron-electron collisions are not explicitly modeled, but the PIC-MCC simulation does inherently include long range coulomb collisions, such as electron-electron collisions and electron-ion collisions [Birdsall 1991]. These long range coulomb

interactions are what maintain a charge balance in the discharge chamber. Because of the large number of ions present in the discharge chamber relative to the number of high energy electrons, these long range coulomb interactions decrease the average energy of the primary electrons instead of increasing it.

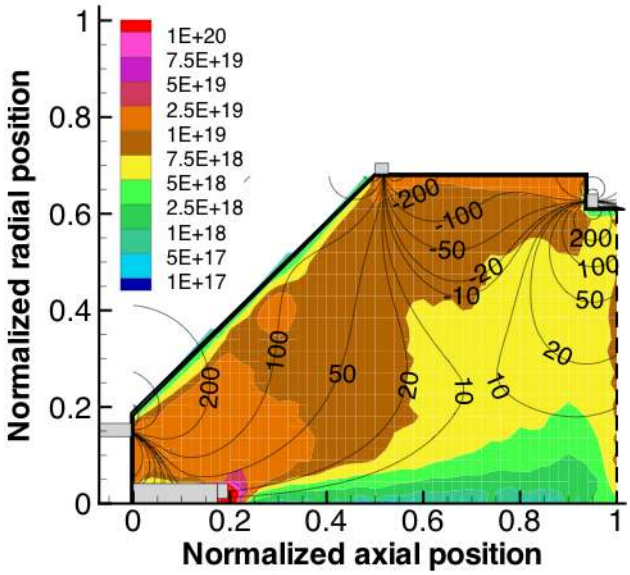

Figure 5.2: Xe number density results in m^{-3} at steady state for the base case of the NSTAR's TH-15 operating condition.

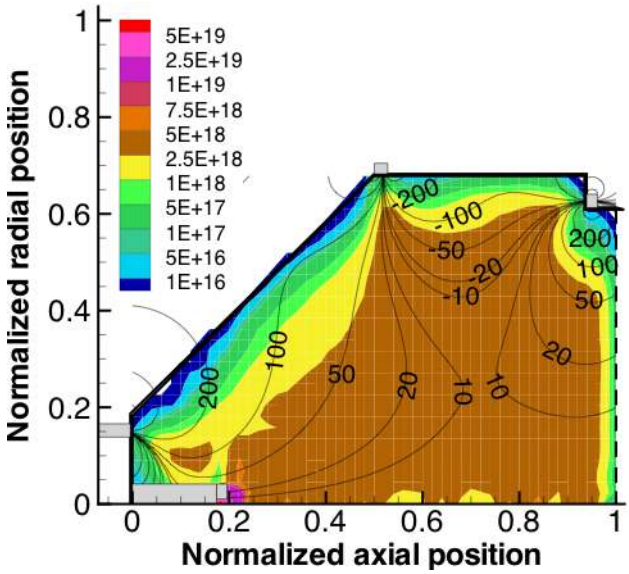

Figure 5.3: Xe^{+} number density results in m^{-3} at steady state for the base case of the NSTAR's TH-15 operating condition.

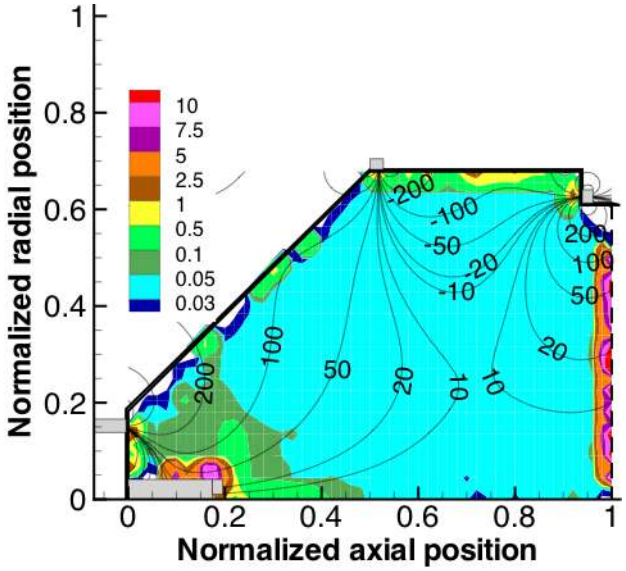

Figure 5.4: Xe^{+} energy results in eV at steady state for the base case of the NSTAR's TH-15 operating condition.

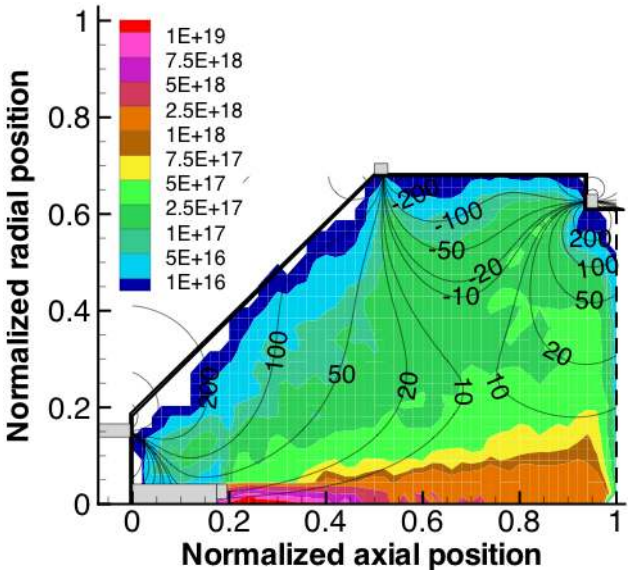

Figure 5.5: Xe^{++} number density results in m^{-3} at steady state for the base case of the NSTAR's TH-15 operating condition.

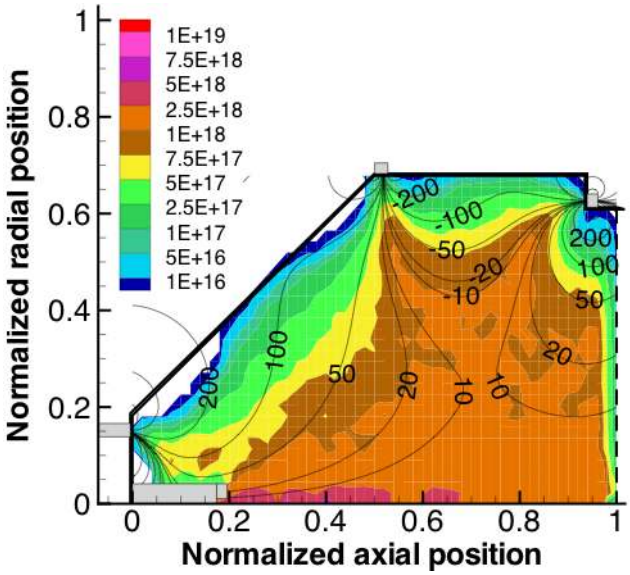

Figure 5.6: Primary electron number density results in m^{-3} at steady state for the base case of the NSTAR's TH-15 operating condition.

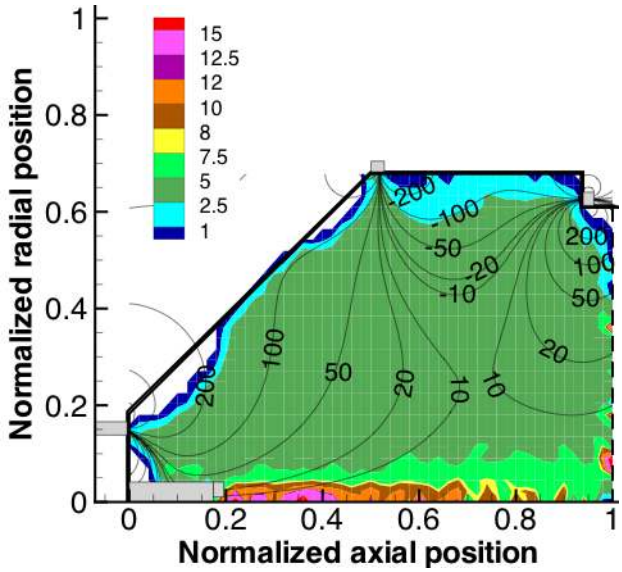

Figure 5.7: Primary electron energy results in eV at steady state for the base case of the NSTAR's TH-15 operating condition.

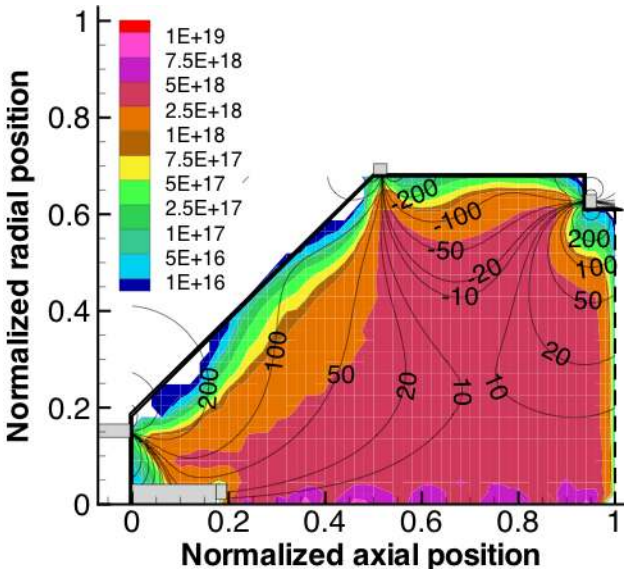

Figure 5.8: Secondary electron number density results in m^{-3} at steady state for the base case of the NSTAR's TH-15 operating condition.

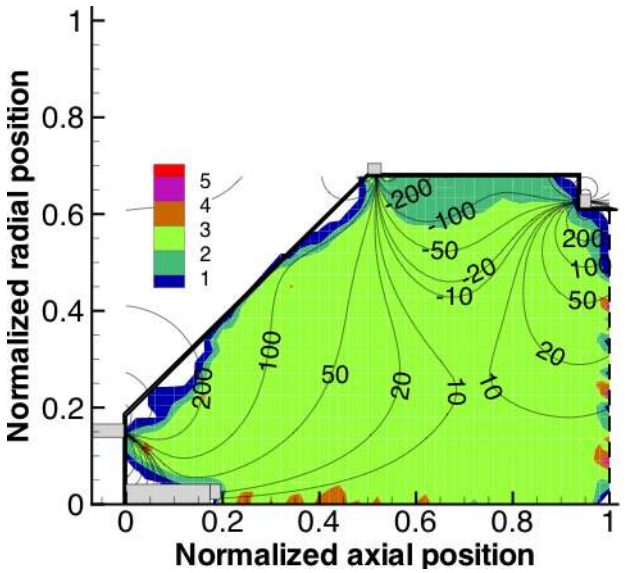

Figure 5.9: Secondary electron energy results in eV at steady state for the base case of the NSTAR's TH-15 operating condition.

Figure 5.10 shows the electron energy distribution function (EEDF) for primary and secondary electrons at the steady state condition. This distribution is for all the electrons in the discharge chamber. The electrons are grouped into 0.2 eV energy bins from 0 eV to 30 eV. After counting the number of particles in each 0.2 eV increment, the relative fraction of the particles in each bin is computed by dividing the total number of particles in that energy bin with the total number of particles. Both EEDF results are found to be skewed towards the low electron energy values. The peak of each EEDF is around 1.2 eV. From these peak points the EEDFs drop gradually. The slope is found to be steeper for the secondary electrons than the primaries. The most notable difference between the two plots is the high energy tail of the primary electron EEDF. There is a small fraction of high energy primaries present. Although the numbers of these high energy primaries is small, their importance to sustaining the discharge is high. Only 3.5% of the primary electrons are found to have an energy value of 12.5 eV and above. The ionization threshold energy required for the creation of Xe^{+} from Xe is 12.1 eV. These 3.5% of the electrons are responsible for the creation of ions inside the discharge chamber. Only 0.8% of the total primary electrons are found to possess more than 21.2 eV of energy, which is the ionization threshold energy for the creation of Xe^{++} from Xe^{+}. About 8.3% of the total primary electrons are found to have electron energies above 8.35 eV and above, which is the excitation threshold for Xe. In the secondary electron group only 0.27% of the electrons are found to have an energy value of 12.5 eV and above. About 1.4% of the secondary electron particles are found to have energies of 8.35 eV and above. As can be seen in Figure 5.10 an insignificant number of secondary electrons are found to possess electron energies greater than 21.2 eV. The EEDF functions displayed in Figure 5.10 point out that a relatively few number of electrons are sustaining the plasma inside the discharge chamber.

5.1.4 Particle Loss Mechanisms

It is interesting to know how different inelastic collision processes affect the high energy primary electrons, and the slow moving secondary electrons inside the discharge chamber. Table 5.4 lists the

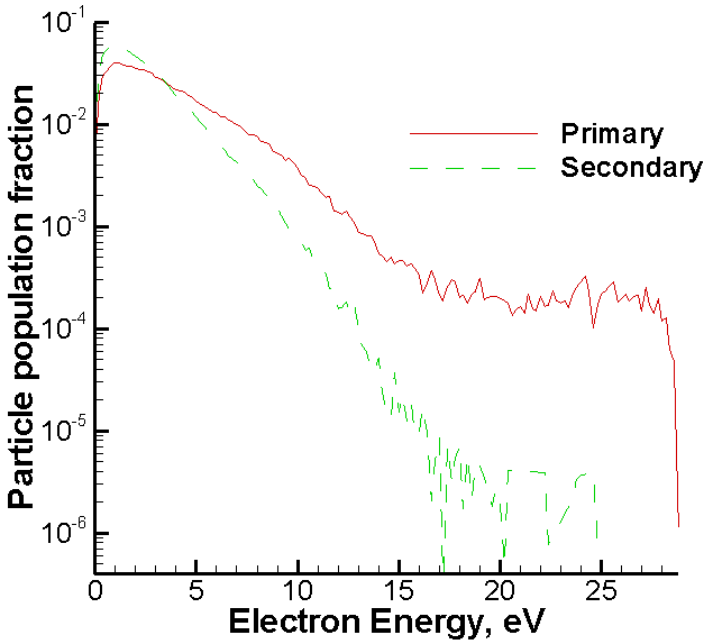

Figure 5.10: Electron energy distribution function results for both primary and secondary electrons at steady state for the NSTAR discharge chamber.

relative percentages of each of the inelastic collision processes include in this PIC-MCC simulation. The results are for both primary and secondary electrons at the steady state condition.

Table 5.4: Percentage of inelastic collision processes for electrons at steady state.

Inelastic Collision Processes	Xe Exc.	Xe Ionz.	Xe^+ Exc.	Xe^+ Ionz.	Xe^+ Recomb.	Xe^{++} Exc.	Xe^{++} Recomb.	Wall Losses
Primary electrons	29.8	15.8	0.66	2.16	0.8	0.22	0.1	16.0
Secondary electrons	4.54	0.75	0.06	0.012	4.76	0	0.58	23.8

These results shown that the most common collisions are those with neutral particles. This is understandable because the neutrals are the most plentiful species in the discharge chamber. As will be shown in the physical parameter survey latter in this chapter, excitation collisions are a significant means by which electrons lose energies. It would seem that wall losses are also a place where electrons

loose a significant amount of energy. The total percentage of electrons recombination collisions with Xe^{+} and Xe^{++} is 6.23 %. As will be shown latter recombination collisions are important to the operation of the discharge chamber plasma.

Table 5.5 lists the percentage of the total discharge current collected at different discharge chamber walls. This table points out that the side wall is the location where the most discharge current is lost and the side flange is where the second most severe place where discharge current is lost. It is not surprising that these two walls have the greatest losses. The surprising result is that the back wall, which has a magnet, losses less current than the slanted wall, which does not have a magnet. It is well understood that electrons escape to the wall through the cusp regions, but it is difficult for electrons to leave the discharge chamber in regions between the magnets. The slanted wall is between the magnets. As has been alluded to earlier in this chapter, there seems to be a hole in the magnetic field on the slanted wall, about halfway between the magnets. A hole in the magnetic field is caused by spacing the permanent magnets too far apart. According to the rules-of-thumb developed by Ogunjobi et al. [2006] these magnets are spaced too far apart for good electron confinement. One way of filling in this hole in the magnetic field is to strengthen the magnets. This modification is considered in this work and a detailed analysis has been performed. The results from this analysis will be presented in the last section of this chapter.

Table 5.5: Percentage of discharge currents collected at various chamber walls and the percentage of discharge current due to different species.

Anode biased walls				By species			
Back wall	Slant wall	Side wall	Side flange	Primary electrons	Secondary electrons	Xe^{+}	Xe^{++}
11.8	17.1	40.8	30.3	42	62.4	-3.8	-0.6

Table 5.5 also lists the percentage of discharge currents due to different charge particles. The slow moving secondary electrons cause about 62% of the discharge current, while the fast moving primary electrons contribute about 42% of the discharge current. This is significant because the 42% contribution by the primaries is a disproportionate percentage of primary electrons to the total

number of electrons in the discharge chamber which is 23%. It is desirable that low energy electrons complete the current circuit in the discharge chamber and not high energy electrons. In Table 5.5 the positively charged particles contributing to the wall currents are listed as being negative percentages. This is done because ions going to the wall reduce the discharge current.

To gain a better understanding of the particle losses to the walls of the discharge chamber, current density, j, profiles along each of the walls is plotted. This is done for each charged particle species in Figure 5.11. These plots localize the wall areas where particles are being lost. A discharge chamber wall surface can be looked as a combination of the following two segments: 1) a magnetic cusp area (if the wall has a magnet on it) and 2) a non-cusp area comprised of wall locations between the cusps of two magnet rings. If two adjacent magnets are spaced too far apart then a hole can develop in the magnet field on the surface of the wall. As discussed by Bennett et al [2007], a wall hole is identified as the wall region where the strength of the magnetic field lines become weak enough to allow a significant number of electrons to reach the walls. Holes in the magnetic field result in poor ion engine performance [Bennett et al. 2007; Mahalingam and Menart 2007a]. The magnetic field strength and magnetic vector potential results for the three magnetic-ring NSTAR ion engine (see Figure 4.3) indicate two such hole regions on the discharge chamber wall surfaces. One hole region is found on the slanted wall surface of the conical section (axially between 0.26-0.32 nondimensional units) and the other hole region is found on the side wall of the cylindrical section (axially between 0.68-0.76 nondimensional units). The magnetic field strength values in the hole regions are found to be weaker (15-20 G on the slant wall hole region and 25-30 G on the side wall hole region).

In Figure 5.11 the steady state species current densities on the four walls of the discharge chamber (back, slanted, side, and flange) are plotted on three graphs. The slanted wall in the conical section and the side wall in the cylindrical section are combined together and plotted versus the axial wall surface. To minimize the statistical fluctuations in the nonuniform grid results, the plotted wall current densities are taken off the overlaid uniform grid. Current density results are plotted for Xe^{+}, Xe^{++}, secondary electrons, and primary electrons. The discharge chamber wall locations

(both axial and radial positions) are given in nondimensional units and the current density results are given in A/m^2.

Figure 5.11(a) shows the species current density collected at the radial locations of the back wall surface. Maximum current density value is observed for the secondary electron at the magnetic cusp location (at r=0.15 nondimensional units) on the back wall surface. Similarly the primary electron current density value is found to be larger at the cusp location. Both electron current density values are found to be dropping sharply before and after the cusp region. The secondary electron current density values at the non-cusp regions are found to be much smaller and the primary electron current values in the non-cusp regions are found to be zero. This occurs because of the strong magnetic field lines at the back wall surface. As shown in Figure 5.11(a) the Xe^{+} ion current density value is found to be 500 times smaller than the secondary electron current density value. The Xe^{++} and Xe^{+} current density results show that both ions are lost at all locations of the back wall surface. The Xe^{++} current density value is found to be smaller than Xe^{+} for most of the radial locations of the back wall. The peak current density values of all species are listed in Table 5.6.

Figure 5.11(b) shows the species current density results collected at the axial locations of the slanted wall and the side wall of the discharge chamber. The species current density results on the axial wall surfaces are smaller compared to the other radial wall surfaces (see Figures 5.11(a) and 5.11(c)). All species current density results are found to peak at three locations as identified in Figure 5.11(b). The first peak is at the hole region of the slanted wall surface (at z=0.27 nondimensional units), the second peak is at the cusp region of magnet-2 (at z=0.51 nondimensional units), and the third peak is at the hole region of the side wall (at z=0.72 nondimensional units). Out of these three peaks, all species are found to have the maximum current density values at the cusp location. The secondary electron is found to have the largest current density value in all of these three peaks. The maximum current density values for each species in the slanted wall hole region, side wall cusp region, and the side wall hole region are listed in Table 5.6. The observation of peak current density results in the slanted wall hole region and the side wall hole region further support the findings of

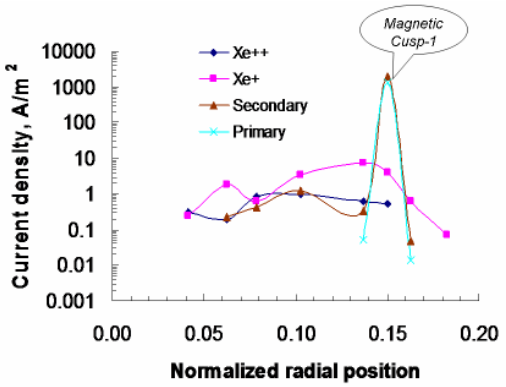

(a) Back wall radial surface.

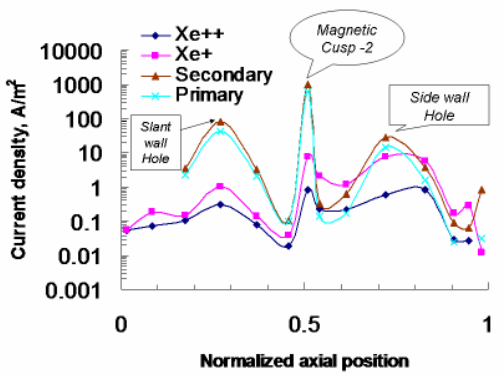

(b) Axial wall surfaces (both conical and cylindrical section).

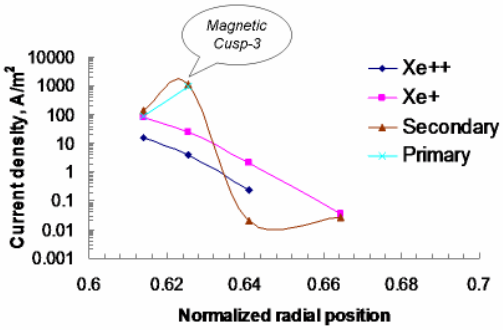

(c) Side flange radial surface.

Figure 5.11: Current density profiles along the walls of the discharge chamber for each of the four different charge particles at steady state for the base case of the NSTAR's TH-15 operating condition.

the magnetic field strength study conducted by Bennett et al [2007]. Only ion currents are found on the slanted wall surface axially from the discharge chamber to 0.2 nondimensional units. This indicates the magnetic field is sufficiently strong over this portion of the wall to stop electrons from reaching the slanted wall surface. At the slanted wall hole region the current density values of both positive and negative charge particles are found to be high. This indicates a hole in the magnet field. The species current density results axially between 0.37 to 0.5 nondimensional units are found to sharply drop from the slanted wall hole region current density results. The slanted wall's total electron current density is found to be 200% higher than the side wall hole region's total electron

Table 5.6: Maximum species current density values in A/m^2 at various discharge chamber wall surfaces at steady state for the base case of the NSTAR's TH-15 operating condition.

Location Details	Xe^{++}	Xe^{+}	Secondary electron	Primary electron
Back wall (Cusp-1)	0.9	7.3	1905.42	1368.67
Slant wall (Hole)	0.305	1.028	83.14	42.25
Side wall (Cusp-2)	0.852	7.85	975.63	624.1
Side wall (Hole)	0.57	7.62	27.9	14.84
Side wall flange (Cusp-3)	16.0	78.37	1103.67	902.67

current density. The slanted wall hole is more critical to discharge chamber performance than the side wall hole. Design changes can be made to plug these holes in the magnetic field. All species current density results at the side wall region closer to the screen grid (axially between 0.86 to 1 nondimensional unit) indicate that this portion of the side wall is well covered by the magnetic field lines from magnet-3.

Figure 5.11(c) shows the species current density results collected at the radial locations of the sidewall flange where magnet-3 is placed. The electron current density results are found to be large at the magnet-3 cusp location (at r=0.625 nondimensional units). Only secondary electron currents are observed radially after the cusp location on the side wall flange. Both Xe^{+} and Xe^{++} ion current density results are found to be large for the regions radially between r=0.61 nondimensional units and r=0.625 nondimensional units. These ion current density results are found to be much higher than the ion current density results observed in the magnet cusp locations on the back wall and the side wall of the discharge chamber. This large increase in ion current density could be due to the

proximity of the side wall flange to the screen grid. The maximum species current density values collected at the side wall flange are listed in Table 5.6.

5.2 Physical Parameter Study

In this particle based plasma model different physical processes have been included to simulate the plasma in an ion engine discharge chamber. Each physical process is put in to the model as it was believed to have some affect on the operation of the plasma. It would be interesting to see the effect of removing each of these physical processes on the output results of the plasma model. This is the reason for this physical parameter study. Because of the long computational times of the PIC-MCC simulation, it is not possible to study all physical process included in the plasma model, but at least a few of them can be looked at. It is the hope of the author that the developed PIC-MCC simulation will be used for analyzing different physical processes inside the ion engine discharge chamber and for a detailed design parametric study in the future. As a first step towards this long term project goal, a detailed physical parametric study is being considered in the present work. For this dissertation work, five different physical cases are considered with the developed PIC-MCC simulation. Apart from the physical parameter study, an alternative magnetic field configuration is being considered as a design parameter study. The results of an alternative magnetic field configuration are presented in the next section.

The main physical processes which are considered in this physical parameter study can be classified into two categories:

1. Electric field effects

2. Particle collision effects

In category two above three inelastic collision processes are studied: 1) electron - neutral excitation collisions, 2)electron - Xe^{+} excitation & electron-Xe^{++} excitation collisions, and 3) three-body recombination collisions between electrons and Xe^{+} or Xe^{++}. All physical parameter simulations

are performed on the same NSTAR discharge chamber with the same operating parameters and numerical parameters as used in the base case. In each physical parameter case, alterations are made to the specific physical process which is being studied. All cases use the same initial guess of particle distributions. All cases are simulated until the solution reaches a steady state condition or close to a steady state condition. Convergence issues are discussed for each case studied.

5.2.1 Electric Field Effects Study

Electric field effects are included in the plasma model in a static sense and a dynamic sense. As discussed in Chapter 2, static electric potentials are inputs to the PIC-MCC simulation and are obtained from experimental knowledge of the electric potentials in a plasma. The dynamic electric fields are obtained by solving Poisson's equation with the charge particle distributions. This is a dynamic model in that the electric fields are updated as the charge particle positions in the discharge chamber change. In addition, the charge particle positions are altered based on the most recent electric field calculated. An artificially high, $\varepsilon_0 = 10.8 \times 10^{-6}$ F/m, is used so that steady state results can be obtained in a reasonable amount of time. The dynamic electric potential results are superimposed on the input static electric potential field to produce the overall potential field.

Figure 5.12 shows a comparison between the static only electric field and the electric field that includes both the static and dynamic effects. The biggest visual difference is in the cathode region. The dynamic electric potentials have smoothed out the static input voltages around the cathode. In essence this means the PIC-MCC simulation developed in this work is not that dependent on experimental data. It may have been better to not enter the experimental data and let the dynamic field solver find its own voltage distribution around the cathode. An attempt is made to consider this option but it is found that the applied electric potential at the wall boundaries penetrate much deeper into the discharge chamber region with a larger sheath region. This indicates maintaining a sheath region through the input static field would restrict the growth of a larger sheath region. Hence I adopt a static input electric potential on top of the dynamic electric potential due to charge

particle distribution. Another difference is that the peak potential in the discharge chamber has increased from 28 volts to 30 volts. Some of the increase in voltage from 28 to 30 volts may be due to random statistical variations. These peak values would probably be reduced if the particle weighting could be lowered. This highlights one of the issues in doing a dynamic field calculation with a physically correct value of the plasma permittivity. Not only must the grid spacing become finer, the particle weighting must increase substantially. Because the grid spacing becomes finer the time step used must become much smaller as well. At this point in PIC history, modeling a large discharge chamber with a full dynamic field calculation is not practical. While not visible in the plot all sheath regions are still present when the dynamic field calculation is invoked.

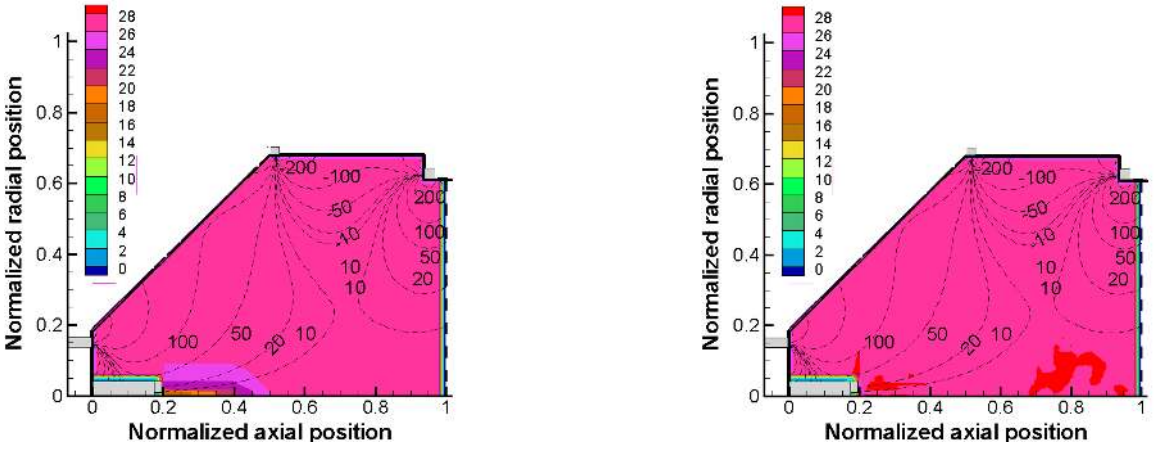

(a) Static Electric Field.

(b) Static and Dynamic Electric Field.

Figure 5.12: Comparison of electric potential distributions. Here the electric potential contours are given in volts.

In this study two alterations to the electric field are considered: the removal of the dynamic electric fields and making the wall sheaths thicker. The effects of each of these changes to the electric field are gauged by comparing their results to the base case results. The situation where the dynamic fields are removed from the PIC-MCC simulation will be referred to as the "no dynamic field" case, and the case where the sheath is thickened will be referred to as the "thick sheath" case.

For the no dynamic field case the Poisson solver is not applied to determine the dynamic electric

field effects caused by the charge particles. Electric field effects for the charge particle advance come only from the input static electric field. The thick sheath case is performed with the same setup as in the base case, except larger sheath regions on all chamber walls, the cathode keeper, and the screen grid are used. A sheath thickness of 6.4 mm is taken for this study. The base case sheath thickness was 3.2 mm.

5.2.1.1 Comparisons of Total Particle and Current Results

Comparisons of total particle results, discharge current, and ion beam current results for the three electric field parameter cases are presented in Table 5.7. The beam ion currents due to Xe^{+} and Xe^{++} are also listed in Table 5.7 to show the Xe^{++} content in the beam current. The base case simulation results were originally presented in Section 5.1; however, these results are presented again in Table 5.7 so that the reader can make easy comparisons between the three cases.

Table 5.7: Comparisons of steady state results for the three different electric field cases.

Discharge Chamber Results	Base Case	No Dynamic ϕ	Thick Sheath
$N_{phys,Xe}$	10.3×10^{16}	9.08×10^{16}	8.23×10^{16}
$N_{phys,Xe^{+}}$	3.06×10^{16}	2.38×10^{16}	2.41×10^{16}
$N_{phys,Xe^{++}}$	0.196×10^{16}	0.233×10^{16}	0.16×10^{16}
$N_{phys,pe}$	0.76×10^{16}	0.62×10^{16}	0.627×10^{16}
$N_{phys,se}$	2.72×10^{16}	9.89×10^{16}	2.16×10^{16}
I_D in A	17.8	13.0	18.3
I_B^{+} in A	1.23	0.95	1.55
I_B^{++} in A	0.55	0.26	0.61
I_B in A	1.78	1.21	2.16

The no dynamic field simulation is performed until a steady state condition is found on the results such as the discharge current, beam current, and total physical particles. The following results have shown convergence within a total number of 4×10^{6} iterations: the discharge current, the beam current, the total ion particles, and the total primary electrons. For the neutrals and the secondary electron particles, convergence was not obtained. The same convergence problem

of the total Xe particles and total secondary electron particles was observed when the developed PIC-MCC simulation without dynamic fields was applied to study the NSTAR TH-12 operation level [Mahalingam and Menart 2007b]. The TH-12 NSTAR calculation was found to take about 31 million iterations to reach convergence on the total Xe and the total secondary electron results, while all other results converged within (<2-5%) for 4×10^6 iterations [Mahalingam and Menart 2007b]. The reason the effect of the secondary electrons does not transfer to the other particles is that the electric field results are static and do not depend on the position of the charged particles. There will be some effect on the number of ions because of ionization collisions, but this effect is small as indicated in for the base case results in Table 5.4. The issue in the static field case is the secondary electrons have a high production rate relative to their ability to leave the discharge chamber. For this reason the number of secondaries will increase until their loss rate balances their production rate. In this parameter study it was felt that a completely converged solution is not required to show the differences between the no dynamic field case and the base case as the particle trends can be clearly seen from the results at 4×10^6 iterations. For this reason the simulation was only run for 4×10^6 iterations, instead of 31 million iterations. To carry this simulation out to convergence would require more than a month of computer run time on ten processors. The no dynamic field results at 4×10^6 iterations are listed in Table 5.7. Extrapolating the heavy neutral particles and the secondary electrons to a steady state condition, indicates the value of $N_{phys,Xe}$ is off by 17% and the value of $N_{phys,se}$ is off by 41%. Thus the expected steady state total physical particles result for Xe is 10.6×10^{16} and the steady state total physical particle results for the secondary electrons is 14.0×10^{16}.

The no dynamic field case's total particle results given in Table 5.7 show that the negative charges are not balanced by the positive charges. In a real ion engine discharge chamber plasma a perfect balance between charges is not achieved, because of the regions close to the walls and the cathode; however, a factor of 3.7 in this imbalance in favor of the electrons is too large. The ratio of the negative to positive charges in the base case is 1.01. This lack of overall charge balance in the no

dynamic field case is further illustrated in Figure 5.13. This figure clearly shows a good charge balance in the bulk of the discharge chamber when the dynamic electric field calculation is used, and a poor charge balance when the dynamic field calculation is not used. This result makes it obvious that accounting for the effect of the charges on the electric fields affects the results, even if an increased plasma permittivity is used. The number in Table 5.7 that stands out between the base case and the no dynamic field case is the difference in the total number of secondary electrons in the discharge chamber for the two cases. The number of secondary electrons in the no dynamic field case is 3.6 times as high as the number of secondary electrons in the base case. It appears that the dynamic fields are strong enough to have ions tug on electrons and aid them in leaving the discharge chamber. In the no dynamic fields calculation there is no long range force between the charged particles and the secondary electrons are not leaving the discharge chamber as easily. The other numbers that are interesting to compare between the no dynamic field and dynamic field calculations are the values of discharge and beam current results. The no dynamic field case provides a discharge current value of 13.0 A which is 13% smaller than the experimental discharge current. In the dynamic field case discharge current is found to be 19% higher than the experimental value. This indicates that the no dynamic field case predicts a better discharge current value. However the no dynamic field case is found to have 31% error in the beam current results compared to the experimental values. These results indicate that using of the dynamic field based on the inflated permittivity assumption is a better computational model than using the no dynamic field case.

The thick sheath simulation reaches a steady state condition on all results within 4×10^6 iterations. The steady state results for the thick sheath simulation are given in Table 5.7. The total physical particle results for the thick sheath case are lower than the base case results. A significant difference between the results for the total Xe^+ and total secondary electron particles exists. The beam current results indicate that there is a 26% increase in the Xe^+ beam ion current in the thick sheath case. The larger grid sheath region can accelerate more ions towards the screen grid which increases the ion beam current. These results seem to indicate that increasing the sheath thickness

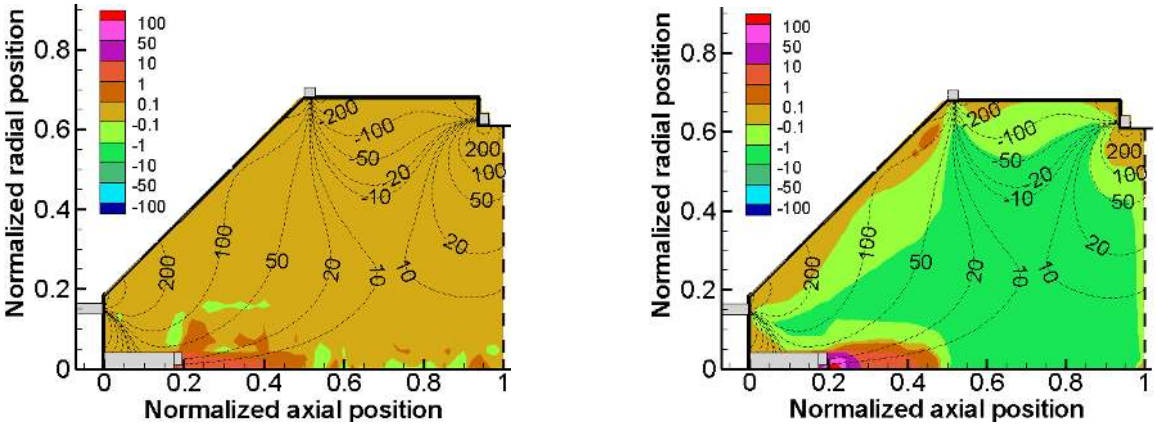

(a) Base Case.

(b) Xe^{++}.

Figure 5.13: Charge density results in C-m^{-3} for the base case and the no dynamic field Case at steady state condition.

increases the particle loss rate from the plasma to the discharge chamber walls.

5.2.1.2 Comparisons of Particle Distribution Results

In this subsection the base case particle distribution results are cross-referenced often. To save space these results are not repeated and the reader is referred back to the plots in Figures 5.2, 5.3, 5.5, 5.6, and 5.8. Figures 5.14 and 5.15 show the steady state plasma particle distribution results for the no dynamic field case and for the thick sheath case.

Comparing the Xe^{+} particle number density results between the base case and the no dynamic field case (see Figures 5.3 and 5.14(a)) clearly shows that there is a difference between the two cases. Maximum ion number density values are different and the shapes of the profiles are different. The no dynamic field case shows a high density island in the middle of the discharge chamber that does not show up when the dynamic fields are applied. The plume region around the cathode is much larger and denser than in the base case. This is most likely due to the static field having large electric potential gradients here, while the dynamic fields have almost eliminated these gradients.

The Xe^{++} number density distribution results (see Figure 5.14(b)) for the no dynamic field case show similar comparisons to the base case results (see Figure 5.5) as the Xe^{+} number density results.

The white spots shown in Figure 5.14(b) are locations where there are no computational particles. This is due to the particle weighting. This did not happen in the base case results shown in Figure 5.5. The interesting aspect of this is that there is a very low Xe^{++} number density region above the cathode plume and in the back of the conical section in the no dynamic field case which does not occur in the base case. It is not understood why this happens.

Comparing the primary electron number density results for the base case and no dynamic field case (see Figures 5.6 and 5.14(c) it can be seen that more primary electrons are found along the discharge chamber centerline in the base case simulation. This indicates that the number of primary electrons becoming secondary electrons after inelastic collisions with heavy particles is larger in the no dynamic field case. This is probably due to voltage profile difference in the cathode plume region. This is also substantiated by the large increase in secondary electrons in the no dynamic field case.

In comparing the secondary electron number density results for the base case to the no dynamic field case large differences can be seen (see Figures 5.8 and 5.14(d)). First, the no dynamic field case shows larger secondary electron number densities at most location in the discharge chamber. The values in the no dynamic field case range from ($> 1 \times 10^{19}$ m^{-3}) in the cylindrical section of the discharge chamber radially from thruster centerline to 0.52 nondimensional units. The average kinetic energy of the secondary electron is found to be 1.6 eV which is smaller than the average kinetic energy value of the secondary electron in the base case simulation, 2.5 eV. At the sheath regions a potential drop of 2.86 volts is maintained from the bulk plasma potential, 28 volts, to the chamber wall potential, 25.14 volts. The higher energy base case secondary electrons have a greater chance of making it over this potential barrier than the lower energy secondary electrons in the no dynamic field case. This the no dynamic field case will increase the number of secondary electrons in the discharge chamber because they are having a harder time escaping to the wall. The point that should be made about the secondary electron distributions is the way in which they follow the magnetic field lines. In the no dynamic field case the secondary electron number density contours follow the magnetic field lines much closer than they do in the base case. Notice that the ion number

density plots in the no dynamic field case do not follow the magnetic field lines. This is reasonable behavior with no coupling between the charged particles. With no particle interactions the light electrons follow the magnetic field lines while the heavy ions do not. In the base case the electrons and ions are seen to have similar contour shapes. The reason for this is the coupling between the electrons and the ions through the dynamic electric fields.

Figures 5.2 and 5.14(e)) shows that no large differences between the base case neutral number density distributions and the no dynamic field neutral particle distribution exists. This along with the smaller number of single ions in the no dynamic field case indicate that the reason for the increased number of secondary electrons is because the secondary electrons are having a hard time escaping from the discharge chamber. This happens because of the no charge separation effects in the no dynamic field case. The one small difference in the two neutral number density plots is the greater neutral particle depletion along the center line in the base case as compared the no dynamic field case.

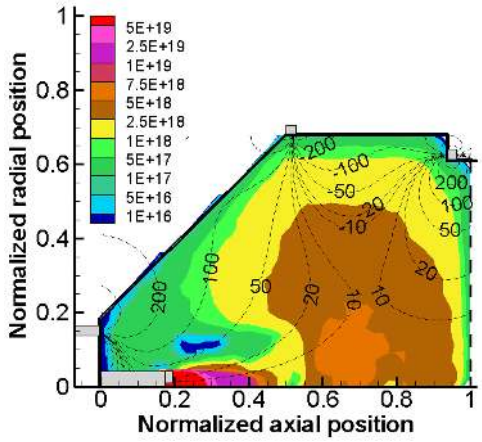

(a) Xe^{+}.

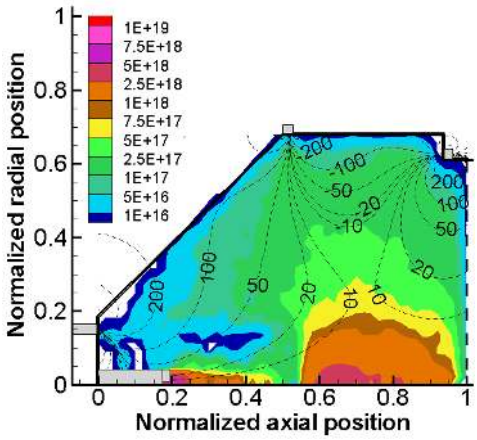

(b) Xe^{++}.

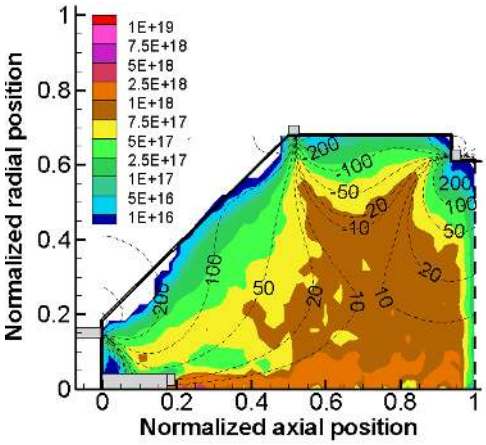

(c) Primary electron.

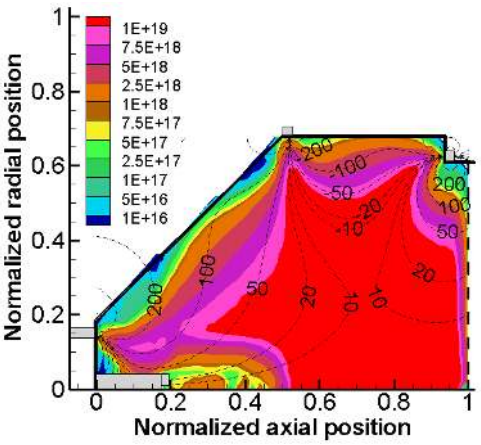

(d) Secondary electron.

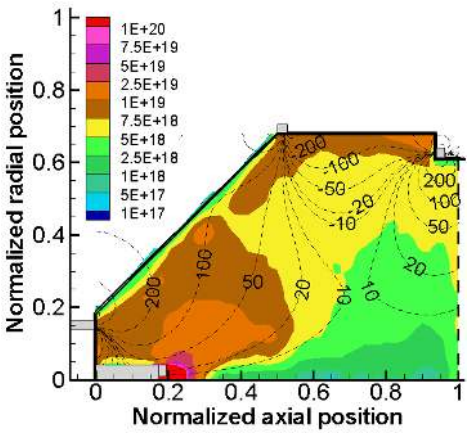

(e) Xe.

Figure 5.14: Plasma particle number density results in m^{-3} for the no dynamic field case.

In the thick sheath case simulation the sheath width is doubled in the input static electric field compared to the base case. The electric potential fall at the sheath is the same between the base case and the thick sheath case. Both of these cases use dynamic electric fields, but because the static sheath is doubled in thickness it will also be bigger when the dynamic field is applied. The electric potentials for the base case are shown in Figure 5.12(b) and the electric potential fields for the thick sheath case are shown in Figure 5.15(a). These plots are almost exactly the same except for the thicker sheaths that can more easily be seen in the thick sheath case. The other difference is the red higher electric potential seen at the centerline at an axial position from 0.7 to 0.9 nondimensional units in the base case. This does not show up in the thicker sheath case. This would indicate to the author that this region in the base case is due to statistical problems.

As can be deduced from the thick sheath results in Table 5.7 the same conclusion can be drawn from the particle distribution plots. This conclusion is that the plasma model developed as part of this work does not have a strong sensitivity to the sheath thickness. The biggest differences between the two cases occur in the primary electron number density plots. The thick sheath case has a smaller number of primary electrons because the larger sheath makes it easier for the primary electrons to reach the discharge chamber walls in the cusp regions.

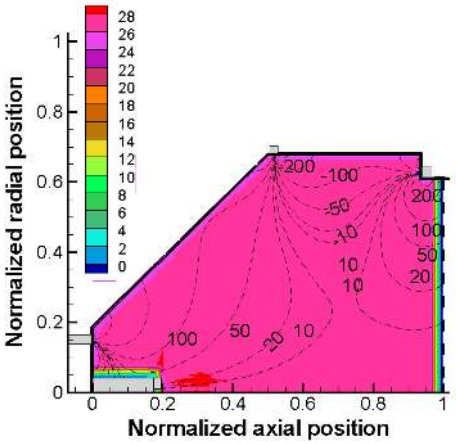

(a) Electric potential in volts.

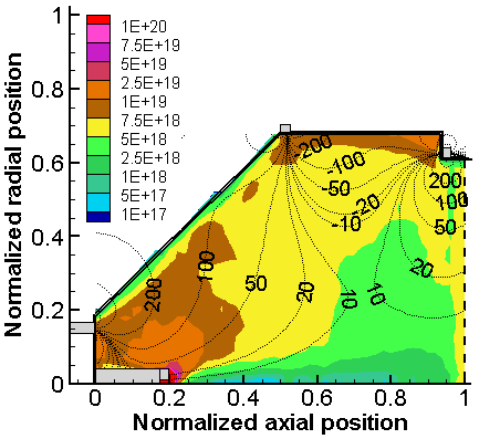

(b) Xe.

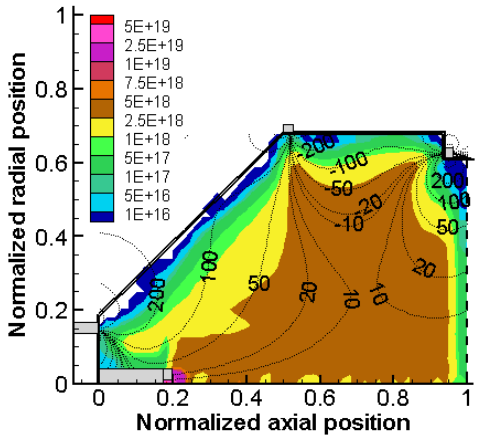

(c) Xe^{+}.

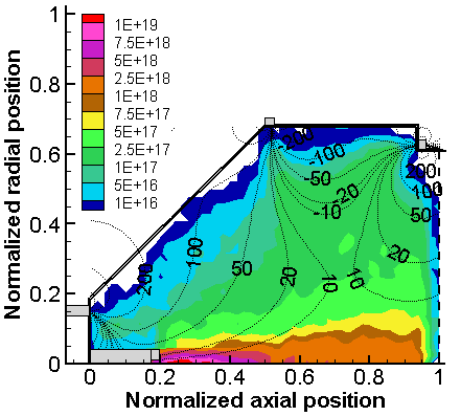

(d) Xe^{++}.

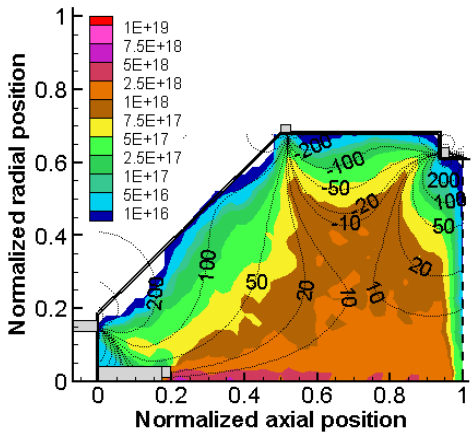

(e) Primary electron.

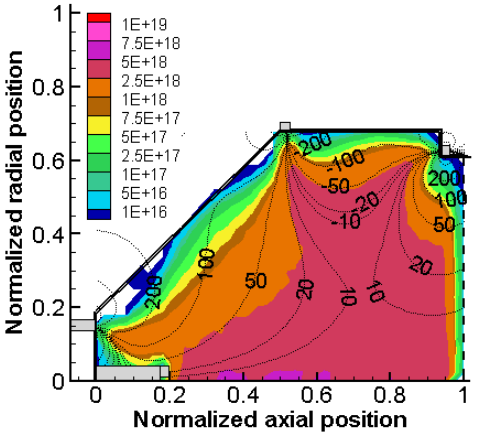

(f) Secondary electron.

Figure 5.15: Plasma particle number density results in m^{-3} for the thicker sheath case.

5.2.2 Particle Collision Study

In this plasma model a number of different types of collisions are included. The most important type of collision is an ionization collision between an electron and a neutral. Without these collisions there would be no plasma. Thus there is no doubt electron-neutral ionization collisions are important to the final results. There are three collision types for which it was desired to gain a better understanding of their effect on the discharge chamber performance. These collisions are electron-neutral excitation, electron-impact ionization, and three body recombination of electrons and ions. These collisions are essentially energy draining mechanisms from the plasma; more efficient discharge chamber operation could be obtained if they were not present. Table 5.4 results for the base case indicate that 34% of the inelastic electron collisions that occur in the discharge chamber are Xe excitation collisions. Hence this collision is believed to be a large energy drain on the plasma. Electron excitation collisions for ions are much smaller, $\sim$1%, but these are checked in this study as well. The third collision type studied is that of three body recombination. Table 5.4 indicates that 6.2% of the inelastic electron collisions are recombination. This is not high compared to the inelastic collisions of electrons with neutrals, but the results of this type of collision are the loss of an ion before it has a chance to leave the discharge chamber and produce thrust. Previous computational models have neglected recombination effects and it is felt that a study should be made to see how important the recombination collision processes are. This study will eliminate each of these three collisions from the PIC-MCC simulation to see their effect on the final results. The results should be compared to the base case results given in Section 5.1.

All cases are run until the numerical results reach steady state condition. The steady state condition is taken based on convergence of the discharge current, beam current, and total physical particle results with number of iterations. Nearly about 70 million iterations are required for reaching steady state condition on these three particle collision cases. The iteration convergence results for the no xe excitation can be found in chapter 4.

5.2.2.1 Comparisons of Total Particle and Current Results

Table 5.8 lists the total particle results, the discharge current and beam current results computed using 4×10^6 for the no ion excitation case and 21×10^6 for the no Xe excitation case and the no recombination case. Base case results are also shown in this table. Table 5.9 and Table 5.10 show the volume averaged collision rates for the same four cases listed above. The percentages of base case particle collision rates are also given. The relative percentage values show how the collision weighting changes relative to the base case values.

The general trends seen in Table 5.8 indicate that removing an energy draining collision from the discharge chamber plasma increases the discharge current and increases the beam current. In addition the number of ions and electrons are increased while the number of neutrals is decreased. This is what one would expect. The unexpected result is the effect of recombination on the magnitude of these changes. It was not surprising that the elimination to the ion excitation collisions does not have much effect on the results because the number of ion excitation collisions is small. It also was not surprising that the elimination of the Xe excitation collisions had a significant effect on the results. Many Xe excitation collisions occur in the plasma. The surprising result was the changes seen when the recombination collisions were removed. There are only 6% of the recombination collision occurring in the plasma. Even though this is the case, there presence affects the discharge chambers performance. The trends in Table 5.9 and Table 5.10 show that eliminating an energy draining collision from the PIC-MCC simulation leaves energy for more ionization collisions. For the no recombination collisions case the primary electron ionization collisions for the production of first ions goes down; however, it goes up for secondary electrons and the number of ionization collisions of Xe^+ to Xe^{++} goes up considerably. this is most likely caused by there being more Xe^+ available to ionize to Xe^{++}.

Table 5.8: Comparisons of steady state results for the four different particle collision cases.

Steady State Results	Base Case	No Ion Excitation	No Xe Excitation	No Bulk Recombination
$N_{phys,Xe}$	10.3×10^{16}	8.31×10^{16}	2.52×10^{16}	2.53×10^{16}
N_{phys,Xe^+}	3.06×10^{16}	2.79×10^{16}	2.39×10^{16}	2.61×10^{16}
$N_{phys,Xe^{++}}$	0.196×10^{16}	0.401×10^{16}	0.77×10^{16}	0.99×10^{16}
$N_{phys,pe}$	0.76×10^{16}	0.826×10^{16}	0.87×10^{16}	1.25×10^{16}
$N_{phys,se}$	2.72×10^{16}	2.81×10^{16}	3.13×10^{16}	3.37×10^{16}
I_D in A	17.8	18.2	21.4	20.4
I_B^+ in A	1.23	0.97	0.78	1.0
I_B^{++} in A	0.55	0.88	2.1	1.8
I_B in A	1.78	1.85	2.88	2.8
I_B^* in A	1.51	1.41	1.83	1.9

5.2.2.2 Comparisons of Particle Distribution Results

Figure 5.16 shows plasma particle number density results for the no ion excitation collision case. No significant differences are observed between these results and those for the base case for Xe^+, primary electrons, secondary electron, and Xe (see Figures 5.2, 5.3, 5.6, and 5.8). However, there are differences in the Xe^{++} particle distribution results (see Figure 5.5 for base case results). The no ion excitation collision results show higher number density values in the bulk of the discharge chamber. The Xe^{++} ion number density values for the no ion excitation collision case are found to be at least two times bigger than the number density values of the base case result.

Table 5.9: Comparisons of volume averaged inelastic collision rates for primary electrons at steady state condition for the four different particle collision parameter cases. Also the relative percentages of inelastic collision rates with respect to the base case inelastic collision rates are given.

Collision Rates ($\times 10^{20} m^{-3} s^{-1}$)	Xe Exc.	Xe Ionz	Xe^+ Exc	Xe^+ Ionz	Xe^+ Recomb	Xe^{++} Exc	Xe^{++} Recomb
Base Case	69.6	36.9	1.54	5.06	1.88	0.52	0.23
In %	100	100	100	100	100	100	100
No Ion Excitation	70.1	37.1	0	5.22	2	0	0
In %	100.7	100.5	0	102.9	106.7	0	0
No Xe Excitation	0	48.1	4.01	11.5	1.6	1.9	0.4
In %	0	130.4	259.5	227.5	85.4	366.6	173.8
No Bulk Recombination	59.1	31.0	3	7.81	0	1.26	0
In %	84.9	84.2	194.6	154.3	0	243.1	0

Table 5.10: Comparisons of volume averaged inelastic collision rates for secondary electrons at steady state condition for the four different particle collision parameter cases. Also the relative percentages of inelastic collision rates with respect to the base case inelastic collision rates are given.

Collision Rates ($\times 10^{20} m^{-3} s^{-1}$)	Xe Exc.	Xe Ionz	Xe^+ Exc	Xe^+ Ionz	Xe^+ Recomb	Xe^{++} Exc	Xe^{++} Recomb
Base Case	10.6	1.76	0.147	0.035	11.1	0.0027	1.36
In %	100	100	100	100	100	100	100
No Ion Excitation	11.0	2.10	0	0.07	11.8	0	0
In %	103.8	119.5	0	201.1	106.3	0	0
No Xe Excitation	0	8.21	1.3	0.65	12.0	0.1	3.21
In %	0	466	885	1867	108.1	3704	234.9
No Bulk Recombination	12.5	3.31	0.60	2.0	0	0.03	0
In %	118	187.8	408.4	574.7	0	1111.1	0

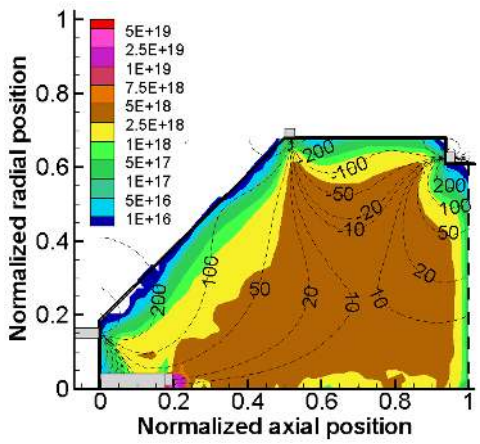

(a) Xe^{+}.

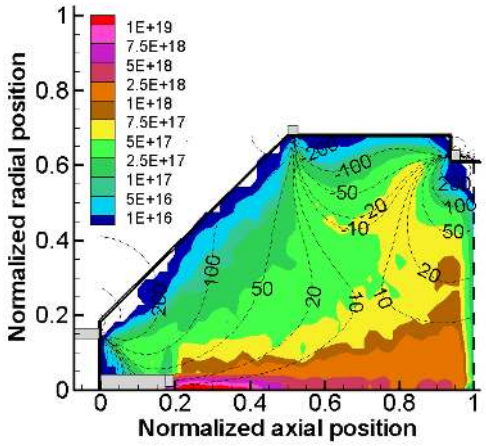

(b) Xe^{++}.

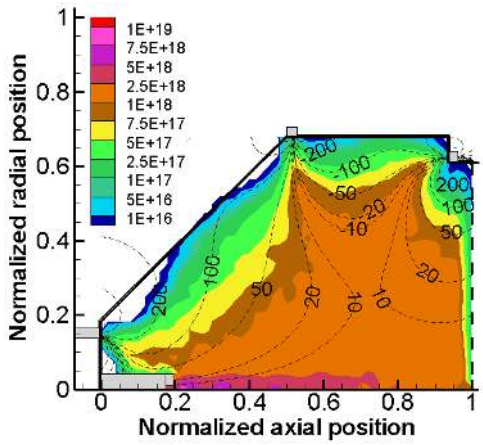

(c) Primary electron.

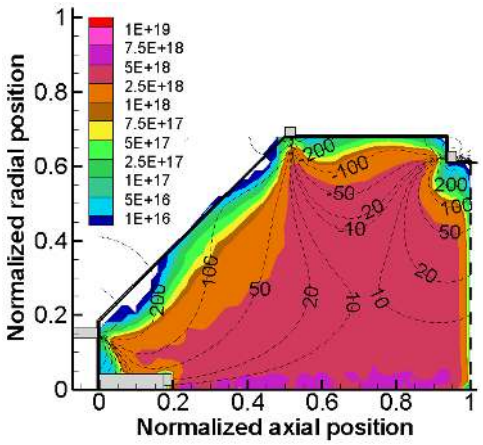

(d) Secondary electron.

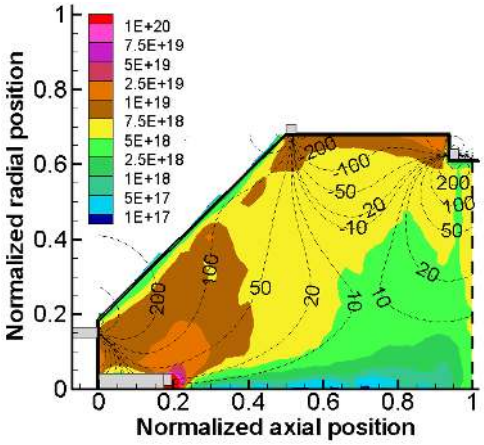

(e) Xe.

Figure 5.16: Plasma particle number density results in m^{-3} for the physical parameter case in which the ion excitation collision processes are turned off.

Figure 5.17 shows plasma particle number density distribution results for the no Xe excitation case. Large difference are seen when the plots for the no Xe excitation case are compared to the corresponding base case results. In the neutral number density plot a severe depletion of neutrals along the discharge chamber centerline is observed in the no Xe excitation case. The Xe number density values along the discharge chamber centerline are found to be an order magnitude smaller than the neutral number density results for the base case. Peak number density values are seen only at the cathode neutral source and at the main plenum source location. This neutral depletion occurs because there are more high energy electrons inside the discharge chamber when the Xe excitation collisions are removed. The neutrals that have been depleted show up as Xe^{++}. There is a substantial increase in Xe^{++} over the base case at the centerline. The Xe^{+} particles are reduced from the base case along the centerline. In general the secondary and primary electron increase in concentration along the centerline.

Figure 5.18 shows the plasma particle number density results for the no bulk recombination case. The no bulk recombination particle results are found to follow trends similar to the no Xe excitation case (compare Figures 5.18 and 5.17). There are a few differences in the results however. In the no bulk recombination no severe reduction of Xe^{+} ions is found along the discharge chamber centerline as in the Xe^{+} number density results of the no Xe excitation case. Also the primary electron number density values are found to be distributed more broadly across the discharge chamber. Severe depletion of neutrals along thruster centerline is still found in the no bulk recombination case as in the no Xe excitation case. Figure 5.18(e) shows this with white area along thruster centerline and the white area indicates that the Xe number density values in this region is below the minimum resolution that the computer code can resolve, i.e., ($\sim 1 \times 10^{15} m^{-3}$. The simulation results of the no Xe excitation case and the no Bulk recombination case show that the plasma is operating closer to the fully ionized regime.

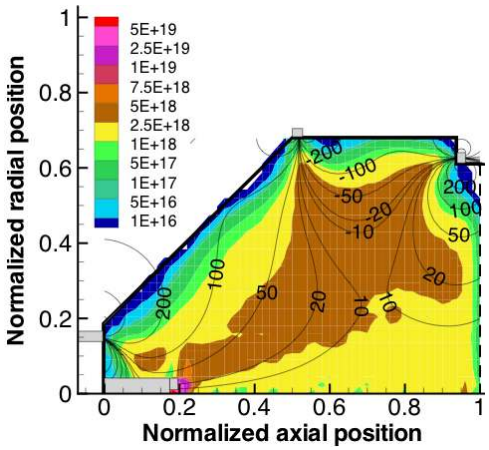

(a) Xe^{+}.

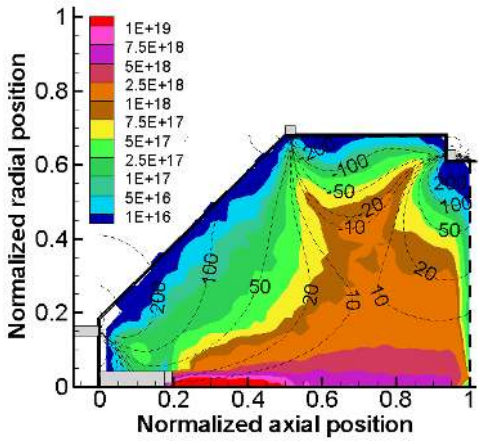

(b) Xe^{++}.

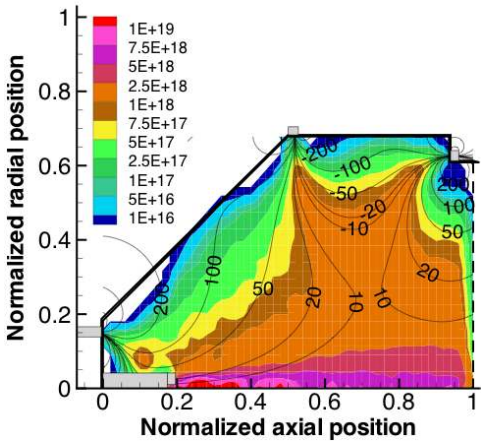

(c) Primary electron.

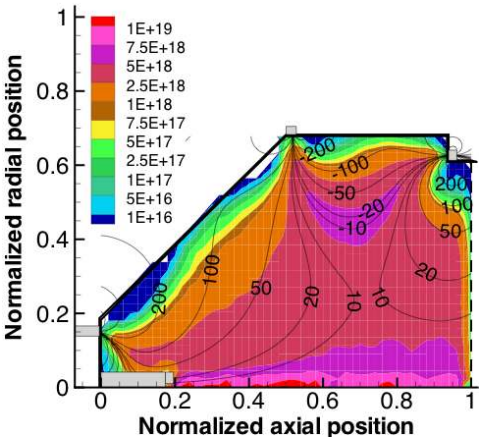

(d) Secondary electron.

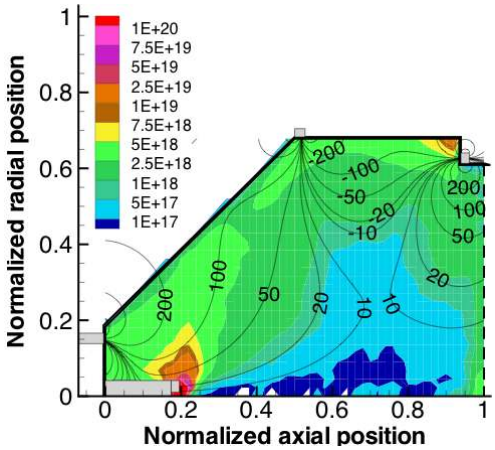

(e) Xe.

Figure 5.17: Plasma particle number density results in m^{-3} for the physical parameter case in which the Xe excitation collision processes are turned off.

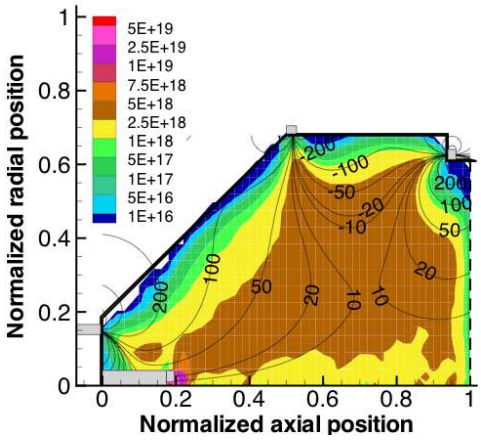

(a) Xe^{+}.

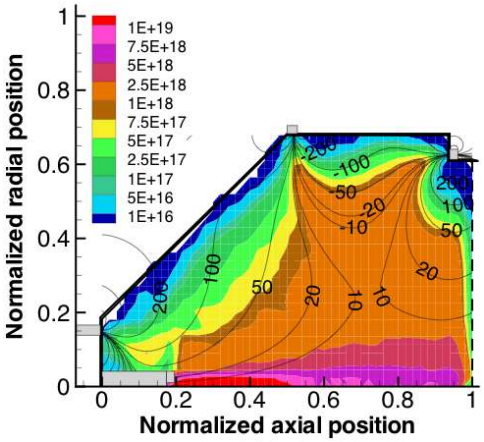

(b) Xe^{++}.

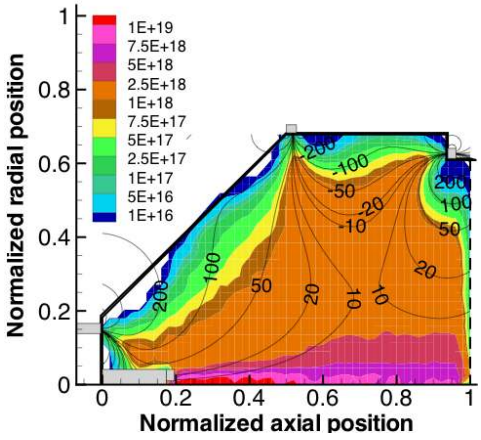

(c) Primary electron.

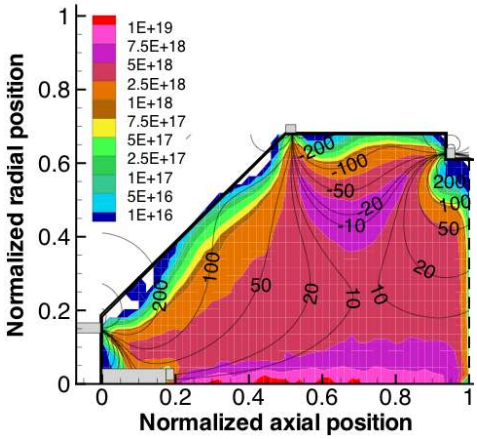

(d) Secondary electron.

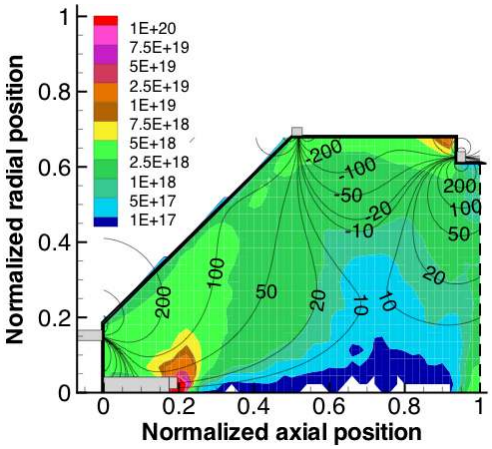

(e) Xe.

Figure 5.18: Plasma particle number density results in m^{-3} for the physical parameter case in which the bulk recombination collision processes are turned off.

5.3 Alternative Magnetic Field Design Study

In this section an alternative magnetic field design for the NSTAR thruster is studied. This alternate design change was suggested by Wirz [2005] from his computational study on the NSTAR discharge chamber. Wirz's study found that by simply doubling the middle magnetic ring (magnet-2) strength, the discharge chamber performance could be improved. Hence this magnetic field configuration is applied on the NSTAR discharge chamber and studied using the PIC-MCC model. This design study will be referred to as the alternate design case.

Comparisons of the two magnetic flux density contours for the base case and the alternate design case are given in Figure 5.19. Figure 5.19 shows that by strengthening the middle magnetic ring, stronger magnetic field lines are found to be moving radially inward from the side wall of the discharge chamber towards the discharge chamber centerline. Figure 5.20 shows the comparisons of the magnetic vector potential results for both the base case and alternate design case. In the alternate design case the 100 gauss-cm line that runs between magnet-1 and magnet-2 covers the slant wall region well. Also in the alternate design case for the regions axially between 0.5 nondimensional units to the screen grid and radially between the thruster centerline to 0.4 nondimensional units, the magnetic vector potential lines are found to be broadened.

The operating conditions and numerical parameters for the alternate design case simulation are the same as in the base case, except for the magnetic field input. Also the simulation is initiated with the same starting point of plasma particle distribution results as considered in the base case simulation. The simulation is run until the total physical particle results, discharge current, and beam current results have reached the steady state condition. The steady state condition is found to be reached on total particle results of all charge particle types, discharge current, and beam current. However, the total neutral particle result was found to be difficult, and did not reach convergence even after performing nearly 62×10^6 iterations. All the other results are found to converge in the 62 million iterations. The extrapolated steady state total neutral particle result in the alternate design

case was found to be differing by 5% from the 62×10^6 iterations result.

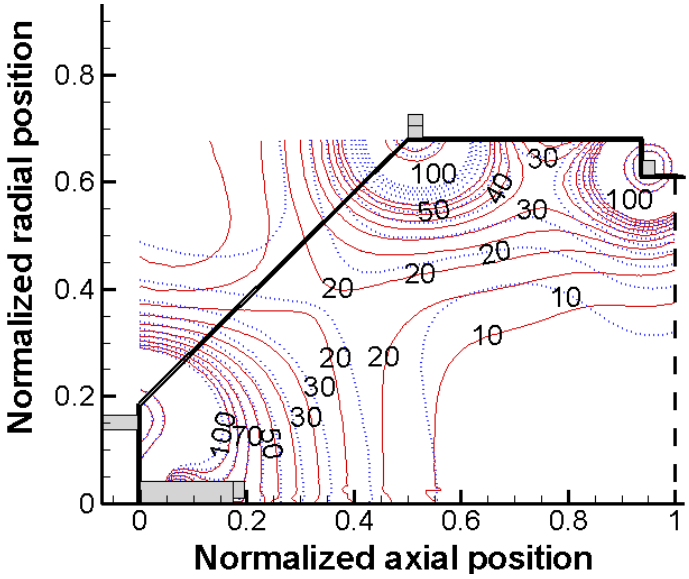

Figure 5.19: Comparisons of magnetic field strength results for the alternate magnet case (shown in solid contour lines) and the base case (shown in dotted lines) for the NSTAR discharge chamber. Here the magnetic field strength contour lines are given in gauss.

5.3.1 Results Comparison

Comparisons of the steady state total physical particle results and current results for the base case and the alternate design case are given in Table 5.11. A significant increase ($\sim$ 120%) is observed in the total Xe^{++} particle result for the alternate design case. The number of primary electrons inside the discharge chamber is found to be increased by 16%, while the total number of secondary electrons is increased by 11%. The total neutral particle result in the alternate design case is found to be decreased by 28% from the base case total neutral particle result .

No significant change is observed in the discharge current results between the base case and alternate design case. However, the total ion beam current result for the alternate design case is found to be increased by 48%. This large increase of I_B in the alternate design case is mainly due to the increase in the ratio of double-to-single ions in the beam current result. Only a slight increase is observed for I_B^+. The beam flatness parameter, F_B, for the alternate design case is found to be

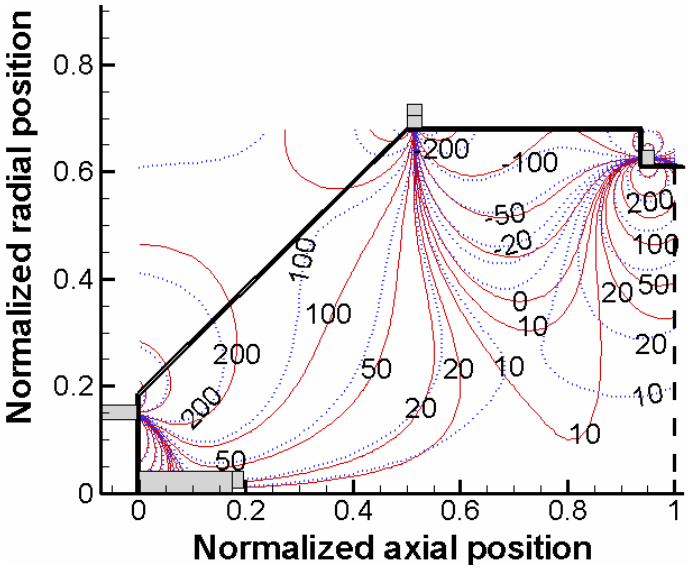

Figure 5.20: Comparisons of magnetic vector potential results for the alternate magnet case (shown in solid contour lines) and the base case (shown in dotted lines) for the NSTAR discharge chamber. Here the magnetic vector potential contour lines are given in gauss-cm.

0.52 and 0.56 for the beam current density profiles of $jB++$ and $jB+$ respectively. These values are higher than the beam flatness parameter results observed in the base case simulation and in the experiments (see Section 5.1.1).

Another result that is interesting to study in the alternate design case is the current density results collected at the chamber walls. The base case's current density results (see Section 5.1.5) reveal two magnetic hole regions other than the 3 magnetic cusp regions at the chamber walls. The first hole is identified at the slant wall (axially between 0.27 to 0.35 nondimensional units) and the second hole is identified at side wall (axially between 0.68 to 0.75 nondimensional units) of the discharge chamber. These two magnetic hole regions are found to be the next highest current density collection areas on the discharge chamber walls after the magnetic cusp regions. In the alternate design case, the magnetic vector potential lines that are running between magnet-1 and magnet-2 cover the slanted wall well compared to the base case (see Figure 5.20). At the slanted wall hole region, the magnetic flux density values are found to be 20 to 30 gauss in the alternate design case. These field strength values are higher than the base case result of 15 to 20 gauss. Similarly the

Table 5.11: Comparisons of steady state results between the base case and the Alternate Design Case.

Steady State Results	Base Case	Alternate Design
$N_{phys,Xe}$	10.3×10^{16}	5.9×10^{16}
N_{phys,Xe^+}	3.06×10^{16}	2.74×10^{16}
$N_{phys,Xe^{++}}$	0.196×10^{16}	0.59×10^{16}
$N_{phys,pe}$	0.76×10^{16}	0.94×10^{16}
$N_{phys,se}$	2.72×10^{16}	3.01×10^{16}
I_D in A	17.78	17.6
I_B^+ in A	1.23	1.1
I_B^{++} in A	0.55	1.5
I_B in A	1.78	2.6
I_B^* in A	1.505	1.85

side wall hole region in the alternate design case is found to be covered with higher magnetic field strength values ($\geq$ 50 gauss) compared to the base case's magnetic field strength values (35 to 40 gauss) at the side wall locations. Mahalingam and Menart [2007a] found that an 0.8 cm thick, uniform 50 gauss magnetic flux density lines that run parallel to the absorbing chamber wall provide good primary electron containment. Hence it is expected that the alternate design case, in which the high magnetic flux density lines are found to be covering the chamber wall well, would provide better containment for the electron particles.

The slanted wall and side wall current density results for the base case and the alternate design case are compared in Figure 5.21. Figure 5.21(a) clearly shows that the hole regions observed in the base case along the slanted wall is plugged well by the stronger magnetic field lines. The electron current density results (both secondary and primary electrons) in the alternate design case are found to be decreasing by a factor of 4 from the base case's electron current density results at the hole region. Similarly the ion current density results are found to be decreasing in the alternate design case. Figure 5.21(b) shows the comparisons of side wall current density results for both electrons and ions for the base case and the alternate design case. The current density results for the axial region where magnet-2's cusp is located is not included in this comparison, since the focus is mainly on the side wall hole region. The electron current density results in the alternate design case are

clearly showing that an insignificant amount of primary electrons are collected at the side wall hole region. This finding supports the rules-of-thumb set by other investigators on magnetic field design [Mahalingam and Menart 2007a; Bennett et al. 2007]. Also the secondary electron current density results are found to be decreased by an order-of-magnitude in the alternate design case compared to the base case's secondary electron current density results at the side wall hole region.

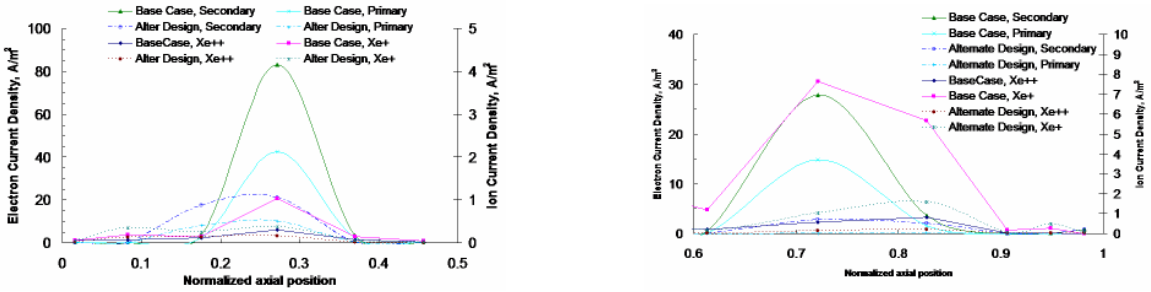

(a) Slant wall.

(b) Side wall.

Figure 5.21: Comparisons of electron and ion current density results at the axial wall surfaces for the base case and the alternate design case. The side wall current density results do not include the middle magnetic ring's cusp region.

Figure 5.22 shows the current density results for the different charge particles on various discharge chamber wall surfaces. Similar to the base case's current density results (see Section 5.1.3) most of the charge particles are lost at the magnetic cusp regions.

5.3.2 Particle Distribution Results

Figure 5.23 shows the steady state Xe^{+} number density results for the alternate design case. The Xe^{+} number density results of the base case and the Xe^{+} number density results of the alternate design case are found to be similar in the bulk of the discharge chamber (compare Figures 5.3 and 5.23). However, in the alternate design case the maximum Xe^{+} number density value in the cathode area is found to be $\sim 2.5 \times 10^{19}$ m^{-3}, while in the base case the maximum Xe^{+} number density value in the cathode area is found to be $> 5 \times 10^{19}$ m^{-3}.

Figure 5.24 shows the alternate design case's steady state Xe^{++} number density results. Smaller

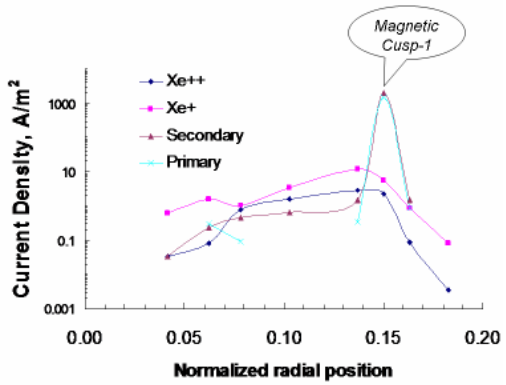

(a) Back wall radial surface.

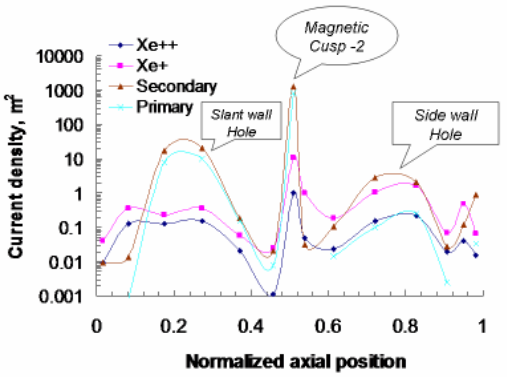

(b) Axial wall surfaces (both conical and cylindrical section).

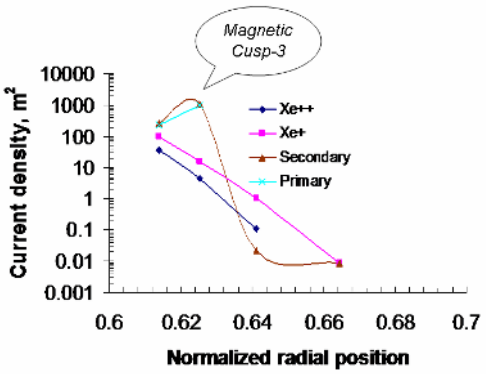

(c) Side flange radial surface.

Figure 5.22: Current density results for the four different charge particles on the discharge chamber wall surfaces at steady state condition for the alternate magnetic field design case.

peak Xe^{++} number density values are found downstream of the cathode keeper region (axially between 0.2 to 0.35 nondimensional units) in the alternate design case than the peak number density values observed in the base case Xe^{++} number density results (see Figures 5.5 and 5.24). In the cylindrical section of the discharge chamber (axially between 0.6 to 0.95 nondimensional units), the alternate design case shows Xe^{++} number density values to be uniform for the regions radially between the thruster centerline to 0.4 nondimensional units. This uniform distribution of the Xe^{++} number density results are responsible for the increase in the ratio of double-to-single ions in the beam current, and for the increased beam flatness in the alternate design case. The Xe^{++} number

density results are indicating that the magnetic field in the alternate design case allowed more radial movement of high energy primary electrons into the discharge chamber which causes the formation of uniform Xe^{++} number density results in the cylindrical section of the discharge chamber. In the base case the magnetic field along thruster centerline confines the primary electrons closer to the centerline causing peak Xe^{++} number density values along chamber centerline (see Figure 5.5). The Xe^{++} number density values are found to be decreasing radially. This occurs because of the increasing magnetic field strength values in the radial direction where the high energy primary electrons are confined.

Figure 5.25 shows the alternate design case's steady state primary electron number density results. No peak primary electron number density values are found in the alternate design case compared to the base case's primary electron results (see Figures 5.25 and 5.6). Also the primary electron number density contours in the cylindrical section are broadened more in the alternate design case indicating the presence of primary electrons. Smaller primary electron number density values near the side wall region indicate the confinement of primary electrons due to the strong magnetic field lines. Figure 5.26 shows the alternate design case's steady state secondary electron number density results. Similar to the primary electron results, no peak secondary electron number density values are observed along discharge chamber centerline in the alternate design case (compare Figures 5.26 and 5.8).

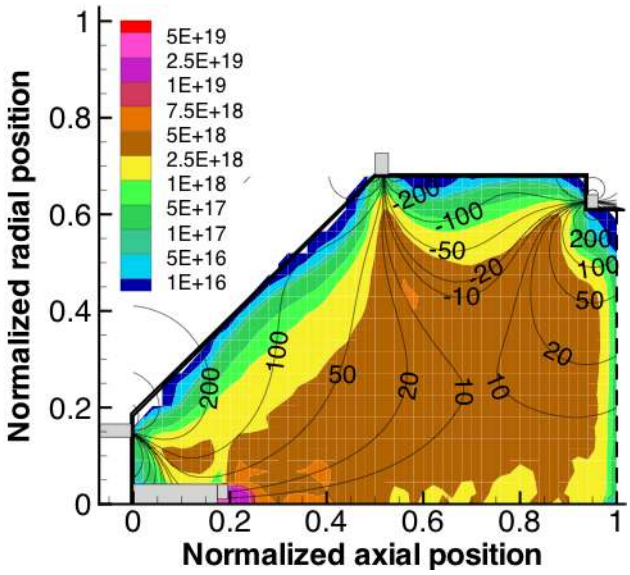

Figure 5.23: Xe^{+} particle number density results are given in m^{-3} for the alternative NSTAR design case at steady state condition.

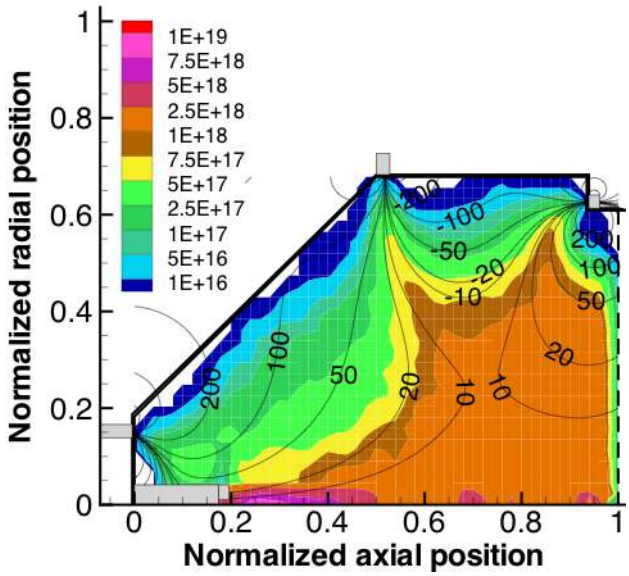

Figure 5.24: Xe^{++} particle number density results are given in m^{-3} for the alternative NSTAR design case at steady state condition.

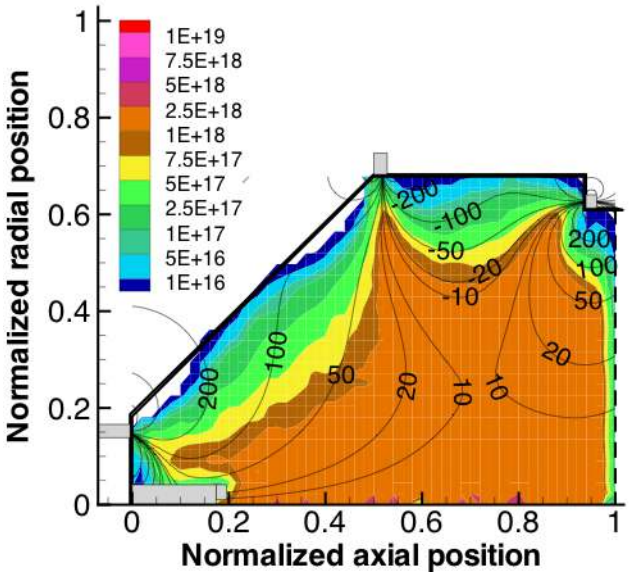

Figure 5.25: Primary electron particle number density results are given in m^{-3} for the alternative NSTAR design case at steady state condition.

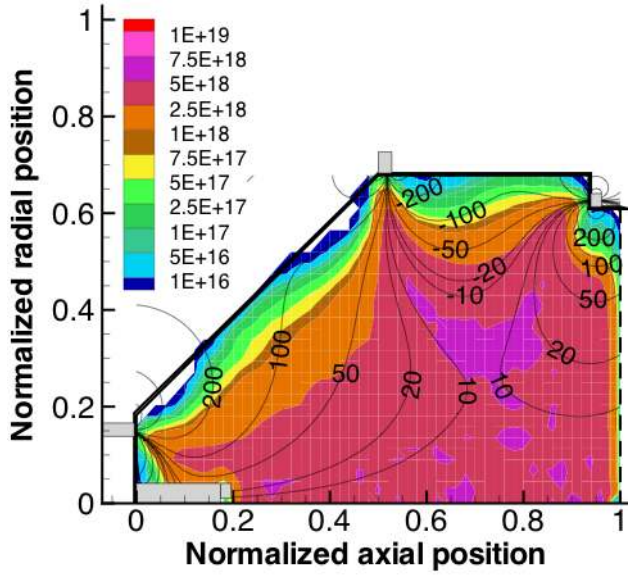

Figure 5.26: Secondary electron particle number density results are given in m^{-3} for the alternative NSTAR design case at steady state condition.

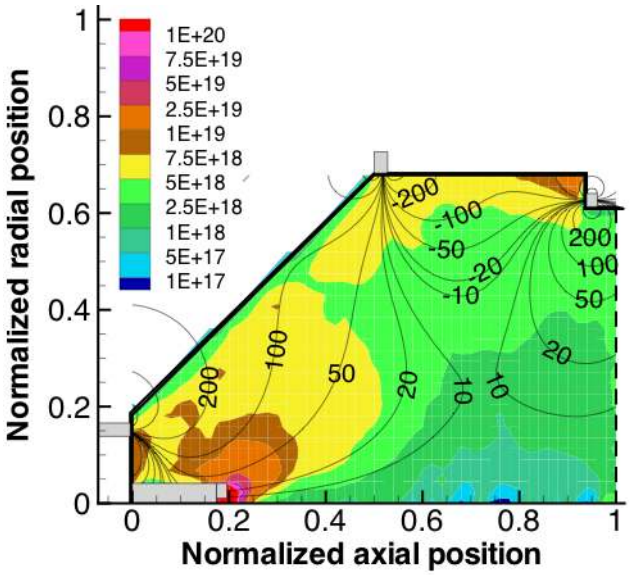

Figure 5.27: Xenon particle number density results are given in m^{-3} for the alternative NSTAR design case at steady state condition.

Figure 5.27 shows the alternate design case's Xe number density results. Neutrals are found to be depleted more in the cylindrical section of the discharge chamber than in the conical section. The neutral number density results in the cylindrical section increase gradually in the radial direction from the centerline to 0.5 nondimensional units, this indicates the depletion of neutrals through the ionization reactions. The increased number of high energy electrons presents in the cylindrical section cause more ionization reactions. In an ion engine discharge chamber it is desirable to have more ionization reactions in the cylindrical section which will possibly allow more ions to be extracted in the beam current through the grids. The alternate design case is found to increase the performance of the NSTAR ion engine.

6

Conclusions and Future Work

6.1 Present Work

In this dissertation a particle based computer model has been developed to study the plasma inside the discharge chamber of an ion engine. The developed computer model is the most comprehensive model that is currently available for simulating the ion engine discharge chamber. This work is unique in that a complete particle based model is used. Other investigations use diffusion approximations or the practice of only looking at a limited number of the particles present in the discharge chamber [Arakawa and Yamada 1990; Arakawa and Wilbur 1991; Mahalingam and Menart 2002; Stueber 2005; Wirz and Katz 2005]. This computer model tracks the neutrals, singly charged ions, doubly charged ions, primary electrons, and secondary electrons throughout the discharge chamber in a detailed fashion. Particle-particle collision types included in the model are Xe excitation, Xe ionization, Xe^{+} excitation, Xe^{+} ionization, Xe^{+} recombination, Xe^{++} excitation, and Xe^{++} recombination. Both electric and magnetic field effects on the charge particles are considered in the present work. Magnetic fields are considered to be static and the electric fields have a static and dynamic component. The dynamic electric field calculation couples the particle trajectory calculation with the electric field calculation. In addition, the dynamic electric field calculation couples ion

movement to electron movement. This simulation is a difficult task and an innovative technique of handling this problem has been devised. Using of an artificial plasma permittivity in the Poisson equation allows relaxation of the numerical parameters required for the discharge chamber plasma simulation. In addition, an input static electric field is considered in the simulation which partially uses the experimentally measured plasma potential data. This technique of electric field solving is approximate, but appears to give reasonable results when compared to experimental data. Also the technique helps including dynamic electric fields to avoid the extremely long computational times required to do the exact dynamic electric field simulation. The developed PIC-MCC simulation has been set up to run on multi-processors.

All the numerical studies in this dissertation are performed on NASA's NSTAR discharge chamber at its full operating power condition. A convergence study is conducted with the developed PIC-MCC simulation for all numerical parameters in the simulation. The convergence is checked in terms of the current results and the particle number density distribution results. The converged numerical parameters are:

$W_{macro} = 1.25 \times 10^{11}$ physical particles, $N_{e,cell} = 35$,

$\Delta t_e = 5 \times 10^{-10}$ s, $\Delta t_{ion} = 5 \times 10^{-8}$ s, $\Delta t_{Xe} = 1 \times 10^{-7}$ s,

$N_z = 100$, $N_r = 82$, $N_{cell} = 8200$,

$N_{iter,charge} = 5 \times 10^6$, $N_{iter,Xe} = \sim 100 \times 10^6$

The particle weight is found to be a critical parameter in this simulation and the numerical noise in the output results are found to scale with the $1/\sqrt{N_{cp}}$ relation established by other PIC investigators [Mardahl 2001]. It was found that when the average number of computer electron particles per cell are within the range of 10-50, the numerical results are less noisy. The number of iterations required for the neutral convergence, $N_{iter,Xe}$, is found to be 20 times bigger than the number of iterations required for the charge particles convergence, $N_{iter,charge}$. While these convergence parameters depend on the problem being analyzed, the values presented above provide the user with a place to start.

Comparisons of numerical results with experimental measurements such as beam current, propellant utilization efficiency, beam profile, currents collected at the discharge chamber walls, ion engine performance results, and particle number density distributions are made. The simulation results are found to be in good agreement with the experimental results in terms of the beam current, propellant utilization efficiency, screen grid ion current, and plasma ion production cost. The computed beam current density profile is in qualitative agreement with the measured results. Steady state results for the particle number density distributions, average energy results of primary electrons, secondary electrons, and singly charged ions are given. The particle distribution results are found to be similar to the experimental measurements at most of the locations inside discharge chamber. The peak number density values near the cathode and smaller number density results near the chamber walls also match well with experimental values. The cathode plasma plume next to the cathode keeper is found to be dominated with Xe^{++} ions. The depletion of neutrals along the thruster centerline is found to be significant as shown by experimental measurements. This indicates a fully ionized plasma ($n_ion > n_0$) in this region. The experimental comparisons performed in this dissertation validate the developed model.

A number of results for the NSTAR ion engine are provide by the model developed for this work. Large amounts of results at the global, intermediate, and local level are presented in this dissertation for the TH-15 operating condition. These results include the particle distributions, particle energy distributions, total particle results, particle collision results, energy loss mechanisms, particle loss percentages to different chamber walls, current densities collected at the chamber wall surfaces, and many ion engine performance parameters. Most of the particle losses to the walls occur at the magnetic cusp regions. The current density results at the chamber wall surfaces reveal two magnetic holes in the NSTAR magnetic field, which are in between the permanent magnets. These two hole regions are formed because of a large spacing between the magnets. Significant numbers of primary electrons lose their energy through Xe excitation processes and only the primary electrons are responsible for the creation of Xe^{++} ions inside the discharge chamber. The slow moving

secondary electrons contribute more to the discharge current than the fast moving primary electrons.

Physical parameter studies are conducted using the developed PIC-MCC simulation to understand the effect of the electric field and particle collisions. In the electric field effect study, the effect of approximating the electric fields through static and dynamic models is given. The dynamic field solver is based on an inflated permittivity which reduces computational times to the point that this full particle model is possible. The inclusion of a dynamic electric field solver does an excellent job of maintaining a charge balance in the discharge chamber. Also studied were the size of the sheaths at the walls. While doubling the sheath thickness does affect the results, it is not a strong effect. This indicates the results are not a strong function of the input sheath thickness to the model. From the particle collision study, the importance of both Xe excitation and three-body electron ion recombination processes are identified as energy draining plasma processes.

An alternative magnetic field design is considered for the NSTAR thruster to try and improve performance. In the alternative design the magnetic field strength of the middle magnet ring is doubled, as recommended by other investigators [Wirz and Katz 2005]. Improved performance results are observed in terms of the beam current, beam flatness parameter, propellant utilization efficiency, and discharge current. This magnetic field design is found to effectively plug the magnetic holes formed in the slanted wall and side wall of the NSTAR discharge chamber.

6.2 Future Work

6.2.1 Use of New PIC-MCC Simulation

The newly developed particle based computational tool presented in this dissertation can be utilized to study other throttling conditions of the NSTAR discharge chamber. At present only two high power throttling levels on the NSTAR discharge chamber, TH-15 and TH-12 conditions (see NSTAR Throttle Table in Appendix), have been simulated using this particle based plasma model. The simulation results for the TH-15 condition are given in this dissertation, while the TH-12 condition

was considered earlier in an earlier work [Mahalingam and Menart 2007b]. Both throttle condition simulation results are observed to match well with measured values for most of the thruster design parameters. Normally a variation of 5-10% between the computed and measured value is found. The present study can be extended to study other throttling conditions to understand the plasma structure (such as the particle distributions and energy distributions) inside the NSTAR discharge chamber. A detailed parametric study can be carried out to see how design alterations to the NSTAR thruster change its performance. While one alternate magnetic field design configuration was explored in this work, there are so many other options for the magnetic circuit. Numerous other design parameters can be studied on the NSTAR discharge chamber as well. A large number of magnetic field configuration designs were studied by Menart and co-workers in the WSU Ion Engine group [Deshpande et al. 2004; Deshpande et al. 2005; Deshpande 2005; Ogunjobi and Menart 2006; Bennett et al. 2007] for modeling the primary electrons inside the discharge chamber. These studies have devised rules-of-thumb for improving the performance of an ion engine in terms of the magnet orientation, spacing between the magnets, the magnetic field strengths, and cathode emission angle in relation to the magnet placement. Utilizing the developed PIC-MCC tool, these rules-of-thumb can be analyzed in a manner that includes a great deal more of the physics occurring in the discharge chamber. In the future NASA's new discharge chamber designs, such as the 40-cm NASA's Evolutionary Xenon Thruster (NEXT), can be studied.

6.2.2 PIC-MCC Model Improvement

Towards the end of this work a number of ideas were formulated for reducing the computational time required by the PIC-MCC simulation. A few of these ideas are listed below:

1. The parallel domain decomposition scheme followed in this work limits the number of processors employed for a run. The maximum number of processors possible is based on the total number of axial grid points and the requirement of having a minimum of 5 axial grid points for each processor. In this work the decomposition partitions are selected based on to maximize

the load balancing between the processors. However it is difficult to maintain load balancing between processors with this 1-D domain decomposition scheme since the plasma in an ion engine discharge chamber is non-uniform and particles are clustered in certain regions of the discharge chamber. This clustering changes as the computation progresses. Hence a domain decomposition scheme based on particles is desired. This can be achieved by adopting either a dual-decomposition scheme or a dynamic load partitioning between processors [Neiter and Cary 2004]. In a dual domain decomposition scheme two separate partitions are considered for the particles and the fields which helps achieve load balancing in both particle and field aspects. The price of this scheme is increased overhead for storing data and extra communications between the two partitions. In a dynamic load partitioning method both particles and fields have the same partition, but the number of computational cells and particles are dynamically adjusted while the simulation progresses. This scheme minimizes the overhead of storing data and also allows concurrent performance of exchanging information while the computations are performed.

The selection of which parallel scheme to be followed in the future depends on the resources available on new projects and how much the developers wish to alter the existing PIC-MCC code. I feel that enabling the dual decomposition parallel scheme would be a less strenuous alteration than the dynamic load balancing, based on the way the existing algorithm is written. The dynamic load balancing parallel scheme requires a full reversion of the basic algorithm used in the PIC-MCC computer code [Mardahl 2001].

2. The particle weight survey given in this work shows that the statistical noise in the simulation can be reduced by using lower particle weights. The problem with using a lower particle weight is the overall CPU time increases. In this work all species are assigned the same particle weight value. In the PIC-MCC simulation, as it stands, all particles have to use the same particle weight. This is computationally burdensome, because particles that are plentiful in the discharge chamber could use a higher weighting, whereas particles that are scarce should use a lower weighting.

For example, neutrals could be assigned a larger particle weight value and primary electrons could be assigned a lower particle weight value. This reduces the total number of computer particles used for the neutrals. Using the right particle weight for each species will reduce CPU time, while maintaining low noise in the results. Implementing such a scheme will require some detailed algorithms for keeping track of the particles after destructive collisions.

3. A non-uniform grid is considered in this work for resolving the sheath regions, high magnetic field strength regions, and the cathode emission source region. Using a structured grid to do this is wasteful. It is recommended that an unstructured mesh [Jacobs and Hesthaven 2006] such as an unstructured finite element scheme be implement into this PIC-MCC algorithm. Doing this will lower the total number of computational cells in the simulation while maintaining spatial resolution. Since the number of grid cells affects the particle weighting and time step size, this will help alleviate the requirements on particle weighting and time step size as well. The current PIC-MCC model's algorithm is based on a finite difference scheme and thus will require significant amounts of work to switch it to an unstructured finite element method.

4. In the PIC-MCC model results presented in this work it was found that the neutral particles take a long time to reach the steady state condition. This long transit time makes the convergence of the neutral particles difficult in a number of cases. The charge particles show converged results well before the neutrals. Other investigators of PIC-MCC models consider altering the mass of the neutral particles to bring them to convergence quicker. While this reduces their time to convergence, this assumption also affects the final results. This scheme should at least be considered in the future.

A

Serial DADI Solver

A.1 ADI Algorithm

The alternating direction implicit (ADI) algorithm is a splitting algorithm developed by Peaceman, Rachford and Douglas [Tannehill et al. 1997] and it is used for solving two-dimensional unsteady heat flow problems. This algorithm is desirable since it turns a large sparse matrix problem into a tridiagonal matrix problem. Solution for the Laplace/Poisson types of equations with the ADI method is possible by adding a fictitious time derivative to the Laplace/Poisson equation [Hewett et al. 1992]. It can be shown as below,

$$-\frac{\partial \phi}{\partial t} + \nabla^2(\varepsilon_a \phi) = -\rho. \tag{A.1}$$

This equation is finite differenced and marched in time to reach the steady state result. Once the solution reaches steady state the time derivative term vanishes leaving the steady state Poisson equation.

Letting $s = -\rho$ Equation (A.1) can be written as

$$\frac{\partial \phi}{\partial t} = \nabla^2(\varepsilon_a \phi) - s. \tag{A.2}$$

A five point stencil as shown in Figure A.1 is used to obtain the finite difference formulation of the

Laplace operator in Equation (A.2) [Birdsall and Langdon 1991] giving

$$\begin{aligned}\nabla^2(\varepsilon_a\phi) =& \frac{2\varepsilon_{a,i+1/2,j}}{\Delta z_{i,j}(\Delta z_{i,j}+\Delta z_{i-1,j})}(\phi_{i+1,j}-\phi_{i,j}) - \frac{2\varepsilon_{a,i-1/2,j}}{\Delta z_{i-1,j}(\Delta z_{i,j}+\Delta z_{i-1,j})}(\phi_{i,j}-\phi_{i-1,j}) \\ &+ \frac{2r_{i,j+1/2}\varepsilon_{a,i,j+1/2}}{(\Delta r^2)_j \Delta r_{j+1/2}}(\phi_{i,j+1}-\phi_{i,j}) - \frac{2r_{i,j-1/2}\varepsilon_{a,i,j-1/2}}{(\Delta r^2)_j \Delta r_{j+1/2}}(\phi_{i,j}-\phi_{i,j-1})\end{aligned} \tag{A.3}$$

where

$$\Delta r_{i,j+1/2} = r_{i,j+1} - r_{i,j} \tag{A.4}$$

and

$$(\Delta r^2)_j = r^2_{i,j+1/2} - r^2_{i,j-1/2}. \tag{A.5}$$

Here the artificial plasma permittivity, ε_a, values are evaluated at the cell face centers, (i+1/2,j), (i-1/2,j), (i,j+1/2), and (i,j-1/2).

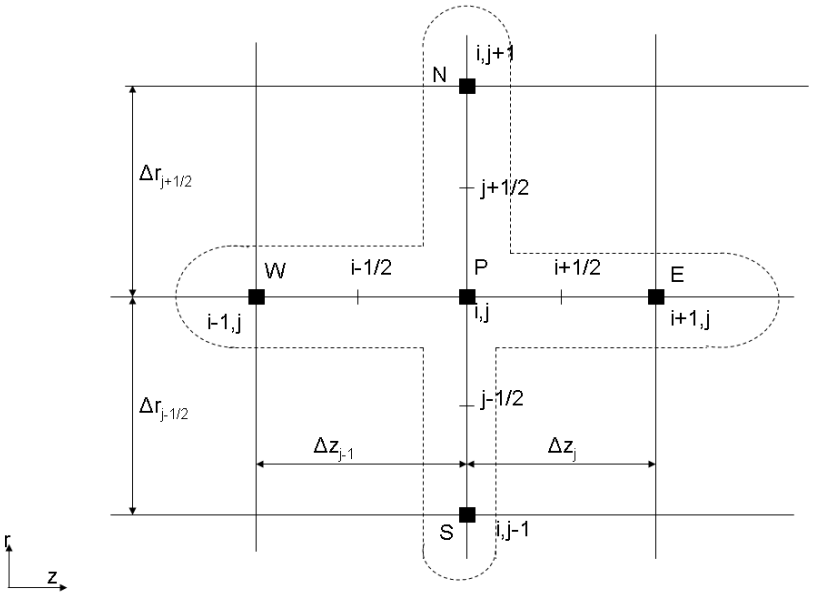

Figure A.1: A five-point finite difference system for the Laplace operator.

In coefficient form, the Laplace operator in Equation (A.3) is

$$\nabla^2(\varepsilon_a\phi) = a'_{E,i}\phi_{i+1,j} + a'_{P,i}\phi_{i,j} + a'_{W,i}\phi_{i-1,j} + a'_{N,j}\phi_{i,j+1} + a'_{P,j}\phi_{i,j} + a'_{S,j}\phi_{i,j-1} \tag{A.6}$$

where

$$a'_{E,i} = \frac{2\varepsilon_{a,i+1/2,j}}{\Delta z_{i,j}(\Delta z_{i,j} + \Delta z_{i-1,j})}, \tag{A.7}$$

$$a'_{W,i} = \frac{2\varepsilon_{a,i-1/2,j}}{\Delta z_{i-1,j}(\Delta z_{i,j} + \Delta z_{i-1,j})}, \tag{A.8}$$

$$a'_{P,i} = -(a'_{E,i} + a'_{W,i}), \tag{A.9}$$

$$a'_{N,j} = \frac{2r_{i,j+1/2}\varepsilon_{a,i,j+1/2}}{(\Delta r^2)_j \Delta r_{j+1/2}}, \tag{A.10}$$

$$a'_{S,j} = \frac{2r_{i,j-1/2}\varepsilon_{a,i,j-1/2}}{(\Delta r^2)_j \Delta r_{j-1/2}}, \tag{A.11}$$

and

$$a'_{P,j} = -(a'_{N,j} + a'_{S,j}). \tag{A.12}$$

Substituting Equation (A.6) into Equation (A.2) and performing a finite difference on the time dependent term (A.2) gives

$$\left[\frac{\phi^{k+1}_{i,j} - \phi^{k}_{i,j}}{\Delta t_f}\right] = a'_{E,i}\phi_{i+1,j} + a'_{P,i}\phi_{i,j} + a'_{W,i}\phi_{i-1,j} + a'_{N,j}\phi_{i,j+1} + a'_{P,j}\phi_{i,j} + a'_{S,j}\phi_{i,j-1} - s_{i,j}. \tag{A.13}$$

Here Δt_f is the fictitious time step size used in the ADI algorithm.

A two-step procedure is used to solve Equation (A.13):

Step 1 (z-pass): In Step 1 of the ADI, the implicitness is applied in the z-direction. Only half of the fictitious time step size, Δt_f, is applied in this pass and hence the implicit ϕ values are represented with a $k + 1/2$ superscript. Thus Equation (A.13) becomes

$$\left[\frac{\phi^{k+1/2}_{i,j} - \phi^{k}_{i,j}}{0.5\Delta t_f}\right] = a'_{E,i}\phi^{k+1/2}_{i+1,j} + a'_{P,i}\phi^{k+1/2}_{i,j} + a'_{W,i}\phi^{k+1/2}_{i-1,j} + a'_{N,j}\phi^{k}_{i,j+1} + a'_{P,j}\phi^{k}_{i,j} + a'_{S,j}\phi^{k}_{i,j-1} - s_{i,j}. \tag{A.14}$$

Simplifying the above equation and grouping like terms gives

$$a_{E,i}\phi^{k+1/2}_{i+1,j} + a_{P,i}\phi^{k+1/2}_{i,j} + a_{W,i}\phi^{k+1/2}_{i-1,j} = RHS^{k}_{i,j} \tag{A.15}$$

where

$$a_{E,i} = -0.5\Delta t_f a'_{E,i}; \tag{A.16}$$

$$a_{W,i} = -0.5\Delta t_f a'_{W,i}; \tag{A.17}$$

$$a_{P,i} = 1 - 0.5\Delta t_f a'_{P,i}; \tag{A.18}$$

and

$$RHS^k_{i,j} = \phi^k_{i,j} + 0.5\Delta t_f \left(a'_{N,j}\phi^k_{i,j+1} + a'_{P,j}\phi^k_{i,j} + a'_{S,j}\phi^k_{i,j-1} - s_{i,j} \right). \tag{A.19}$$

Equation (A.15) shows the tridiagonal system of equations for each j row of grid points. Hence a tridiagonal matrix is solved for each j row of grid points using a tridiagonal matrix algorithm (TDMA). In this manner the intermediate electric potential values, $\phi^{k+1/2}_{i,j}$, are calculated for all the grid points.

Step 2 (r-pass): In step 2 the direction of implicitness is alternated to the r-direction and new values are obtained for the ϕ values coming from the r-direction derivatives. Here the remaining half fictitious time step is used to get the potential values at the next iteration level, $k+1$. For this step Equation (A.13) becomes

$$\left[\frac{\phi^{k+1}_{i,j} - \phi^{k+1/2}_{i,j}}{0.5\Delta t_f} \right] = a'_{E,i}\phi^{k+1/2}_{i+1,j} + a'_{P,i}\phi^{k+1/2}_{i,j} + a'_{W,i}\phi^{k+1/2}_{i-1,j} + a'_{N,j}\phi^{k+1}_{i,j+1} + a'_{P,j}\phi^{k+1}_{i,j} + a'_{S,j}\phi^{k+1}_{i,j-1} - s_{i,j}. \tag{A.20}$$

Simplifying the above equation and grouping like terms gives

$$a_{N,j}\phi^{k+1}_{i,j+1} + a_{P,j}\phi^{k+1}_{i,j} + a_{S,j}\phi^{k+1}_{i,j-1} = RHS^{k+1/2}_j \tag{A.21}$$

where

$$a_{N,j} = -0.5\Delta t_f a'_{N,j}; \tag{A.22}$$

$$a_{W,j} = -0.5\Delta t_f a'_{W,j}; \tag{A.23}$$

$$a_{P,j} = 1 - 0.5\Delta t_f a'_{P,j}; \tag{A.24}$$

and

$$RHS^{k+1}_{i,j} = \phi^{k+1/2}_{i,j} + 0.5\Delta t_f \left(a'_{E,i}\phi^{k+1/2}_{i+1,j} + a'_{P,i}\phi^{k+1/2}_{i,j} + a'_{W,i}\phi^{k+1/2}_{i-1,j} - s_{i,j} \right). \tag{A.25}$$

Equation (A.21) gives a system of equations that allow a TDMA solution for each i column of grid points. Now the electric potential values are available at the $k+1$ level. This completes one iteration

of the ADI scheme which uses two passes. The two-pass ADI iterations are performed repeatedly until the solution reaches steady state.

A.2 Serial DADI Solver

In the DADI scheme the fictitious time step size is varied from iteration to iteration to accelerate the speed of convergence. This is the reason why this algorithm is known as a dynamic alternating direction implicit (DADI) scheme. The DADI procedure is described here. More details of the DADI scheme can be found from references [Doss and Miller 1979; Hewett et al. 1992].

Since the primed coefficients of the Laplace operator term given in Equations (A.7)-(A.12) are constant, they are precomputed before performing the DADI solver. Also the initial fictitious time step size [Doss and Miller 1979] for the DADI solver's first iteration is given by

$$\Delta t_f^0 = \min\left(0.1\left[(\Delta z_{i,j})^2 + (\Delta r_{i,j})^2\right]/\varepsilon_a\right). \tag{A.26}$$

The DADI iteration steps are given below:

1. Iteration index, k is set to zero.

2. Two successive ADI sweeps are performed using the fictitious time step size, Δt_f^k to obtain the potential solutions from ϕ^k to ϕ^{k+1}.

3. A single ADI sweep is performed with twice the fictitious time step size $2\Delta t_f^k$ to obtain the potential solutions from ϕ^k to $\overline{\phi}^{k+1}$. This step is conducted to see whether the selected Δt_f^k should be increased or reduced.

4. A check for steady state is made by calculating the residual value of the Poisson equation based on the newly available electric potential values. The residual is given by

$$r_{norm}^k = \frac{\sqrt{\sum_{i=1}^{N_z}\sum_{j=1}^{N_r}\left[\nabla^2(\varepsilon_a\phi_{i,j}^{k+1}) + \rho_{i,j}\right]^2}}{\sqrt{\sum_{i=1}^{N_z}\sum_{j=1}^{N_r}\left[\rho_{i,j}\right]^2}}. \tag{A.27}$$

Here the Laplace operator is expanded as given in Equation (A.6). The residual value, r^k_{norm} is compared with a minimum tolerance value, *tol*, specified by the user. If the residual value falls below the tolerance limit, the solution is converged and a steady state has been reached; otherwise, the iterations of the DADI technique are continued.

5. If the solution does not reach convergence, the fictitious time step size is varied. To determine the new fictitious time step Δt_f^{k+1}, a test parameter value is calculated based on the L_2 norm of the solutions obtained in step 1 and step 2. The L_2 norms are given by

$$L_{\phi diff} = \|\phi_{i,j}^{k+1} - \overline{\phi}_{i,j}^{k+1}\|, \tag{A.28}$$

and

$$L_{\phi error} = \|\phi_{i,j}^{k+1} - \phi_{i,j}^{k}\|. \tag{A.29}$$

The test parameter is then computed as

$$TP = \frac{L_{\phi diff}}{L_{\phi error}}. \tag{A.30}$$

6. This test parameter value is used to find the multiplicative factor, f_w by which the Δt_f^k can be altered for the next iteration. Table 3.3 shows the multiplicative factor values for different test parameter ratios [Mardahl 2001]. The new Δt_f^{k+1} becomes

$$\Delta t_f^{k+1} = f_w \Delta t_f^k. \tag{A.31}$$

If the test parameter ratio goes more than 0.6, the fictitious time step is reduced by $1/8^{th}$ and the solution obtained in the current iteration is discarded. The $\phi_{i,j}$ values are reset to the ϕ values at the beginning of the iteration.

7. The iteration index is increased by one, k=k+1 and steps 2 through 7 should be repeated until the desired convergence is obtained.

For the next Poisson solution call, the previous Poisson electric potential results are utilized as an initial guess. The initial fictitious time step size for the next Poisson solution is set to 1/4 of the final iteration fictitious time step size of the previous call.

Table A.1: Fictitious time step control in the DADI solver.

TP	f_w
< 0.02	8.0
0.02 - 0.05	4.0
0.05 - 0.1	2.0
0.1 - 0.3	0.80
0.3 - 0.4	0.50
0.4 - 0.6	0.25
> 0.6	0.125

B

History of NSTAR Ion Engine

Since all of the results presented in this dissertation are for the NSTAR (NASA Solar Electric Propulsion Technology Application Readiness Program) ion engine it is reasonable to present some information on the history of this engine. This appendix gives details on the NSTAR engine and the highly successful Deep Space 1 mission that used NSTAR ion engines for its propulsion. The details of the NSTAR ion engine presented here are obtained from the following papers: [Brophy et al. 2000; Polk et al. 1999; Polk et al. 2000; Polk et al. 1997; Anderson et al. 1999; Anderson et al. 2000; Sengupta et al. 2002; Sengupta et al. 2003; Sengupta et al. 2004; Sengupta 2005; Williams 2000; Herman and Gallimore 2004a; 2004b; Herman 2005].

B.1 Development of NSTAR's Discharge Chamber

The idea of the NSTAR program was conceived over three decades of design studies conducted at the NASA Lewis Research Center (currently called Glenn Research Center), JPL, and Hughes Research Labs under various ion engine programs. These ion engine programs focused on identifying and developing ion thruster discharge chambers that were feasible for the requirements of deep space missions and other space applications such as satellite station keeping and orbit-transfer of space vehicles. The key system parameters such as the power input levels, payload capability, thruster

efficiency, specific impulse, low ion beam production cost, and expected life time operation in space were considered in these ion engine programs. Long-duration tests were conducted on identifying the life-limiting mechanisms of the ion engine components, such as the grid optics, and hollow cathodes. From these years of ion engine studies, the following discharge chamber designs were implemented on an ion thruster called NSTAR: ring-cusp magnetic fields, xenon propellant, conical-cylindrical shaped discharge chamber, non-ferromagnetic materials for walls, hollow cathode assembly, cathode keeper assembly, low-sputter yield materials for ion grids, beam voltage supplies, electric circuit arrangement, and power operating range. The path to reach the above design features on the modern NSTAR ion engine traversed years of investigative studies performed on the ion engine discharge chamber.

The ion engine discharge chamber with a ring-cusp magnetic field configuration had been found to improve the ion containment and gave lower ion beam production costs over the line-cusp magnetic field configuration [Sovey 1984]. Similar performance results were also reported in the work by Matossian and Beattie [1991] with the ring-cusp magnetic field configurations on the NSTAR ion engine discharge chamber. The above two studies were conducted on a cylindrically shaped discharge chamber made of iron. Along with the magnetic fields study, the effects of different propellants were also explored at NASA and Hughes Research Labs. The propellants studied were the inert gases argon, xenon, krypton, and other liquefied gases such as mercury and cesium. Though mercury has a lower threshold ionization compared to the inert gases, it is not been considered as a propellant option for several years. The main reason is mercury's ecological concerns and health risks. In the inert gases list, the beam ion production cost using xenon propellant on the NSTAR ion engine discharge chamber was found to be lower than argon and krypton [Sovey 1984]. In a comparison between xenon and mercury, the xenon propellant was found to give 15 eV less ion beam production cost [Matossian and Beattie 1991]. Later at NASA GRC, a modified NSTAR functional model thruster (FMT) was considered for ion propulsion systems. In the new ion engine discharge chamber design [Patterson et al. 1993], a partial conical section was considered at the back wall of the discharge

chamber. The partial conical section was considered to minimize the weight of the discharge chamber and improve the structural and vibration strength of the engine assembly in the spacecraft. A non-ferromagnetic material, aluminum, was used on the discharge chamber to reduce the ion thruster mass. This thruster was tested for the operating conditions between 0.7-4.9 kW input power and provided specific impulses between 2290 - 4030 s, thruster efficiencies between 0.45-0.72, propellant utilization efficiencies between 0.81-0.87, and ion beam production costs between 280 W/A - 190 W/A.

As part of the NSTAR program two flight thrusters (FT), and four engineering model thrusters (EMT) were developed. The engineering model discharge chambers EMT1, EMT2, EMT3 and EMT4 were fabricated at NASA GRC while the two flight thrusters FT1 and FT2 were fabricated at the Hughes Electron Dynamics Division. The EMTs were developed to study the performance characterization, wear rates of different discharge chamber components, and to predict the lifetime of the ion thruster on the Deep Space 1 (DS1) mission. The design features on the EMT thrusters were mostly inherited from the FMT developed at NASA GRC [Patterson et al. 1993]. However, new design modifications on the EMT discharge chambers were made in sequences based on the tests performed on the EMT thrusters. Later these major design modifications were incorporated in the design of the FTs. The wear and the long duration tests on the EMT1 and EMT2 thruster were performed to study the major life limiting components of the ion engine discharge chamber. The erosion of the accelerator grid plate was expected to be the major life limiting component on the ion engine, followed by the erosion of the hollow cathodes and screen grid plate. A 2000-hr wear test was performed on the EMT1 thruster at the maximum operating power, 2.3 kW (TH-15), since this operating condition was believed to be the most severe for wear. In this initial EMT1 setup, the screen grid was allowed to float at the plasma potential by electrical isolation, and the cathode assembly did not include a cathode keeper enclosure. During the 2000 hr test, severe erosion of the discharge cathode orifice plate and cathode heater was observed. The screen grid electric potential was found to be well below the cathode potential which would increase the impingement of ions

on the screen grid. This caused erosion of the screen grid plate. Because of these test some major alterations on the EMT1 design were made. The screen grid was electrically connected to the cathode common potential and an enclosed cathode keeper around the discharge cathode tube was employed. After the alterations, the EMT1 thruster was subjected to a 1000-hr wear test at the full power operating level (TH-15). During this test, no significant erosion of the hollow cathode orifice plate and the screen grid were observed. The cathode keeper assembly was found to protect the cathode orifice plate well, and in subsequent NSTAR thruster designs an enclosed cathode keeper assembly was used.

Following the wear tests, a life demonstration test (LDT) was performed to characterize the performance of the ion thruster under different operating conditions; and to develop the NSTAR throttle table. The 8200 hr LDT was conducted on the EMT2 thruster. The LDT performance results provided an accurate prediction of the expected end-of-life (EOL) performance of the NSTAR thruster on the DS1 mission [Brophy et al. 2000]. Apart from the wear and life demonstration tests, the EMT thrusters were subjected to structural and thermal endurance tests [Sovey et al. 1997]. Also a life demonstration test was conducted on the spare flight thruster FT2 at JPL as part of the NSTAR program. In this extended life test (ELT), the FT2 was subjected to process more than 230 kg of xenon, to operate at different throttle levels, and to demonstrate the life time of the different components on the ion engine discharge chamber [Sengupta et al. 2003]. The life test was began just prior to the launch of DS1 spacecraft and was voluntarily terminated on June 2003 after 30,352 hours of operation. Five different throttle conditions TH-12, TH-15, TH-8, TH-5 and TH-0 were used during this life test. The dominant test point was the TH-15 throttle level for a total of 13,951 hours of operation in three test segments. Details of the various test segments during the extended life test can be found in Sengupta et al. [2003]. At the end of the ELT, only a slight performance degradation of the ion thruster was observed for the throttle levels between TH0 and TH12. A larger performance degradation of the discharge chamber was observed at the TH-15 level up to 10% on the engine efficiency and the measured thrust values. Significant erosion of the discharge cathode

keeper and accelerator grid wear were observed during this ELT. The cathode keeper wear caused full exposure of the cathode heater and cathode orifice plate. Though the accelerator grid wear was severe, the accelerator grid was found to be operational for the mid to lower throttle levels [Sengupta et al. 2003].

Apart from the NSTAR program, the University of Michigan's PEPL lab [Herman 2005; Williams 2000] and NASA's JPL [Sengupta et al. 2004; Sengupta 2005; Sengupta et al. 2006] had conducted experimental studies on NSTAR type discharge chambers. The PEPL lab utilized NASA GRC's FMT while JPL had fabricated their own NSTAR type discharge chamber to perform studies. These experimental studies were focused on investigating the plasma potential mapping and to measure the plasma structure under different NSTAR throttle conditions.

B.2 Deep Space One Mission

The Deep Space 1 mission in short known as DS1 was undertaken to validate twelve high-risk technologies in space as part of the first mission of NASA's New Millennium Program (NMP) [Marc D. Rayman 2001]. The Solar Electric Propulsion System (SEPS) validation was one of the advanced technologies that was being tested during this mission. Also this was the first mission where the primary propulsion of a spacecraft was based on an ion engine. Under the SEPS development, NASA GRC and JPL partnered on an effort called the NASA Solar Electric Propulsion Technology Application Readiness (NSTAR) program to design and develop an ion thruster for the DS1 mission. Other industrial partners on the NSTAR program were Boeing Electron Dynamic Devices (formerly Hughes Electron Dynamics Devices), Spectrum Astro, Inc., Moog Scientific Products, Inc., and Physical Science, Inc. The NSTAR program included the design of a flight qualified ion thruster assembly, development of a power processing unit (PPU), development of a digital control interface unit (DCIU), and the development of a xenon feed system (XFS). Two flight qualified xenon ion thrusters (FT1 and FT2) were designed to deliver a total change of speed of 4.5 km/s while using

Table B.1: NSTAR Throttle Table.

NSTAR Throttle Levels	P_{IN} (kW)	V_B (V)	I_B (A)	V_D (V)	I_D (A)	Main Xe Flow (sccm)	Cathode Xe Flow (sccm)	T (mN)	I_{sp} (s)	η_t
TH15	2.29	1100	1.76	25.14	13.13	23.43	3.70	92.4	3120	0.618
TH14	2.17	1100	1.67	25.40	12.35	22.19	3.35	87.6	3157	0.624
TH13	2.06	1100	1.58	25.40	11.60	20.95	3.06	82.9	3185	0.630
TH12	1.94	1100	1.49	25.40	10.87	19.86	2.89	78.2	3174	0.628
TH11	1.82	1100	1.40	25.40	10.17	18.51	2.72	73.4	3189	0.631
TH10	1.70	1100	1.30	25.83	9.50	17.22	2.56	68.2	3177	0.626
TH9	1.57	1100	1.20	25.40	8.86	15.98	2.47	63.0	3136	0.618
TH8	1.44	1100	1.10	25.10	8.24	14.41	2.47	57.8	3109	0.611
TH 7	1.33	1100	1.76	25.14	13.13	12.90	2.47	52.5	3067	0.596
TH 6	1.21	1100	0.91	25.40	12.35	11.33	2.47	47.7	3058	0.590
TH 5	1.09	1100	0.81	25.40	11.60	9.82	2.47	42.5	3002	0.574
TH 4	0.97	1100	0.71	25.40	10.87	8.30	2.47	37.2	2935	0.554
TH 3	0.85	1100	0.61	25.40	10.17	6.85	2.47	32.0	2836	0.527
TH 2	0.74	1100	0.52	25.83	9.50	5.77	2.47	27.4	2671	0.487
TH 1	0.60	850	0.53	25.40	8.86	5.82	2.47	24.5	2736	0.472
TH 0	0.47	650	0.51	25.10	8.24	5.98	2.47	20.6	1972	0.420

81 kg of xenon [Brophy et al. 2000]. The input power for the DS1 flight ion engine depended on the solar energy obtained from the solar panel's relative location to the sun. Hence the ion engines were designed to operate at a wide range of power levels from 0.5 kW to 2.3 kW (see Table B.1). Also as part of the NSTAR program four engineering model thrusters (EMT) were designed and developed to perform ground based long duration tests to demonstrate the ion engine performance over the throttling levels considered in the in-flight thruster, characterization of the engine and plume interactions, and in understanding the life-limiting failure mechanisms during the operation. Out of the two flight qualified thrusters, the FT1 thruster was considered for the space mission while the FT2 thruster was retained at JPL to perform long duration tests. These thrusters and their design modifications that lead to the FTs design are discussed in detail in the DS1 mission report by Brophy et al. [2000].

The developed NSTAR flight thruster was assembled on the DS1 spacecraft and launched into space on October 24, 1998. The primary mission on the path of the DS1 spacecraft was to fly by

the asteroid called Braille (1992KD) in July 1999 after 1800 hours of operation. The DS1 spacecraft fulfilled its primary mission in September 1999; However NASA continued the mission and operated the DS1 spacecraft to fly by comet Borrelly. In this extended mission, the DS1 spacecraft flew by comet Borrelly on September 22, 2001 and successfully passed within 2,200 kilometers of the comet. The data collected from the DS1 spacecraft images were helpful to scientists in analyzing the comet's surface, to measure and identify the gases coming from the comet, to measure the interaction of solar wind with the comet, and to investigate the presence of water. In the extended mission, the DS1 ion thruster had operated in space for 14,000 hours, which makes the NSTAR the first ion thruster to operate for such a long time in space. NASA had hyper extended the DS1 mission to perform a series of long duration tests on the ion thruster performance. Finally the DS1 mission was concluded on December 18, 2001 and the ground control of the spacecraft was terminated. During this three year, 2 months mission, the DS1 ion thruster operated for 16,265 hours ($\sim$ 677 days) utilizing 73 kg xenon propellant. The expected design life of the NSTAR ion thruster from the ground test was about 8000 hours of operation at its full operating power level while processing 83 kg of xenon propellant [Brophy et al. 2000; Bond et al. 1999]. The DS1's in-flight ion thruster was operated twice its designed lifetime. It should be noted here that the flight ion thruster, on average, was operated at the 0.88 kW power level [Brophy 2002], while the estimated design life time was based on operating the thruster at the full power 2.3 kW.

The DS1 mission's huge success has demonstrated that ion engines can be considered a viable option for future deep space missions. The validation of a long life for the NSTAR ion thruster, both in space and during the extended life tests on the ground, have made NASA consider ion propulsion systems for future, distance space missions. The upcoming DAWN mission in September 2007, NASA's JPL will be using the DS1's NSTAR ion propulsion system for the study of two of the largest protoplanets, Ceres and Vesta, in the asteroid belt between Mars and Jupiter [Marc D. Rayman 2007]. In contrast to the NSTAR DS1 mission, the Dawn mission will employ three NSTAR thrusters and each ion engine is expected to operate at a change of speed of 11 km/s with a xenon

throughput capability of 150 kg of xenon [Brophy et al. 2003; Brophy et al. 2005]. The total xenon tank capacity planned for the Dawn mission can hold up to 450 kg of xenon. Dawn's expected spacecraft lifetime will be nearly 10 years in space and the cumulative ion thruster operation will be more than 5 years.

References

Anderson, J. R., Goodfellow, K. D., Polk, J. E., Rawlin, V. K., Sovey, J. S., and Patterson, M. J. 2000. Performance Characteristics of the NSTAR Ion Thruster During an On-Going Long Duration Ground Test. IEEE. IEEE Aerospace Conference Proceedings.

Anderson, J. R., Goodfellow, K. D., Polk, J. E., Shotwell, R. F., Rawlin, V. K., Sovey, J. S., and Patterson, M. J. 1999. Results of an On-going Long Duration Test of the DS1 Flight Spare Engine. AIAA-99-2857. Joint Propulsion Conference.

Ansoft Corporation. 2007. MAXWELL-2D.

Arakawa, Y. and Ishihara, K. 1991. A Numerical Code for Cusped Ion Thrusters. IEPC-91-118. 22nd International Electric Propulsion Conference, Viareggio, Italy.

Arakawa, Y. and Wilbur, P. J. 1991. Finite Element Analysis of Plasma Flows in Cusped Discharge Chambers. *Journal of Propulsion and Power 7,* 1, 125–128.

Arakawa, Y. and Yamada, T. 1990. Monte Carlo Simulation of Primary Electron Motions in Cusped Discharge Chambers. AIAA-90-2654. 21st International Electric Propulsion Conference, Orlando, FL.

Bell, E. W., Djuric, N., and Dunn, G. H. 1993. Electron-Impact Ionization of In+ and Xe+. *Physical Review A 48,* 6 (December), 4286–4291.

Bennett, W., Ogunjobi, T. A., and Menart, J. A. 2007. Computational Study of the Effects of Cathode Placement, Electron Energy, and Magnetic Field Strength on the Confinement of Electrons. AIAA paper 2007-5248. 43rd AIAA/ASME/SAE/ASEE Joint Propulsion Conference and Exhibit, Cincinnati, OH.

Bird, G. A. 1994. *Molecular Gas Dynamics and the Direct Simulation of Gas Flows.* Oxford University Press.

Birdsall, C. K. 1991. Particle-in-cell charged-particle simulations, plus Monte Carlo collisions with neutral atoms, PIC-MCC. *IEEE Transactions on Plasma Science 19*, 65–85.

Birdsall, C. K. and Langdon, A. B. 1991. *Plasma Physics via Computer Simulation.* Adam Hilger.

Bond, T. A., Benson, G., Christensen, J., Gallagher, J. T., and Matranga, M. 1999. The NSTAR Ion Propulsion Subsystem for DS1. AIAA-1999-2972. 37th AIAA/ASME/SAE/ASEE Joint Propulsion Conference and Exhibit, Seattle, WA.

Bowers, K. J. 2001. Accelerating a Particle-in-Cell Simulation Using a Hybrid Counting Sort. *Journal of Computational Physics 173*, 393–411.

Boyd, I. D., Sun, Q., Cai, C., and Tatum, K. E. 2005. Particle Simulation of Hall Thruster Plumes in the 12V Vacuum Chamber. IEPC-2005-138. The 29th International Electric Propulsion Conference, NJ.

Brophy, J. R. 2002. NASA's Deep Space 1 Ion Engine (plenary). *Review of Scientific Instruments 73,* 2 (February), 1071–1078.

Brophy, J. R., Brinza, D. E., Polk, J. E., Henry, M. D., and Sengupta, A. 2002. The DS1 Hyper-Extended Mission. AIAA-2002-3673. 38th AIAA/ASME/SAE/ASEE Joint Propulsion Conference and Exhibit, Indianapolis, IN.

Brophy, J. R., Kakuda, R. Y., Polk, J. E., Anderson, J. R., Marcucci, M. G., Brinza, D., Henry, M. D., Fujii, K. K., Mantha, K. R., Stocky, J. F., Sovey, J., Patterson, M. J., Rawlin, V. K., Hamley, J., Bond, T., Christensen, J., Cardwell, H., Benson, G., Gallagher, J., Matranga, M., and Bushway, D. 2000. Ion propulsion system (nstar) ds1 technology validation report. Tech. rep., JPL.

Brophy, J. R., Marcucci, M. G., Ganapathi, G. B., Garner, C. E., Henry, M. D., Nakazono, B., and Noon, D. 2003. The Ion Propulsion System For Dawn. AIAA-2003-4542. 39th AIAA/ASME/SAE/ASEE Joint Propulsion Conference and Exhibit, Huntsville, AL.

Brophy, J. R., Marcucci, M. G., Ganapathi, G. B., Gates, J., Garner, C. E., Klatte, M., Lo, J., Nakazono, B., and Pixler, G. 2005. Implementation of the Dawn Ion Propulsion System. AIAA-2005-4071. 41st AIAA/ASME/SAE/ASEE Joint Propulsion Conference and Exhibit, Tucson, AZ.

Brophy, J. R. and Wilbur, P. J. 1985. Simple Performance Model for Ring and Line Cusp Ion Thruster. *AIAA Journal 23,* 11, 1731–1736.

Bruhwiler, D. 2005. . OOPIC User Forum. .

Bruhwiler, D. L., Giacone, R. E., Cary, J. R., Verboncoeur, J. P., Mardahl, P., Esarey, E., Leemans, W. P., and Shadwick, B. A. 2001. Particle-in-cell Simulations of Plasma Accelerators and Electron-Neutral Collisions. *Physical Review Special Topics-Accelerators and Beams 4*, 101302.

Dababneh, M. S., Kauppila, W. E., Downing, J. P., Laperriere, F., Pol, V., Smart, J. H., and Stein, T. S. 1980. Measurements of Total Scattering Cross Sections for Low-Energy Positrons and Electrons Colliding with Krypton and Xenon. *Physical Review A 22,* 5 (November), 1872–1877.

Deshpande, S. S. 2005. Computer simulations of trajectories of primary electrons inside the discharge chamber of an ion engine. M.S. thesis, Wright State University.

Deshpande, S. S., Mahalingam, S., and Menart, J. A. 2004. Computational Study of Primary Electrons in the Cusp Region of an Ion Engine's Discharge Chamber. AIAA paper 2004-4109. 40th AIAA/ASME/SAE/ASEE Joint Propulsion Conference and Exhibit, Ft Lauderdale, FL.

Deshpande, S. S., Ogunjobi, T., and Menart, J. A. 2005. Computational Study of Magnet Placement on the Discharge Chamber of an Ion Engine. AIAA paper 2005-4254. 41st AIAA/ASME/SAE/ASEE Joint Propulsion Conference and Exhibit, Tucson, AZ.

Domonkos, M. T. 2002. A Particle and Energy Balance Model of the Orificed Hollow Cathode. AIAA paper 2002-4240. 38th AIAA/ASME/SAE/ASEE Joint Propulsion Conference and Exhibit, Indianapolis, IN.

Domonkos, M. T., Gallimore, A. D., Jr, G. J. W., and Patterson, M. J. 1999. Low-Current Hollow Cathode Evaluation. AIAA paper 1999-2575. 35th AIAA/ASME/SAE/ASEE Joint Propulsion Conference and Exhibit, Los Angeles, CA.

Doss, S. and Miller, K. 1979. Dynamic ADI Methods for Elliptic Equations. *SIAM J. Numer. Anal. 16,* 5 (October), 837–856.

Elliott, F. W., Foster, J. E., and Patterson, M. J. 2004. An Overview of the High Power Electric Propulsion Program. AIAA paper 2004-3453. 40th AIAA/ASME/SAE/ASEE Joint Propulsion Conference and Exhibit, Fort Lauderdale, FL.

Emhoff, J. W. and Boyd, I. D. 2004. Progress in NEXT Ion Optics Modeling. AIAA paper 2004-3786. 40th AIAA/ASME/SAE/ASEE Joint Propulsion Conference and Exhibit, Ft Lauderdale, FL.

Foster, J. E., Soulas, G. C., and Patterson, M. J. 2000. Plume and Discharge Plasma Mea-

surements of an NSTAR-type Ion Thruster. AIAA-2000-3812. 36th AIAA/ASME/SAE/ASEE Joint Propulsion Conference and Exhibit, Huntsville, AL.

Fox, J. M., Batishcheva, A. A., Batishchev, O. V., and Sanchez, M. M. 2006. Adaptively Meshed Fully-Kinetic PIC-Vlasov Model For Near Vacuum Hall Thrusters. AIAA paper 2006-4324. 42nd AIAA/ASME/SAE/ASEE Joint Propulsion Conference, Sacramento, CA.

Fridman, A. and Kennedy, L. A. 2004. *Plasma Physics and Engineering*. Taylor Francis Group.

Goebel, D. M., Jameson, K. K., Watkins, R., and Katz, I. 2004. Hollow Cathode and Keeper-Region Measurements Using Ultra-Fast Miniature Scanning Probes. AIAA paper 2004-3430. 40th AIAA/ASME/SAE/ASEE Joint Propulsion Conference and Exhibit, Ft Lauderdale, FL.

Goebel, D. M., Wirz, R. E., and Katz, I. 2006. Analytical Ion Thruster Discharge Performance Model. AIAA paper 2006-4486. 42nd AIAA/ASME/SAE/ASEE Joint Propulsion Conference and Exhibit, Sacramento, CA.

Griffiths, D. J. 1989. *Introduction to Electrodynamics*, 2nd ed. Prentice Hall, Englewood, NJ.

Hayashi, M. 1983. Determination of Electron-Xenon Total Excitation Cross-Sections, from Threshold to 100 eV, from Experimental Values of Townsend's α. *Journal of Physics D: Applied Physics 16*, 581–589.

Herman, D. A. 2005. The Use of Electrostatic Probes to Characterize the Discharge Plasma Structure and Identify Discharge Cathode Erosion Mechanisms in Ring-Cusp Ion Thrusters. Ph.D. thesis, University of Michigan.

Herman, D. A. and Gallimore, A. D. 2004a. Discharge Chamber Plasma Structure of a 30-cm NSTAR-type Ion Engine. AIAA-2004-3794. 40th AIAA/ASME/SAE/ASEE Joint Propulsion Conference and Exhibit, Fort Lauderdale, FL.

Herman, D. A. and Gallimore, A. D. 2004b. Near Discharge Cathode Assembly Plasma Potential Measurements in a 30-cm NSTAR-type Ion Engine amidst Beam Extraction. AIAA-2004-3958. 40th AIAA/ASME/SAE/ASEE Joint Propulsion Conference and Exhibit, Fort Lauderdale, FL.

Hewett, D. W., Larson, D. J., and Doss, S. 1992. Solution of Simultaneous Partial Differential Equations Using Dynamic ADI:Solution of the Streamlined Darwin Field Equations. *J. Comp. Phys 101*, 11–24.

Hiatt, J. M. and Wilbur, P. J. 1986. Ring Cusp Discharge Chamber Performance Optimization. *Journal of Propulsion and Power 2,* 5, 390–397.

Hirakawa, M. and Arakawa, Y. 1993. Plasma Particle Simulation in Cusped Ion Thrusters. IEPC-93-242. 23rd International Electric Propulsion Conference, Seattle, WA.

Hockney, R. W. and Eastwood, J. W. 1988. *Computer Simulation Using Particles*, 1st Edition ed. Adam Hilger.

Jacobs, G. B. and Hesthaven, J. S. 2006. High-order Nodal Discontinuous Galerkin Particle-in-cell Method on Unstructured Grids. *Journal of Computational Physics 214*, 96–121.

Jahn, R. G. 1968. *Physics of Electric Propulsion.* McGraw-Hill.

Jameson, K. K., Goebel, D. M., and Watkins, R. M. 2005. Hollow Cathode and Keeper-Region Plasma Measurements. AIAA paper 2005-3667. 41st AIAA/ASME/SAE/ASEE Joint Propulsion Conference and Exhibit, Tucson, AZ.

Kamayema, I. and Wilbur, P. J. 1998. Potential Hill Model of High Energy Ion Production near High Current Hollow Cathodes. ISTS paper 98-a-2-17. 21st International Symposium on Space Technology and Science, Japan.

Katz, I., Anderson, J. R., Polk, J. E., and Brophy, J. R. 2003. One-Dimensional Hollow Cathode Model. *Journal of Propulsion and Power 19,* 4, 595–600.

Kawamura, E., Birdsall, C. K., and Vahedi, V. 2000. Physical and Numerical Methods of Speeding up Particle Codes and Paralleling as Applied to RF Discharges. *Plasma Sources Sci. Technol. 9*, 413–428.

Kim, H. C., Iza, F., Yang, S. S., Radmilovic-Radjenovic, M., and Lee, J. K. 2005. Particle and Fluid Simulations of Low-Temperature Plasma Discharges:Benckmarks and Kinetic Effects. *Journal of Physics D: Applied Physics 38,* R283-R301, 083505.

Kolev, I., Bogaerts, A., and Gijbels, R. 2005. Influence of Electron Recapture by the Cathode Upon the Discharge Characteristics in DC Planar Magnetron. *Physical Review E 72*, 056402.

Lam, L. T. S. F. 1982. Relativistic Effects in Electron Scattering by Atoms III. Elastic Scattering by Krypton, Xenon and Radon. *J. Phys. B: At. Mol. Phys. 15,* 1 (January), 119–142.

Lapenta, G. and Brackbill, J. U. 1994. Dynamic and Selective Control of the Number of Particles in Kinetic Plasma Simulations. *Journal of Computational Physics 115*, 213–227.

Luginsland, J. W., McGee, S., and Lau, Y. Y. 1998. Virtual Cathode Formation Due to Electromagnetic Transients. *IEEE Transactions on Plasma Science 26,* 3, 901–904.

Mahalingam, S. 2002. Primary electron modeling in the discharge chamber of an ion engine. M.S. thesis, Wright State University.

Mahalingam, S. and Menart, J. A. 2002. Primary Electron Modeling in the Discharge Chamber of an Ion Engine. AIAA paper 2002-4262. 38th AIAA/ASME/SAE/ASEE Joint Propulsion Conference and Exhibit, Indianapolis, IN.

Mahalingam, S. and Menart, J. A. 2005. Computational Model Tracking Primary Electrons, Secondary Electrons and Ions in the Discharge Chamber of an Ion Engine. AIAA paper 2005-4253. 41st AIAA/ASME/SAE/ASEE Joint Propulsion Conference and Exhibit, Tucson, AZ.

Mahalingam, S. and Menart, J. A. 2006. Ion Engine Discharge Chamber Plasma Modeling Using a 2-D PIC Simulation. AIAA paper 2006-4488. 42nd AIAA/ASME/SAE/ASEE Joint Propulsion Conference and Exhibit, Sacramento, CA.

Mahalingam, S. and Menart, J. A. 2007a. Computational Study of Primary Electron Confinement by Magnetic Fields in the Discharge Chamber of an Ion Engine. *Journal of Propulsion and Power 23,* 1, 69–72.

Mahalingam, S. and Menart, J. A. 2007b. Particle Based Plasma Simulations for an Ion Engine Discharge Chamber. AIAA paper 2007-5247. 43rd AIAA/ASME/SAE/ASEE Joint Propulsion Conference and Exhibit, Cincinnati, OH.

Marc D. Rayman. 2001. Deep Space 1 Mission.

Marc D. Rayman. 2007. Dawn Mission.

Mardahl, P. 2001. PIC Code Charge Conservation, Numerical Heating, and Parallelization; Application of XOOPIC to Laser Amplification via Raman Backscatter. Ph.D. thesis, University of California, Berkeley.

Mardahl, P. J. and Verboncoeur, J. P. 1998. Progress in Parallelizing XOOPIC. IEEE paper 1998. 25th Anniversary IEEE Conference Record, Plasma Science, Cincinnati, OH.

Marek, A., Kudrna, P., Pickova, I., Holik, M., Bilyk, O., and Tichy, M. 2005. 2D PIC Simulation of the DC Discharge in Cylindrical Magnetron. ISBN 80-86732-59-2. WDS'05 Proceedings of Contributed Papers, Part II 362-367.

Matossian, J. N. and Beattie, J. R. 1989. Model for Computing Volume-Averaged Plasma Properties in Electron-Bombardment Ion Thrusters. *Journal of Propulsion and Power 5,* 2, 188–196.

Matossian, J. N. and Beattie, J. R. 1991. Characteristics of Ring-Cusp Discharge Chambers. *Journal of Propulsion and Power 7,* 6, 968–974.

Menart, J. A. 1998. Magnetic field codes. NASA Internal Memo.

Mikellides, I., Katz, I., Goebel, D. M., and Polk, J. E. 2005a. Theoretical Model of a Hollow Cathode Plasma for the Assesment of Insert and Keeper Lifetimes. AIAA paper 2005-4234. 41st AIAA/ASME/SAE/ASEE Joint Propulsion Conference and Exhibit, Tucson, AZ.

Mikellides, I. G., Katz, I., Goebel, D. M., and Polk, J. E. 2005b. Hollow Cathode Theory and Experiment: II. A Two-Dimensional Theoretical Model of the Emitter Region. *Journal of Applied Physics 98*, 113303.

Milder, N. L. 1962. Comparative measurements of singly and doubly ionized mercury produced by electron-bombardment ion engine. Technical Note TN D-1219, NASA.

Morris, D. and Gilchrist, B. 2004. Electron Emission for Electric Propulsion:Reducing Power by Mitigating Space Charge Limits. AIAA paper 2004-3497. 40th AIAA/ASME/SAE/ASEE Joint Propulsion Conference and Exhibit, Ft Lauderdale, FL.

Mura, P. H. D. 1952. Investigation of the photoelectric work function of titanium. Technical Report AD0001286, PRINCETION UNIVERSITY.

Nedelea, T. and Urbassek, H. M. 2004. Particle-In-Cell Study of Charge-State Segregation in Expanding Plasmas Due to Three-body Recombination. *Journal of Physics D: Applied Physics 37*, 2981–2986.

Neiter, C. and Cary, J. R. 2004. VORPAL:A Versatile Plasma Simulation Code. *J. Comp. Phys. 196*, 448–472.

NIST. 2007. Nist atomic spectra database. http://physics.nist.gov/PhysRefData/ASD/index.html.

Ogunjobi, T. A. and Menart, J. A. 2006. Computational Study of Ring-Cusp Magnet Configurations that Provide Maximum Electron Confinement. AIAA paper 2006-4489. 42nd AIAA/ASME/SAE/ASEE Joint Propulsion Conference and Exhibit, Sacramento, CA.

Okawa, Y. and Takegahara, H. 2001. Numerical Study of Beam Extraction Phenomena in an Ion Thruster. *Japan Journal of Appl. Phys. 40,* 1, 31–321.

Parker, S. E. 2002. Nearest-Grid-Point Interpolation in Gyrokinetic Particle-in-Cell Simulation. *Journal of Computational Physics 178*, 520–532.

Passaro, A., Nania, F., and Vicini, A. 2006. Full 3D PIC Simulation of Hall Effect Thrusters. AIAA paper 2006-3246. 37th AIAA Plasmadynamics and Lasers Conference, San Francisco, CA.

Patterson, M. J., Foster, J. E., Haag, T. W., Rawlin, V. K., Soulas, G. C., and Roman, R. F. 2002. NEXT:NASA's Evolutionary Xenon Thruster. AIAA paper 2002-3832. 38th AIAA/ASME/SAE/ASEE Joint Propulsion Conference and Exhibit, Indianapolis, IN.

Patterson, M. J., Haag, T. W., and Hovan, S. A. 1993. Performance of the NASA 30 cm Ion Thruster. IEPC paper 93-108. 23rd AIAA/AIDAA/DGLR/JSASS International Electric Propulsion Conference, Seattle, WA.

Polk, J. E., Anderson, J. R., Brophy, J. R., Rawlin, V. K., Patterson, M. J., and Sovey, J. S. 1997. The Effect of Engine Wear on Performance in the NSTAR 8000 Hour Ion Engine Endurance Test. AIAA-97-3387. 33rd AIAA/ASME/SAE/ASEE Joint Propulsion Conference and Exhibit, Seattle, WA.

Polk, J. E., Anderson, J. R., Brophy, J. R., Rawlin, V. K., Patterson, M. J., Sovey, J. S., and Hamley, J. 1999. An Overview of the Results from an 8200 Hour Wear Test of the NSTAR Ion Thruster. AIAA-99-2446. 35th AIAA/ASME/SAE/ASEE Joint Propulsion Conference and Exhibit, Los Angeles, CA.

Polk, J. E., Goebel, D., Brophy, J. R., Beatty, J., Monheiser, J., Giles, D., Hobson, D., Wilson, F., Christensen, J., Pano, M. D., Ohlinger, S. H. W., Hill, D. N., Williams, J., Wilbur, P., Laufer, D. M., and Farnell, C. 2003. An Overview of the Nuclear Electric

Xenon Ion System (NEXIS) Program. AIAA paper 2003-4713. 39th AIAA/ASME/SAE/ASEE Joint Propulsion Conference and Exhibit, Huntsville, AL.

Polk, J. E., Goebel, D. M., Watkins, R. M., Jameson, K. K., Yoneshige, L., Przybylowski, J., and Chu, L. 2006. Characterization of Hollow Cathode Performance and Thermal Behavior. AIAA paper 2006-5150. 42nd AIAA/ASME/SAE/ASEE Joint Propulsion Conference and Exhibit, Sacramento, CA.

Polk, J. E., Kakuda, R. Y., Anderson, J. R., Brophy, J. R., Rawlin, V. K., Patterson, M. J., Sovey, J., and Hamley, J. 1999. Validation of the NSTAR Ion Propulsion System on the Deep Space One Mission:Overview and Initial Research. AIAA paper 99-2274.

Polk, J. E., Kakuda, R. Y., Anderson, J. R., Brophy, J. R., Rawlin, V. K., Sovey, J. S., and Hamley, J. 2000. In-Flight Performance of the NSTAR Ion Propulsion System on the Deep Space One Mission. IEEE 2000. IEEE Aerospace Conference Proceedings.

Press, W. H. 1992. *Numerical Recipes in Fortran 77*, 1 ed.

Raizer, Y. P. 1991. *Gas Discharge Physics*. Springer-Verlag Berlin Heidelberg.

Raju, G. G. 2006. *Gaseous Electronics Theory and Practice*. Taylor Francis Group.

Rejoub, R., Lindsay, B. G., and Stebbings, R. F. 2002. Determination of the Absolute Partial and Total Cross Sections for Electron-Impact Ionization of the Rare Gases. *Physical Review A 65,* 1, 042713.

Sakurabayashi, T., Hatayama, A., and Bacal, M. 2004. Effects of the Weak Magnetic Field and Electron Diffusion on the Spatial Potential and Negative Ion Transport in the Negative Ion Source. *Review of Scientific Instruments 75,* 5, 1770–1773.

Saloman, E. B. 2004. Energy Levels and Observed Spectral Lines of Xenon, Xe I through Xe LIV. *J. Phys. Chem. Ref. Data 33,* 3, 765–921.

Sandonato, G. M., Barroso, J. J., and Montes, A. 1996. Magnetic Confinement Studies for Performance Enhancement of a 5-cm Ion Thruster. *IEEE Transactions on Plasma Science 24,* 6, 1319–1329.

Sawdey, A. and O'Keefe, M. 1997. Program Analysis of Overlap Area Usage in Self-Similar Parallel Programs. Springer-Verlag. Proceedings of the Tenth International Workshop on Languages and Compilers for Parallel Computing,Minneapolis, MN.

Scharfe, M. K., Gascon, N., Cappelli, M. A., and Fernandez, E. 2006. Comparison of Hybrid Hall Thruster Model To Experimental Measurements. *Physics of Plasmas 13*, 083505.

Sengupta, A. 2005. Experimental Investigation of Discharge Plasma Magnetic Confinement in an NSTAR Ion Thruster. AIAA paper 2005-4609. 41st AIAA/ASME/SAE/ASEE Joint Propulsion Conference and Exhibit, Tucson, AZ.

Sengupta, A., Anderson, J. R., Brophy, J. R., Rawlin, V. K., and Sovey, J. S. 2002. Performance Characteristics of the Deep Space 1 Flight Spare Ion Thruster Long Duration Test After 21,300 Hours of Operation. AIAA-2002-3959. 38th AIAA/ASME/SAE/ASEE Joint Propulsion Conference and Exhibit, Indianapolis, IN.

Sengupta, A., Brophy, J. R., and Goodfellow, K. D. 2003. Status of the Extended Life Test of the Deep Space 1 Flight Spare Ion Engine After 30,352 Hours of Operation. AIAA paper 2003-4558. 39th AIAA/ASME/SAE/ASEE Joint Propulsion Conference and Exhibit, Huntsville, AL.

Sengupta, A., Goebel, D., Fitzgerald, D., Owens, A., Tynan, G., and Doerner, R. 2004. Experimentally Determined Neutral Density and Plasma Parameters in a 30cm Ion Engine. AIAA paper 2004-3613. 40th AIAA/ASME/SAE/ASEE Joint Propulsion Conference and Exhibit, Fort Lauderdale, FL.

Sengupta, A., Goebel, D., and Owens, A. 2006. Neutral Density Measurments in an NSTAR

Ion Thruster. AIAA paper 2006-4491. 42nd AIAA/ASME/SAE/ASEE Joint Propulsion Conference and Exhibit, Sacramento, CA.

Soulas, G. C. 2001. Performance Evaluation of Titanium Ion Optics for the NASA 30 cm Ion Thruster. IEPC paper 01-092. International Electric Propulsion Conference.

Soulas, G. C., Haag, T. W., Patterson, M. J., and Rawlin, V. K. 1999. Titanium Optics for Ion Thrusters. IEPC paper 99-149. International Electric Propulsion Conference.

Sovey, J. S. 1984. Improved Ion Containment Using a Ring-Cusp Ion Thruster. *Journal of Spacecraft 21,* 5, 488–495.

Sovey, J. S., Hamley, J. A., Haag, T. W., Patterson, M. J., Pencil, E. J., Peterson, T. T., Pinero, L. R., Power, J. L., Rawlin, V. K., Sarimento, C. J., Anderson, J. R., Becker, R. A., Brophy, J. R., Polk, J. E., Benosn, G., Bond, T. A., Cardwell, G. I., Christensen, J. A., Freick, K. J., Hart, D. J. H. S. L., McDowell, J., Norenberg, K. A., Phelps, T. K., Solis, E., Yost, H., and Gallimore, M. M. A. D. 1997. Development of an Ion Thruster and Power Processor for New Millennium's Deep Space 1 Mission. AIAA-1997-2778. 33rd AIAA/ASME/SAE/ASEE Joint Propulsion Conference and Exhibit, Seattle, WA.

Strinic, A. 2007. Swarm studies, cross sections from experimental data. http://mail.phy.bg.ac.yu/ cep/lge/Research/swarmstudies.htm.

Stueber, T. J. 2004. Discharge Chamber Primary Electron Modeling Activities in Three Dimension. AIAA paper 2004-4105. 40th AIAA/ASME/SAE/ASEE Joint Propulsion Conference and Exhibit, Ft. Lauderdale, FL.

Stueber, T. J. 2005. Ion Thruster Discharge Chamber Simulation in Three Dimension. AIAA paper 2005-3688. 41st AIAA/ASME/SAE/ASEE Joint Propulsion Conference and Exhibit, Tucson, AZ.

Szabo, J. J. 2001. Fully Kinetic Numerical Modeling of a Plasma Thruster. Ph.D. thesis, Massachusetts Institute of Technology.

Taccogna, F., Longo, S., Capitelli, M., and Schneider, R. 2005. Self-similarity in Hall Plasma Discharges: Applications to Particle Models. *Physics of Plasmas 12*, 053502.

Tannehill, J. C., Anderson, D. A., and Pletcher, R. H. 1997. *Computational Fluid Mechanics and Heat Transfer*, 2 ed. Taylor Francis.

Tech-X Corporation. 2007. OOPIC Pro.

Tech-X Corporation 2007. *OOPIC Pro User's Guide*, Version 1.2.0 ed. Tech-X Corporation, Boulder, CO 80303.

Vahedi, V. and Surendra, M. 1995. A Monte Carlo Collision Model for the Particle-In-Cell Method: Applications to Argon and Oxygen Discharges. *Comp. Phys. Comm. 87*, 179–198.

VanNoord, J. L. 2007. NEXT Ion Thruster Thermal Model. AIAA paper 2007-5218. 43rd AIAA/ASME/SAE/ASEE Joint Propulsion Conference and Exhibit, Cincinnati, OH.

Vaughn, J. A. and Wilbur, P. J. 1988. Ring Cusp/Hollow Cathode Discharge Chamber Performance Studies. IEPC 364-373. Proceedings of 20th International Electric Propulsion Conference.

Verboncoeur, J. P. 2001. Symmetric Spline Weighting for Charge and Current Density in Particle Simulation. *Journal of Computational Physics 174*, 421–427.

Verboncoeur, J. P., Langdon, A. B., and Gladd, N. T. 1995. An Object-Oriented Electromagnetic PIC Code. *Computer Physics Communications 87*, 199–211.

Verboncoeur, J. P., Lindsay, B. G., and Stebbings, R. F. 1996. Comparison of Collision Rate in Particle-in-Cell, Monte Carlo, and Boltzmann Codes. *Journal of Applied Physics 80,* 3, 1299–1303.

Wang, J., Cao, Y., Kafafy, R., and Decyk, V. 2006. Electric Propulsion Plume Modeling Using Parallel Supercomputers. AIAA paper 2006-3559. 37th AIAA Plasmadynamics and Lasers Conference, San Francisco, CA.

Wang, J., Polk, J., Brophy, J. R., and Katz, I. 2003. Three-Dimensional Particle Simulations of Ion-Optics Plasma Flow and Grid Erosion. *Journal of Propulsion and Power 19,* 6, 1192–1199.

Williams, G. J. 2000. The Use of Laser-Induced Fluorescence to Characterize Discharge Cathode Erosion in a 30cm Ring-Cusp Ion Thruster. Ph.D. thesis, University of Michigan.

Wirz, R. and Katz, I. 2005. Plasma Processes of DC Ion Thruster Discharge Chambers. AIAA paper 2005-3690. 41st AIAA/ASME/SAE/ASEE Joint Propulsion Conference and Exhibit, Tucson, AZ.

Yashko, G., Giffin, G., and Hastings, D. 1997. Design Considerations for Ion MicroThrusters. IEPC-97-072. International Electric Propulsion Conference.

Yee, K. S. 1966. Numerical Solution of Initial Boundary Value Problems Involving Maxwell's Equations in Isotropic Media. *IEEE Transactions on Antennas Propagation 14*, 302–307.